MSSM Higgs Boson Production at a Future Linear Collider
and
Measurement of $F_2^{c\bar{c}}$ and $F_2^{b\bar{b}}$ at Low Q^2 DIS at H1

Dissertation
zur Erlangung des Doktorgrades
des Fachbereichs Physik
der Universität Hamburg

vorgelegt von
Tatsiana Klimkovich
aus Gomel

Hamburg
2005

Gutachter der Dissertation : Univ. Prof. Dr. R.-D. Heuer
Univ. Prof. Dr. B. Naroska

Gutachter der Disputation : Univ. Prof. Dr. R.-D. Heuer
Univ. Prof. Dr. P. Schleper

Datum der Disputation : 17.10.2005

Vorsitzender des Prüfungsausschusses : Univ. Prof. C. Hagner

Vorsitzender des Promotionsausschusses : Univ. Prof. Dr. G. Huber

Dekan des Fachbereichs : Univ. Prof. Dr. G. Huber

Abstract

In the first part of the thesis the potential of the e^+e^- International Linear Collider (ILC) operated at a centre of mass energy of 500 to 1000 GeV is studied for the measurement of the MSSM Higgs boson production. The process of associated Higgs boson production with subsequent Higgs decays into b-quarks $e^+e^- \rightarrow HA \rightarrow b\bar{b}b\bar{b}$ is analysed under the general assumption of the maximal cross section, $\sin^2(\beta - \alpha) = 1$, at a centre of mass energy of 500 GeV and 800 GeV and an assumed integrated luminosity of 500 fb^{-1}. The Higgs boson masses and production cross sections can be measured by reconstructing the $b\bar{b}b\bar{b}$ final states. The precision of these measurements is evaluated in dependence of the Higgs boson masses. Under the assumed experimental conditions a statistical accuracy ranging from several hundred MeV to 1.0 GeV is achievable on the Higgs boson mass. The topological cross section $\sigma(e^+e^- \rightarrow HA \rightarrow b\bar{b}b\bar{b})$ can be determined with the relative precision of 1.5 - 6.6%. The 5σ discovery limit corresponds to a Higgs mass of around 385 GeV for the degenerate H and A Higgs boson masses at $\sqrt{s} = 800$ GeV with an integrated luminosity of 500 fb^{-1}. The general analysis is applied to the process $e^+e^- \rightarrow H_2H_3 \rightarrow b\bar{b}b\bar{b}$ in two CP violating MSSM scenarios and studied at a centre of mass energy of 500 GeV and 800 GeV with an integrated luminosity of 500 fb^{-1}. The potential of the Higgs mass determination for the benchmark point SPS 1a for the process $e^+e^- \rightarrow HA \rightarrow b\bar{b}b\bar{b}$ at $\sqrt{s} = 1$ TeV with an integrated luminosity of 1000 fb^{-1} is also investigated. The sensitivity to the CP violating parameter, the phase of the soft SUSY-breaking trilinear coupling of the top (bottom) squarks to the Higgs boson $\arg(A_{t,b})$ is demonstrated.

In the second part of the thesis the measurements of inclusive charm and beauty cross sections in e^+p collisions at HERA for values of photon virtuality $12 \leq Q^2 \leq 60$ GeV^2 and of the Bjorken scaling variable $0.0002 \leq x \leq 0.005$ are presented. The analysis is based on a sample of e^+p neutral current scattering events corresponding to an integrated luminosity of 57.4 pb^{-1}, taken in the years 1999-2000 with the H1 detector, at an e^+p centre of mass energy $\sqrt{s} = 319$ GeV. The method of determining the fractions of events containing charm and beauty quarks is based on the impact parameter in the transverse plane of tracks from decays of long lived c and b hadrons as reconstructed in the H1 vertex detector. The values of the structure functions $F_2^{c\bar{c}}$ and $F_2^{b\bar{b}}$ are obtained. This is the first measurement of $F_2^{b\bar{b}}$ in this kinematic range. The results are found to be compatible with the predictions of perturbative quantum chromodynamics and with previous measurements of $F_2^{c\bar{c}}$. The charm cross section contributes on average 24% of the inclusive ep cross section, and the beauty fraction increases from 0.4% at $Q^2 = 12$ GeV^2 to 1.5% at $Q^2 = 60$ GeV^2.

Zusammenfassung

Der erste Teil der vorliegenden Arbeit behandelt eine Studie zur Abschätzung des Potentials des geplanten International Linear Colliders (ILC), der Kollisionen von Elektronen und Positronen bei Schwerpunktsenergien im Bereich von 500–1000 GeV erforschen soll. Untersucht wird die Messung der MSSM-Higgsboson-Produktion. Hierzu wird die assoziierte Higgsboson-Produktion mit anschließendem Zerfall der Higgsbosonen in b-Quarks $\mathrm{e}^+\mathrm{e}^- \rightarrow \mathrm{HA} \rightarrow \mathrm{b\bar{b}b\bar{b}}$ unter der allgemeinen Annahme eines maximalen Wirkungsquerschnittes $\sin^2(\beta - \alpha) = 1$ bei zwei Schwerpunktsenergien ($\sqrt{s} = 500$ GeV und 800 GeV) und einer angenommenen integrierten Luminosität von $\mathcal{L} = 500\ \mathrm{fb}^{-1}$ analysiert. Sowohl für die Messung der Higgsbosonen-Massen, als auch für die Bestimmung der für die Produktion geltenden Wirkungsquerschnitte werden die $\mathrm{b\bar{b}b\bar{b}}$-Endzustände rekonstruiert. Die Präzision beider Messungen wird in Abhängigkeit der Higgsbosonen-Massen bestimmt. Unter experimentellen Bedingungen wird die erreichbare Genauigkeit der Higgsbosonen-Massen im Bereich von einigen 100 MeV bis hin zu 1,0 GeV liegen. Der topologische Wirkungsquerschnitt $\sigma(\mathrm{e}^+\mathrm{e}^- \rightarrow \mathrm{HA} \rightarrow \mathrm{b\bar{b}b\bar{b}})$ kann mit einer relativen Genauigkeit von 1,5 - 6,6% gewonnen werden.

Die Grenze des Entdeckungspotentials von 5σ liegt bei etwa 385 GeV für $\sqrt{s} = 800$ GeV und $\mathcal{L} = 500\ \mathrm{fb}^{-1}$ für Higgsbosonen mit entarteten H- und A-Massen. Die Analyse wurde auf den Prozeß $\mathrm{e}^+\mathrm{e}^- \rightarrow \mathrm{H}_2\mathrm{H}_3 \rightarrow \mathrm{b\bar{b}b\bar{b}}$ in zwei CP-verletzenden MSSM Szenarien angewendet und bei einer Schwerpunktsenergie von 500 GeV bzw. 800 GeV und einer integrierten Luminosität von $500\ \mathrm{fb}^{-1}$ untersucht. Das Potential der Massenbestimmung der Higgsbosonen für den Referenzpunkt SPS 1a für den Prozeß $\mathrm{e}^+\mathrm{e}^- \rightarrow \mathrm{HA} \rightarrow \mathrm{b\bar{b}b\bar{b}}$ bei $\sqrt{s} = 1$ TeV und $\mathcal{L} = 1000\ \mathrm{fb}^{-1}$ wird untersucht.

Die Sensitivität auf den CP-verletzenden Parameter, d.h. die Phase der weichen, die Supersymmetry brechenden, trilinearen Kopplung des top (bottom) Squarks an das Higgsboson $\arg(A_{t,b})$, wird gezeigt.

Im zweiten Teil der Arbeit wird die Messung der inklusiven Charm- und Beauty-Wirkungsquerschnitte bei Positron-Proton-Kollisionen ($\mathrm{e}^+\mathrm{p}$) am HERA-Beschleuniger bei DESY für Werte der Photon-Virtualität von $12 \leq Q^2 \leq 60\ \mathrm{GeV}^2$ und der Bjorkenschen Skalen-Variablen $0,0002 \leq x \leq 0,005$ präsentiert. Für die Analyse werden $\mathrm{e}^+\mathrm{p}$-Streuereignisse mit Austausch eines neutralen Stroms verwendet. Die Daten wurden in den Jahren 1999 und 2000 mit dem H1-Detektor bei einer $\mathrm{e}^+\mathrm{p}$-Schwerpunktsenergie von $\sqrt{s} = 319$ GeV aufgezeichnet. Dieses entspricht einer integrierten Luminosität von $\mathcal{L} = 57,4\ \mathrm{pb}^{-1}$.

Die Bestimmung der Anteile von Ereignissen mit Charm- und Beauty-Quarks beruht auf der Messung des sogenannten Impact-Parameters in der Ebene senkrecht zur Strahlrichtung der Zerfallsprodukte langlebiger b- und c-Hadronen mit dem H1-Vertex-Detektor.

Aus den Daten erhält man die Werte der beiden Strukturfunktionen $F_2^{c\bar{c}}$ und $F_2^{b\bar{b}}$, wobei dieses die erste Messung von $F_2^{b\bar{b}}$ im oben angegebenen kinematischen Bereich darstellt. Die Ergebnisse sind sowohl mit den Vorhersagen der perturbativen Quantenchromodynamik, als auch mit früheren Messungen von $F_2^{c\bar{c}}$ vergleichbar. Der Charm-Wirkungsquerschnitt trägt durchschnittlich zu 24% zum inklusiven $\mathrm{e}^+\mathrm{p}$-Wirkungsquerschnitt bei, während der Beauty-Anteil von $0,4\%$ bei $Q^2 = 12\ \mathrm{GeV}^2$ auf $1,5\%$ bei $Q^2 = 60\ \mathrm{GeV}^2$ zunimmt.

Contents

Introduction

The main goals of a future $\mathrm{e^+e^-}$ International Linear Collider (ILC) are the discovery of new phenomena in particle physics as well as precision measurements of the properties of already discovered particles. The Standard Model (SM) is the theory which describes three out of four known interactions: electromagnetic, weak and strong ones (gravitation is not included into the SM). Till now this theory has been confirmed experimentally. The only component of the SM, which to date has not been observed in the experiment, is the Higgs boson. The Higgs mechanism is responsible for electroweak symmetry breaking and the generation of the masses of the weak $\mathrm{W^\pm}$ and Z bosons as well as the masses of fermions (in the SM the electroweak symmetry breaking is provided by one Higgs doublet, which introduces an additional spin-0 particle, the Higgs boson). The search for this particle is the main purpose of the *pp* collider LHC (Large Hadron Collider) at CERN.

Due to some drawbacks of the SM (see Section 1.1.7), other theories beyond the SM have been developed. The most popular of such theories is Supersymmetry with the MSSM as a Minimal Supersymmetric extension of the Standard Model. The MSSM contains two Higgs doublets with five physical Higgs states: two CP-even Higgs bosons, the lighter of which is denoted as h and the heavier H, one CP-odd Higgs boson A and two charged bosons $\mathrm{H^\pm}$. The Higgs sector can be parametrised by m_A and $\tan\beta$, where $\tan\beta$ is the ratio of vacuum expectation values of the two Higgs doublets. The LHC will be able to discover at least the lightest neutral Higgs boson h in all MSSM parameter space. However, there is a "wedge" region in the parameter space (see Section 3.3) where the LHC will be able to discover only the lightest Higgs boson, without differentiating it from the SM Higgs boson and, therefore, not recognising the supersymmetric nature of the electroweak symmetry breaking. In this thesis the possibility to discover heavy neutral MSSM Higgs bosons at a future Linear Collider in the parameter space inaccessible at the LHC will be shown, reflecting the complementarity of the ILC to the LHC.

The process of associated Higgs boson production at a future $\mathrm{e^+e^-}$ Linear Collider with subsequent Higgs boson decays into b-quarks

$$\mathrm{e^+e^- \to HA \to b\bar{b}b\bar{b}}$$

will be analysed under the general assumption of the maximal process cross section, $\sin^2(\beta-\alpha) = 1$, at a centre of mass energy of 500 GeV and 800 GeV and an assumed integrated luminosity of 500 $\mathrm{fb^{-1}}$. The study of the Higgs pair production process is motivated by a so-called decoupling limit of the MSSM in which the h boson approaches the properties of the SM Higgs boson. The closer the MSSM scenario moves towards the decoupling limit the more difficult it becomes to distinguish the Higgs sector from that of the SM. In such a scenario the detection of heavier neutral Higgs bosons would be crucial for establishing an extended Higgs sector. The distinct feature of this scenario is the vanishing coupling of the heavy CP-even Higgs boson to weak bosons, $\cos(\beta-\alpha) \to 0$:

$$g_\mathrm{HZZ,HWW} \sim \cos(\beta-\alpha). \tag{1}$$

As a consequence, the H boson production via the fusion and Higgsstrahlung processes is significantly suppressed, whereas the cross section of the $e^+e^- \to HA$ process reaches its maximal value making associated heavy Higgs pair production a promising channel for the detection of the H and A bosons at a future e^+e^- Linear Collider:

$$g_{\mathrm{HAZ}} \sim \sin(\beta - \alpha). \quad (2)$$

It should also be emphasised that in the decoupling limit the H and A bosons are almost degenerate in mass and have similar decay properties.

In the CP conserving scenario of the MSSM the mass eigenstates are equal to CP eigenstates. However, it is possible in the MSSM to explicitly or spontaneously break CP symmetry by radiative corrections. The SM fails to provide enough of CP violation to explain the cosmological matter-antimatter asymmetry. The CP violating effects in the MSSM can help to reduce this crisis.

CP violation is introduced in the MSSM Higgs potential via loop effects and manifests itself in complex phases of $\mathcal{L}_{\mathrm{MSSM}}$, in particular, the phases of $A_{t,b}$, the soft SUSY-breaking trilinear couplings of the top (bottom) squark to the Higgs boson, and $m_{\tilde{g}}$, the mass of the gluino. The phase of $A_{t,b}$ is the only parameter to introduce the CP violation in the Higgs potential on one-loop level. On two-loop level the phase of $m_{\tilde{g}}$ enters as an additional parameter, which can provide CP violation. If CP is broken in the Higgs sector, then the Higgs boson mass eigenstates do not anymore correspond to CP eigenstates. There are three neutral Higgs bosons H_1, H_2, H_3 ($m_{H_1} \leq m_{H_2} \leq m_{H_3}$) which have mixed CP parities. The parametrisation of the Higgs sector is chosen to be in m_{H^+} and $\tan\beta$, because the Higgs boson A is not a mass eigenstate anymore.

The general study of the MSSM Higgs boson pair production will be applied to two CP violating scenarios analysed at a centre of mass energy of 500 and 800 GeV with an integrated luminosity of 500 fb^{-1}. In these scenarios, the process

$$e^+e^- \to H_2H_3 \to b\bar{b}b\bar{b}$$

will be studied. The general analysis will also be applied to the SPS 1a benchmark point for SUSY searches at $\sqrt{s} = 1$ TeV and an integrated luminosity 1000 fb^{-1}.

In the last section of the first part of the thesis the sensitivity to the parameter $\arg(A_{t,b})$ of the CP violating MSSM scenario at the ILC will be demonstrated. The results of this analysis have been published in [1] and [2].

In the second part of the thesis, e^+p collisions will be used to study the structure of the proton. The advantage of lepton-nucleon collisions in studying the structure of matter lies in the fact that leptons are point-like objects and their interactions are well understood.

The measurement of the charm and beauty contributions to the proton structure function, $F_2^{c\bar{c}}$ and $F_2^{b\bar{b}}$, at low Q^2 is an important test of the theory of strong interactions, perturbative chromodynamics (pQCD), where threshold effects at $Q^2 \sim m^2_{\mathrm{c,b}}$ should be treated properly in the description of heavy flavour production. The partons are originally treated in QCD as massless, and the large mass of heavy quarks needs to be taken into account. Therefore, different schemes exist for heavy flavour production description. If $Q^2 \ll m^2_{\mathrm{c,b}}$, heavy flavour production is described within the massive scheme, where the c and b quarks are treated as massive and, therefore, do not contribute to the parton distribution of the proton. If $Q^2 \gg m^2_{\mathrm{c,b}}$, heavy flavour production is described in the massless scheme, in which heavy quarks are treated as massless partons and described by parton distribution functions (PDFs). However, these schemes do not give a reliable description over the whole Q^2 kinematic range. Therefore, several theoretical models have been developed within the variable flavour number scheme (VFNS), which take into account threshold effects at $Q^2 \sim m^2_{\rm c,b}$ and describe the production of heavy quarks over the whole Q^2 range. The aim of this analysis is to test the validity of such perturbative QCD calculations for charm and beauty production in e^+p collisions at HERA.

In the VFNS heavy flavour production is described by the evolution of c and b parton distribution functions, where the quarks have non-zero mass. In this analysis such an ansatz will be tested with real data by measuring the charm and beauty contributions to the proton structure function, i.e. $F_2^{c\bar{c}}$ and $F_2^{b\bar{b}}$.

The importance of the correct knowledge of the PDFs of the proton at high Q^2 is essential for future experiments, in particular at the LHC. This can be shown in the example of the Higgs boson production at the LHC via the process of bottom quark fusion ($\rm b\bar{b} \rightarrow H$) (Fig. 1). The SM cross section for this process is low due to the low Yukawa coupling. However, in a two Higgs doublet model, e.g. in the MSSM, the Yukawa coupling of some or all of the Higgs bosons (h, H, A, $\rm H^{\pm}$) to the bottom quark could be enhanced for large values of $\tan\beta$ [3]. For the cross section calculation of such a process the knowledge of the beauty PDF $f_b(x, Q^2)$ probed at the scale $Q = m_{\rm H}/2$ or $Q = m_{\rm H}/4$ is needed. Therefore, a direct measurement of $F_2^{b\bar{b}}$ at high Q^2 is important [4].

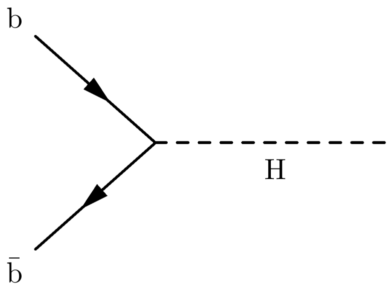

Figure 1: *Bottom quark fusion process for Higgs boson production at the LHC.*

The present measurement is performed at low Q^2, where it is important to check the validity of the theoretical descriptions of heavy quark production around the threshold region which will improve the understanding of the gluon/beauty PDF across all values of Q^2.

In the present analysis, the property of long lifetime of charm and beauty hadrons will be exploited to separate the events, coming from charm, beauty and light quarks. In this method the distance of closest approach (or impact parameter), in the transverse plane, of all tracks, reconstructed using precise spatial information from the H1 vertex detector will be used. This will help to avoid statistical limitations of exclusive measurements (e.g. $\rm D^*$ method for charm tagging and muon-jet method for beauty tagging) and to reduce the uncertainty due to the model dependence. The measured $F_2^{c\bar{c}}$ and $F_2^{b\bar{b}}$ will be compared with pQCD calculations in the VFNS and massive scheme. $F_2^{c\bar{c}}$ will also be compared with other measurements obtained using $\rm D^*$ cross sections. This is the first measurement of $F_2^{b\bar{b}}$ in the low Q^2 region. The results of this analysis have been published in [5] and [6].

Part I

MSSM Higgs Boson Production at a Future Linear Collider

Chapter 1

Theoretical Motivation for the Higgs Boson Mechanism

The main goal of the next particle physics experiments is the search of the Higgs boson, a particle, responsible for electroweak symmetry breaking. In this chapter, the theoretical introduction into the Standard Model (SM) of particle physics and Minimal Supersymmetric extension of the SM (MSSM) will be given. The Higgs mechanism will be explained in both models. Within the MSSM the Higgs bosons will be introduced in CP conserving (CPC) and CP violating (CPV) scenarios.

1.1 The Standard Model

The Standard Model of particle physics gives a remarkably successful description of presently known phenomena. In this section, the main steps for the formation of the electroweak theory using the Lagrangian formalism will be presented and the theoretical motivation for the existence of the Higgs boson will be explained. In the last sections, the theoretical problems and experimental facts, which cannot be explained in the SM, will be discussed.

1.1.1 Historical Overview of the Development of the Standard Model

A fast progress in elementary particle physics began after the success of quantum electrodynamics (QED) as a gauge field theory of the electromagnetic force, when this theory could be extended to the weak- and strong forces. First, the charmed quark was discovered in 1974 at SLAC and Brookhaven, for which B. Richter and S.C.C. Ting were awarded the Nobel prize in 1976. This discovery is usually called the "November Revolution". Since that time, the quarks were treated not like some mathematical objects to classify the hadrons, as they were originally proposed by Gell-Mann and independently by Zweig, but like real constituents of the hadrons.

After the discovery of charmed quarks there were four known quarks (u, d, s and c) and four leptons (e, μ, ν_e and ν_μ). This led to the idea of a symmetry between quarks and leptons (actually, the idea of a fourth flavour had been introduced much earlier by Bjorken and Glashow [7]). Glashow, Salam and Weinberg [8] proposed the $SU(2) \otimes U(1)$ unified theory of the electroweak interactions (GSW electroweak theory) for the leptonic sector. However, the idea of the unification of the electromagnetic and weak interactions was proposed by Schwinger and Glashow already in the early sixties. Weinberg and Salam solved the problem of the heavy gauge boson masses, required in order to explain the short range of the weak interactions, by introducing spontaneous symmetry breaking via the Higgs mechanism [9]. This introduced gauge boson masses without explicitly breaking the gauge symmetry. The GSW theory was extended later by Glashow, Iliopoulos and Maiani (GIM) [10] in 1970 to include quarks as well as leptons.

The GSW theory led to the following important predictions:

- the existence of neutral currents;
- the prediction of the heavy gauge boson masses around 90 GeV;
- the existence of the new boson, responsible for electroweak symmetry breaking. This scalar neutral particle is called Higgs boson.

The first two predictions were confirmed in experiments. The first prediction was confirmed in 1973 at CERN and led to the award of the Nobel prize in 1979 to Glashow, Salam and Weinberg. The second prediction was confirmed in 1983 by the discovery of the $W^{\pm}$ and Z bosons at CERN in $p\bar{p}$ collisions, for which C. Rubbia and S. van der Meer were awarded the Nobel prize in 1985.

The only question left open is the existence of the Higgs boson. This particle is still under search. It might just be too heavy to be produced with the present accelerators. No predictions for its mass exist within the Standard Model. Direct searches at LEP set a lower bounds for the Higgs boson mass $m_{\mathrm{H}} > 114.4$ GeV [11].

The gauge theory of the strong interactions was proposed by Fritzsch and Gell-Mann [12] in 1973. In 1979 the gauge boson of the strong interaction, the gluon, was discovered in 3-jet production in e^+e^- annihilation at the DESY laboratory in Hamburg. In contrast to photons, gluons carry colour charge, the charge of strong interactions, which leads to gluon self-interaction. The colour charge has been established firmly at CERN's LEP collider. The gluon self-interaction leads to asymptotic freedom, as shown by Gross and Wilczek [13] and independently by Politzer [14] thus explaining why the quarks can be observed as almost free pointlike particles inside hadrons at high energy scales. They were awarded a Nobel prize in 2004. This also explained the success of the Quark Parton Model, which assumes quasi-free partons inside the hadrons. In this case the cross sections, if expressed in dimensionless scaling variables, are independent of energy. The observation of scaling in deep inelastic lepton-nucleon scattering led to the award of the Nobel Prize to Freedman, Kendall and Taylor in 1990. However, quantum chromodynamics (QCD) predicts logarithmic scaling violations, which were observed in both deep inelastic scattering (DIS) and e^+e^- processes and could be used for precise determinations of the strong coupling constant of QCD.

The third generation of quarks and leptons had been introduced into the SM by Kobayashi and Maskawa in order to be able to explain the observed CP violation in the kaon system within the SM. Later, the beauty quark was discovered at Fermilab in Batavia (USA) and the $\tau-$lepton at SLAC, both in 1976. The top quark was discovered in 1995 at Fermilab. Thus, the existence of the third generation of quarks and leptons was confirmed.

1.1.2 Basic Concepts of the Standard Model

Groups of particles observed in Nature show very similar properties, thus suggesting the existence of symmetries. The quarks come in three colours, which leads to the SU(3) group structure for the strong interactions. Weak interactions suggest the grouping of fermions into doublets, leading to the SU(2) group structure of the weak interactions. The electromagnetic interactions don't change the quantum numbers of the interacting particles, so the simple U(1) group is sufficient.

The SM of strong and electroweak interactions is based on the idea of the gauge symmetry of the following unitary groups:

$$SU(3)_C \otimes SU(2)_L \otimes U(1)_Y, \tag{1.1}$$

where C stands for colours, L for left-handed leptons and quarks and Y for weak hypercharge (see Section 1.1.3). The SM interactions and their properties are summarised in Table 1.1. The particle spectrum of the three generations of the SM with the electroweak quantum numbers is presented in Table 1.2. The definition of the quantum numbers will be explained in the next chapter.

Interaction	Theory	Symmetry	Gauge bosons	Charge
Strong	QCD	$SU(3)$	gluons $g_1 ... g_8$	colour
Electroweak	GSW	$SU(2) \otimes U(1)$	γ, $\mathrm{W}^{\pm}$, Z	weak isospin, weak hypercharge

Table 1.1: *The Standard Model interactions.*

	Generations			**Quantum numbers**		
	1.	2.	3.	Q	I_w^3	Y_w
leptons	$\begin{pmatrix}\nu_e\\ e\end{pmatrix}_L$	$\begin{pmatrix}\nu_\mu\\ \mu\end{pmatrix}_L$	$\begin{pmatrix}\nu_\tau\\ \tau\end{pmatrix}_L$	0	1/2	−1
				−1	−1/2	−1
	e_R	μ_R	τ_R	-1	0	-2
quarks	$\begin{pmatrix}u\\ d'\end{pmatrix}_L$	$\begin{pmatrix}c\\ s'\end{pmatrix}_L$	$\begin{pmatrix}t\\ b'\end{pmatrix}_L$	2/3	1/2	1/3
				−1/3	−1/2	1/3
	u_R	c_R	t_R	2/3	0	4/3
	d_R	s_R	b_R	-1/3	0	-2/3

Table 1.2: *The SM particle spectrum with the electroweak quantum numbers (electric charge Q, third component of weak isospin I_w^3 and weak hypercharge Y_w). The quarks come in three colours, which have not been indicated. The primes for the left-handed quarks d', s', b' indicate the interaction eigenstates of the electroweak theory, which are mixtures of the mass eigenstates. The mixing matrix is the Cabibbo-Kobayashi-Maskawa (CKM) matrix.*

1.1.3 Electroweak Theory

The original aim of Glashow was to unify weak and electromagnetic interactions, to combine them into a single theoretical framework, in which they would appear not as unrelated phenomena, but rather as different manifestations of one fundamental *electroweak* interaction. There is a structural difference between the electromagnetic and weak vertex factors: the former are purely vectorial (γ^μ), whereas the latter contain vector (V) and axial vector (A) parts. In particular, the $\mathrm{W}^{\pm}$ coupling is "maximally" mixed V-A in character ($\gamma^\mu(1-\gamma^5)$). This can be incorporated by the absorption of the matrix $(1-\gamma^5)$ into the particle spinor [15]:

$$\psi_L \equiv \frac{(1-\gamma^5)}{2}\psi, \quad \psi_R \equiv \frac{(1+\gamma^5)}{2}\psi, \tag{1.2}$$

and introducing right-handed and left-handed fermions. The chirality equals helicity only for massless particles or in the ultrarelativistic regime ($E \gg mc^2$). The weak force couples only to left-handed states, whereas the electromagnetic force couples to both types. But apart from that these currents are strikingly similar.

The Dirac Lagrangian for spinor fields ψ is [1]

$$\mathcal{L} = i\bar{\psi}\gamma^{\mu}\partial_{\mu}\psi - m\bar{\psi}\psi. \tag{1.3}$$

Substituting ψ with ψ_L and ψ_R for $m = 0$ Lagrangian it follows that

$$\mathcal{L} = i\bar{\psi}\gamma \cdot \partial\psi = i\bar{\psi}_R\gamma \cdot \partial\psi_R + i\bar{\psi}_L\gamma \cdot \partial\psi_L, \tag{1.4}$$

since γ_5 anticommutes with γ_{μ} [15]. The electrons, muons, taus and quarks have L and R components, but neutrinos, if massless, have only an L component. From now on only electron and ν_e will be considered in the Lagrangian; the muon, tau and quark terms can be added in a similar way. The lepton Lagrangian is

$$\mathcal{L} = i\bar{e}_R\gamma \cdot \partial e_R + i\bar{e}_L\gamma \cdot \partial e_L + i\bar{\nu}_e\gamma \cdot \partial\nu_e. \tag{1.5}$$

Due to the internal symmetry of (1.5) the following "isospinor" can be written:

$$L = \begin{pmatrix} \nu_e \\ e \end{pmatrix}_L \tag{1.6}$$

and an isosinglet

$$R = e_R. \tag{1.7}$$

A non-Abelian charge $I_w = \frac{1}{2}$ (weak isospin) can be assigned to the doublet L. Then, ν_e has a third component $I_w^3 = \frac{1}{2}$ and e_L has $I_w^3 = -\frac{1}{2}$. The isosinglet e_R has $I_w = 0$. After this assigning the Lagrangian has a form

$$\mathcal{L} = i\bar{R}\gamma \cdot \partial R + i\bar{L}\gamma \cdot \partial L, \tag{1.8}$$

which is invariant under the transformations:

$$SU(2) : \begin{cases} L \to e^{-(i/2)\boldsymbol{\tau}\cdot\boldsymbol{\alpha}}L, \\ R \to R, \end{cases} \tag{1.9}$$

which are rotations in the weak isospin space. They generate the group $SU(2)$. In (1.9), $\boldsymbol{\tau} = \{\tau_1, \tau_2, \tau_3\}$ are Pauli matrices and $\boldsymbol{\alpha} = \{\alpha_1, \alpha_2, \alpha_3\}$ are real numbers. The relation between the electric charge Q and I_w^3 is

$$\begin{aligned} L: &\quad Q = I_w^3 - \frac{1}{2}, \\ R: &\quad Q = I_w^3 - 1. \end{aligned} \tag{1.10}$$

$SU(2)$ is not the maximal symmetry of $\mathcal{L}$. There can be also done a simple $U(1)$ transformation on e_R

$$U(1) : e_R \to e^{i\beta}e_R, \tag{1.11}$$

where β is any real number. This influences $\mathcal{L}$ by an overall phase; ν_e and e_L must pick up the same phase, since otherwise this would be a special case of $SU(2)$ transformation. This phase, however, is not necessarily the same as that of R. Therefore

$$U(1) : \begin{pmatrix} \nu_e \\ e_L \\ e_R \end{pmatrix} \to \begin{pmatrix} e^{in\beta} & 0 & 0 \\ 0 & e^{in\beta} & 0 \\ 0 & 0 & e^{i\beta} \end{pmatrix} \begin{pmatrix} \nu_e \\ e_L \\ e_R \end{pmatrix} \tag{1.12}$$

---

[1] Here, $\hbar = c = 1$ is assumed.

where n should be found. This $U(1)$ symmetry leads to a conserved charge, of which e_R possesses one value, and ν_e as well as e_L another value. Weinberg suggested that this charge is a *weak hypercharge* Y_w, defined by a quasi-Gell-Mann-Nishijima relation

$$Q = I_w^3 + \frac{Y_w}{2}. \tag{1.13}$$

Comparing (1.13) with (1.10), it is clear that L has Y_w = -1 and R has Y_w = -2. Therefore in (1.12) $n = \frac{1}{2}$, i.e. left-handed fields couple, with half the strength of the right-handed field, to the hypercharge gauge field.

The next step is to require local gauge invariance of $SU(2)$ (i.e. space-time dependence of $\boldsymbol{\alpha}$) and $U(1)$ (i.e. space-time dependence of β). Gauging $SU(2)$ means that the three gauge potentials $\mathbf{W}_\mu^{\mathbf{i}}$ are introduced in a way that, acting on the isospinor L, the ordinary derivative is replaced by the covariant derivative:

$$SU(2) : \partial_\mu L \rightarrow D_\mu L = \partial_\mu L - \tfrac{i}{2} g \boldsymbol{\tau} \cdot \mathbf{W}_\mu L, \tag{1.14}$$

where g is the $SU(2)$ coupling constant and $\boldsymbol{\tau}$ are the Pauli-matrices. The photon is not one of $\mathbf{W}_\mu^{\mathbf{i}}$ gauge fields, since e_R, being a singlet, does not interact with the gauge field, but does interact with the photon.

Gauging $U(1)$ introduces another potential B_μ and a coupling constant g'. Since L has half the hypercharge of R, the covariant derivatives are

$$\begin{aligned} D_\mu L &= \partial_\mu L + \frac{i}{2} g' B_\mu L, \\ D_\mu R &= \partial_\mu R + i g' B_\mu R. \end{aligned} \tag{1.15}$$

Putting all the covariant derivatives into Lagrangian (1.8) and adding the kinetic gauge field terms gives the Lagrangian

$$\begin{aligned} \mathcal{L}_1 = {} & i\bar{R}\gamma^\mu(\partial_\mu + i g' B_\mu) R + i\bar{L}\gamma^\mu \left(\partial_\mu + \frac{i}{2} g' B_\mu - \frac{i}{2} g \boldsymbol{\tau} \cdot \mathbf{W}_\mu \right) L \\ & - \frac{1}{4}(\partial_\mu \mathbf{W}_\nu - \partial_\nu \mathbf{W}_\mu + g \mathbf{W}_\mu \times \mathbf{W}_\nu)^2 - \frac{1}{4}(\partial_\mu B_\nu - \partial_\nu B_\mu)^2. \end{aligned} \tag{1.16}$$

So the electroweak Lagrangian (1.16) is derived by requiring a local $SU(2) \times U(1)$ invariant form. The final two terms are the kinetic energy and self-coupling of the $\mathbf{W}_\mu$ fields $-\frac{1}{4}\mathbf{W}_{\mu\nu}\mathbf{W}^{\mu\nu}$ and the kinetic energy of the B_μ field $-\frac{1}{4}B_{\mu\nu}B^{\mu\nu}$.

1.1.4 Higgs Mechanism

The Lagrangian $\mathcal{L}_1$ in (1.16) describes massless gauge bosons and massless fermions. Mass terms such as $\frac{1}{2}M^2 B_\mu B^\mu$ and $-m\bar{\psi}\psi$ are not gauge invariant and so cannot be added. The generation of particle masses in a gauge invariant way can be achieved with the so-called *Higgs mechanism* [9]. That is, to break spontaneously the gauge symmetry, which has the paramount virtue that the theory remains renormalisable.

The Higgs mechanism should be formulated in such a way that the W$^\pm$ and Z^0 become massive and the photon remains massless. For this purpose, an $SU(2) \times U(1)$ gauge invariant Lagrangian for the mass terms should be added to $\mathcal{L}_1$. This is done by introducing a complex scalar doublet (Higgs field) [15]:

$$\phi = \begin{pmatrix} \phi^+ \\ \phi^0 \end{pmatrix}. \tag{1.17}$$

From (1.13), it carries the quantum numbers

$$\phi: \ I_w = \frac{1}{2}, \ \ Y_w = 1. \tag{1.18}$$

Both ϕ^+ and ϕ^0 are complex fields, and it is possible to put [15]:

$$\phi = \begin{pmatrix} \phi^+ \\ \phi^0 \end{pmatrix} \equiv \begin{pmatrix} \frac{1}{\sqrt{2}}(\phi_3 + i\phi_4) \\ \\ \frac{1}{\sqrt{2}}(\phi_1 + i\phi_2) \end{pmatrix}, \tag{1.19}$$

where ϕ_1, ..., ϕ_4 are real. By virtue of (1.18), the covariant derivative of ϕ is

$$D_\mu \phi = \left(\partial_\mu - \frac{i}{2} g \boldsymbol{\tau} \cdot \mathbf{W}_\mu - \frac{i}{2} g' B_\mu \right) \phi. \tag{1.20}$$

The Higgs field ϕ also interacts with e^- and ν_e with strength y_e, so the overall Lagrangian containing ϕ is

$$\mathcal{L}_2 = (D_\mu \phi)^\dagger (D_\mu \phi) - \frac{m^2}{2} \phi^\dagger \phi - \frac{\lambda}{4} (\phi^\dagger \phi)^2 - y_e (\bar{L} \phi R + \bar{R} \phi^\dagger L), \tag{1.21}$$

where λ is a Higgs self-interaction coupling constant, m is a mass parameter and y_e is a Yukawa coupling. The interaction term in $\mathcal{L}_2$, written out fully, is

$$-y_e(\bar{\nu_e} e_R \phi^+ + \bar{e_L} e_R \phi^0 + \bar{e_R} \nu_e \phi^- + \bar{e_R} e_L \bar{\phi^0}), \tag{1.22}$$

and

$$\phi^\dagger \phi = (\phi^+)^* \phi^+ + (\phi^0)^* \phi^0 = \frac{1}{2}(\phi_1^2 + \phi_2^2 + \phi_3^2 + \phi_4^2). \tag{1.23}$$

The Lagrangian $\mathcal{L}_2$ in (1.21) can be presented like $\mathcal{L}_2 = T - V$, where T is a "kinetic" term and V is a "potential". Then, a potential V is:

$$V(\phi, \phi^\dagger) = \frac{m^2}{2} \phi^\dagger \phi + \frac{\lambda}{4} (\phi^\dagger \phi)^2. \tag{1.24}$$

The ground state is obtained by minimising the potential V:

$$\frac{\partial V}{\partial \phi} = \frac{m^2}{2} \phi^\dagger + \frac{\lambda}{4} 2 (\phi^\dagger \phi) \phi^\dagger = 0. \tag{1.25}$$

If $m^2 > 0$, the minimum occurs at $\phi = \phi^\dagger = 0$. If $m^2 < 0$, there is a local maximum at $\phi = 0$, and a minimum at

$$(\phi^\dagger \phi)_0 = -\frac{m^2}{\lambda} \equiv v^2. \tag{1.26}$$

The function V is shown in Fig. 1.1, plotted against ϕ_1 and ϕ_2. The minima of V lie along the circle $|\phi| = v$, which form a set of degenerate vacuum states related to each other by rotation. The physical fields, which are excitations above the vacuum, are then realized by performing perturbations about $|\phi| = v$, not about $\phi = 0$.

The value v is a vacuum expectation value (VEV) of the Higgs potential. This is the so-called procedure of spontaneous breaking of the gauge symmetry, which led to a degenerate vacuum [16]. It is called "spontaneous" because no external force is responsible. The true symmetry is hidden by the arbitrary selection of a particular (asymmetrical) ground state. As it will be shown further, it is done to identify the mass terms in Lagrangian.

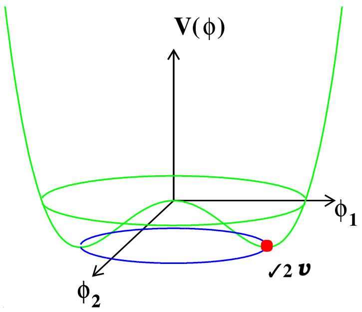

Figure 1.1: *The potential V of the Higgs field. The minimum at $|\phi| = v$ obeys a rotational symmetry, which is broken spontaneously.*

The isospin frame can be chosen in a way that

$$(\phi_1^2)_0 = -2\frac{m^2}{\lambda},\ (\phi_2)_0 = (\phi_3)_0 = (\phi_4)_0 = 0, \tag{1.27}$$

or

$$(\phi_1)_0 = \left(-2\frac{m^2}{\lambda}\right)^{1/2} \equiv \sqrt{2}v \tag{1.28}$$

and

$$(\phi)_0 = \begin{pmatrix} 0 \\ v \end{pmatrix}; \quad v \text{ is real.} \tag{1.29}$$

For excitations of ϕ above the vacuum, $\phi(x)$ can be written as

$$\phi(x) = \begin{pmatrix} \frac{1}{\sqrt{2}}(\phi_3 + i\phi_4) \\ \\ v + \frac{1}{\sqrt{2}}(\phi_1 + i\phi_2) \end{pmatrix}. \tag{1.30}$$

But the fact that the theory is local means that a special gauge at each point in space can be applied, so $\phi(x)$ may be reduced to the form

$$\phi(x) = \begin{pmatrix} 0 \\ \\ v + \frac{1}{\sqrt{2}}\sigma(x) \end{pmatrix} \tag{1.31}$$

at every point. From (1.20) $D_\mu\phi$ is then [15]:

$$D_\mu\phi = \begin{pmatrix} 0 \\ \\ \frac{1}{\sqrt{2}}\partial_\mu\sigma \end{pmatrix} - \left[\frac{ig}{2}\begin{pmatrix} W_\mu^3 & W_\mu^1 - iW_\mu^2 \\ W_\mu^1 + iW_\mu^2 & -W_\mu^3 \end{pmatrix} + \frac{ig'}{2}B_\mu\right]\begin{pmatrix} 0 \\ \\ v + \frac{1}{\sqrt{2}}\sigma \end{pmatrix} \tag{1.32}$$

$$D_\mu\phi = -\frac{i}{2}\begin{pmatrix} gv(W_\mu^1 - iW_\mu^2) + \frac{g\sigma}{\sqrt{2}}(W_\mu^1 - iW_\mu^2) \\ \\ i\sqrt{2}\partial_\mu\sigma + v(-gW_\mu^3 + g'B_\mu) + \frac{\sigma}{\sqrt{2}}(-gW_\mu^3 + g'B_\mu) \end{pmatrix}. \tag{1.33}$$

Hence

$$\begin{aligned}(D_\mu\phi)^\dagger(D_\mu\phi) &= \frac{1}{2}(\partial_\mu\sigma)^2 + \frac{g^2v^2}{4}[(W_\mu^1)^2 + (W_\mu^2)^2] + \frac{v^2}{4}(gW_\mu^3 - g'B_\mu)^2 \\ &\quad + \text{cubic} + \text{ quartic terms.}\end{aligned} \tag{1.34}$$

Here, σ is a massive scalar, which is called a Higgs particle. Its mass can be received from (1.21) from a mass term $\sim \sigma^2$ and $m_{\mathrm{H}}^2 \sim v^2\lambda$. In (1.34) one can see that electroweak gauge bosons receive masses! The neutral gauge bosons are defined as

$$Z_\mu = \frac{gW_\mu^3 - g'B_\mu}{\sqrt{g^2 + g'^2}} \equiv \cos\theta_W W_\mu^3 - \sin\theta_W B_\mu \tag{1.35}$$

and the orthogonal field

$$A_\mu = \frac{g'W_\mu^3 + gB_\mu}{\sqrt{g^2 + g'^2}} \equiv \sin\theta_W W_\mu^3 - \cos\theta_W B_\mu, \tag{1.36}$$

where the Weinberg angle θ_W is given by

$$\frac{g}{\sqrt{g^2 + g'^2}} = \cos\theta_W, \quad \frac{g'}{g} = \tan\theta_W. \tag{1.37}$$

The physical weak intermediate bosons W$^\pm$ are defined as

$$W_\mu^\pm = \frac{W_\mu^1 \mp iW_\mu^2}{\sqrt{2}}. \tag{1.38}$$

From (1.34) it follows that W_μ^1, W_μ^2 and Z_μ pick up masses

$$M_{W_1}^2 = M_{W_2}^2 = \frac{g^2v^2}{2}, \quad M_Z^2 = \frac{g^2v^2}{2\cos^2\theta_W} = \frac{M_W^2}{\cos^2\theta_W} \tag{1.39}$$

and A_μ is massless.

An attractive feature of the SM is that the same Higgs doublet, which generates W$^\pm$ and Z masses is also sufficient to give masses to the leptons and quarks (from (1.16)). The fermion masses are

$$m_f = y_f v, \tag{1.40}$$

where y_f are Yukawa couplings of the Higgs boson to fermions. Yukawa couplings are proportional to the fermion masses. Therefore, the Higgs boson couples predominantly to heavy fermions.

The Fermi coupling G_F is dependent on vacuum expectation value of the Higgs potential v as $G_F = 1/(2\sqrt{2}v^2)$. Therefore, the VEV can be calculated and $\approx$ 174 GeV.

The resulting Lagrangian can be presented in a form

$$\mathcal{L} = \mathcal{L}_{Yukawa} + \mathcal{L}_{gauge} + \mathcal{L}_{Higgs}. \tag{1.41}$$

In the seventies, 't Hooft and Veltman demonstrated that this theory is renormalisable [17].

1.1.5 Theoretical Limits on the Higgs Boson Mass

The SM Higgs boson mass is $m_H^2 \sim v^2\lambda$, where the vacuum expectation value v is fixed by the Fermi coupling and quartic Higgs self-coupling λ is a free parameter. Therefore the mass of the Higgs boson is not predicted by the theory. Nevertheless, stringent upper and lower bounds can be derived from internal consistency conditions (vacuum stability) and extrapolations of the model to high energies (triviality), respectively.

The introduction of a Higgs boson solved the problem of the elastic scattering of massive longitudinally polarised W_L bosons, $W_LW_L \to W_LW_L$ (Fig. 1.2, three upper diagrams) [18, 19].

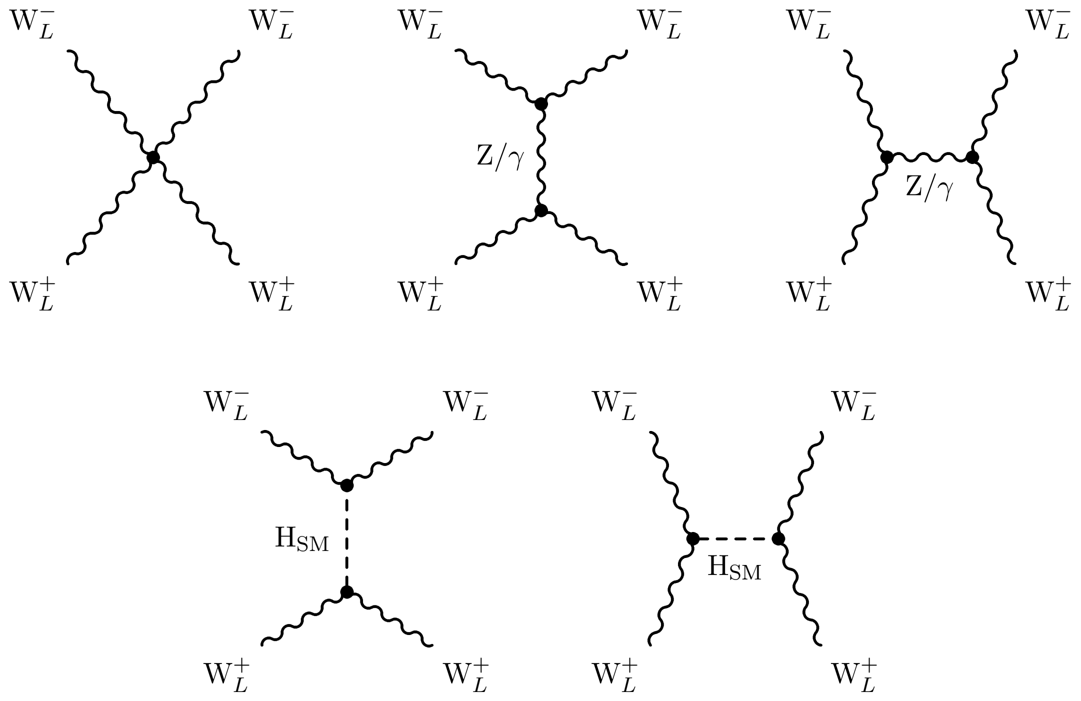

Figure 1.2: *The cancellation of the divergent* $W_L W_L$ *cross-sections (three upper diagrams) by Higgs boson exchange graphs (two lower diagrams).*

At high energies the amplitude of this process grows with energies for longitudinally polarised particles and can violate unitarity. The term of the scattering amplitude rising as the fourth power in the energy is cancelled by virtue of the non-Abelian gauge symmetry, but still the amplitude remains quadratically divergent in the energy. However, the quadratic rise in the energy can be damped by exchanging a new scalar particle Higgs boson (Fig. 1.2, two lower diagrams). Thus, unitarity can be restored by introducing a weakly coupled Higgs particle.

Based on a general principle of time-energy uncertainty, particles must decouple from a physical system if their mass grows indefinitely. The mass of the Higgs particle must therefore be bounded to restore unitarity in the perturbative regime. From the asymptotic expansion of the elastic $W_L W_L$ S-wave scattering amplitude including W and Higgs exchanges ($W_L W_L \to W_L W_L$) it follows that [20]

$$m_{\mathrm{H}} \leq 850 \text{ GeV}.$$

Other upper and lower bounds on the SM Higgs mass follow from hypotheses on the energy scale Λ up to which the SM can be extended before new physical phenomena emerge, which would be associated with new strong interactions between the fundamental particles. The evolution of the quartic coupling λ with the energy (i.e. the field strength) due to quantum fluctuations is the key to these bounds. The basic contributions come from the Higgs boson and top quark loops (Fig. 1.3). The Higgs loop itself gives rise to an indefinite increase of the coupling (Fig. 1.3 (b)), while the fermionic top quark loop, with increasing top mass, drives the coupling to smaller values, finally even to values below zero (Fig. 1.3 (c)).

Let us consider the upper limit first. For moderate top masses, the quartic coupling λ rises indefinitely, $\partial\lambda/\partial t \sim +\lambda^2$, and the coupling becomes strong shortly before the reaching

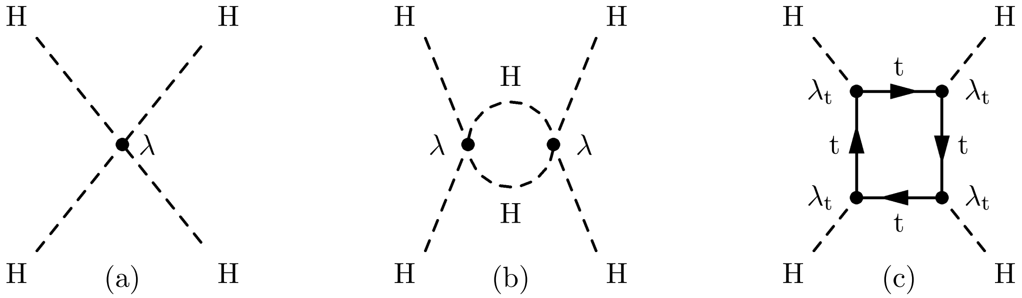

Figure 1.3: *Loop corrections to the quartic Higgs self coupling λ. Higgs loops increase the coupling λ (b). The fermionic top quark loop drives λ to smaller values (c).*

a Landau pole [18]:

$$\lambda(\mu^2) = \frac{\lambda(v^2)}{1 - \frac{3\lambda(v^2)}{8\pi^2}\log\frac{\mu^2}{v^2}}. \tag{1.42}$$

Reexpressing the initial value of λ by the Higgs mass, the condition $\lambda(\Lambda) < \infty$, can be translated into an upper bound on the Higgs mass:

$$m_{\mathrm{H}}^2 \leq \frac{8\pi^2 v^2}{3\log\frac{\Lambda^2}{v^2}}. \tag{1.43}$$

This mass bound is related logarithmically to the energy Λ up to which the SM is assumed to be valid.

The requirement of vacuum stability leads to a lower bound on the Higgs mass. The top-loop corrections reduce λ for increasing top Yukawa coupling; λ becomes negative if the top mass becomes too large. In this case, the self-energy potential would become deep negative and the ground state would no longer be stable. To avoid this instability, the Higgs mass must exceed a minimal value for a given top mass. This lower bound depends on the cut-off value Λ.

In Fig. 1.4 the upper and lower theoretical bounds on the SM Higgs mass are presented in dependence on the energy scale Λ. The theoretical bounds imply that, if the SM is to be self-consistent up to the grand unification scale $\Lambda_{GUT} \approx 10^{16}$ GeV, where the couplings of the electromagnetic, weak and strong interactions will have the same value, the Higgs mass should be between 130 and 190 GeV.

1.1.6 Experimental Limits on the SM Higgs Mass

A direct search for the Higgs boson has been done at the LEP experiments at CERN (1989-2000), using e^+e^- collisions at $\sqrt{s} = 91 - 209$ GeV. In the data of the year 2000, mostly at energies $\sqrt{s} > 205$ GeV, ALEPH reported an excess of about three standard deviations beyond the background prediction [22], arising mainly from a few four-jet candidates with clean b-tags and kinematic properties suggesting a SM Higgs boson with mass in the vicinity of 115 GeV. The data of the other three LEP experiments did not show evidence for such an excess, but did not, however, exclude a 115 GeV Higgs boson. The combined data of four experiments [11] showed that the overall significance decreased to about 1.7 standard deviation. From all LEP experiments a 95% confidence level lower bound of 114.4 GeV is obtained for the SM Higgs boson mass (yellow (light grey) area in Fig. 1.5).

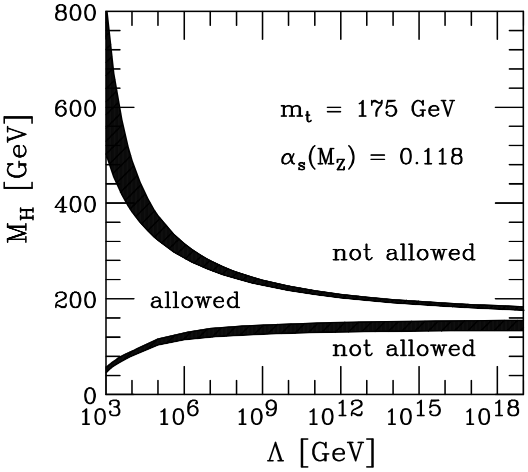

Figure 1.4: *The dependence of the theoretical bounds on the SM Higgs mass on the cut-off scale* Λ*. The upper solid area indicates the sum of the theoretical uncertainties in the* m_H *upper bound, when keeping* $m_t = 175$ *GeV fixed. The lower solid area represents the theoretical uncertainties in the* m_H *lower bounds derived from stability requirements, using* $m_t = 175$ *GeV and* $\alpha_s = 0.118$ *[21].*

Indirect experimental bounds for the SM Higgs boson mass can be obtained from fits to precision measurements of electroweak observables, like $\sin^2\theta_W$ and others, and to the measured top and $W^\pm$ masses. These measurements are sensitive to $\log m_{\mathrm{H}}$ through radiative corrections. Higgs boson loops contribute to the self-energy of the Z and W. There is also the correlation of the m_{H} measurement with other parameters of the SM, such as hadronic correction to α_{EM} or the top quark mass.

In Fig. 1.5 the observed value of $\Delta\chi^2 \equiv \chi^2 - \chi^2_{min}$ as a function of m_{H} is plotted for the fit including the data from LEP and SLD experiments [23]. The solid line is the current best fit including the new world average top mass $m_{\mathrm{t}} = 172.7 \pm 2.9$ GeV [24]. The blue (grey) band represents an estimate of the theoretical error due to missing higher order corrections. The current best fit value is $m_{\mathrm{H}} = 90.7$ GeV, which is below direct exclusion limit. The upper bound from the fit corresponds to $m_{\mathrm{H}} < 186$ GeV at 95% confidence level including theory uncertainty (which corresponds to $\Delta\chi^2 = 2.7$ for the blue band).

1.1.7 Unsolved Problems of the Standard Model

There are a number of problems where the Standard Model fails to give an explanation. First of all, to date the Higgs boson has not been observed experimentally. The other interesting facts, which came from the experiments and till now didn't find an explanation in the SM are the following:

Cosmological matter-antimatter asymmetry. Antimatter is rare on the Earth. It can be produced in large quantities only at the accelerators. The measurements show that the whole solar system is made of matter. Antiprotons are seen at cosmic rays at about the 10^{-4} level compared to protons [25]. Therefore the Universe had to possess at early times (when the temperature T was ≥ 38 MeV) an asymmetry between the number of baryons and the number of antibaryons, which prevented the annihilation catastrophe. In order to generate the observed baryon asymmetry, three requirements [26, 25] need

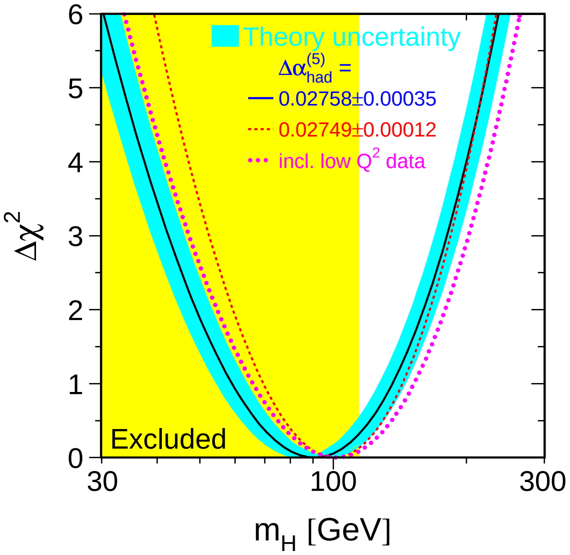

Figure 1.5: *Indirect experimental bounds for the SM Higgs boson mass represented as* $\Delta\chi^2 \equiv \chi^2 - \chi^2_{min}$ *in dependence on* m_H *[23]. The solid line is the current best fit including the new world average top mass* m_t = *172.7* ± *2.9 GeV [24]. The blue (grey) band represents an estimate of the theoretical error due to missing higher order corrections. The dashed line is the fit results for different values of the hadronic contribution to vacuum polarisation* $\Delta\alpha^{(5)}_{had}$*. The thick dotted line is the result of the fit which includes the most precise available low energy data. The yellow (light grey) area shows the 95% CL exclusion limit on* m_H *from the direct search.*

to be fulfilled:

1. the non-conservation of baryon number;
2. CP violation;
3. existence of non-equilibrium processes.

At temperatures above the electroweak phase transition temperature (T_c), the SM fulfils these requirements, but the rate of CP violating processes is too small to induce the required baryon asymmetry [27]. The only source of CP violation in the SM is CKM-matrix, relating the weak eigenstates of the quarks to their mass eigenstates. Moreover, the preservation of the generated baryon asymmetry after the electroweak phase transition requires a strongly first order phase transition, with $v(T_c)/T_c \geq 1$, where $v(T_c)$ is the Higgs vacuum expectation value at the critical temperature T_c. For the experimentally allowed values of the Higgs mass, the requirement is not fulfilled in the SM [28].

What is dark matter and dark energy? WMAP experiment (Wilkinson Microwave Anisotropy Probe) has performed an investigation of cosmic microwave background (CMB) anisotropy by observing the temperature difference between any two directions using two nearly identical sets of optics [29]. As was found:

$$\Omega_m = 0.27 \pm 0.04,$$

Figure 1.6: *Divergent loop contributions to the Higgs boson mass from fermion loop (left) and boson loop (right). The quadratic divergences from these graphs are not cancelled in the SM.*

$$\Omega_b = 0.044 \pm 0.04,$$
$$\Omega_\Lambda = 0.73 \pm 0.04,$$
$$\Omega_{tot} = 1.02 \pm 0.02,$$

where Ω_m is a matter (dark matter and visible matter) fraction of the flat universe, Ω_b is a baryon fraction and Ω_Λ is a dark energy fraction. That means that only $\approx 4\%$ of the universe energy consists of usual matter. Till now there is no explanation for the dark matter and dark energy components. Some of the supersymmetric particles (see Section 1.2) can be the candidates for the dark matter.

Neutrino oscillations. Several last experiments have shown that neutrinos oscillate, which indicates that they are not massless. The upper limits to neutrino masses are set.

The following theoretical problems cannot be explained in the SM:

Hierarchy problem. The electroweak symmetry breaking of the SM has the special feature that the energy scale at which it must occur is known. The argument follows from the scattering of longitudinally polarised gauge bosons ($W_L^+ W_L^- \to W_L^+ W_L^-$). The requirement of unitarity condition sets the upper limit for the Higgs boson mass at 850 GeV. Therefore a weakly interacting Higgs boson, if it exists, will appear below the TeV scale. The SM will have to be extended to describe physics at arbitrary high energies. A new framework will be required at the grand unified scale ($\Lambda_{GUT} \approx 10^{16}$ GeV) or at reduced Planck scale ($M_P = 2.4 \times 10^{18}$ GeV), where quantum gravitational effects become important.

The argument against the simplest version of the SM is purely theoretical and arises when radiative corrections to the Higgs boson mass are computed. m_H^2 receives enormous quantum corrections from the virtual effects of every particle which couples, directly or indirectly, to the Higgs field. For example, in the left diagram of Fig. 1.6 there is a correction to m_H^2 from a loop containing a dirac fermion f with mass m_f. If the Higgs field couples to f with a term in the Lagrangian $-\lambda_f H \bar{f} f$, then the Feynman diagram in this figure yields a correction [30]

$$\Delta m_H^2 = \frac{|\lambda_f^2|}{16\pi^2}\left[-2\Lambda_{UV}^2 + 6m_f^2 \ln\left(\frac{\Lambda_{UV}}{m_f}\right) + ...\right], \tag{1.44}$$

where Λ_{UV} is an ultraviolet momentum cutoff used to regulate the loop integral, and should be interpreted as the energy scale at which new physics enters to alter the high-energy behaviour of the theory. Each of the leptons and quarks of the SM can play the role of f; for quarks the equation should be multiplied by 3 to account for colour.

Furthermore, there is a contribution similar to equation (1.44) from the virtual effects of any arbitrary heavy particles which might exist. For example, suppose there exists a heavy complex scalar particle S with mass m_S which couples to the Higgs with a Lagrangian term $-\lambda_S|H|^2|S|^2$. Then the right Feynman diagram in Fig. 1.6 gives a correction [30]

$$\Delta m_H^2 = \frac{\lambda_S}{16\pi^2}\left[\Lambda_{UV}^2 - 2m_S^2 \ln\left(\frac{\Lambda_{UV}}{m_S}\right) + ...\right]. \tag{1.45}$$

The problem is that if Λ_{UV} is of order of M_P, say, then the correction to m_H^2 is some 30 orders of magnitude larger than the aimed-for value of $m_H^2 \sim (100 \text{ GeV})^2$. This is only directly a problem for corrections to the Higgs scalar boson (mass)^2, because quantum corrections to fermion and gauge boson masses do not have the quadratic sensitivity to Λ_{UV}^2. However, the quarks and leptons and the electroweak gauge bosons Z^0, $W^{\pm}$ of the SM all owe their masses to the Higgs boson, so that the entire mass spectrum of the SM is directly or indirectly sensitive to the cutoff Λ_{UV}. Therefore

$$m_H^2 = m_{H_0}^2 + \Delta m_H^2 + counterterm, \tag{1.46}$$

where the counterterm must be adjusted to a precision of roughly 1 part in 10^{15} in order to cancel the quadratically divergent contributions to Δm_H^2. This adjustment must be made at each order in perturbation theory. This is known as the *hierarchy problem.*

Coupling unification. After the precise measurements of the $SU(3) \otimes SU(2) \otimes U(1)$ coupling constants, the possibility of coupling constant unification within the SM could be excluded, since after extrapolation to high energies the three coupling constants would not meet in a single point. This is demonstrated in the left Fig. 1.7, which shows the evolution of the inverse of the couplings as a function of the logarithm of the energy. This means, that the unification can only be obtained, if new physics enters between the electroweak and the Planck scale. As it will be shown later, this unification can be achieved within Supersymmetry (Section 1.2.1).

Large number of free parameters. The SM has 18 free parameters without neutrino masses. This is a large number if to take into account that this is a fundamental theory, where all scales, couplings and masses should emerge naturally and without individual tuning. Unfortunately, even the main extensions of the SM are not able to reduce this number, unless SUSY breaking mechanism is known.

Integration of gravity. The SM does not include gravitational interaction. Gravity is a sort of a non-quantised gauge theory of space and time, while the three SM interactions are described by gauge theories of fields in space and time. Therefore, the unification of all four interactions is not achieved in the SM.

1.2 Beyond the Standard Model

Although the SM is a very successful theory till now, the last missing component of the SM, the Higgs boson, needed for electroweak symmetry breaking, to date has not been found. Taking into account the theoretical problems, unsolved in the SM, some other theories beyond the SM have been developed. *Supersymmetry* is, at present, a favourite candidate of many theorists for new physics. In this section, the main steps in the construction of Supersymmetry will be described. The Higgs mechanism in the framework of the Minimal Supersymmetric extension of the SM (MSSM) will be explained.

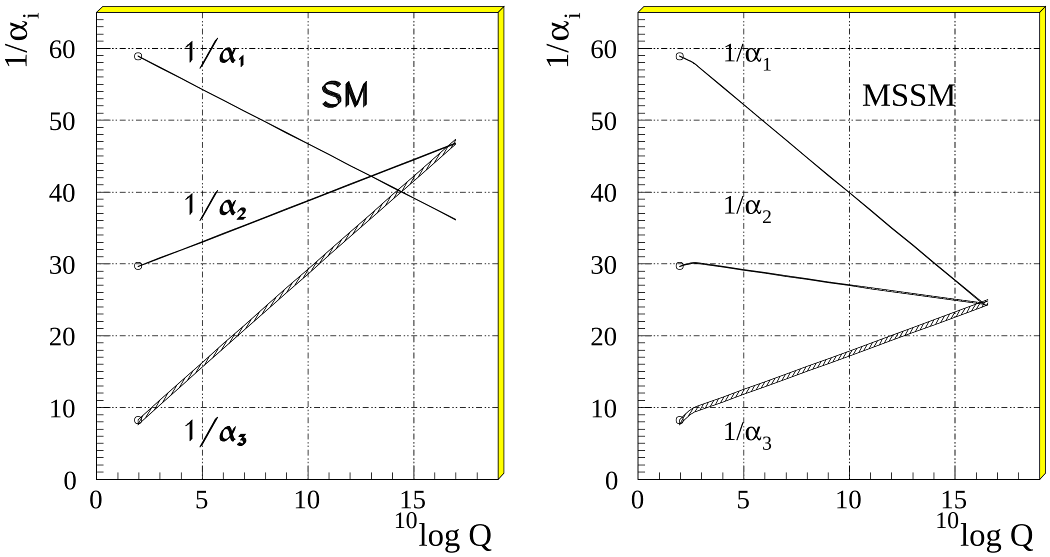

Figure 1.7: *Evolution of the inverse of the three coupling constants in the SM (left figure) and in a supersymmetric extension of the SM (MSSM) (right figure). Only in the latter case unification is obtained [31, 32]. The SUSY particles are assumed to contribute only above the effective SUSY scale M_{SUSY} of about 1 TeV, which causes a change in the slope in the evolution of couplings. The thickness of the lines represents the error in the measurements of the coupling constants [33].*

1.2.1 Supersymmetry

Returning to the hierarchy problem and comparing the equations (1.44) and (1.45), one can see that the effect of scalar particles on the Higgs mass renormalisation is quite different from that of fermions. If each of the quarks and leptons of the SM is accompanied by two complex scalars with

$$\lambda_S = \lambda_f^2, \tag{1.47}$$

the quadratic divergences, containing Λ_{UV}^2, coming from these two terms cancel each other. In order for this cancellation to persist to all orders in perturbation theory it must be the result from a special symmetry, a *Supersymmetry* (SUSY) [30, 31, 34]. Therefore SUSY solves the hierarchy problem of the SM.

A supersymmetry transformation turns a bosonic state into a fermionic state, and vice versa. The operator Q which generates such transformations must be an anticommuting operator, with

$$Q|Boson\rangle = |Fermion\rangle, \qquad Q|Fermion\rangle = |Boson\rangle. \tag{1.48}$$

The generators Q and $Q^\dagger$ must satisfy an algebra of anticommutation and commutation relations with the schematic form [30]:

$$\{Q, Q^\dagger\} = P^\mu, \tag{1.49}$$

$$\{Q, Q^\dagger\} = \{Q, Q^\dagger\} = 0, \tag{1.50}$$

$$[P^\mu, Q] = [P^\mu, Q^\dagger] = 0, \tag{1.51}$$

where P^μ is the momentum generator of space-time translations. Here, the indices on Q and $Q^\dagger$ are suppressed.

Theories with extended supersymmetry have more than one distinct copy of the supersymmetry generators Q, $Q^\dagger$. They are mathematically interesting, but do not have any phenomenological prospects, since extended symmetry in four-dimensional field theories cannot allow for chiral fermions or parity violation as observed in the SM. The ordinary, non-extended, phenomenologically viable type of supersymmetric model is sometimes called N=1 SUSY, with N referring to the number of supersymmetries (the number of distinct copies of $Q, Q^\dagger$).

The single-particle states of a supersymmetric theory fall naturally into irreducible representations of the supersymmetry algebra which are called *supermultiplets*. Each supermultiplet contains both fermion and boson states, which are commonly known as *superpartners* of each other.

The supersymmetry operators Q, $Q^\dagger$ also commute with the generators of gauge transformations. Therefore particles in the same supermultiplet must also be in the same representation of the gauge group, and so must have the same electric charge, weak isospin, and colour degrees of freedom.

For every supermultiplet the number of bosonic degrees of freedom n_B must be equal to the number of fermionic degrees of freedom n_F. The simplest possibility of such a supermultiplet has a single fermion (with two helicity states, so $n_F = 2$) and two real scalars (each with $n_B = 1$). It is natural to assemble the two real scalar degrees of freedom into a complex scalar field. This combination of a two component fermion and a complex scalar field is called a *chiral* or *matter* or *scalar* supermultiplet.

The next simplest possibility for a supermultiplet contains a spin-1 vector boson. If the theory is to be renormalisable this must be a gauge boson which is massless, at least before the gauge symmetry is spontaneously broken. A massless boson has two helicity states, so $n_B = 2$. Its superpartner is therefore a massless spin-1/2 fermion, again, with two helicity states, so $n_F = 2$. The fermionic partners of the gauge bosons are called *gauginos*. Such a combination of spin-1/2 gauginos and spin-1 gauge bosons is called a *gauge* or *vector* supermultiplet.

In a supersymmetric extension of the SM [35] each of the known fundamental particles must be in either a chiral or gauge supermultiplet and have a superpartner with spin differing by 1/2 unit. The names for the spin-0 partners of the quarks and leptons are constructed by prepending an "s", which is a short for scalar. Thus they are called *squarks* and *sleptons* and are symbolised with a tilde above the usual SM notation.

Because of the structure of supersymmetric theories, only a $Y = +1/2$ Higgs chiral supermultiplet can have the Yukawa couplings necessary to give masses to charge +2/3 up-type quarks (up, charm, top). Only a Y = -1/2 Higgs can have a Yukawa couplings necessary to give masses to charge -1/3 down-type quarks (down, strange, bottom) and to charged leptons. The $SU(2)_L$-doublet complex scalar fields corresponding to these two cases are called H_2 and H_1 respectively. The weak isospin components of H_2 with $I^3_w = (+1/2, -1/2)$ have electric charges 1, 0 respectively, and are denoted (H_2^+, H_2^0). Similarly, the $SU(2)_L$-doublet complex scalar H_1 has $I^3_w = (+1/2, -1/2)$ components (H_1^0, H_1^-). The neutral scalar that corresponds to the physical SM Higgs boson is in a linear combination of H_1^0 and H_2^0.

The generic nomenclature for a spin 1/2 superpartner of a SM boson is to append "-ino" to the name of the SM particle, so the fermionic partners of the Higgs scalars are called *higgsinos*.

All of the chiral supermultiplets of a minimal phenomenologically viable extension of the SM (MSSM) are summarised in Table 1.3. All the superpartners of SM particles are really new particles, and cannot be identified with some other SM state.

The fermionic partners of the SM vector bosons are generically referred as *gauginos*. The $SU(3)_C$ colour gauge interactions of QCD are mediated by the gluon g, whose spin-1/2 colour-octet supersymmetric partner is the gluino $\tilde{g}$. The electroweak gauge symmetry

Superfield	Boson, spin 0		Fermion, spin 1/2	
$\hat{L}$	sleptons	$\tilde{L} = (\tilde{\nu}, \tilde{e}_L)$	leptons	$L = (\nu, e_L)$
$\hat{E}$	(×3 families)	$\tilde{E} = \tilde{e}^*_R$	(×3 families)	$E = e^\dagger_R$
$\hat{Q}$	squarks	$\tilde{Q} = (\tilde{u}_L, \tilde{d}_L)$	quarks	$Q = (u_L, d_L)$
$\hat{U}$	(×3 families)	$\tilde{U} = \tilde{u}^*_R$	(×3 families)	$U = u^\dagger_R$
$\hat{D}$		$\tilde{D} = \tilde{d}^*_R$		$D = d^\dagger_R$
$\hat{H}_1$	Higgs	$H_1 = (H^0_1, H^-_1)$	higgsinos	$\tilde{H}_1 = (\tilde{H}^0_1, \tilde{H}^-_1)$
$\hat{H}_2$		$H_2 = (H^+_2, H^0_2)$		$\tilde{H}_2 = (\tilde{H}^+_2, \tilde{H}^0_2)$

Table 1.3: *Chiral supermultiplets in the MSSM.*

Superfield	Fermion, spin 1/2	Boson, spin 1
$\hat{G}$	gluino $\tilde{g}$	gluon g
$\hat{W}$	winos $\tilde{W}^\pm$, $\tilde{W}^0$	W bosons $W^\pm$, W^0
$\hat{B}$	bino $\tilde{B}^0$	Hypercharge B^0

Table 1.4: *Gauge supermultiplets in the MSSM.*

$SU(2)_L \times U(1)_Y$ has associated with it spin-1 gauge bosons $W^\pm$, W^0 and B^0, with spin-1/2 superpartners $\tilde{W}^\pm$, $\tilde{W}^0$ and $\tilde{B}^0$, called *winos* and *bino*. After electroweak symmetry breaking, the W^0 and B^0 weak eigenstates mix to give mass eigenstates Z^0 and γ. The corresponding gaugino mixtures of $\tilde{W}^0$ and $\tilde{B}^0$ are called *zino* $\tilde{Z}^0$ and *photino* $\tilde{\gamma}$. If SUSY were unbroken, they would be mass eigenstates with masses m_Z and 0. Table 1.4 summarises the gauge supermultiplets of the MSSM.

The winos $\tilde{W}^\pm$ and charged higgsinos $\tilde{H}^-_1$ and $\tilde{H}^+_2$ can mix and form two mass eigenstates with charge ±1 called *charginos*, $\tilde{\chi}^\pm_i$ (i=1,2). By convention, they are labelled in ascending order in mass $m_{\tilde{\chi}^+_1} \leq m_{\tilde{\chi}^+_2}$. The mixture of $\tilde{W}^0$, $\tilde{B}^0$, $\tilde{H}^0_1$ and $\tilde{H}^0_2$ form four neutral mass eigenstates called *neutralinos* χ^0_i (i=1,2,3,4) with masses $m_{\tilde{\chi}^0_1} \leq m_{\tilde{\chi}^0_2} \leq m_{\tilde{\chi}^0_3} \leq m_{\tilde{\chi}^0_4}$. In the limit of heavy masses $m_{\chi^0_i} \gg m_Z$ the following mass eigenstates are obtained:

$$\chi^0_i = \left[\tilde{B}^0,\, \tilde{W}^0,\, \sqrt{\frac{1}{2}}(\tilde{H}^0_1 - \tilde{H}^0_2),\, \sqrt{\frac{1}{2}}(\tilde{H}^0_1 + \tilde{H}^0_2) \right]. \tag{1.52}$$

Neutralinos are Majorana fermions, i.e. they form their own antiparticles.

The SUSY Lagrangian is invariant under a so-called *R-parity* transformations:

$$P_R = (-1)^{3(B-L)+2s}, \tag{1.53}$$

where s is a spin of the particle, B and L are baryon and lepton numbers, respectively. Standard Model particles and the Higgs bosons have even R-parity ($P_R = +1$), while all their SUSY partners have odd R-parity (P_R = -1). If R-parity is exactly conserved, then there can be no mixing between the sparticles and the $P_R = +1$ particles. Furthermore, every interaction vertex in the theory contains an even number of P_R = -1 sparticles. This has three important phenomenological consequences:

- The lightest sparticle with P_R = -1, called the *lightest supersymmetric particle* (LSP), must be absolutely stable. If the LSP is electrically neutral, it interacts only weakly with ordinary matter, and so can make an attractive candidate for the non-baryonic dark matter, which seems to be required by cosmology (see Section 1.1.7);

- Each sparticle other than the LSP must eventually decay into a state which contains an odd number of LSPs (usually just one);

- In collider experiments, sparticles can be produced in even numbers.

As it turned out within the MSSM model the unification of the coupling constants can be achieved if the SUSY masses are of the order of one TeV (Fig. 1.7 (right)). The SUSY particles are assumed to contribute effectively to the running of the constants only for energies above the typical SUSY mass scale, which causes the change in the slope of the lines near 1 TeV. From a fit requiring unification the values of $M_{SUSY} \approx 10^{3.4}$ GeV and $M_{GUT} \approx 10^{15.8}$ GeV can be received [32]. Therefore gauge couplings unification is a compelling hint for SUSY Grand Unification Theories (GUTs).

When one takes into account gravity, supersymmetry must be a local symmetry. The resulting locally supersymmetric theory is called *supergravity* (SUGRA). In SUGRA, the spin-2 graviton has a spin-3/2 fermion superpartner *gravitino*. The gravitino mass is traditionally called $m_{3/2}$.

1.2.2 SUSY Breaking Mechanisms

The interesting feature of the MSSM is that none of the superpartners of the SM particles has been discovered yet. Therefore, SUSY must be a broken symmetry in the vacuum state chosen by Nature. Since none of the fields of the MSSM can develop non-zero VEV to break SUSY without spoiling the gauge invariance, it is supposed that spontaneous supersymmetry breaking takes place via some other fields.

Spontaneous supersymmetry breaking (dynamical or not) requires to extend the MSSM. At the moment it is a usual approach to assume that the MSSM, which is the theory at the electroweak scale, is an effective low energy theory. At high scale spontaneous SUSY breaking occurs and is introduced in MSSM by adding extra terms which break supersymmetry explicitly in the effective MSSM Lagrangian. The extra supersymmetry-breaking couplings should be soft (of positive mass dimension) in order to be able to naturally maintain a hierarchy between the electroweak scale and the Planck (or some other very large) scale.

The most common scenario for producing low-energy SUSY breaking is called the *hidden sector* one [36]. According to this scenario, there exist two sectors: the usual matter belongs to the "visible" one, while the second, "hidden" sector, contains fields which lead to SUSY breaking. These two sectors interact with each other by exchange of some fields called *messengers*, which mediate SUSY breaking from the hidden to the visible sector (Fig. 1.8). In visible sector, these messengers appear as calculable soft terms. The MSSM soft terms arise indirectly or radiatively, rather than from tree-level renormalisable couplings to the supersymmetry-breaking order parameters.

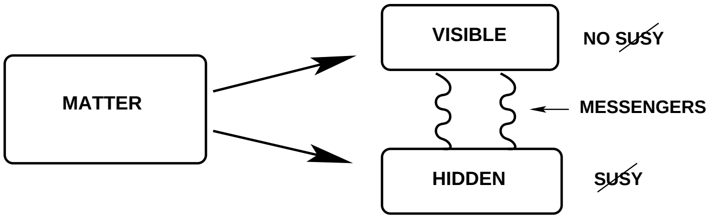

Figure 1.8: *Hidden sector SUSY breaking mechanism.*

There might be various types of messenger fields: gravity, gauge, etc. The hidden sector is the weakest part of the MSSM and it contains a lot of ambiguities. There are four main scenarios for SUSY breaking mechanism in the hidden sector [31]:

1. **Gravity mediated SUSY breaking (SUGRA).** This mechanism is based on effective nonrenormalisable interactions arising as a low-energy limit of supergravity theories. In this case, two sectors interact with each other via gravity. The weak point of this theory is that it is not truly substantiated due to the lack of a consistent theory of quantum (super)gravity. Other problems of supergravity mechanism are the large freedom of parameters and the absence of automatic suppression of flavour violation. The LSP particle in this model is neutralino. The sneutrino also could be, in principle, the LSP.

2. **Gauge mediated SUSY breaking (GMSB).** Here, the SUSY breaking effects are mediated to the observable world via gauge interactions. The messengers are the gauge bosons and matter fields of the SM and some GUT theory. The advantage of this scenario is that one can construct a renormalisable model with dynamic SUSY breaking, where, in principle, all the parameters can be calculated. The LSP is the gravitino in this scenario. The problem of the gauge mediated SUSY breaking scenario emerges in the Higgs sector since the Higgs mass mixing parameters, which break an unwanted Peccei-Quinn symmetry, cannot be generated by gauge interactions only.

3. **Anomaly mediated SUSY breaking (AMSB).** This mechanism assumes no SUSY breaking at the tree level. SUSY breaking is generated conformal anomaly. The problem which has to be solved in this mechanism is the appearance of the negative slepton mass squared (tachyons) at the tree level.

4. **Gaugino mediated SUSY breaking.** This is the less developed scenario so far. It is based on a paradigm of a brane world. According to this paradigm, there exists a multidimensional world where our four dimensional space-time represents a brane of four dimensions. The fields of the SM live on the brane, while gravity and some other fields can propagate in the bulk. There also exists another brane where supersymmetry is broken. SUSY breaking is mediated to our brane via the fields propagating in the bulk. It is assumed that the gaugino field plays an essential role in this mechanism (Fig. 1.9). LSP can be wino or higgsino in this scenario.

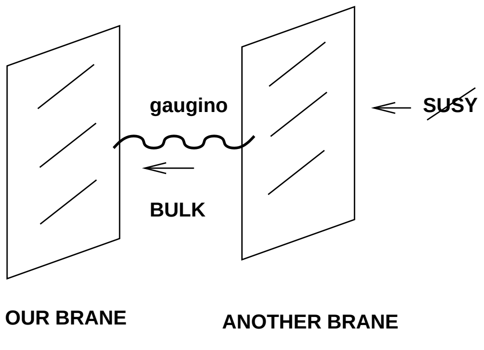

Figure 1.9: *Gaugino mediated SUSY breaking.*

1.2.3 Higgs Mechanism in the MSSM

The general form of the MSSM Lagrangian can be expressed as

$$\mathcal{L} = \mathcal{L}_{Yukawa} + \mathcal{L}_{gauge} + \mathcal{L}_W, \tag{1.54}$$

where $\mathcal{L}_W$ contains a superpotential W, which is given by

$$W_{\text{MSSM}} = \hat{U}\boldsymbol{y_u}\hat{Q}\hat{H}_2 - \hat{D}\boldsymbol{y_d}\hat{Q}\hat{H}_1 - \hat{E}\boldsymbol{y_e}\hat{L}\hat{H}_1 + \mu\hat{H}_2\hat{H}_1. \tag{1.55}$$

Here, the dimensionless Yukawa coupling parameters $\boldsymbol{y_u}$, $\boldsymbol{y_d}$, $\boldsymbol{y_e}$ are 3×3 matrices in family space. All gauge and family indices are suppressed here. The μ term is the supersymmetric version of the Higgs boson mass term in the SM. The Yukawa matrices determine the masses and CKM mixing angles of the ordinary quarks and leptons, after the neutral scalar components of $\hat{H}_1$ and $\hat{H}_2$ get VEVs. The terms $\hat{H}_1^*\hat{H}_1$ and $\hat{H}_2^*\hat{H}_2$ are forbidden in the superpotential, since it must be analytic in the chiral superfields (or equivalently in the scalar fields). Therefore, both $\hat{H}_1$ and $\hat{H}_2$ are needed in order to give Yukawa couplings, and thus masses, to all of the down-type and up-type quarks and leptons, respectively. Since the top quark, bottom quark and tau lepton are the heaviest fermions in the SM, it is often useful to make an approximation that only the (3,3) family components of each of $\boldsymbol{y_u}$, $\boldsymbol{y_d}$ and $\boldsymbol{y_e}$ are important. In this limit, only the third family and Higgs fields contribute to the MSSM superpotential.

The classical scalar potential for the Higgs scalar fields in the MSSM is given by

$$\begin{aligned} V \;=\;& (|\mu|^2 + m_{H_1}^2)(|H_1^0|^2 + |H_1^-|^2) + (|\mu|^2 + m_{H_2}^2)(|H_2^0|^2 + (|H_2^+|^2) \\ & + m_{12}^2(H_2^+H_1^- - H_2^0H_1^0) + \text{c.c.} \\ & + \frac{1}{8}(g^2 + g'^2)(|H_2^0|^2 + |H_2^+|^2 - |H_1^0|^2 - |H_1^-|^2)^2 \\ & + \frac{1}{2}g^2|H_2^+H_1^{0*} + H_2^0H_1^{-*}|^2. \end{aligned} \tag{1.56}$$

This potential has a minimum which breaks electroweak symmetry down to electromagnetism $SU(2)_L \times U(1)_Y \to U(1)_{EM}$, in accord with experiment. The freedom to make $SU(2)_L$ transformations allows to rotate away a possible VEV for one of the weak isospin components of one of the scalar fields, so $H_1^+ = 0$ can be taken at the minimum of the potential. Then one finds that a minimum of the potential satisfying $\partial V/\partial H_1^+ = 0$ must also have $H_2^+ = 0$. Then the scalar potential looks like

$$\begin{aligned} V \;=\;& (|\mu|^2 + m_{H_1}^2)|H_1^0|^2 + (|\mu|^2 + m_{H_2}^2)|H_2^0|^2 - (m_{12}^2H_2^0H_1^0 + \text{c.c.}) \\ & + \frac{1}{8}(g^2 + g'^2)(|H_2^0|^2 - |H_1^0|^2)^2, \end{aligned} \tag{1.57}$$

where only m_{12}^2 depends on the phases of the fields. Therefore the redefinition of the phases of H_1 and H_2 can absorb any phase in m_{12}^2, so m_{12}^2 can be taken real and positive. Using a $U(1)_Y$ gauge transformation it is possible to make $\langle H_1^0\rangle$ and $\langle H_2^0\rangle$ real without loss of generality. It follows that CP cannot be spontaneously broken by the Higgs scalar potential, since all the VEVs and couplings can be simultaneously chosen to be real.

The potential develops a stable minimum, if the following conditions are met:

$$m_{12}^4 \;>\; (|\mu|^2 + m_{H_1}^2)(|\mu|^2 + m_{H_2}^2), \tag{1.58}$$

$$2m_{12}^2 \;<\; 2|\mu|^2 + m_{H_1}^2 + m_{H_2}^2. \tag{1.59}$$

If $m_{H_1}^2 = m_{H_2}^2$, these equations cannot be satisfied. In models derived from the minimal supergravity or gauge-mediated boundary conditions, $m_{H_1}^2 = m_{H_2}^2$ holds at tree-level at the input scale, but the X_t contribution (see below) to the renormalisation group (RG) equation for $m_{H_2}^2$ naturally pushes it to negative or small values $m_{H_2}^2 < m_{H_1}^2$ at the electroweak scale (RG equations are a crucial tool in determining the Lagrangian at the electroweak scale, given a set of boundary conditions on the theory at the much higher input scale) [30]:

$$\begin{aligned} 16\pi^2 \frac{d}{dt} m_{H_2}^2 &= 3X_t - 6g_2^2|M_2|^2 - \frac{6}{5}g_1^2|M_1|^2, && (1.60) \\ 16\pi^2 \frac{d}{dt} m_{H_1}^2 &= 3X_b + X_\tau - 6g_2^2|M_2|^2 - \frac{6}{5}g_1^2|M_1|^2, && (1.61) \end{aligned}$$

where

$$\begin{aligned} X_t &= 2|y_t|^2(m_{H_2}^2 + m_{\hat{Q}_3}^2 + m_{\hat{U}_3}^2) + 2|a_t|^2, && (1.62) \\ X_b &= 2|y_b|^2(m_{H_1}^2 + m_{\hat{Q}_3}^2 + m_{\hat{D}_3}^2) + 2|a_b|^2, && (1.63) \\ X_\tau &= 2|y_\tau|^2(m_{H_1}^2 + m_{\hat{L}_3}^2 + m_{\hat{E}_3}^2) + 2|a_\tau|^2, && (1.64) \end{aligned}$$

where $y_{t,b,\tau}$ are Yukawa couplings and $a_{t,b,\tau}$ are soft couplings. X_t, X_b, X_τ are positive, so their effect is always to decrease the Higgs masses as one evolves the RG equations downward from the input scale to the electroweak scale. Since y_t is the largest of the Yukawa couplings because of the experimental fact that the top quark is heavy, X_t is typically expected to be larger than X_b and X_τ. Unless this effect is large, the parameter space in which the electroweak symmetry is broken would be quite small. So in the models derived from the minimal supergravity or gauge-mediated boundary conditions, electroweak symmetry breaking is driven purely by quantum corrections and this mechanism is known as *radiative electroweak symmetry breaking.*

Having established the condition necessary for H_1^0 and H_2^0 to get non-zero VEVs, $\langle H_1^0 \rangle = v_1$ and $\langle H_1^0 \rangle = v_2$ for VEVs at the minimum of the potential can be written. Then

$$v_1^2 + v_2^2 = v^2 = \frac{2m_Z^2}{g^2 + g'^2} \approx (174\ GeV)^2, \qquad (1.65)$$

$$m_W^2 = \frac{g^2(v_1^2 + v_2^2)}{2}. \qquad (1.66)$$

The ratio of the two VEVs is traditionally written as

$$\tan\beta \equiv \frac{v_2}{v_1}. \qquad (1.67)$$

The Higgs scalar fields in the MSSM consist of two complex $SU(2)_L$-doublets, or eight real, scalar degrees of freedom. When the electroweak symmetry is broken, three of them are the would-be Nambu-Goldstone bosons G^0, $G^\pm$ which become the longitudinal modes of the Z^0 and $W^\pm$ massive vector bosons. The remaining five Higgs scalar mass eigenstates consist of one CP-odd neutral scalar A^0, two CP-even neutral scalars h^0 and H^0 and two charged scalars $H^\pm$. The tree level masses of these fields can be found by expanding the scalar potential around the minimum, obtaining

$$\begin{aligned} m_{A^0}^2 &= \frac{2m_{12}^2}{\sin 2\beta}, && (1.68) \\ m_{h^0,H^0}^2 &= \frac{1}{2}\left(m_{A^0}^2 + m_Z^2 \mp \sqrt{(m_{A^0}^2 + m_Z^2)^2 - 4m_Z^2 m_{A^0}^2 \cos^2 2\beta} \right), && (1.69) \\ m_{H^\pm}^2 &= m_{A^0}^2 + m_W^2. && (1.70) \end{aligned}$$

At tree level the following important predictions can be made:

$$\begin{aligned} m_{h^0} &< m_Z|\cos 2\beta|, \quad (1.71)\\ m_{h^0} &< m_{A^0}, \quad (1.72)\\ m_{H^0} &> m_Z, \quad (1.73)\\ m_{H^\pm} &> m_W. \quad (1.74) \end{aligned}$$

The tree-level mass formulas given above for the Higgs mass eigenstates are subject to quite significant quantum corrections which are especially important to take into account in the case of h^0. The largest of such contributions typically come from top-stop loop corrections to the terms in the scalar potential. Their origin are incomplete cancellations between virtual top and stop loops, reflecting the breaking of supersymmetry. The mass relations are also affected by the potentially large mixing between $\tilde{t}_L$ and $\tilde{t}_R$ due to the top Yukawa coupling. In the limit of stop quark masses $m_{\tilde{t}_1}$, $m_{\tilde{t}_2}$ much larger than the top quark mass m_t, the one loop radiative correction to (1.69) looks like [37]

$$\Delta(m^2_{h^0}) = 2N_C \frac{g^2}{(4\pi)^2} \frac{m_t^4}{m_W^2} \log\left(\frac{m_{\tilde{t}_1} m_{\tilde{t}_2}}{m_t^2}\right), \quad (1.75)$$

where N_C is the colour factor and equals 3 for tops. Taking into account this and other corrections, the value of m_h can be as large as 135 GeV [38].

The two CP-even Higgs boson degrees of freedom mix. The mixing matrix of the Higgs mass eigenstates in the basis of the weak eigenstates a (CP-odd) and h_1, h_2 (CP-even) is

$$\begin{pmatrix} A \\ h \\ H \end{pmatrix} = \begin{pmatrix} 1 & 0 & 0 \\ 0 & \cos\alpha & -\sin\alpha \\ 0 & \sin\alpha & \cos\alpha \end{pmatrix} \begin{pmatrix} a \\ h_1 \\ h_2 \end{pmatrix}, \quad (1.76)$$

where the mixing angle α is determined at tree level by

$$\frac{\sin 2\alpha}{\sin 2\beta} = -\frac{m^2_{A_0} + m^2_Z}{m^2_{H^0} - m^2_{h^0}}; \quad \frac{\cos 2\alpha}{\cos 2\beta} = -\frac{m^2_{A_0} - m^2_Z}{m^2_{H^0} - m^2_{h^0}}. \quad (1.77)$$

In contrast to the SM, the Higgs masses are predicted in terms of the fundamental parameters of the MSSM. At tree level, the MSSM Higgs sector is parametrised by m_A and $\tan\beta$.

The size of MSSM Higgs couplings to quarks, leptons and gauge bosons is similar to the SM, yet modified by the mixing angles α and β. They are presented in Table 1.5 normalised to the SM values.

	g_u	g_d	g_V
h	$\frac{\cos\alpha}{\sin\beta}$	$-\frac{\sin\alpha}{\cos\beta}$	$\sin(\beta-\alpha)$
A	$\frac{1}{tan\beta}$	$\tan\beta$	0
H	$\frac{\sin\alpha}{\sin\beta}$	$\frac{\cos\alpha}{\cos\beta}$	$\cos(\beta-\alpha)$

Table 1.5: *Higgs bosons couplings in the MSSM relative to the SM couplings to up- and down-type fermions, g_u and g_d, and gauge bosons g_V ($V =$ W,Z).*

1.2.4 CP Violation in MSSM

As it was mentioned in Section 1.1.7 the size of CP violation in the SM is insufficient to drive the cosmological baryon asymmetry. CP violating (CPV) effects in the MSSM can help to reduce this crisis [28].

In the previous section it was shown that the MSSM Higgs potential is invariant under CP at the tree level. In this case Higgs CP eigenstates are equal to the mass eigenstates. Only the CP-even weak eigenstates mix with each other, but they do not mix with the CP-odd eigenstate. Recently, it has been shown [39], that the tree-level CP invariance of the MSSM Higgs sector can be broken sizably by loop effects at the observable level, especially by contributions from third generation scalar quarks.

Several new parameters which could, in principle, possess CP violating phases are introduced in the MSSM, which are absent in the SM. They are the following:

- the mass parameter μ, which involves the bilinear mixing of the two Higgs chiral superfields in the superpotential;
- the soft SUSY breaking gaugino masses m_λ, where λ collectively denotes $\tilde{g}$, $\tilde{W}$, $\tilde{B}$, i.e. the gauginos of the gauge groups $SU(3)_C$, $SU(2)_L$ and $U(1)_Y$, respectively;
- the soft bilinear Higgs mixing mass m_{12}^2;
- the soft trilinear Yukawa couplings A_f of scalar fermions to the Higgs particles (Fig. 1.10).

In the constrained version of the MSSM only two phases $\arg(\mu)$ and $\arg(A_{t,b})$ (for simplicity we fix $A_t = A_b$) are usually taken as independent CP violating parameters [40]. The CP invariance of the Higgs potential is broken involving one-loop effects if

$$\mathrm{Im}(m_{12}^{*2}\, \mu A_{t,b}) \neq 0. \tag{1.78}$$

The phase of m_{12}^{*2} can be rotated away at tree level and the phase of μ can be absorbed in the phase redefinition of $A_{t,b}$. Therefore, only the phase $\arg(A_{t,b})$ is responsible for the introduction of CP violation effects at one-loop level. At two-loop level also $\arg(m_{\tilde{g}})$ can provide CP violation. In Fig. 1.11 the CP violating one-loop contributions to the Higgs potential are shown. In figure (a) the tree level quartic coupling of the Higgs potential between the weak Higgs eigenstates h_i is shown. In (b) and (c) the trilinear coupling A_t is introduced via loop effects, thus, introducing CP violation into the Higgs potential.

CP violation in the Higgs potential of the MSSM leads to mixing mass terms between the CP-even and CP-odd Higgs fields. Thus, one has to consider a (4×4)-mass matrix for the

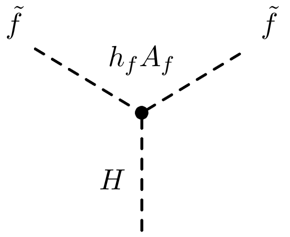

Figure 1.10: *Trilinear coupling A_f in the MSSM. The phase of this coupling introduces CP violation.*

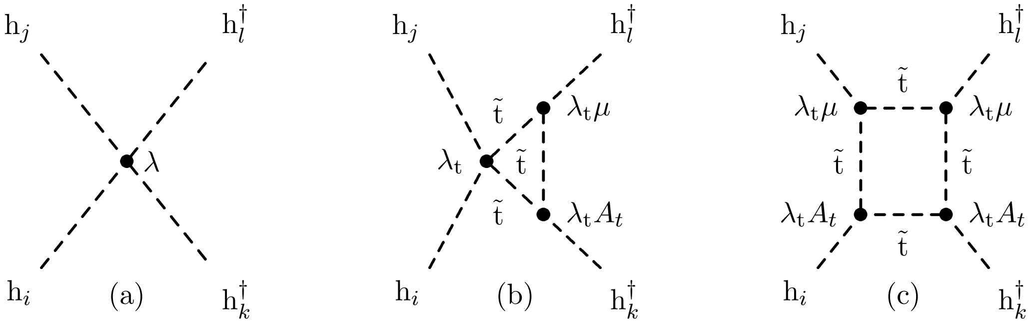

Figure 1.11: *Introduction of CP violating effects into the Higgs potential.*

neutral Higgs bosons. In the weak basis $\{h_1, h_2, a_1, a_2\}$, the neutral Higgs boson mass matrix $\mathcal{M}_0^2$ may be cast into the form

$$\mathcal{M}_0^2 = \begin{pmatrix} \mathcal{M}_S^2 & \mathcal{M}_{SP}^2 \\ (\mathcal{M}_{SP}^2)^T & \mathcal{M}_P^2 \end{pmatrix}, \tag{1.79}$$

where $\mathcal{M}_S^2$, $\mathcal{M}_P^2$ and $\mathcal{M}_{SP}^2$ denote the (2×2)-matrices of the scalar, preudoscalar and scalar-pseudoscalar squared mass terms of the neutral Higgs bosons. Since the Goldstone particle G^0 does not mix with other neutral fields, the (4×4)-matrix $\mathcal{M}_0^2$ reduces to a (3×3)-matrix $\mathcal{M}_N^2$, which in the weak basis $\{h_1, h_2, a\}$ may be expressed by

$$\mathcal{M}_N^2 = \begin{pmatrix} (\mathcal{M}_S^2)_{11} & (\mathcal{M}_S^2)_{12} & \frac{1}{\cos\beta}(\mathcal{M}_{SP}^2)_{12} \\ (\mathcal{M}_S^2)_{21} & (\mathcal{M}_S^2)_{22} & -\frac{1}{\sin\beta}(\mathcal{M}_{SP}^2)_{21} \\ \frac{1}{\cos\beta}(\mathcal{M}_{SP}^2)_{12} & -\frac{1}{\sin\beta}(\mathcal{M}_{SP}^2)_{21} & -\frac{1}{\sin\beta\cos\beta}(\mathcal{M}_P^2)_{12} \end{pmatrix}. \tag{1.80}$$

The resulting RG-improved Higgs boson mass matrix $\mathcal{M}_N^2$ is symmetric and positive definite [41] and can therefore be diagonalised by an orthogonal transformation O as follows:

$$O^T \mathcal{M}_N^2 O = \mathrm{diag}\left[M_{\mathrm{H}_1}^2, M_{\mathrm{H}_2}^2, M_{\mathrm{H}_3}^2\right], \tag{1.81}$$

where the mass eigenstates $M_{\mathrm{H}_1}^2$, $M_{\mathrm{H}_2}^2$, $M_{\mathrm{H}_3}^2$ are defined as

$$M_{\mathrm{H}_1}^2 \leq M_{\mathrm{H}_2}^2 \leq M_{\mathrm{H}_3}^2. \tag{1.82}$$

Thus, explicit radiative CP violation in the Higgs sector leads to a generation of sizable off-diagonal scalar-pseudoscalar contributions of (2×2)-matrix $\mathcal{M}_{SP}^2$ to the general (3×3)-matrix $\mathcal{M}_N^2$. Each of the individual CP violating off-diagonal scalar-pseudoscalar mixing entries $\mathcal{M}_{SP}^2$ in the neutral mass-squared matrix contains terms scaling qualitatively as

$$\mathcal{M}_{SP}^2 \sim \frac{m_t^4}{v^2} \frac{\mathrm{Im}(\mu A_t)}{32\pi^2 M_{\mathrm{SUSY}}^2} \left(1, \frac{|A_t|^2}{M_{\mathrm{SUSY}}^2}, \frac{|\mu|^2}{\tan\beta\, M_{\mathrm{SUSY}}^2}, \frac{2\mathrm{Re}(\mu A_t)}{M_{\mathrm{SUSY}}^2}\right), \tag{1.83}$$

and could be of order M_{Z}^2. As it is seen, CP violating effects in the neutral Higgs boson mass matrix become significant, if $\mathrm{Im}(\mu A_t)/M_{\mathrm{SUSY}}^2$ is large.

In such a minimal SUSY scenario of explicit radiative CP violation, the three neutral Higgs bosons M_{H_1}, M_{H_2} and M_{H_3} have in general mixed CP parities, i.e. the Higgs boson mass eigenstates are not equal to Higgs CP eigenstates h_1, h_2, a.

In the presence of CP violating mixing between the neutral Higgs bosons, it becomes necessary to parametrise the MSSM Higgs sector in terms of $\tan\beta$ and the charged Higgs

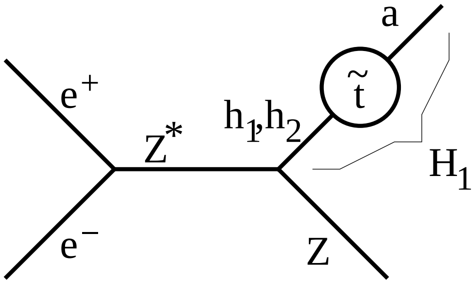

Figure 1.12: *Higgsstrahlung Process.*

boson mass m_{H^+}, since the CP-odd Higgs boson mass m_A, used in the CP conserving (CPC) scenario, is no longer associated with a physical Higgs mass eigenstate.

The couplings of the Higgs mass eigenstates to the SM fermions and bosons can be obtained from the orthogonal matrix O_{ij} $(i,j{=}1{,}2{,}3)$ (see (1.81)). The couplings to the SM bosons V (V=Z,W) are [41]

$$\begin{aligned} g_{\mathrm{H}_i\mathrm{VV}} &= \cos\beta\, O_{1i} + \sin\beta\, O_{2i}, && (1.84)\\ g_{\mathrm{H}_i\mathrm{H}_j\mathrm{V}} &= O_{3i}\,(\cos\beta\, O_{2j} - \sin\beta\, O_{1j}) - O_{3j}\,(\cos\beta\, O_{2i} - \sin\beta\, O_{1i}). && (1.85)\end{aligned}$$

The couplings H_iZZ and $\mathrm{H}_i\mathrm{W}^+\mathrm{W}^-$ are related to the $\mathrm{H}_i\mathrm{H}_j$Z couplings through

$$g_{\mathrm{H}_k\mathrm{VV}} = \varepsilon_{ijk} g_{\mathrm{H}_i\mathrm{H}_j\mathrm{Z}}. \qquad (1.86)$$

The unitarity provides the constraint

$$\sum_{i=1}^{3} g^2_{\mathrm{H}_i\mathrm{VV}} = 1. \qquad (1.87)$$

Equation (1.84) shows that only the CP-even weak eigenstates h_1 and h_2 couple to the Z in Higgsstrahlung, as in the CP conserving case. This can be illustrated in the Higgsstrahlung process $\mathrm{e}^+\mathrm{e}^- \to \mathrm{H}_1\mathrm{Z}$ in Fig, 1.12, where a mass eigenstate H_1 consists of the admixture of the CP eigenstates h_1, h_2 and a. Only CP-even weak Higgs states h_1 and h_2 couple to the Z boson. However, the Higgs mass eigenstate H_1 also carries a CP-odd component a, which does not couple to the Z but introduced via loop effects.

1.3 Summary

The Standard Model of modern particle physics is a successful theory of electromagnetic, weak and strong interactions. However, the Higgs boson, the last missing component of the SM, needed for electroweak symmetry breaking, to date has not been found.

The development of some other theories beyond the SM was motivated by unsolved theoretical problems of the SM. Supersymmetry is the most popular of such theories at present. It solves the hierarchy problem, can provide particle candidates for cold dark matter, provides the possibility of coupling unification giving a hint to grand unification and offers a theoretical link to incorporate gravity. SUSY can provide CP violation, necessary for the explanation of the universe baryon asymmetry. However, it has some weak points like the absence of the clear picture of the supersymmetry breaking mechanism. The problem of the large number of free parameters of the SM is also not solved. In SUSY extensions of the SM this number is further increased.

In the Minimal Supersymmetric extension of the SM the SUSY breaking mechanism is introduced via soft terms in the Lagrangian, which preserves the solution of the hierarchy problem up to the large energy scale. The electroweak symmetry breaking mechanism in MSSM is driven purely by quantum corrections. Two Higgs doublet fields manifest themselves via five physical Higgs bosons.

Chapter 2

The International Linear Collider Project

The International Linear Collider (ILC) is the next international high energy collider project. It is an e^+e^- collider, which will operate at a centre of mass energies $\sqrt{s} = 91.2$ to 800 GeV or 1 TeV. It has a rich research potential in deeper investigation of the Standard Model as well as its possible extensions like Supersymmetry or extra dimensions. The Linear Collider is complementary to the LHC in its physics program. It will allow, for example, to investigate the properties of Higgs boson precisely if it is found at the LHC. In this chapter the operation principles of the Linear Collider machine will be described as well as a possible detector concept.

2.1 Linear Collider Machine

The International Linear Collider is foreseen to be the next high energy experiment to solve some of the existing problems in particle physics and to make more precise measurements of the known values. In its physics purposes it is in many ways complementary to the LHC experiment.

The ILC is the next generation project, following LEP collider, which approached the technical frontier of a circular electron accelerators. The energy loss of the accelerated electrons per turn due to synchrotron radiation is $\delta E \simeq E_b^4/(Rm_0^4)$, where E_b is the beam energy, R is the radius of the accelerator and m_0 is the mass of the accelerated particle. At the highest LEP energies these losses reached with about 3 GeV per turn the limit of the RF power. Therefore e^+e^- ring accelerators are not appropriate to reach high collision energies any more. Such losses do not exist for Linear Collider. The main problems here are the high gradient of the acceleration cavities, in order to get the required energy with a technically reasonable length of the accelerator, and the luminosity. The bunches are brought into collision only once, hence the permanent creation of new beam particles allowing high beam intensities is required. Compared to a proton machine, the advantages of an e^+e^- collider are the well defined initial state and low backgrounds, the possibility to tune $\sqrt{s}$ and the possibility of polarised beams.

This study is performed for a Linear Collider, based on TESLA (TeV-Energy Superconducting Linear Accelerator) technology [42], proposed by the TESLA collaboration, centred at DESY. Two other technologies like NLC (Next Linear Collider) [43] and GLC (Global Linear Collider) [44], developed by SLAC and KEK, respectively, are based on warm X-band radio frequency (RF) technology whereas TESLA technology is based on cold L-band RF. In 2004, ICFA (International Committee for Future Accelerators) formed the International Technology Recommendation Panel (ITRP) to evaluate the two technologies and to recommend a single choice on which to base the Linear Collider. In August 2004 ITRP has made the recommendation that the Linear Collider be based on superconducting RF technology [45]. The decision was based on a set of criteria that addressed scientific, technical, cost, schedule, and operability issues for each technology.

The warm technology allows a greater energy reach for a fixed length, and the damping rings and positron source are simpler. The superconducting technology has features, some of which follow from the low RF, that are considered attractive and will facilitate the future design [45]:

- The large cavity aperture and long bunch interval simplify operations, reduce the sensitivity to ground motion, permit inter-bunch feedback, and may enable increased beam current.
- The main linac and RF systems, the most expensive components of the machine, are of comparatively lower risk.
- The construction of the superconducting XFEL free electron laser will provide prototypes and test many aspects of the linac.
- The industrialisation of most major components of the linac is underway.
- The use of superconducting cavities significantly reduces power consumption.

The following physics operation factors favoured the cold machine:

- The long separation between bunches in a cold machine allows full integration of detector signals after each bunch crossing. In a warm machine, the pileup of energy from multiple bunch crossings is a potential problem, particularly in forward regions. The dedicated study of physics analysis in the Higgs sector showed a severe degradation of the achievable precision if the time-stamp capability of the detector is significantly worse than 5.6 ns, corresponding to four bunch crossings at the warm machine [46].
- The energy spread is somewhat smaller for the cold machine, which leads to better precision for measuring particle masses.
- If desired, in a cold machine the beams can be collided head-on in one of the interaction regions, whereas in the warm machine such an option is impossible. Zero crossing angle might simplify shielding from background. However, a non-zero crossing angle permits the measurement of beam properties before and after the collision, providing a better tool for precise determination of energy and polarisation of colliding particles.

It is also important, that the final design allows maximum flexibility for physics, including the possibilities of increased luminosity, positron polarisation, as well as the operation at the Z pole, WW threshold, and in e^-e^-, $e^-\gamma$, or $\gamma\gamma$ modes, where the photons can be obtained through Compton backscattering of a laser beam.

The overall layout of the future Linear Collider working initially at centre of mass energies of $\sqrt{s} = 91.2$ to 500 GeV and $\sqrt{s} = 800$ GeV or 1 TeV after upgrade is shown in Fig. 2.1. The total length is about 33 km long. The main components are a pair of linear accelerators, one for electrons and one for positrons, pointing at each other. Unlike a storage ring collider, a linear collider cannot serve several interaction regions simultaneously with the same beam,

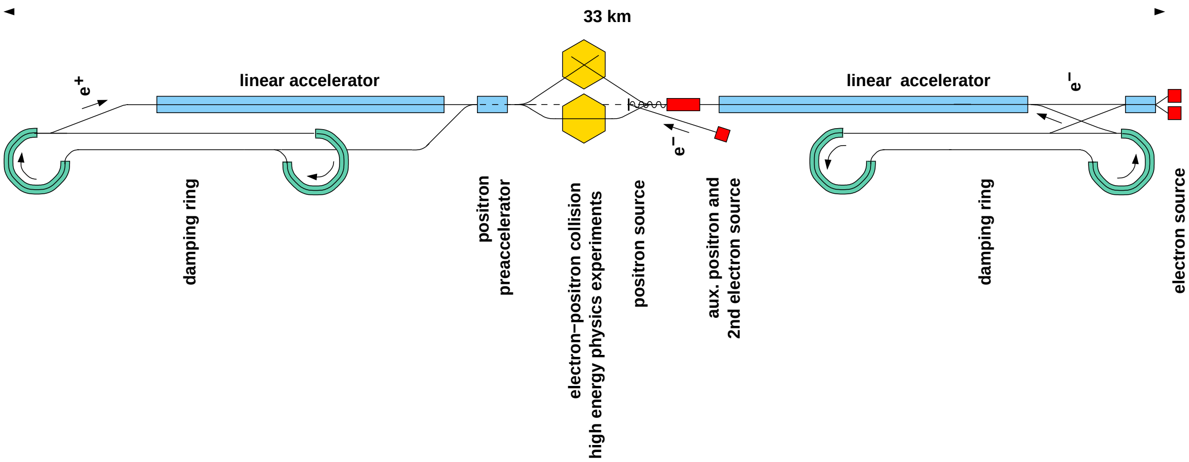

Figure 2.1: *The linear accelerator. Particles are accelerated and brought to collision at one or two central interaction regions with* $\sqrt{s} = 91.2$ *to 800 GeV or 1 TeV.*

but it is possible to switch the beam between two experimental stations. Therefore the second interaction point (IP) in the layout of TESLA facility is integrated. Unlike the primary IP which has a zero crossing angle, the second IP will have a crossing angle of $\sim$ 34 mrad, and is therefore suitable for the $e\gamma$ and $\gamma\gamma$ collider modes of operation. The second IP can also be used for e^+e^- collisions, with the same luminosity as the primary IP (assuming that the so-called crab-crossing scheme is used). e^-e^- collisions (at one or both of the IPs) can be provided by reversing magnet polarities and adding a polarised electron source to the (nominal) positron branch of the collider.

Each linear accelerator is constructed from about ten thousand one-meter long 9-cell niobium superconducting cavities (Fig. 2.2) cooled by superfluid Helium to T = 2K and operating at L-band frequency (1.3 GHz). The design gradient at $\sqrt{s} = 500$ GeV is $E_{acc} = 23.4$ MV/m. Pulsed RF electromagnetic fields are guided five times per second for the duration of one millisecond into the cavities to accelerate the particles. As the power dissipation in the cavity is extremely small, the power transfer efficiency from the RF source to the particles is very high, thus keeping the electrical power consumption within acceptable limits ($\sim$100 MW), even for a high average beam power. The high beam power is the first essential requirement to obtain a high rate of electron-positron collisions. The second requirement is extremely small sizes of the electron and positron beams at the IP. The relatively low RF of the TESLA is ideally suited for conserving the ultra-small size of the beams during acceleration (due to much weaker wakefields in the larger cavities of accelerators working at low RF).

The electron beam is generated in a polarised laser-driven gun. Polarised electrons are produced by illuminating a GaAs cathode with circularly polarised laser light. After a short section of conventional linac, the beam is accelerated to 5 GeV in superconducting structures identical to the ones used for the main linac. The baseline design assumes that the electrons are stored in a damping ring very similar to the one required for the positron beam. Damping rings are used to reduce the emittances produced by the particle sources to the small values required for the Linear Collider. Emittance reduction is achieved via the process of radiation damping, i.e. the combination of synchrotron radiation in bending fields with energy gain in RF cavities. The design of the damping ring has to ensure a small emittance and a sufficient damping rate.

The positron injection system has to provide a total charge of about $5 \cdot 10^{13}$ e^+ per beam

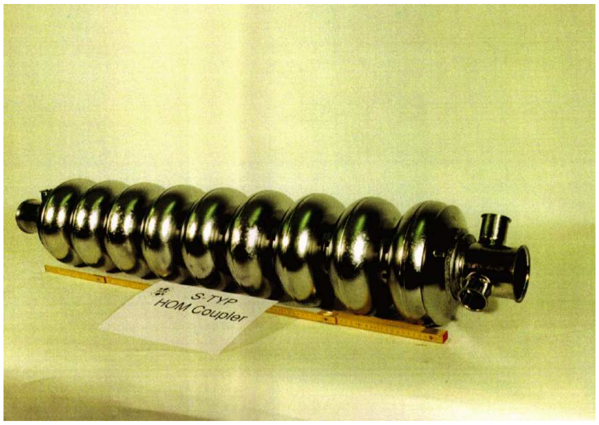

Figure 2.2: *The 9-cell niobium superconducting cavity for a future Linear Collider.*

pulse, which is not realistically feasible with conventional (electron on thick target) source. Instead, positrons are produced from γ-conversion in a thin target, after which they are preaccelerated in a conventional 200 MeV L-band linac, followed by a 5 GeV superconducting accelerator. The photons are generated by passing the high-energy electron beam through an undulator placed after the main linac, before transporting the beam to the IP. Passage through the undulator causes the energy spread in the electron beam to increase from $0.5 \cdot 10^{-3}$ to $1.5 \cdot 10^{-3}$, with an average energy loss of 1.2%. Placing the positron source upstream of the IP has removed the need to collimate a substantial fraction of the high power spent-beam, which has posed technical and radiation safety problems.

Besides providing a sufficiently high positron beam intensity, the undulator based source offers several additional advantages:

- Use of a thin target leads to a smaller positron beam with a smaller transverse emittance than from a conventional (thick target) source.
- The considerable investment and operating costs for a high-power electron linac needed in a conventional scheme are avoided.
- Production of polarised positrons is possible by replacing the planar undulator with a helical undulator. The experiment E-166 [47] at SLAC is going to justify the relevance of the scheme proposed by Balakin and Mikhailichenko [48] in which a helical undulator is employed to generate photons of several MeV with circular polarisation which are then converted in a relatively thin target to generate longitudinally polarised positrons.

Besides $\sqrt{s}$ of the colliding beams, the second key parameter for a Linear Collider is the luminosity L, given by

$$L = \frac{n_b N_e^2 f_{rep}}{4\pi\sigma_x^*\sigma_y^*} \times H_D, \tag{2.1}$$

where n_b is the number of bunches per pulse, N_e - number of e^- (e^+) per bunch, f_{rep} - pulse repetition frequency, $\sigma_{x,y}^*$ - horizontal (vertical) beam size at IP, H_D - disruption enhancement factor (typically $H_D \approx 2$).

An important constraint on the choice of IP parameters is the effect of beamstrahlung: the particles emit hard synchrotron radiation in the strong electromagnetic space-charge field

$\sqrt{s}$	500 GeV	800 GeV
Accelerating gradient E_{acc}	23.8 MV/m	35 MV/m
RF-frequency f_{RF}	1.3 GHz	1.3 GHz
Repetition rate f_{rep}	5 Hz	4 Hz
Beam pulse length T_p	950 μs	860 μs
No. of bunches per pulse n_b	2820	4886
Bunch spacing Δt_b	337 ns	176 ns
Charge per bunch N_e	$2 \cdot 10^{10}$	$1.4 \cdot 10^{10}$
x Emittance at IP $\gamma \varepsilon_x$	$10 \cdot 10^{-6}$ m	$8 \cdot 10^{-6}$ m
y Emittance at IP $\gamma \varepsilon_y$	$0.03 \cdot 10^{-6}$ m	$0.015 \cdot 10^{-6}$ m
x Beam size at IP σ_x^*	553 nm	391 nm
y Beam size at IP σ_y^*	5 nm	2.8 nm
Bunch length at IP σ_z	0.3 mm	0.3 mm
Beamstrahlung δ_E	3.2%	4.3%
Luminosity L_{e+e-}	$3.4 \cdot 10^{34}$ cm^{-2}s^{-1}	$5.8 \cdot 10^{34}$ cm^{-2}s^{-1}

Table 2.1: *Machine parameters of a future Linear Collider (TESLA concept) for $\sqrt{s} = 500$ GeV baseline operation and for an upgrade to 800 GeV.*

of the opposing bunch. The average fractional beam energy loss from beamstrahlung is approximately given by:

$$\delta_E \approx 0.86 \frac{r_e^3 N_e^3 \gamma}{\sigma_z (\sigma_x^* + \sigma_y^*)^2} \ , \tag{2.2}$$

where r_e is the classical electron radius, γ is the relativistic factor $E_{beam}/m_e c^2$. Beamstrahlung causes a reduction and a spread of the collision energy and can lead to background in the detector. The energy loss δ_E is therefore typically limited to a few percent. By choosing a large aspect ratio $R = \sigma_x^*/\sigma_y^* >> 1$, δ_E becomes independent of vertical size and the luminosity can be increased by making σ_y^* as small as possible.

The main LC parameters (TESLA concept) for the $\sqrt{s} = 500$ GeV baseline design and for an upgrade to 800 GeV are listed in the Table 2.1.

2.2 A Detector for a Linear Collider

Linear Collider detector design is driven predominantly by physics requirements due to the large luminosity and relatively low background and radiation damage of the detector. The detector used in the simulation follows the proposal for TESLA Linear Collider detector presented in the Technical Design Report (TDR) [49].

The Higgs mechanism predicts the Higgs boson couplings to scale with the particle masses, therefore the excellent parton flavour and gauge boson type identification at a Linear Collider are mandatory. This will require a good performance of the detector's vertexing, tracking, particle flow (Section 2.2.3) and hermeticity. In this thesis a large version of a future Linear Collider detector is considered, namely with a time projection chamber (TPC) as a tracking device. Fig. 2.3 shows the detector layout for TESLA concept. The interaction region is surrounded by a tracker consisting of a multi-layered pixel micro-vertex detector (VTX) as the innermost part and a large TPC supplemented with additional silicon detectors in the forward region (FTD) and two barrels of silicon detector (SIT) between VTX and TPC. In

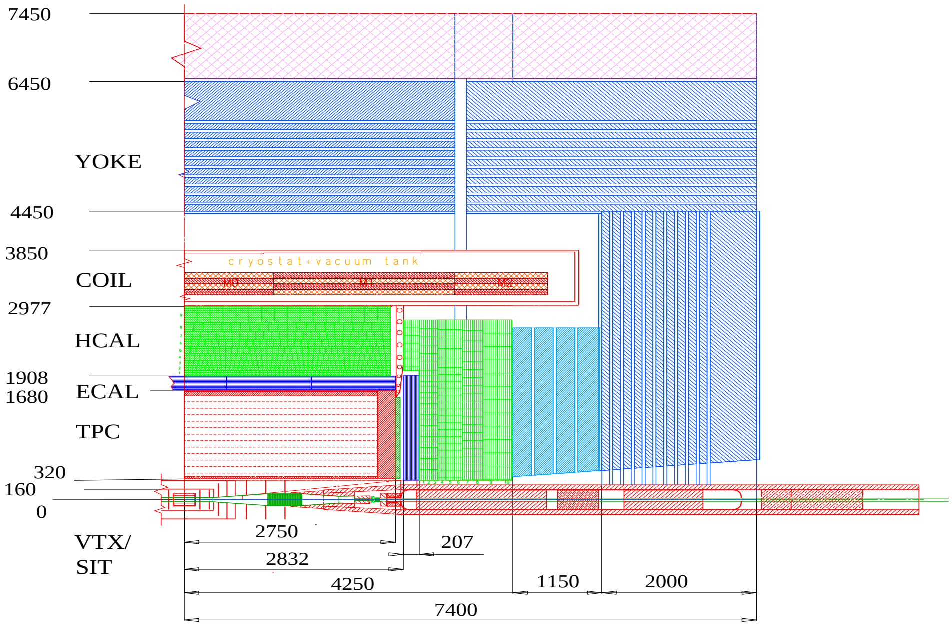

Figure 2.3: *Side view of a Linear Collider detector quadrant (TESLA concept). Dimensions are in mm.*

the radial direction follow an electromagnetic calorimeter, a hadron calorimeter, the coils of a superconducting magnet and an instrumented iron flux return yoke. The solenoidal magnetic field is 4 Tesla.

2.2.1 Vertexing

For the investigation of electroweak symmetry breaking, the decay properties of the Higgs boson should be studied in addition to the production mechanism. With the vertex detector it should be possible to distinguish the channels of the light Higgs boson decay ($b\bar{b}$, $c\bar{c}$, gg, $\tau^+\tau^-$) and to recognize extended Higgs sector decays in the case of models with two Higgs doublets, the latter may manifest themselves via the production and decay of heavy Higgs particles by processes such as $e^+e^- \rightarrow H^0A^0 \rightarrow b\bar{b}b\bar{b}$ or $e^+e^- \rightarrow H^+H^- \rightarrow t\bar{b}\bar{t}b$. The first decay channel will be studied in detail in this thesis. The final states from such decays can be discriminated against multi-fermion background due to their distinctive signatures with multiple b jets. The vertex detector will also play a crucial role in t quark identification.

The average impact parameter of B decay products is approximately 300 μm, but that of tau and charm is 3-4 times smaller. This will require the vertex detector to be as close as possible to the beam pipe and to have a good impact parameter resolution. Moreover, the determination of the vertex mass and charge will permit greatly improved b/c separation and the classification of jets as b or $\bar{b}$, c or $\bar{c}$. At higher collider energies the events are more complex and contain a larger number of jets with various flavours. The detector design needs to be pushed to the limit as regards layer thickness to avoid strong multiple scattering effects and to reduce a material budget in front of the TPC.

The vertex detector performance is represented by a multilayered Si-based pixel detector with minimum material, and an innermost layer as close as possible to the IP. There are different technology options which are currently considered for the vertex detector, namely charged-coupled devices (CCDs) [50, 51], CMOS pixels [52], DEPFET [53] and hybrid pixel

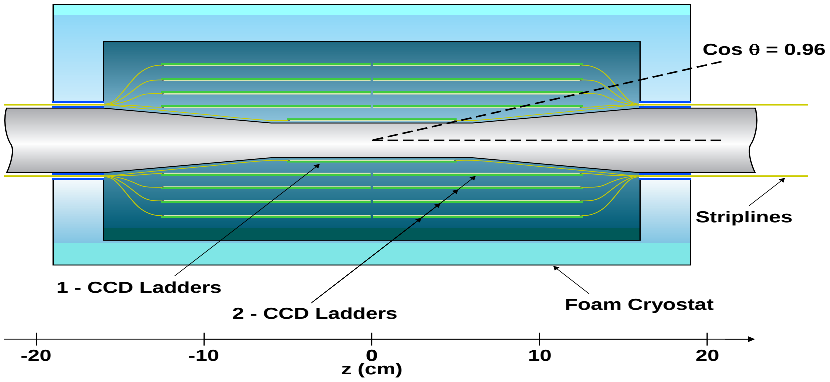

Figure 2.4: *Cross-section of CCD-based vertex detector.*

sensors [54].

Fig. 2.4 shows the CCD-based detector represented as a series of nested cylinders placed inside the low-mass foam cryostat, used to permit an operating temperature of around 180 K. With an inner layer radius of 12-15 mm defined by the final focus system, it has been demonstrated that a pixel-based detector with pixels of size well below 50×50 μm^2 is required in order to avoid confusion (cluster merging) within the cores of high energy jets. The innermost 3 layers extend to $|\cos\theta| = 0.96$, with 5-layer coverage to $|cos\theta| = 0.9$. The outer 4 layers provide stand-alone track reconstruction. Having found the tracks in layers 2-5 (and rejected fake tracks by linking to the outer tracking system) the layer 1 hits are used solely to refine the track extrapolation to the IP, which is particularly important for low momentum particles.

The proposed CCD detector option with a total number of pixels of 799×10^6 assumes a pixel size 20×20 μm^2. The overall CCD thickness about 50 μm results in a material budget close to 0.06% X_0 per layer (X_0 is a radiation length), that is needed for an acceptable amount of multiple scattering of low momentum tracks. The achievable resolution of the track impact parameter to the IP in the $r\phi$ projection is

$$\sigma(d_0) = 3.1\ \mu\text{m} \oplus \frac{4.6\ \mu\text{m}}{p\sin^{3/2}\theta}, \tag{2.3}$$

where $\oplus$ symbolises the quadratic sum. Here, p is the track momentum and θ is the polar angle [51]. The first constant term depends on the point resolution and geometrical stability of the detector and the second term represents the resolution degradation due to multiple scattering, which increases with decreasing p and polar angle θ.

2.2.2 Tracking

A model independent Higgs production analysis can be done using the process HZ → $\text{H}l^+l^-$ via the recoil mass of l^+l^- and their angular distributions. Requiring the measuring error on $M_{l^+l^-}$ and on the mass recoiling to the l^+l^- system to be small puts a strict limit on tracker momentum resolution:

$$\sigma\left(\frac{1}{p_t}\right) \leq 5\cdot10^{-5}\ [\text{GeV/c}]^{-1}, \tag{2.4}$$

where p_t is the transverse momentum.

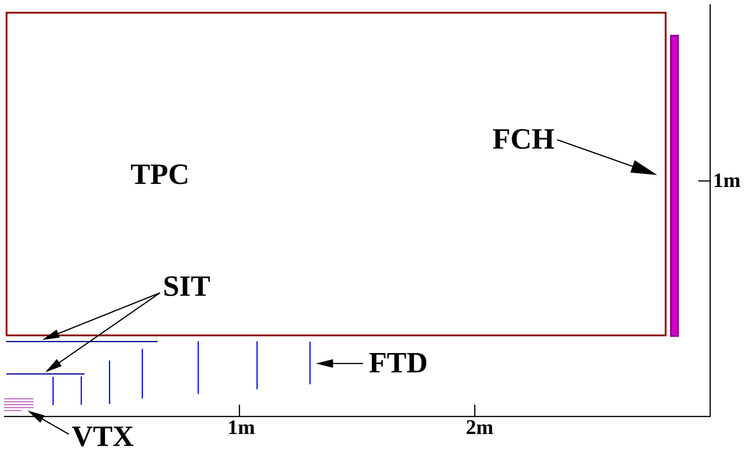

Figure 2.5: *General layout of LC tracking system.*

The general layout of a Linear Collider tracking system is shown in Fig. 2.5 with pixel silicon vertex detector (VTX) in the centre (2.2.1). All tracking system is immersed in the magnetic field of 4 Tesla.

One of the candidates for the main tracker of a LC is a time projection chamber (TPC) [55] because it has an excellent 3D resolution, measures many space points per track, facilitates efficient pattern recognition in events with high local track density and introduces low material budget. This compensates the comparatively moderate point resolution and double-hit resolution. Additionally the measurement of the specific energy loss dE/dx is possible allowing for charge particle identification in the range of intermediate particle momentum ($2 < p < 15$ GeV/c). The TPC is foreseen to be 5 m long, with an inner radius of 36.2 cm and outer radius of 161.8 cm. The TPC is filled with a gas mixture of Ar-CO$_2$-CH$_4$ (93-2-5)% or Ar-CH$_4$ (90-10)%. After a charged particle traversed the TPC volume, the electrons, produced by ionisation of the gas, drift under the electric field (applied parallel to the magnetic field) to the end plates. A signal readout is based on gas avalanche micro detectors such as Gas Electron Multipliers (GEM) [56] as amplification device and readout pads at the endplate. The other possibility of amplification are Micromegas [57]. Most gas avalanche micro detectors show a natural suppression of ion feedback, which is a potential problem of any TPC. Moreover, in comparison with a conventional wire amplification system, GEMs limit the transverse movement of electron cloud due to the $\vec{E} \times \vec{B}$ effect. The desired momentum resolution of the TPC only is $\sigma(1/p_t) < 2 \cdot 10^{-4}$ [GeV/c]$^{-1}$ and $\sigma(dE/dx) \leq 5\%$.

The overall momentum resolution is improved by 30% by adding 2 layers of cylindrical double-sided silicon strip detector (SIT) [58] between VTX and TPC. A second cylinder at radius 16 cm improves the track reconstruction efficiency, mostly for long lived particles. The required resolution is 10 μm in $r\phi$ and 50 μm in z. In the forward direction seven silicon discs (FTD) perpendicular to z are added, the three planes closest to the interaction point consist of active pixel sensors with a pixel size of 50×300 μm^2 while the remaining four discs are silicon strip detectors with resolution of 25 μm. Since the combined VTX and TPC resolution degrades at low polar angle θ due to a shorter projected track length, silicon discs information helps to reduce significantly the momentum error in the forward regions. In addition they improve the polar angle resolution in the forward region which is particularly important for electrons from Bhabha scattering, used to measure the luminosity spectrum from their acolinearity.

In the region above $\theta = 12°$, the forward chamber (FCH) assists the TPC in the pattern recognition. FCH may be implemented as straw-tubes similar to the ones developed for the ATLAS experiment [59, 60]. A point resolution for the full chamber of 50 μm can be reached.

2.2.3 Calorimetry

Complex hadronic final states are the typical feature of many new physics signatures at a future Linear Collider. They must be measured well to be able to distinguish them from Standard Model processes. Very often they proceed through decays, such as $\mathrm{t} \to \mathrm{bW}$, $\mathrm{W} \to \mathrm{q\bar{q}'}$ or $\mathrm{Z} \to \mathrm{q\bar{q}}$. For this purpose an excellent jet reconstruction and a good jet energy resolution is required:

$$\frac{\sigma_{E_{jet}}}{E_{jet}} \approx \frac{0.3}{\sqrt{E_{jet}(GeV)}}. \tag{2.5}$$

Experience at LEP and SLC has shown that the best energy resolution for jets is achieved by means of reconstruction algorithms exploiting particle flow objects. This is described in Section 4.1. The best realization of this strategy is in a dense and hermetic sampling calorimeter with a very high granularity. The requirement of hermeticity and excellent jet energy resolution also forces the choice to include the hadronic barrel calorimeter inside the coil, which keeps the amount of inactive material in front of the calorimeters low.

An electromagnetic calorimeter is foreseen as a Si-W high granularity calorimeter with tungsten absorbers and thin silicon diode pads [61]. It achieves an energy resolution of

$$\frac{\sigma_{E_{el}}}{E_{el}} = \frac{10\%}{\sqrt{E_{el}}} \oplus 1\%. \tag{2.6}$$

There are two solutions for hadronic calorimeter (HCAL) proposed:

1. A tile calorimeter with stainless steel as absorber and scintillator plates of 3×3 to 5×5 cm^2 cell size as active medium [62]. It has a high transverse and longitudinal segmentation to allow for software compensation and efficient separation of close-by showers. The readout using silicon photomultipliers working in the limited Geiger mode, is under study and shows promising results [63]. This type of HCAL would reach an energy resolution for hadrons of

$$\frac{\sigma_{E_h}}{E_h} = \frac{35\%}{\sqrt{E_h}} \oplus 3\%. \tag{2.7}$$

2. A digital readout calorimeter with a 1 cm^2 cell size, where the active layers are gas detectors and absorber plates are made of stainless steel. The detecting medium can be made of resistive plate chambers, wire chambers operated in limited Geiger mode or even thin wire chambers like in the ALEPH electromagnetic calorimeter. The signals are collected on small pads.

2.2.4 Magnet, Muon System and Forward Detectors

The fact that the main expected signature for the production and decay of supersymmetric particles is missing energy and a big interest in forward peaked processes like $\mathrm{e^+e^-} \to \mathrm{WW}\nu_\mathrm{e}\bar{\nu}_\mathrm{e}$, $\mathrm{We}\nu$ and in $\gamma\gamma$ events puts a requirement on hermeticity and particle detection at small angles. This means a good coverage of the detector and measurement capability in the forward direction. This is also essential for luminosity spectrum measurement.

The LC magnet, based on design of the CMS magnet [64], provides a solenoidal magnetic field of 4 Tesla along z in the central region of the detector. The tracking detectors, ECAL and HCAL are all located inside the magnet. The instrumented iron return yoke serves as a muon detector. The main requirement, of a high integral field homogeneity in a volume of 6 m in diameter, is especially important for successful TPC operation. The magnet consists of the solenoid and of the iron yoke, subdivided between the barrel yoke and the two endcap yokes.

The muon detector will serve for muon identification and for catching of hadronic showers leaking out of the hadron calorimeter. Its readout can be based either on resistive plate chambers (RPC) [65] or scintillating tiles.

In the very forward region on both sides of the interaction point, the calorimetric coverage of the solid angle is completed by the low angle tagger (LAT) and the luminosity calorimeter (LCAL) [66]. Both devices will at the same time be a part of the masking system shielding the detector from the backgrounds.

The LAT will be used to provide a good calorimetric coverage in the region between 83.1 and 27.5 mrad. Its design foresees a tungsten sampling calorimeter with silicon detectors as active elements.

The LCAL will cover the region down to very small angles, 4.6 mrad, serving both as a fast luminosity monitor and a low angle calorimeter. Its design foresees a sampling calorimeter with tungsten absorber, interleaved with active layers of silicon or diamond sensors. In the region of the LCAL close to the beam, electromagnetic doses of the order of 1 MGy per year are expected. Conventional Si detectors might not survive long enough in this environment, therefore the extremely radiation hard diamond sensors can be an attractive alternative [67].

2.3 The Detector Simulation

The detector response is simulated with the parametric fast simulation program SIMDET [68]. The detector components are implemented according to TESLA TDR [49]. The program applies Gaussian smearing to charged particle momenta and impact parameters with resolutions obtained from the GEANT3 [69] application Monte Carlo program BRAHMS [70]. The calorimetric response is treated in a way also using a parametrisation of results from the program BRAHMS. Pattern recognition is emulated by means of cross reference tables between generated particles and detector response. A particle flow algorithm defines the output of the program (Section 4.1). After simulation particles are classified as:

- electrons;
- photons;
- muons;
- charged hadrons: pions, kaons, protons;
- neutral hadrons: long-lived kaons and neutrons;
- clusters of unresolved particles.

Beamstrahlung is taken into account by using CIRCE [71]. An $\mathrm{e^+e^-} \to \mathrm{H_2H_3} \to \mathrm{b\bar{b}b\bar{b}}$ event for CPV MSSM scenario generated with the Monte Carlo program HZHA [72] at $\sqrt{s} = 500$ GeV and passed through a full simulation program BRAHMS is shown in Fig. 2.6.

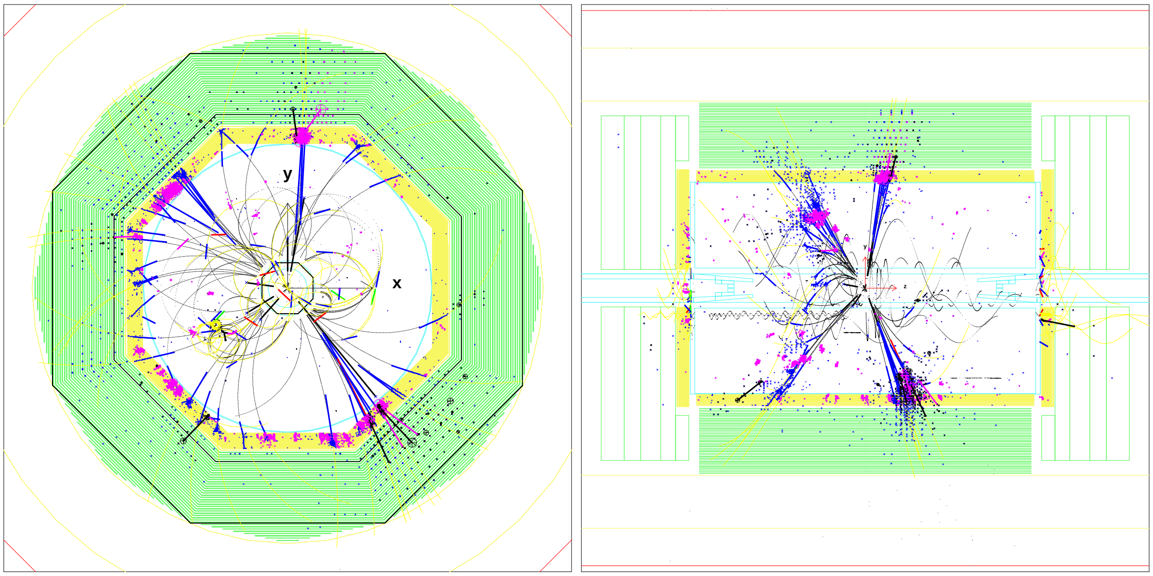

Figure 2.6: *Radial (left figure) and side (right figure) view of an* $\mathrm{e^+e^-} \to \mathrm{H_2H_3} \to \mathrm{b\bar{b}b\bar{b}}$ *event for CP violating MSSM scenario generated with the Monte Carlo program HZHA at* $\sqrt{s} = 500$ *GeV and passed through a full simulation program BRAHMS.*

Chapter 3

MSSM Higgs Boson Production at a Future Linear Collider

In this thesis, the MSSM Higgs boson production at a future e^+e^- Linear Collider will be analysed. The International Linear Collider in its physics program is a complementary machine to the LHC. This property will be demonstrated in this thesis, where the production of heavy neutral MSSM Higgs bosons at e^+e^- Linear Collider will be investigated.

In this chapter, the main processes for the MSSM Higgs boson production at the ILC will be discussed, including the Higgs pair production, the topic of this thesis [1, 2].

3.1 MSSM Higgs Boson Production

There are several MSSM Higgs boson production processes at an e^+e^- Linear Collider. The most important ones are presented in Fig. 3.1:

Higgsstrahlung process (a) :

$$\mathrm{e^+e^-} \rightarrow \mathrm{hZ},\ \mathrm{HZ}.$$

This is one of the most important Higgs production processes in the MSSM. Only CP-even Higgs bosons can couple in this channel. The Higgs boson production can be analysed independently of the Higgs decay channel via the recoil mass. The Higgsstrahlung is also one of the main Higgs production processes in the SM.

Boson fusion processes (b), (c) :

$$\mathrm{e^+e^-} \rightarrow \mathrm{W^{+*}W^{-*}}\nu_\mathrm{e}\nu_\mathrm{e} \rightarrow \mathrm{h}\nu_\mathrm{e}\nu_\mathrm{e},\ \mathrm{H}\nu_\mathrm{e}\nu_\mathrm{e},$$

$$\mathrm{e^+e^-} \rightarrow \mathrm{Z^*Z^*e^+e^-} \rightarrow \mathrm{he^+e^-},\ \mathrm{He^+e^-}.$$

This channel also exists in the SM. The WW fusion process dominates at high energies, whereas Higgsstrahlung process dominates at low energies. The ZZ fusion channel in (c) is suppressed with respect to the WW fusion channel in (b) by a factor of ≈10 due to the smaller coupling of the Z to the leptons and the Higgs boson.

Higgs pair production process (d) :

$$\mathrm{e^+e^-} \rightarrow \mathrm{hA},\ \mathrm{HA}.$$

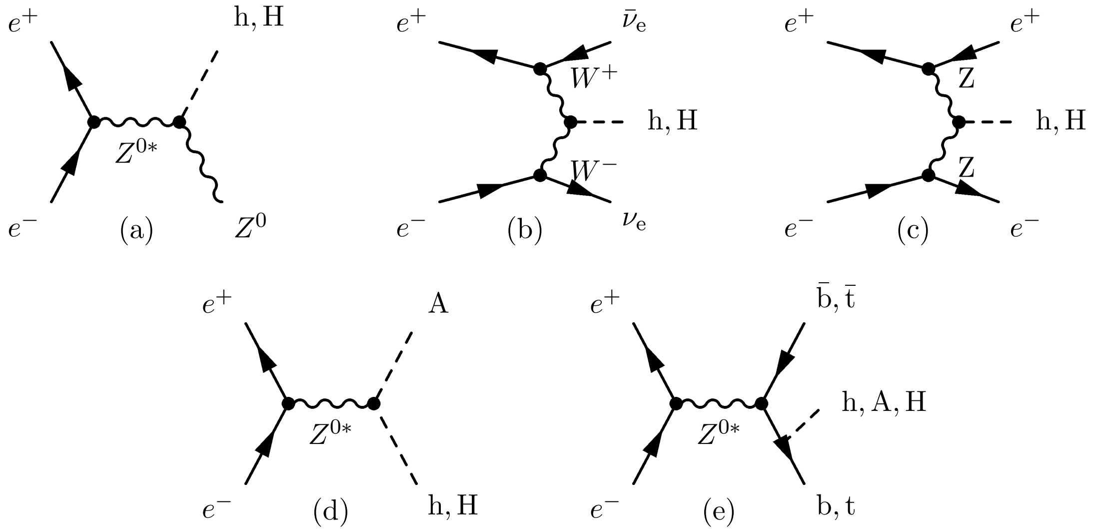

Figure 3.1: *The Higgs boson production processes in the MSSM at an* e^+e^- *Linear Collider (see description in Section 3.1).*

This is another main Higgs production process in the MSSM besides Higgsstrahlung. Higgs pairs contain CP-odd and CP-even Higgs bosons (i.e. only hA and HA channels are possible). The cross section of this channel is complementary to the one of the Higgsstrahlung, as will be shown below. The process $e^+e^- \to HA$ is analysed in this thesis.

Yukawa production process (e) :

$$e^+e^- \to h f\bar{f},\ A f\bar{f},\ H f\bar{f},\ \text{where } f = b, t.$$

This process can contribute to very small parts of the parameter space, typically for very large $\tan\beta$ and very small Higgs masses m_h.

The processes of Higgsstrahlung and Higgs pair production are complementary in the MSSM. The tree level cross sections for the processes $e^+e^- \to hZ$, $e^+e^- \to HZ$, $e^+e^- \to hA$ and $e^+e^- \to HA$ are expressed in the following way [19]:

$$e^+e^- \to hZ : \quad \sigma_{hZ} = \sin^2(\beta-\alpha)\ \sigma^{SM}_{HZ}(m_h), \tag{3.1}$$

$$e^+e^- \to HZ : \quad \sigma_{HZ} = \cos^2(\beta-\alpha)\ \sigma^{SM}_{HZ}(m_H), \tag{3.2}$$

$$e^+e^- \to hA : \quad \sigma_{hA} = \cos^2(\beta-\alpha)\ \bar{\lambda}_{hA}\ \sigma^{SM}_{HZ}(m_h), \tag{3.3}$$

$$e^+e^- \to HA : \quad \sigma_{HA} = \sin^2(\beta-\alpha)\ \bar{\lambda}_{HA}\ \sigma^{SM}_{HZ}(m_H), \tag{3.4}$$

where σ^{SM}_{HZ} is the cross-section of the SM Higgsstrahlung process $e^+e^- \to H_{SM}Z$, which is at tree-level given by [18]

$$\sigma^{SM}_{HZ}(m_H) = \frac{m_Z{}^4}{2v^4}\frac{(4\sin^2\theta_W - 1)^2 + 1}{96\pi s}\sqrt{\lambda_{HZ}}\frac{\lambda_{HZ} + 12 m_Z{}^2/s}{(1 - m_Z{}^2/s)^2}, \tag{3.5}$$

where $\sqrt{s}$ is the centre of mass energy. The symbol $\bar{\lambda}$ denotes the kinematic phase-space factor:

$$\bar{\lambda}_{HA} = \frac{\lambda^{3/2}_{HA}}{\lambda^{1/2}_{ZH}(12M_Z^2/s + \lambda_{ZH})} \tag{3.6}$$

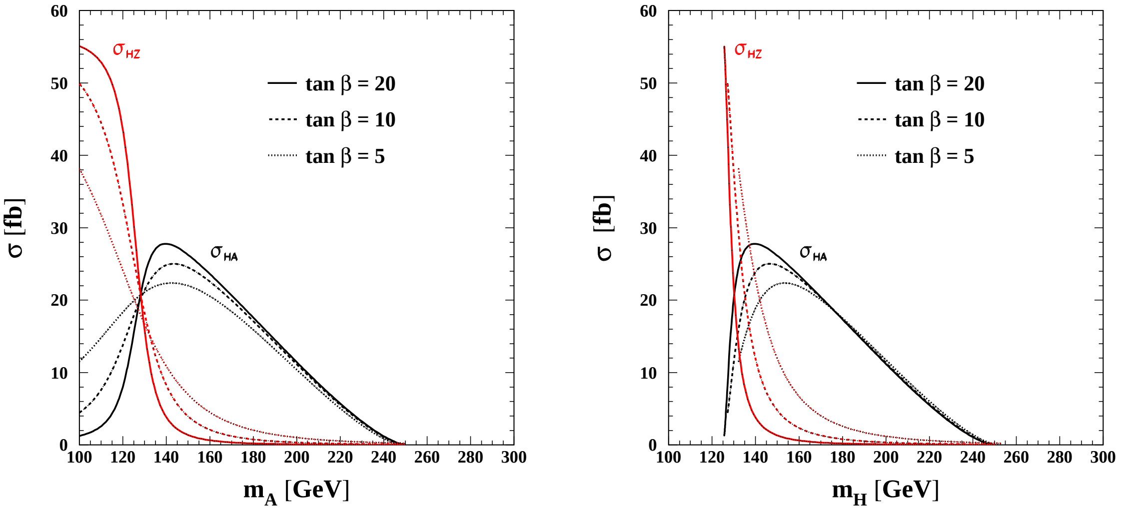

Figure 3.2: *Dependence of the MSSM Higgs boson production cross sections for the processes* $\mathrm{e^+e^- \to HZ}$ *(red curves) and* $\mathrm{e^+e^- \to HA}$ *(black curves) on the Higgs boson mass* m_A *(left figure) and* m_H *(right figure) for different* $\tan\beta$ *in the CP conserving scenario. The centre of mass energy is 500 GeV. The calculations are done with the MC program HPROD [73].*

with

$$\lambda_{ij} \equiv \lambda(m_i, m_j) = \frac{1-(m_i+m_j)^2/s}{1-(m_i-m_j)^2/s}.$$

As one can see, the process (3.1) is complementary to the process (3.3), and the process (3.2) is complementary to (3.4), obeying the sum rule $\sin^2(\beta-\alpha)+\cos^2(\beta-\alpha)=1$. The cross section dependences of the processes $\mathrm{e^+e^- \to HZ}$ and $\mathrm{e^+e^- \to HA}$ on the Higgs masses m_A and m_H at $\sqrt{s}=500$ GeV are shown in Fig. 3.2 for different values of $\tan\beta$.

Similar, but more complex, sum rules regulate the relative rates in the CP violating (CPV) scenario. Using the couplings from (1.84) and (1.85), the cross sections for the processes $\mathrm{e^+e^- \to H}_i\mathrm{Z}$ and $\mathrm{e^+e^- \to H}_i\mathrm{H}_j$ are given by [74]

$$\mathrm{e^+e^- \to H}_i\mathrm{Z} \;:\qquad \sigma_{\mathrm{H}_i\mathrm{Z}} = g^2_{\mathrm{H}_i\mathrm{ZZ}}\;\sigma^{\mathrm{SM}}_{\mathrm{HZ}}(m_{\mathrm{H}_i}), \tag{3.7}$$

$$\mathrm{e^+e^- \to H}_i\mathrm{H}_j \;:\qquad \sigma_{\mathrm{H}_i\mathrm{H}_j} = g^2_{\mathrm{H}_i\mathrm{H}_j\mathrm{Z}}\;\bar\lambda_{\mathrm{H}_i\mathrm{H}_j}\;\sigma^{\mathrm{SM}}_{\mathrm{HZ}}(m_{\mathrm{H}_i}). \tag{3.8}$$

In the CPV scenario, in contrast to the CP conserving scenario (CPC), each of three neutral Higgs bosons H_i (i = 1,2,3) can be produced via Higgsstrahlung $\mathrm{e^+e^- \to H}_i\mathrm{Z}$ or in pairs $\mathrm{e^+e^- \to H}_i\mathrm{H}_j$ ($i \neq j$), because H_i are the mixtures of CP-odd and CP-even eigenstates.

The kinematic properties of the CPC and CPV Higgstrahlung and pair production processes are expected to be very similar. In the Higgsstrahlung, only CP-even Higgs states h and H couple to the Z boson in the CPC scenario and the CP-even component of H_i in the CPV scenario. The Higgs pair production process always involves CP-even and CP-odd states. Therefore, the production angle distributions are expected to be similar in CPC and CPV scenarios. Since both CP-odd and CP-even states have spin 0, the Higgs decay angle distributions should be the same for CPC and CPV scenarios.

For the Yukawa channel the situation is different, since either the CP-odd or CP-even Higgs boson can be produced directly, resulting in different angular distributions. Therefore, CPV Higgs bosons will have angular distributions different than pure CP-odd or CP-even Higgs states.

3.2 Higgs Boson Decays

As it was mentioned before, the Higgs-fermion couplings are proportional to the fermion masses. That means, that the Higgs boson will predominantly couple to heavy particles. In Fig. 3.3 (left) the branching ratios of the SM Higgs boson as a function of its mass are shown. For the Higgs boson masses $m_{\mathrm{Z}} \leq m_{\mathrm{H}} \lesssim 140$ GeV, the main SM Higgs boson decay channels are to fermion pairs, especially to $\mathrm{b\bar{b}}$ due to the high beauty mass. Other Higgs boson branching ratios, like decays to $\tau^+\tau^-$, gg and $\mathrm{c\bar{c}}$, also should be considered in this Higgs boson mass region. Below the $\mathrm{t\bar{t}}$ and above the ZZ threshold, the Higgs boson decays almost exclusively into the WW or ZZ pairs. At $m_{\mathrm{H}} \approx 140$ GeV, decays into WW* pairs, with one or two gauge bosons being virtual, become comparable to the $\mathrm{b\bar{b}}$ channel.

The total SM Higgs boson decay width is shown in Fig. 3.3 (right) for a top mass $m_t = 175$ GeV. For $m_{\mathrm{H}} \lesssim 140$ GeV the Higgs particle is very narrow, $\lesssim 10$ MeV. Its width rapidly increases after opening real/virtual gauge boson channels and reaches ~1 GeV at the ZZ threshold.

The Higgs boson decays in the MSSM will strongly depend on the value of $\tan\beta$ (Fig. 3.4). The lightest neutral MSSM Higgs boson h will decay mainly into fermion pairs since the mass is smaller than ~135 GeV.

The main decay modes of the three neutral Higgs bosons for values of $\tan\beta > 1$ and for Higgs masses less than ~140 GeV are decays into $\mathrm{b\bar{b}}$ and $\tau^+\tau^-$ pairs with branching ratios of ~90% and 8%, respectively. Decays into $\mathrm{c\bar{c}}$ pairs and gluons are suppressed, especially for large $\tan\beta$. For large masses, the top decay channels $\mathrm{H, A} \rightarrow \mathrm{t\bar{t}}$ open up, yet for large $\tan\beta$ this mode remains suppressed and the neutral Higgs bosons decay almost exclusively into $\mathrm{b\bar{b}}$ and $\tau^+\tau^-$ pairs. Only at the edges of the Higgs parameter space these rules are modified. If M_{h} approaches the maximal value, the couplings become SM-like and the decay modes follow

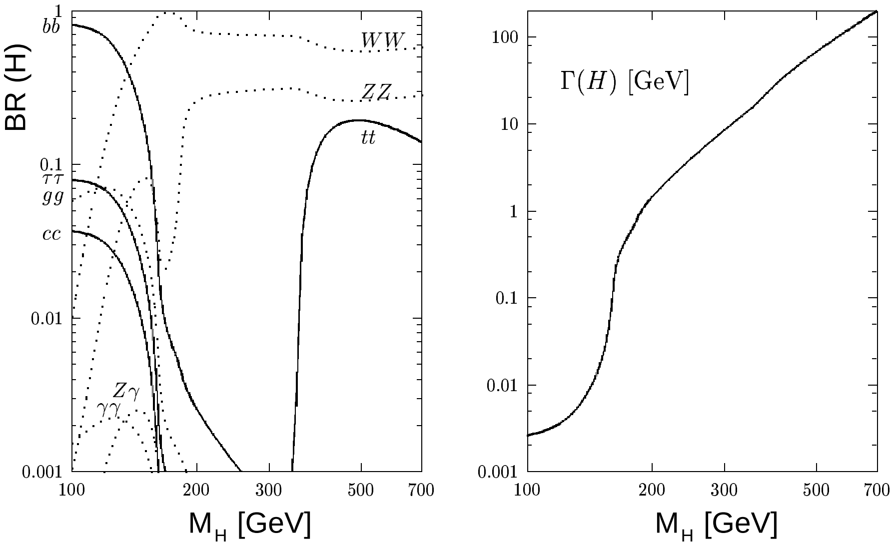

Figure 3.3: *SM Higgs bosons branching ratios (left) and the total decay width (right) as a function of Higgs mass [75].*

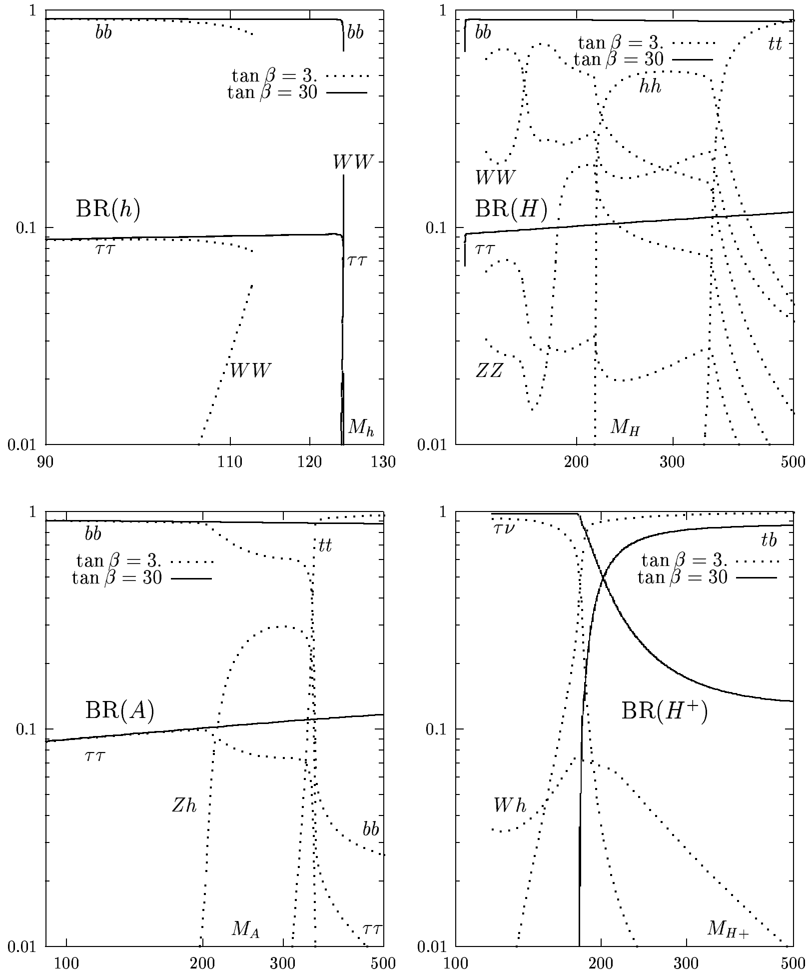

Figure 3.4: *MSSM Higgs (h, H, A, H^+) decay branching ratios as a function of the Higgs mass (in GeV) [76].*

the pattern of the SM.

For small values of $\tan\beta \sim 1$ the decay pattern of the heavy neutral Higgs bosons is more complicated [76]. The b decays are in general not dominant any more. Instead, cascade decays to pairs of light Higgs bosons and mixed pairs of Higgs and gauge bosons are important. Moreover, decays to gauge boson pairs play a major role. However, for very large masses, the neutral Higgs bosons decay almost exclusively to top quark pairs.

3.3 Motivation for MSSM Higgs Boson Pair Production Analysis

The present analysis is motivated by the existing LHC "wedge" region for the MSSM Higgs boson production (Fig. 3.5), where only one Higgs boson h^0 can be discovered [77]. In this region, the extended nature of the supersymmetric Higgs sector might not be observable, unless cascade decays of supersymmetric particles into the Higgs bosons are accessible. Beyond its discovery, a limited number of measurements of Higgs boson properties can be carried out at

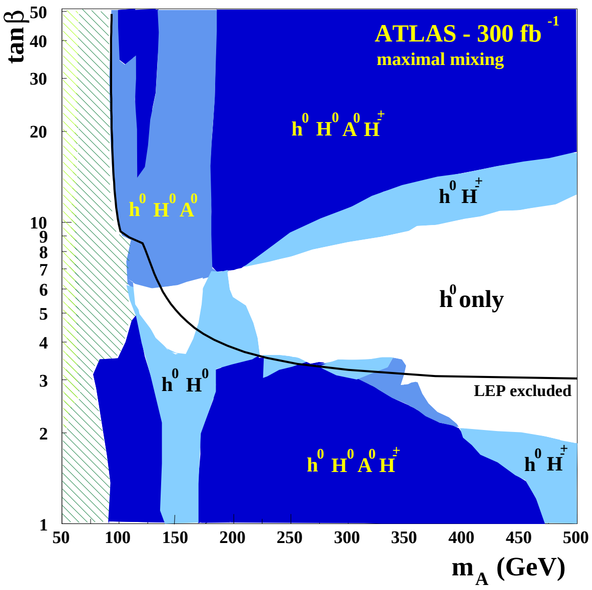

Figure 3.5: *Higgs bosons which are observable in the ATLAS experiment with 300* fb^{-1} *in the maximal mixing scenario of the MSSM in the plane of* $\tan\beta$ *vs.* m_A*. In the white region only the lightest* h^0 *boson is observable at the LHC if only SM-like decays are accessible [77].*

the LHC. It will be shown in this thesis, that with the ILC, the heavy neutral Higgs bosons can be observed in the parameter region in Fig. 3.5, where the LHC will not be able to discover them. Moreover, at the Linear Collider the h^0 boson can be distinguished from the SM Higgs boson through the accurate determination of its couplings over the whole parameter region, shown in Fig. 3.5, and, thus, reveal its supersymmetric nature (which is not covered in present analysis).

It is a subject of this thesis, to study MSSM neutral Higgs bosons in pair production at a future $\mathrm{e^+e^-}$ Linear Collider. This analysis extends previous studies [78, 79]. The analysed topology is the $\mathrm{b\bar{b}b\bar{b}}$ final state. In the following we will assume the $\mathrm{e^+e^-} \rightarrow \mathrm{HA}$ production process as shown in Fig. 3.6. However, this assumption does not restrict the generality of this study and the analysis developed in this thesis is applicable to the process $\mathrm{e^+e^-} \rightarrow \mathrm{hA}$ as well as to the processes of associated Higgs pair production in CP violating MSSM scenarios.

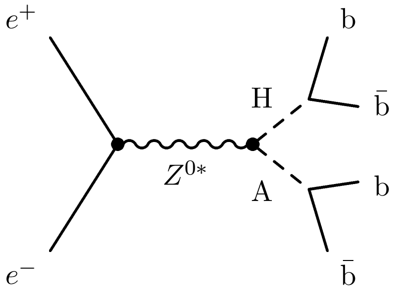

Figure 3.6: *Higgs pair production process* $\mathrm{e^+e^-} \rightarrow \mathrm{HA} \rightarrow \mathrm{b\bar{b}b\bar{b}}$ *at the ILC.*

The study of the heavy neutral Higgs pair production process is motivated by the so-called decoupling limit of the MSSM in which the h boson approaches the properties of the SM Higgs boson. The closer the MSSM scenario moves towards the decoupling limit the more difficult it becomes to distinguish the Higgs sector from the SM. In such a scenario the detection of heavier neutral Higgs bosons would be crucial for establishing an extended Higgs sector. The decoupling limit is approached relatively fast for large values of the H and A boson masses, $m_{\mathrm{A}}, m_{\mathrm{H}} > 200$ GeV, in a large area of the MSSM parameter space. The distinct feature of this scenario are vanishing couplings of the heavy CP-even Higgs boson to the W and Z boson, $\cos(\beta-\alpha) \rightarrow 0$:

$$\mathrm{g_{HZZ,HWW}} \sim \cos(\beta-\alpha). \tag{3.9}$$

As a consequence, the H boson production via the fusion and Higgsstrahlung processes is significantly suppressed, whereas the cross section of the $\mathrm{e^+e^-} \rightarrow \mathrm{HA}$ process reaches its maximal value making associated heavy Higgs pair production a promising channel for the detection of the H and A bosons at a future $\mathrm{e^+e^-}$ Linear Collider:

$$\mathrm{g_{HAZ}} \sim \sin(\beta-\alpha). \tag{3.10}$$

It should also be emphasised that in the decoupling limit the H and A bosons are almost degenerate in mass and have similar decay properties.

The possibility of the A and H Higgs boson production at an $\mathrm{e^+e^-}$ Linear Collider can be a good basis for a quantitative comparison with single Higgs production $\gamma\gamma \rightarrow \mathrm{A}$, $\gamma\gamma \rightarrow \mathrm{H}$ at $\gamma\gamma$-colliders [80, 81].

Chapter 4

Analysis Tools

In this chapter the analysis tools used for study of the MSSM Higgs boson pair production at a future Linear Collider will be described. The techniques of particle flow algorithm, jet finding, b-tagging and kinematic fit will be explained.

4.1 Particle Flow Algorithm

The particle flow algorithm is based on the idea to replace, for the charged fraction of the events, the energy and angle information as measured in the calorimeter by the much more accurate particle momentum as measured in the tracking detector [82]. The fine-granularity imaging calorimeter helps to reconstruct also the neutral part of the event carefully. This allows the reconstruction of almost all individual particles in an event.

The algorithm works as follows. First, tracks are measured with tracking system and associated to calorimetric clusters to define charged particle flow objects (electrons, muons and charged hadrons). Since momentum measurement with tracking system is much more accurate than direction and energy measurements with calorimeters, the tracking information is used for estimation of the four-momentum of the charged objects. Calorimetric clusters with no associated tracks are regarded as neutral particle flow objects (photons and neutral hadrons). Measurement of the four-momentum of neutral objects are solely based on the calorimetric information. It results in measuring charged particles by tracker, gammas by ECAL and neutral hadrons by HCAL.

4.2 Jet Finding

A so-called "DURHAM"(or $k_\perp-$) clustering algorithm [83, 84] is used for jet finding in the present analysis. It is defined in a similar way to the JADE-algorithm [85, 86], just replacing invariant mass by transverse momentum as the jet resolution variable. The scaled transverse momentum is first calculated for every pair of final-state particles (k, l) and defined as

$$y_{kl} = \frac{2(1 - \cos\theta_{kl}) min(E_k^2, E_l^2)}{s}, \tag{4.1}$$

where θ_{kl} is the relative angle between two particles, E_k and E_l are particle energies and s is the centre of mass energy squared. Then the two particles (i, j) with the smallest value of y_{kl} are combined together and replaced by a *pseudoparticle* with four-momentum $p_{(ij)}$ if their y_{ij} is smaller than some given resolution parameter y_{cut}. This procedure is repeated until all pairs of objects (particles and/or pseudoparticles) have $y_{kl} > y_{cut}$. Whatever objects remain at this stage are called jets.

Several recombination schemes may be used. They differ among themselves in the way in which the four-momentum $p_{(ij)}$ of a pseudoparticle is defined in terms of the momenta (p_i, p_j) of the recombined particles and/or pseudoparticles. In the E-scheme, for example, the four-momenta are simply added together, giving $p_{(ij)} = p_i + p_j$.

4.3 B-Tagging

The identification of b-quarks plays a crucial role in this analysis. Efficient tagging of jets containing heavy flavour hadrons will be achieved with a highly granular micro-vertex detector (Section 2.2.1), allowing for precise reconstruction of track parameters in the vicinity of the primary interaction point.

The procedure of tagging b-jets exploits information from the single track as well as secondary vertex information. Secondary vertices are searched within jets using the package ZVTOP [87] developed for the SLD experiment, where tracks are described as probability tubes and seed vertices are defined as regions where these tubes overlap. Afterwards an attempt is made to assign additional tracks by an iterative procedure. For each found vertex the invariant total mass and momentum are calculated from the four-momenta of particle flow objects assigned to the vertex. Three dimensional decay length and decay length significance are also computed.

For a jet flavour separation a neural network is developed [88]. A detailed description of the neural network implementation for the full simulation of the TESLA detector with the BRAHMS program [70] can be found in [89, 90]. Three different neural networks are introduced for jets with no, one and more than one secondary vertices found. The inputs for the first class are:

- the first and second most significant impact parameters for a track in the jet, in the $r\phi$ and rz projections;
- the momentum of these tracks and the angle of the tracks with respect to the jet axis;
- the impact parameter joint probability in $r\phi$ and rz [91].

If a jet contains at least one secondary vertex, the neural network inputs are:

- the maximal distance significance between vertices found in the jet by ZVTOP, and the maximal distance between the vertices found;
- the mass and momentum of the reconstructed hadronic decay, calculated using tracks associated to vertices found by ZVTOP;
- the number of tracks associated to secondary vertices found by ZVTOP;
- the χ^2 probability for all of the secondary and associated tracks for a fit to a single vertex found by ZVTOP;
- the impact parameter joint probability in $r\phi$ and rz.

The neural networks are trained on event samples simulated with SIMDET using the same variables and jet classification as in BRAHMS. For the analysis, a jet-wise tag, referred hereafter as jet b-tag variable, is used. For a jet with neural network output x it is defined as

$$B(x) = \frac{f_b(x)}{f_b(x) + f_{udsc}(x)}, \tag{4.2}$$

where $f_b(x)$ and $f_{udsc}(x)$ are probability density functions of neural network output in a samples of b– and udsc–jets, respectively. Tagging of c-jets proceeds in a similar way. Fig. 4.1 shows the di-jet mass sum distribution for the CP violating MSSM scenario process $\mathrm{e^+e^-} \rightarrow \mathrm{H_2H_3} \rightarrow \mathrm{b\bar{b}b\bar{b}}$ with $m_{\mathrm{H_2}} = 140.5$ GeV, $m_{\mathrm{H_3}} = 154.7$ GeV after some kinematic cuts before and after using b-tag output (see Chapter 6 for more explanations). An event wise b-tag efficiency using all four jets of 70.5% was achieved rejecting nearly all events with no bottom quarks in the final state.

Fig. 4.2 shows b-tag and c-tag purity versus efficiency curves for $\mathrm{Z} \rightarrow \mathrm{q\bar{q}}$ events simulated at a centre of mass energy of $\sqrt{s} = 91.2$ GeV. Results obtained with SIMDET and BRAHMS are compared in this figure. The c-tag performance agrees within 5% over the entire range of efficiency. Some discrepancy in modelling of the b-tag is observed in the region of high efficiency and low purity. This discrepancy occurs due to not adequate modelling of the resolution tails in the impact parameter joint probability distribution by SIMDET. However, $\mathrm{b\bar{b}b\bar{b}}$ analysis imposes b-tag requirements strong enough not to be sensitive to this discrepancy. Some flavour tag related systematic studies have been performed. It has been found that the b-tag performance is nearly independent of the centre of mass energy in the range from $\sqrt{s} = 91.2$ to 500 GeV. Furthermore, possible changes in micro-vertex detector configuration are found to have marginal impact on the b-tag performance. For example, removing innermost silicon layer changes the selection efficiency by not more than 5%. These studies confirm the stability of b-tagging. However, c-tag and e.g. b-quark charge tagging are dependent on the innermost layer [89].

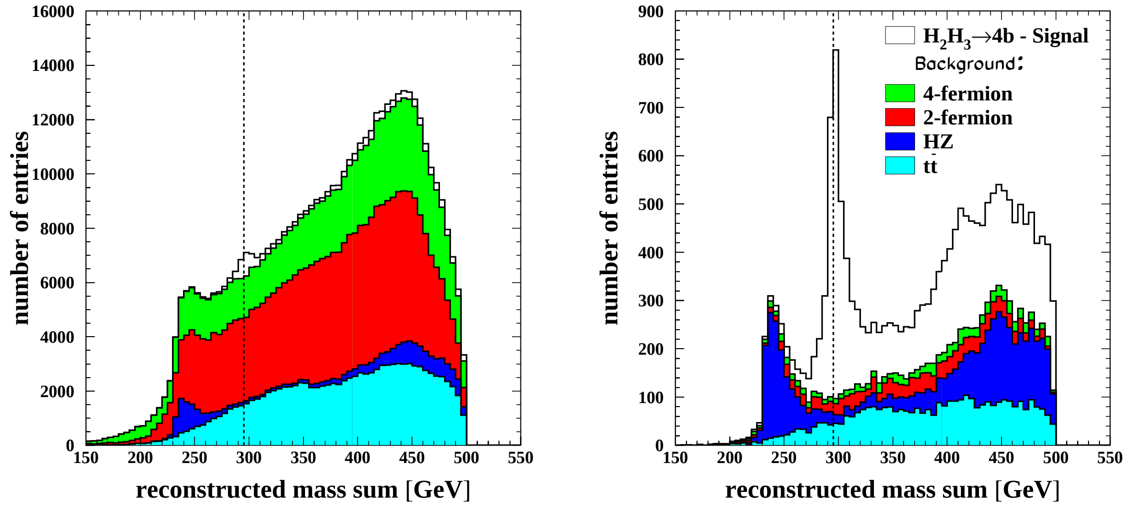

Figure 4.1: *The di-jet mass sum distribution for the CP violating MSSM scenario process* $\mathrm{e^+e^-} \rightarrow \mathrm{H_2H_3} \rightarrow \mathrm{b\bar{b}b\bar{b}}$ *with* $m_{\mathrm{H_2}}$ *= 140.5 GeV,* $m_{\mathrm{H_3}}$ *= 154.7 GeV after some kinematic cuts before (left figure) and after (right figure) using b-tag output.*

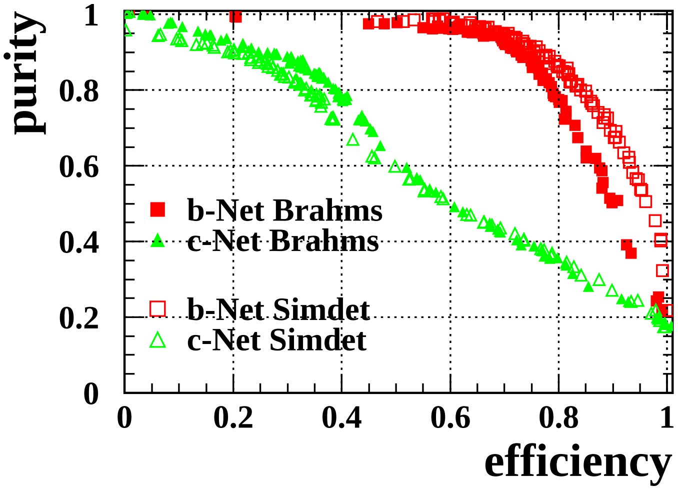

Figure 4.2: *b-tag and the c-tag purity of the neural network versus efficiency curves for* $\mathrm{Z} \rightarrow \mathrm{q\bar{q}}$ *events simulated with SIMDET and BRAHMS at a centre of mass energy of* $\sqrt{s}$ *= 91.2 GeV. Filled squares (triangles) correspond to the neural network output for the b-events (c-events) simulated with BRAHMS. Open squares (triangles) correspond to the neural network output for the b-events (c-events) simulated with SIMDET. The neural networks are trained on event samples simulated with SIMDET using the same variables and jet classification as in BRAHMS.*

4.4 Kinematic Fit

The mass resolution of the reconstructed Higgs bosons is improved by means of a kinematic fit which is performed using code developed by DELPHI [92]. In the $\mathrm{b\bar{b}b\bar{b}}$ analysis, conservation of four-momentum is required, leading in total to four constraints. The method is based on the minimisation of the function:

$$Q(\vec{y},\vec{\lambda}) = (\vec{y}-\vec{y_0})^T V^{-1}(\vec{y}-\vec{y_0}) + 2\vec{\lambda}\vec{f}(\vec{y}), \tag{4.3}$$

where $\vec{f}(\vec{y})$ are constraints, $\vec{y}$ are fitted jet parameters, $\vec{y_0}$ are measured jet parameters, $\vec{\lambda}$ are Lagrange multipliers and V is the error matrix ($V_{kl} = \sigma^2_{y_k y_l}$). The following constraints $\vec{f}(\vec{y}) = 0$ for a so-called $4C\ fit$ are used:

$$\begin{cases} \sum E_i - \sqrt{s} = 0, \\ \sum p_{xi} = 0, \\ \sum p_{yi} = 0, \\ \sum p_{zi} = 0, \end{cases} \tag{4.4}$$

where E_i is the energy of a jet number i, $p_{xi,yi,zi}$ are its momentum components.

The purpose of the fit is to find such jet parameters $\vec{y}$ under constraints $\vec{f}(\vec{y})$ which will fit the measured jet parameter values $\vec{y_0}$ best of all, taking into account their errors and constraints. The fitted parameters must obey:

$$\frac{dQ}{d\vec{y}} = \vec{0}, \tag{4.5}$$

$$\frac{dQ}{d\vec{\lambda}} = \vec{0}. \tag{4.6}$$

The most straightforward choice of the parameters $\vec{y}$ for a fit are the polar coordinates, i.e. the absolute value of jet momentum p_i and two angles θ_i and ϕ_i. In this coordinate system the errors are not correlated. The diagonal covariance matrix (V^{polar}) has for every jet the following form:

$$V^{polar} = \begin{pmatrix} \sigma_p^2 & 0 & 0 \\ 0 & \sigma_\theta^2 & 0 \\ 0 & 0 & \sigma_\phi^2 \end{pmatrix}. \tag{4.7}$$

Jet angular and momentum resolution functions σ_p, σ_θ, σ_ϕ can be derived from Monte Carlo studies by the comparison of the reconstructed jet angles and momenta with the generated ones. For this purpose the process $\mathrm{e^+e^-} \to \mathrm{d\bar{d}}$ was simulated for different centre of mass energies. After the association of the quarks with the jets and applying a jet resolution parameter cut $\log_{10}(y_{32})$ > -3.5 [1], the following values were calculated for every jet in dependence on quark momentum:

$$\frac{p_{quark} - p_{jet}}{p_{quark}},$$
$$\theta_{quark} - \theta_{jet},$$
$$\phi_{quark} - \phi_{jet},$$

where p_{quark}, θ_{quark} and ϕ_{quark} are quark momentum and angles on a generated level, p_{jet}, θ_{jet} and ϕ_{jet} are jet momentum and angles after the reconstruction. The distributions ($\frac{p_{quark}-p_{jet}}{p_{quark}}$) are shown in Fig. 4.3-4.4 for different quark momenta (in GeV). The width of the Gaussian fit to the central part of these distributions defines jet momentum resolution value σ_p . Similar distributions are obtained for ($\theta_{quark} - \theta_{jet}$) and ($\phi_{quark} - \phi_{jet}$) and the resolutions σ_θ and σ_ϕ are calculated.

The functional dependences of σ_p and $\sigma_{\theta,\phi}$ on quark momentum are received by fitting the distributions by the following functions (Fig. 4.5):

$$\sigma_p = \begin{cases} 0.02 + \frac{0.20}{\sqrt{p_{quark}}}, & p_{quark} < 100 \text{ GeV} \\ 0.04, & p_{quark} \geq 100 \text{ GeV} \end{cases}, \tag{4.8}$$

$$\sigma_{\theta,\phi} = -0.01 + \frac{0.20}{\sqrt{p_{quark}}}. \tag{4.9}$$

For the samples of $\mathrm{e^+e^-} \to \mathrm{HA} \to \mathrm{b\bar{b}b\bar{b}}$ events with (m_{H},m_{A}) = (150,100) GeV, the performance of the kinematic fit using (4.8) and (4.9) error matrix parametrisation is illustrated in Fig. 4.6 where the distributions of the reconstructed di-jet mass sum and mass difference are presented (see Chapter 6 for more explanations). Dashed histograms show raw spectra obtained using only measured jet angles and energies. Solid histograms show spectra obtained after applying 4C kinematic fit. As it is seen, after 4C kinematic fit the resolution of the di-jet mass sum reconstruction is significantly improved.

---

[1] Jet resolution parameter y_{32} is defined as DURHAM jet discriminating variable (Section 4.2) $y_{32} = \frac{2(1-\cos\theta_{32})min(E_3^2,E_2^2)}{s}$ and characterises the transition from 3-jet topology to a 2-jet topology event.

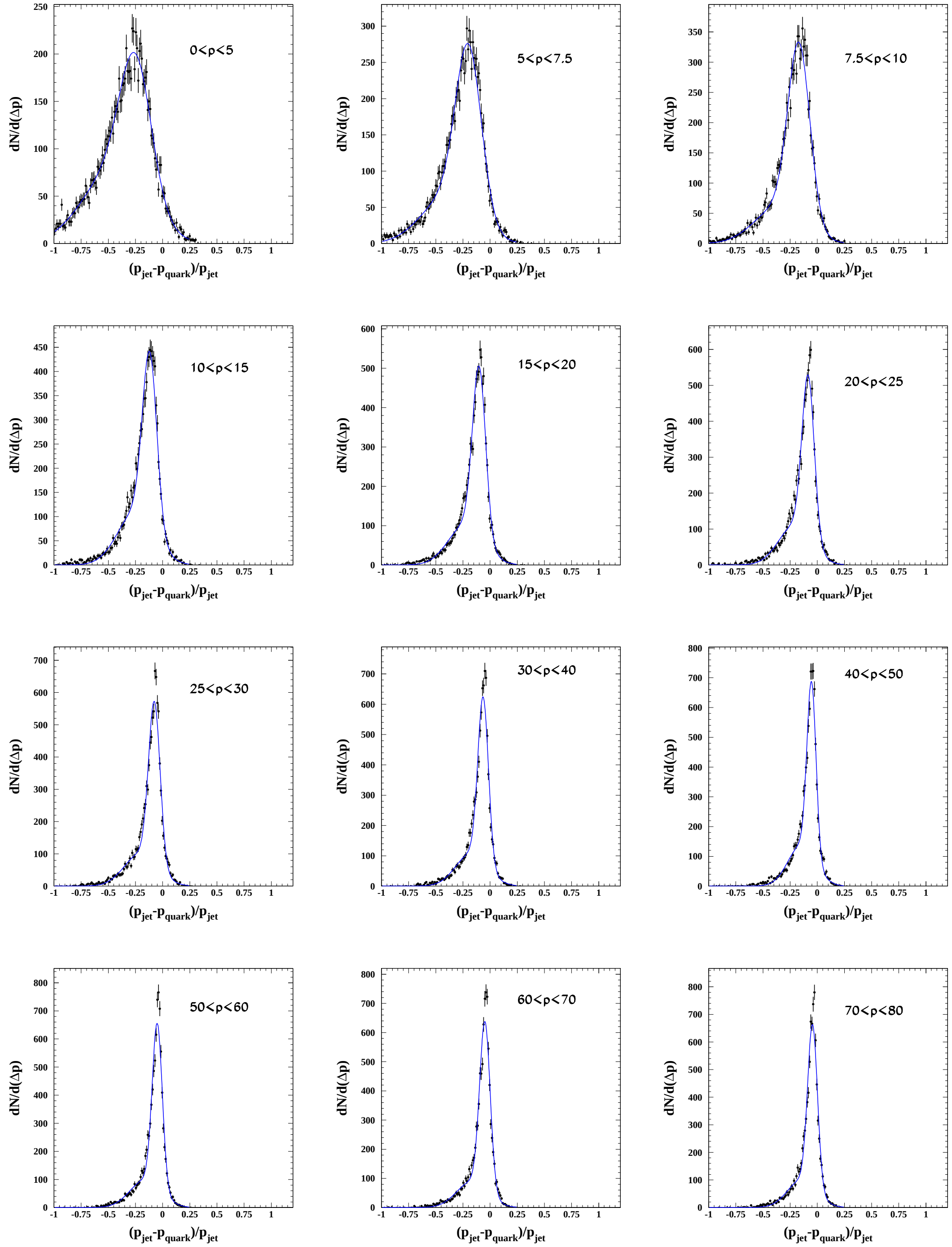

Figure 4.3: *The distributions of* $\frac{p_{quark}-p_{jet}}{p_{quark}}$ *for different quark momentum regions (in GeV). The central part of the distributions is fitted with Gaussian function.*

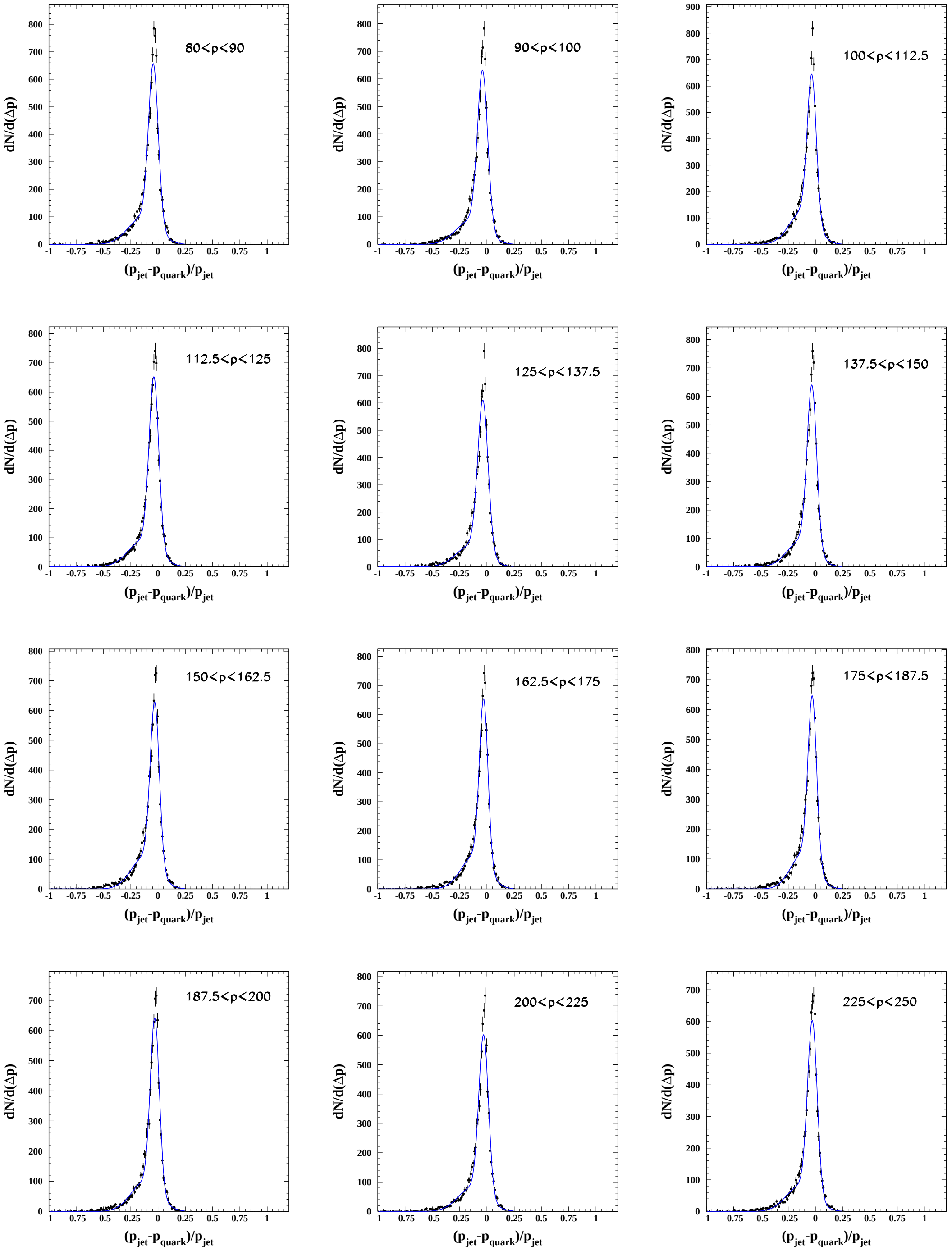

Figure 4.4: *The distributions of* $\frac{p_{quark}-p_{jet}}{p_{quark}}$ *for different quark momentum regions (in GeV). The central part of the distributions is fitted with Gaussian function.*

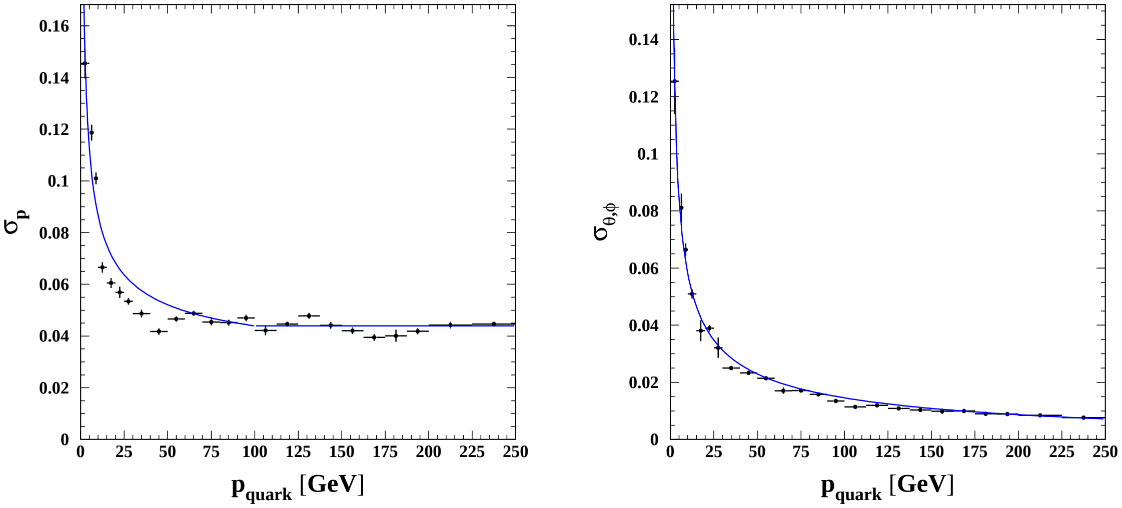

Figure 4.5: *Jet momentum resolution (left figure) and angular resolution (right figure) dependence on quark momentum. The fitted functions are (4.8) and (4.9).*

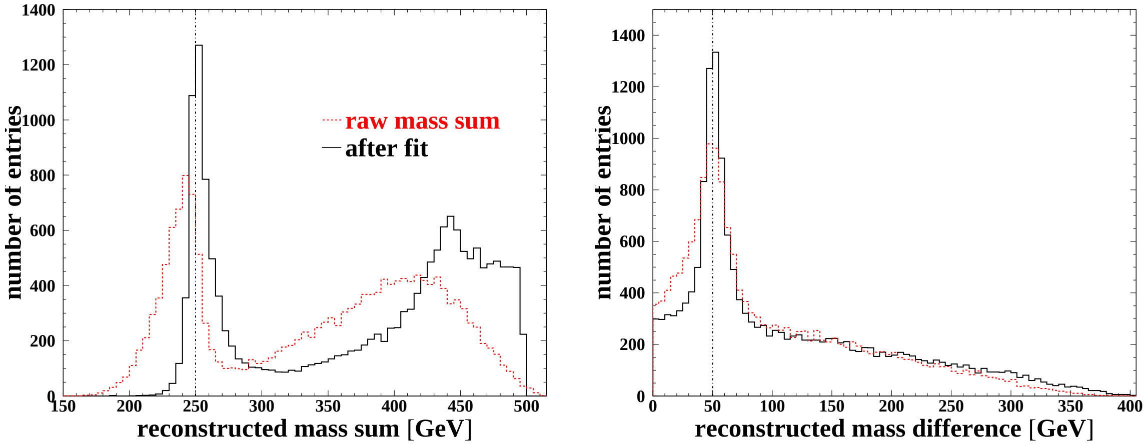

Figure 4.6: *Distributions of the reconstructed di-jet mass sum (left figure) and di-jet mass difference (right figure) in the sample of the* HA → $b\bar{b}b\bar{b}$ *events with* (m_H,m_A) = *(150,100) GeV at* $\sqrt{s}$ = 500 GeV. *Dashed histograms show raw spectra obtained using only measured jet angles and energies. Solid histograms show spectra obtained after applying 4C kinematic fit. Three entries per event contribute to these distributions, corresponding to three possible di-jet pairings (see Chapter 6).*

Chapter 5

Physics Processes and Monte Carlo Samples

The process of the MSSM Higgs boson production at a future e^+e^- Linear Collider, considered in this study, is $e^+e^- \rightarrow HA$ with subsequent Higgs decays to $b\bar{b}$ pairs. In this chapter, the simulated Monte Carlo samples for signal and background processes used in the analysis will be summarised. In the last section the SM background processes will be described. All samples of generated events are passed through parametric fast simulation program SIMDET [68] for Linear Collider detector.

5.1 Signal Processes for General MSSM Analysis

Samples of $e^+e^- \rightarrow HA$ events are generated for several Higgs boson mass hypotheses with PYTHIA 6.2 [93], including initial state radiation. The Higgsstrahlung cross section in the SM is computed using the program HPROD [73].

For the case of $\sin^2(\beta-\alpha) = 1$ (maximal $e^+e^- \rightarrow HA$ cross section, see Section 3.1), which is assumed for these studies, the signal cross sections and number of events at centre of mass energies of $\sqrt{s}$ = 500, 800 GeV and an assumed luminosity of L = 500 fb^{-1} are given in

$\sqrt{s}$ = 500 GeV			$\sqrt{s}$ = 800 GeV		
(m_H,m_A) [GeV]	σ_{HA} [fb]	N_{events}	(m_H,m_A) [GeV]	σ_{HA} [fb]	N_{events}
(150,100)	33.62	13616	(300,150)	10.55	4273
(200,100)	25.30	10247	(290,200)	9.54	3864
(250,100)	16.61	6727	(300,250)	7.49	3033
(150,140)	28.39	11498	(300,300)	5.70	2309
(150,150)	26.90	10895	(350,350)	2.23	903
(200,150)	18.85	7634	(400,150)	6.46	2616
(250,150)	10.67	4321	(400,200)	5.17	2094
(200,200)	11.25	4556	(400,250)	3.70	1499

Table 5.1: *Tree level cross sections σ_{HA} and number of events for $e^+e^- \rightarrow HA$ expected for the Higgs boson mass hypotheses (m_H,m_A) considered in the study. Numbers are given for $\sin^2(\beta-\alpha)$=1 and the Higgs boson branching fractions of $Br(H \rightarrow b\bar{b}) = Br(A \rightarrow b\bar{b})$ = 90%. The cross sections are calculated including ISR at centre of mass energies of $\sqrt{s}$ = 500, 800 GeV and an assumed luminosity of L = 500 fb^{-1}.*

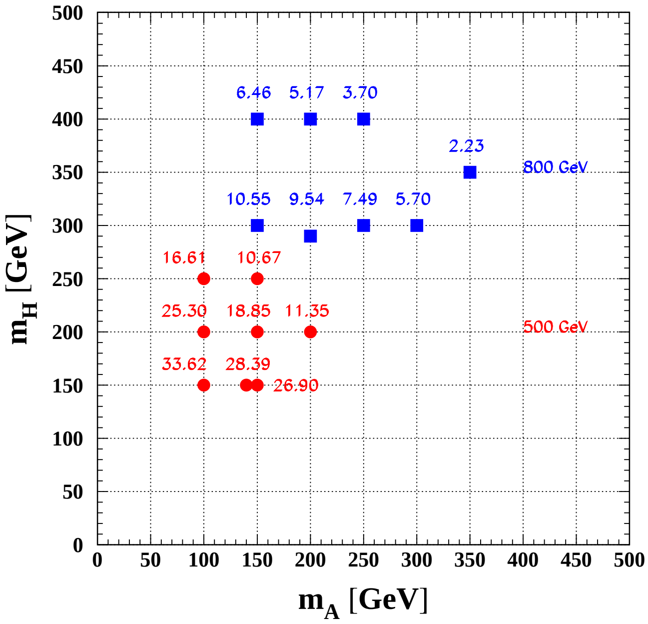

Figure 5.1: *Higgs boson mass grid for different mass hypotheses* (m_{H},m_{A}) *considered in the study for* $\sqrt{s}$ = *500 GeV (round red points) and 800 GeV (square blue points). The numbers indicate cross sections for* $\mathrm{e^+e^-} \to \mathrm{HA}$ *in fb.*

Table 5.1. The branching fractions of the Higgs bosons into b quarks are set to their typical values in the MSSM: $\mathrm{Br(H \to b\bar{b}) = Br(A \to b\bar{b})}$ = 90%. The generated mass grids for both energies are also shown in Fig. 5.1.

For the case of the degenerate H and A Higgs boson masses, in addition to the two hypotheses (m_{H},m_{A}) = (300,300) GeV and (350,350) GeV, presented in Table 5.1, four additional mass points close to the kinematic limit are generated at $\sqrt{s}$ = 800 GeV. Their cross sections and expected number of events for an integrated luminosity of 500 fb^{-1} are shown in Table 5.2.

To investigate the possibility of distinguishing between different mass combinations having close mass sums and mass differences, a so-called minigrid of such mass combinations is generated at $\sqrt{s}$ = 500 GeV. The H and A Higgs boson mass hypotheses, their cross sections and

(m_{H},m_{A}) [GeV]	σ_{HA} [fb]	N_{events}
(360,360)	1.084	439
(370,370)	0.713	289
(380,380)	0.393	159
(390,390)	0.140	57

Table 5.2: *Tree level cross sections* σ_{HA} *and number of events for* $\mathrm{e^+e^-} \to \mathrm{HA}$ *expected for the degenerate H and A Higgs boson mass hypotheses* (m_{H},m_{A}) *with* m_{H}=m_{A} *considered in the study. Numbers are given for* $\sin^2(\beta-\alpha)$=*1 and the Higgs boson branching fractions of* $\mathrm{Br(H \to b\bar{b}) = Br(A \to b\bar{b})}$ = *90%. The cross sections are calculated including ISR at a centre of mass energies of* $\sqrt{s}$ = *800 GeV and an assumed luminosity of L* = *500* fb^{-1}.

$(m_{\mathrm{H}},m_{\mathrm{A}})$ [GeV]	σ_{HA} [fb]	N_{events}
(151,137)	28.50	11543
(155,137)	27.89	11295
(159,137)	27.26	11040
(153,139)	27.91	11304
(157,139)	27.29	11052
(151,141)	27.93	11312
(155,141)	27.31	11061
(159,141)	26.69	10809
(153,143)	27.33	11069
(157,143)	26.71	10818
(151,145)	27.34	11073
(155,145)	26.73	10826
(159,145)	26.11	10575

Table 5.3: *Tree level cross sections* σ_{HA} *and number of events for* $\mathrm{e^+e^-} \rightarrow \mathrm{HA}$ *expected for the minigrid of H and A Higgs boson mass hypotheses* $(m_{\mathrm{H}},m_{\mathrm{A}})$*. Numbers are given for* $\sin^2(\beta-\alpha)=1$ *and the Higgs boson branching fractions of* $\mathrm{Br(H \rightarrow b\bar{b}) = Br(A \rightarrow b\bar{b})}$ *= 90%. The cross sections are calculated including ISR at a centre of mass energies of* $\sqrt{s}$ *= 500 GeV and an assumed luminosity of L = 500 fb*$^{-1}$*.*

expected number of events for an assumed luminosity of 500 fb^{-1} are presented in Table 5.3.

5.2 Signal and Background Processes for CP Violating Scenario

The general MSSM analysis is applied to two CP violating scenarios, which have been chosen using the Monte Carlo program HZHA [72]. The first scenario is analysed at $\sqrt{s}$ = 500 GeV, and the second at 800 GeV. The properties of the three neutral Higgs mass eigenstates are displayed in Table 5.4. The signal events $\mathrm{e^+e^-} \rightarrow \mathrm{H}_i\mathrm{H}_j \rightarrow \mathrm{b\bar{b}b\bar{b}}$ are generated using PYTHIA 6.2 for $\sqrt{s}$ = 500 and 800 GeV, for a luminosity of L = 500 fb^{-1}.

For the chosen CP violating scenarios the neutral Higgs bosons have the masses and branching fractions presented in Table 5.5. The topological cross sections for the different Higgs pair production processes are shown in Table 5.6. The biggest Higgs pair production topological cross section is for the process $\mathrm{e^+e^-} \rightarrow \mathrm{H_2H_3} \rightarrow \mathrm{b\bar{b}b\bar{b}}$ for both scenarios. Therefore, it is chosen for further analyses (Section 6.6.1). In addition to the SM background processes described in Section 5.4 the background from $\mathrm{e^+e^-} \rightarrow \mathrm{H}_i\mathrm{Z}^0$ should also be taken into account. Their contribution have been estimated using the HZHA program (Table 5.6). The generation of

	Scenario N1 at 500 GeV	Scenario N2 at 800 GeV
$\tan\beta$	19	5
$m_{\mathrm{H^+}}$ [GeV]	164	300
$\mathrm{Re}(A_t)$ [GeV]	285	1000
$\mathrm{Im}(A_t)$ [GeV]	771	0.175

Table 5.4: *The parameters for two CP violating scenarios analysed at* $\sqrt{s}$ *= 500 and 800 GeV.*

	Scenario N1 at 500 GeV	Scenario N2 at 800 GeV
m_{H_1} [GeV]	112.0	118.0
m_{H_2} [GeV]	140.5	282.2
m_{H_3} [GeV]	154.7	292.2
$\mathrm{Br}(\mathrm{H}_1 \to \mathrm{b\bar{b}})$ [%]	83.2	82.5
$\mathrm{Br}(\mathrm{H}_2 \to \mathrm{b\bar{b}})$ [%]	79.1	45.3
$\mathrm{Br}(\mathrm{H}_3 \to \mathrm{b\bar{b}})$ [%]	79.6	79.1

Table 5.5: *Higgs boson masses and branching fractions in two CP violating scenarios with parameters from Table 5.4. The first scenario is analysed at* $\sqrt{s}$ = *500 GeV, the second at 800 GeV and an assumed luminosity of* L = *500* fb^{-1}.

		Scenario N1 at 500 GeV		Scenario N2 at 800 GeV	
		$\sigma \times \mathrm{Br}$ [fb]	N_{events}	$\sigma \times \mathrm{Br}$ [fb]	N_{events}
Signal	$\mathrm{H}_1\mathrm{H}_2 \to \mathrm{b\bar{b}b\bar{b}}$	$4.196 \cdot 10^{-1}$	210	$7.598 \cdot 10^{-6}$	0
	$\mathrm{H}_2\mathrm{H}_3 \to \mathrm{b\bar{b}b\bar{b}}$	$1.261 \cdot 10^{1}$	6305	$1.852 \cdot 10^{0}$	926
	$\mathrm{H}_1\mathrm{H}_3 \to \mathrm{b\bar{b}b\bar{b}}$	$3.428 \cdot 10^{0}$	1714	$2.574 \cdot 10^{-2}$	13
Background	$\mathrm{H}_1\mathrm{Z}^0 \to \mathrm{b\bar{b}q\bar{q}}$	$3.463 \cdot 10^{1}$	17315	$1.672 \cdot 10^{1}$	8360
	$\mathrm{H}_2\mathrm{Z}^0 \to \mathrm{b\bar{b}q\bar{q}}$	$6.043 \cdot 10^{0}$	3022	$1.794 \cdot 10^{-2}$	9
	$\mathrm{H}_3\mathrm{Z}^0 \to \mathrm{b\bar{b}q\bar{q}}$	$6.276 \cdot 10^{-1}$	314	$1.476 \cdot 10^{-5}$	0

Table 5.6: *Topological cross sections* $\sigma \times \mathrm{Br}$ *and number of events for different Higgs pair production processes* $\mathrm{e^+e^-} \to \mathrm{H}_i\mathrm{H}_j \to \mathrm{b\bar{b}b\bar{b}}$ *and processes* $\mathrm{e^+e^-} \to \mathrm{H}_i\mathrm{Z}^0 \to \mathrm{b\bar{b}q\bar{q}}$ *in two CP violating scenarios with the parameters from Table 5.4. The first scenario is analysed at* $\sqrt{s}$ = *500 GeV, the second at 800 GeV with an assumed luminosity of* L = *500* fb^{-1}.

these processes is done with PYTHIA 6.2.

5.3 Signal and Background Processes for the SPS 1a point

The present analysis is applied to one of the so-called benchmark points for SUSY searches SPS 1a [94]. SPS 1 is a typical mSUGRA scenario which consists of a point with an intermediate value of $\tan\beta$ and a model line attached to it (SPS 1a) as well as of a "typical" mSUGRA point with relatively high $\tan\beta$ (SPS 1b). The parameters for the SPS 1a point are $m_0 = 100$ GeV, $m_{1/2} = 250$ GeV, $A_0 = -100$ GeV, $\tan\beta = 10$, $\mu > 0$. For this point, the Higgs masses are $m_{\mathrm{h}^0} = 113.7$ GeV, $m_{\mathrm{A}^0} = 394.7$ GeV, $m_{\mathrm{H}^0} = 394.9$ GeV, $m_{\mathrm{H}^\pm} = 403.6$ GeV according to the Hdecay and FeynHiggsFast programs [75, 95].

The analysis is done for a centre of mass energy of $\sqrt{s} = 1$ TeV, at which the cross section for the process $\mathrm{e^+e^-} \to \mathrm{HA}$ is 2.5 fb. An assumed luminosity is 1000 fb^{-1}. The branching ratio for the H (A) Higgs boson to $\mathrm{b\bar{b}}$ is 0.64 (0.40). The total width is $\Gamma_{\mathrm{tot}} = 0.785$ GeV (1.251 GeV) for H (A). The number of expected signal events is 640. The signal is generated with PYTHIA 6.2.

5.4 Standard Model Background Processes

A precise analysis in high energy physics requires a good knowledge of all possible background sources. The process analysed in this thesis has a four-jet topology. Therefore it is vital to suppress the background sources which have a similar signature. Such background events come from the following four groups:

1. Two-photon events.
2. Two-fermion events.
3. Four-fermion events.
4. $\mathrm{t\bar{t}}$ events.

Next every background source will be considered in details:

1. Two-photon events. At a future Linear Collider a beam-beam interaction will be a very important background source for the analyses. The dominant effect is a so-called *beamstrahlung*, i.e. radiation of photons from beam particles in the strong field of the opposite bunch. This can lead to a hadronic reaction $\gamma\gamma \rightarrow$ hadrons (Fig. 5.2). The scattered photons will be radiated mostly in the beam direction. Although the rate of the quark pairs, produced in two-photon processes, is much lower than that of $\mathrm{e^+e^-}$ pairs, these processes have a tail to higher transverse momenta and, therefore, leading to two-jet topology. However, they can be separated by requiring four-jet events.

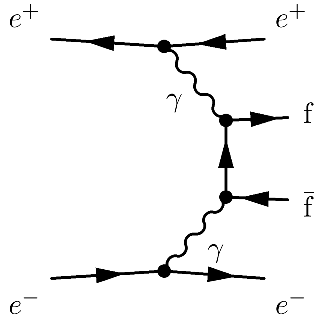

Figure 5.2: *The* $\gamma\gamma \rightarrow \mathrm{f\bar{f}}$ *process. Two photons are radiated from the incoming beams and can create hadronic final states in their collision*

2. Two-fermion events. These events come from the process $\mathrm{e^+e^-} \rightarrow \mathrm{Z^0}\gamma^* \rightarrow \mathrm{q\bar{q}}$ [1] and have the highest topological cross section in comparison with other background sources (see below). The biggest part of the events coming from such processes have the emitted photon in the initial state (left diagram in Fig. 5.3), a so-called initial state radiation (ISR). The effective centre of mass energy in this case corresponds to the mass of Z boson and the cross section of two-fermion process is significantly increased. The photon in most cases will be emitted with small angle and, therefore, stays undetected. Such kind of events are called *radiative return* events. They are very easy to reject by making a cut on visible energy.

In the case if two-fermion events do not have ISR photon, all the energy will be visible in detector (middle diagram in Fig. 5.3). This leads to a two-jet topology events. However, gluon radiation from quarks can lead to more than two jets in the final state (right diagram in Fig. 5.3). But the energy of the jets, coming from gluons, is usually smaller than that

---

[1] $\mathrm{e^+e^-} \rightarrow \mathrm{t\bar{t}}$ events can lead to more complicated topology, rather than to four jets, which will be shown later.

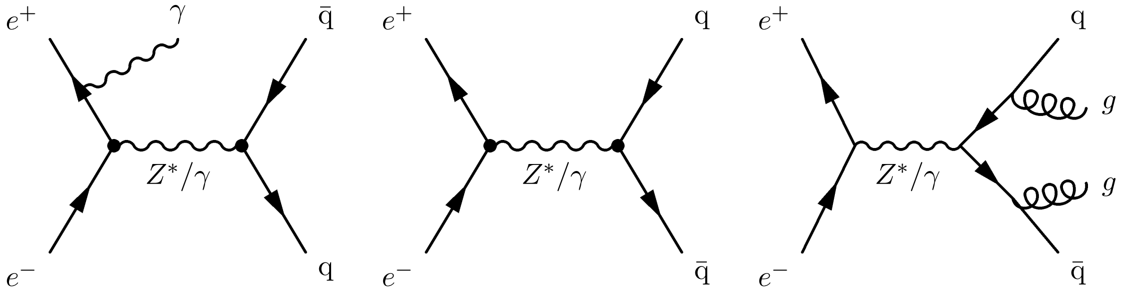

Figure 5.3: *Two-fermion background events. Left diagram: radiative return event. Middle diagram: two-jet topology event* $e^+e^- \to q\bar{q}$. *Right diagram: two quark event with gluon radiation in the final state.*

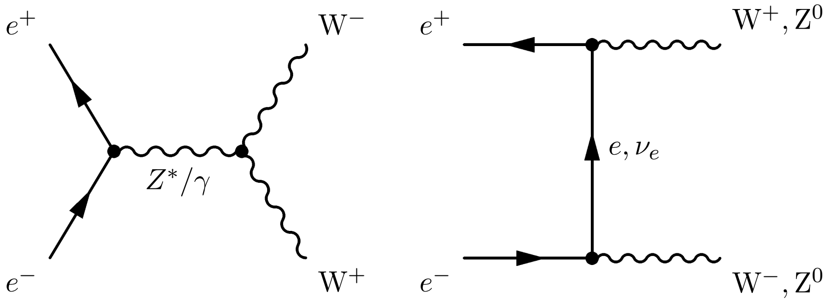

Figure 5.4: *The four-fermion processes* $e^+e^- \to W^+W^-$ *and* $e^+e^- \to Z^0Z^0$.

coming from the primary quarks, therefore they will be emitted predominantly in the quark direction. If such kind of events build four-jet topology, this can be an important background. To suppress it, the fact that the energy of the gluon jets is small, should be used. The di-jet mass of two-fermion events will form continuous background, whereas the signal processes will form the invariant mass of the Higgs bosons.

A small fraction of two-fermion jets can come from b-quarks with gluon radiation containing b-hadrons. They can be separated using b-tagging.

3. Four-fermion events. Four-fermion background events have a kinematic topology, identical to a signal one. Therefore it is more difficult to separate such kind of background than two-fermion one. The main processes, contributing to it, are presented in Fig. 5.4. A pair production of W and Z bosons, decaying into quark pairs, is the most complicated background for our signal process. The pairs of W are produced in triple gauge coupling process with ZWW coupling or in t channel production. The Z pairs are produced in the t channel process only.

The W bosons decay hadronically in 68% cases as $W \to q\bar{q}'$. The events consist of four jets coming from four primary quarks. The mass of the di-jets with correct pairing is each of 80.3 GeV. The quark combinations in W decays are ud and cs, the other combinations are either suppressed via Cabbibo-Kobayashi-Maskawa matrix or kinematically forbidden (like tb combination).

The cross section of ZZ background is more than ten times smaller than that of WW production due to smaller number of diagrams and the larger coupling of the W to leptons. The total hadronic branching fraction is 69%. The Z decays as $Z \to q\bar{q}$. In 15% of the cases the Z decays to $b\bar{b}$ pair. Again, the correct di-jet pairing has a mass of 91.2 GeV.

Both ZZ and WW events will peak in forward/backward directions, whereas HA signal events will be produced centrally, therefore this background can be suppressed by applying cuts on the polar angle of the thrust vector $\cos\theta_T$ and thrust value T (see Chapter 6).

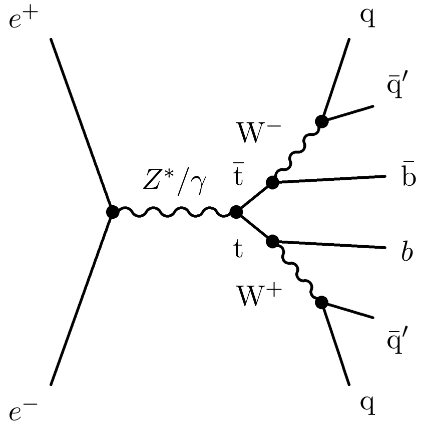

Figure 5.5: $e^+e^- \rightarrow t\bar{t}$ *background process with six jets decay topology.*

4. $t\bar{t}$ **events.** Another background source, coming from the process $e^+e^- \rightarrow Z^0\gamma^* \rightarrow t\bar{t}$, can have a six-jet topology containing b jets. This is a fully hadronic decay of the t quark $t\bar{t} \rightarrow W^+bW^-\bar{b} \rightarrow q\bar{q}'bq\bar{q}'\bar{b}$ (Fig. 5.5). This background can be suppressed by applying a cut on the jet resolution parameter y_{56}.

For the background estimation in this study, the following processes are generated using PYTHIA 6.2:

$$\begin{aligned}
&e^+e^- \rightarrow t\bar{t},\\
&e^+e^- \rightarrow W^+W^-,\\
&e^+e^- \rightarrow Z^0Z^0,\\
&e^+e^- \rightarrow q\bar{q}, \quad (q = u, d, s, c, b).
\end{aligned}$$

Their cross sections and expected number of events for $\sqrt{s} = 500$, 800 GeV with an assumed luminosity of L = 500 fb^{-1} and $\sqrt{s} = 1000$ GeV with L = 1000 fb^{-1} are given in Table 5.7.

Process	500 GeV		800 GeV		1000 GeV	
	$\sigma \times$ Br [fb]	N_{events}	$\sigma \times$ Br [fb]	N_{events}	$\sigma \times$ Br [fb]	N_{events}
$t\bar{t} \rightarrow W^+bW^-\bar{b}$	$6.69 \cdot 10^2$	334500	$1.65 \cdot 10^2$	82500	$1.135 \cdot 10^2$	113500
$W^+W^- \rightarrow q\bar{q}q\bar{q}$	$4.13 \cdot 10^3$	2065000	$2.34 \cdot 10^3$	1170000	$1.741 \cdot 10^3$	1741000
$Z^0Z^0 \rightarrow q\bar{q}q\bar{q}$	$3.11 \cdot 10^2$	155500	$1.74 \cdot 10^2$	87000	9.816	9816
$Z^0/\gamma^* \rightarrow q\bar{q}$	$1.29 \cdot 10^4$	6450000	$5.45 \cdot 10^3$	2725000	$3.533 \cdot 10^3$	3533000
Total background		9005000		4064500		5397316

Table 5.7: *Topological cross sections* $\sigma \times$ Br *and expected number of events for SM background processes at* $\sqrt{s} = 500$*, 800 GeV with an assumed luminosity of L = 500 fb*$^{-1}$ *and at* $\sqrt{s} = 1000$ *GeV with L = 1000 fb*$^{-1}$*.*

Chapter 6

Analysis of MSSM Higgs Bosons in Pair Production

In this chapter, the general analysis of the MSSM Higgs boson pair production at the ILC $e^+e^- \rightarrow HA$ with subsequent Higgs decays into $b\bar{b}$ pairs will be explained. Firstly, the assumption of the maximal process cross section, $\sin^2(\beta-\alpha) = 1$, will be taken. For this assumption, the analysis will be done for different m_H and m_A hypotheses at $\sqrt{s}$ = 500 GeV and 800 GeV with an integrated luminosity of 500 fb^{-1}. Then, the case of the degenerate H and A masses will be considered.

The general analysis will be applied to two CP violating scenarios at $\sqrt{s}$ = 500 GeV and 800 GeV with an assumed luminosity of 500 fb^{-1} as well as to the SPS 1a point for SUSY searches at $\sqrt{s}$ = 1 TeV with an integrated luminosity of 1000 fb^{-1}.

6.1 Analysis for $\sqrt{s}$ = 500 GeV

In this section, the analysis of Higgs mass reconstruction in pair production process $e^+e^- \rightarrow HA$ with Higgs boson decays into $b\bar{b}$ pairs will be described for one arbitrary chosen mass hypothesis (m_H,m_A) = (150,100) GeV at $\sqrt{s}$ = 500 GeV with an integrated luminosity of 500 fb^{-1}. The case of maximal allowed process cross section, $\sin^2(\beta - \alpha) = 1$, will be assumed. The simulated signal and background samples are described in Chapter 5.

6.1.1 Event Selection

Events of the $b\bar{b}b\bar{b}$ topology are characterised by four high multiplicity hadronic jets, containing decay products of b-hadrons. A cut-based technique is employed to separate signal from background. The selection criteria are optimised separately for a centre of mass energy of 500 GeV and 800 GeV (see Section 6.2). Each event is required to pass the following cuts at $\sqrt{s}$ = 500 GeV:

1. The visible energy E_{vis}, i.e. the total energy deposited in the detector, must be greater than 340 GeV. This cut is effective against background coming from events with ISR (Initial State Radiation) and neutrinos.
2. Each event is forced into four jets using the DURHAM algorithm (see Section 4.2) and the number of tracks per jet is required to be greater than three.
3. To separate centrally produced H and A bosons from the WW and ZZ events, peaking in forward/backward direction, a cut on the polar angle of the thrust vector [93],

$|\cos\theta_T| < 0.8$ is applied.

4. Further suppression of the WW and ZZ background events is achieved by requiring the event thrust value T to be less than 0.88. This value is large for events which are oriented along a longitudinal axis, such as two-jet like events.

5. Two-fermion background is suppressed by applying a cut on the DURHAM jet resolution parameter, $\log_{10} y_{34} \geq -2.9$ [1]. This value separates three- and four-jet like events and is low for two-fermion events and higher for four-fermion events.

6. High multiplicity six-jet events originating from the production of $\mathrm{t\bar{t}}$ events are reduced by requiring the number of particle flow objects N_{pflow} in the event to be less than 130 (see Section 4.1).

7. The background from $\mathrm{e^+e^-} \rightarrow \mathrm{t\bar{t}}$ events is further reduced by applying a cut on the jet resolution parameter $\log_{10} y_{56}$. This parameter characterises the transition from a 6-jet topology to a 5-jet topology event and it is larger for 6-jet events than for events with fewer than six jets. The cut of $\log_{10} y_{56} \leq$ -3.1 is applied. This cut helps to separate the background coming from fully hadronic top decays.

8. Finally, the b-tag information is exploited to enhance the purity of the selected event sample. First, the b-tag variable for each jet is calculated as described in Section 4.3. The four b-tag variables are sorted in descending order, $B_1 > B_2 > B_3 > B_4$. The two quantities B_{12}, B_{34} are then defined as

$$B_{12} = \frac{B_1 B_2}{B_1 B_2 + (1 - B_1)(1 - B_2)},$$

$$B_{34} = \frac{B_3 B_4}{B_3 B_4 + (1 - B_3)(1 - B_4)}.$$

   The value of B_{12} has to be greater than 0.75.

9. The value of B_{34} is required to be greater than 0.05.

Fig. 6.1 and 6.2 show the distributions of the selection variables for the different sources of background and for the signal with $(m_{\mathrm{H}},m_{\mathrm{A}})$ = (150,100) GeV at $\sqrt{s} = 500$ GeV. The numbers of expected signal and background events, retained after selection, and the signal efficiencies are presented in cutflow Table 6.1. It shows that such cuts like those on visible energy, number of tracks per jet, polar angle of the thrust vector and b-tag cuts are very effective to separate signal from background. Especially it should be stressed that after all kinematic selection cuts i.e. before b-tag cuts the signal efficiency is 54% while the background is drastically reduced (1.6% of the initial value). After b-tag cuts only 1.3% of the background events, left after kinematic selection (1-7 cuts), remain, while the signal efficiency is 43%. This confirms, that the new tool for b-tagging is very powerful. The number of signal events remaining after the selection cuts is three times bigger than the number of background events.

---

[1] The jet resolution parameter y_{34} is defined as DURHAM jet discriminating variable (Section 4.2) $y_{34} = \frac{2(1-\cos\theta_{34})min(E_3^2,E_4^2)}{s}$ and characterises the transition from a 4-jet topology to a 3-jet topology event.

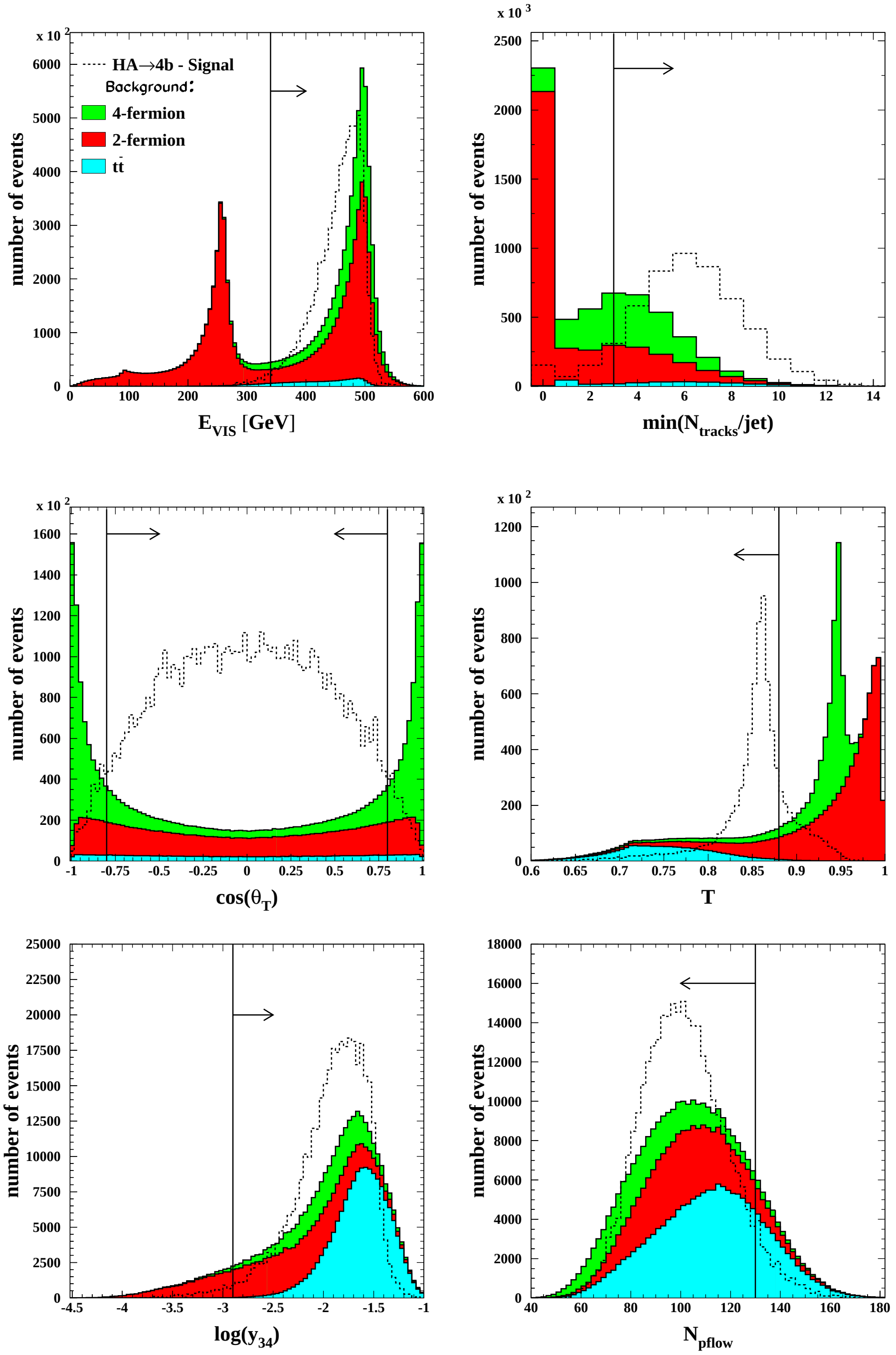

Figure 6.1: *Distributions of the selection variables (visible energy* E_{vis}*, number of tracks per jet* $N_t racks/jet$*,* $\cos\theta_T$*, thrust value* T*, jet resolution parameter* $\log_{10} y_{34}$ *and number of particle flow objects* N_{pflow}*) at* $\sqrt{s}$ *= 500 GeV. The signal distributions for the channel* $\mathrm{HA} \rightarrow \mathrm{b\bar{b}b\bar{b}}$ *with (*m_{H}*,*m_{A}*) = (150,100) GeV are shown with arbitrary normalisation. The vertical lines with arrows indicate cuts, imposed on these variables. The distributions are shown after all cuts preceding the current variable.*

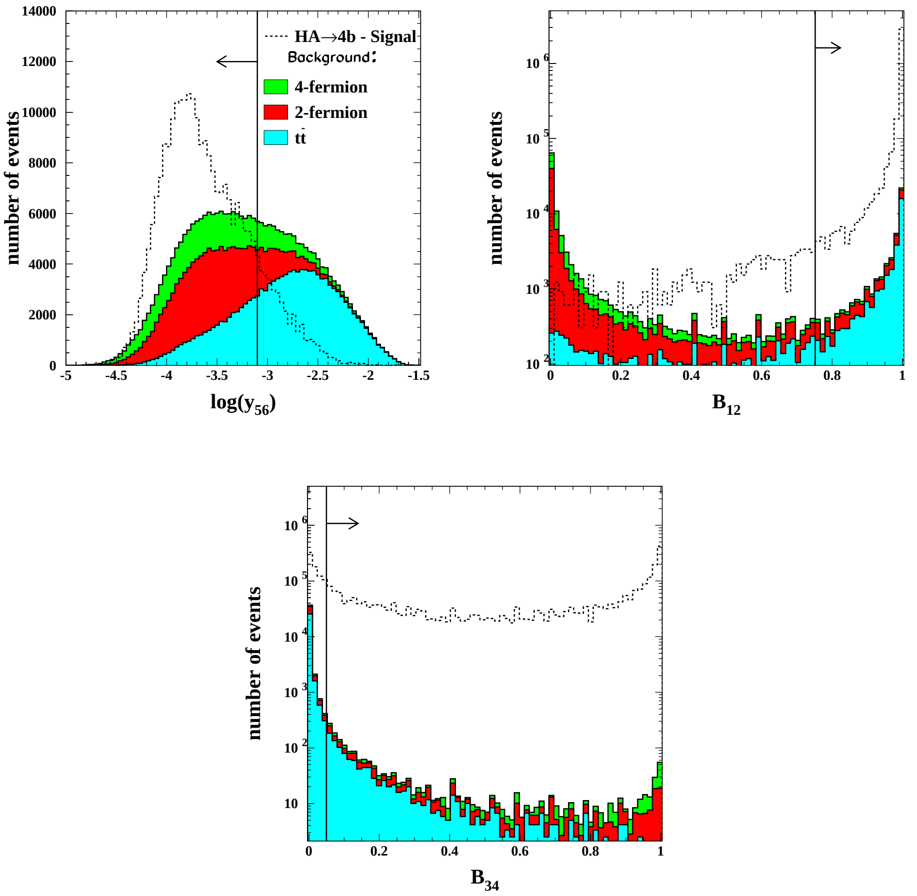

Figure 6.2: *Distributions of the selection variables (jet resolution parameter* $\log_{10} y_{56}$ *and b-tag variables* B_{12} *and* B_{34}*) at* $\sqrt{s}$ *= 500 GeV. The signal distributions for the channel* $\mathrm{HA} \to \mathrm{b\bar{b}b\bar{b}}$ *with* (m_H,m_A) *= (150,100) GeV are shown with arbitrary normalisation. The vertical lines with arrows indicate cuts, imposed on these variables. The distributions are shown after all cuts preceding the current variable.*

Cut	Tot. BG	ZZ	WW	2-ferm.	$t\bar{t}$	Sig. eff. [%]	Signal
	9005000	155500	2065000	6450000	334500	100.0	13616
1	6035874	146909	1957360	3651766	279839	98.29	13383
2	2675297	105981	1309760	1047851	211705	91.35	12438
3	1357078	39789	383774	772600	160915	85.07	11583
4	335995	8167	50257	119448	158123	67.82	9235
5	306624	7832	48523	92288	157981	66.59	9067
6	265119	7499	46254	84886	126480	63.19	8604
7	148084	5975	35270	70218	36621	54.40	7407
8	41912	1761	809	10136	29206	53.22	7247
9	1960	272	19	473	1196	42.63	5805

Table 6.1: *Number of remaining background events, signal efficiency and number of expected signal events after each of the nine cuts for the mass hypothesis (m_{H},m_{A}) = (150,100) GeV in the* HA → $b\bar{b}b\bar{b}$ *channel at $\sqrt{s}$ = 500 GeV with an assumed luminosity of 500 fb^{-1}. The first column is the number of the cut, the second one is the number of total background events.*

6.1.2 Mass Reconstruction

The spectra of the di-jet mass sum and mass difference, obtained in the HA → $b\bar{b}b\bar{b}$ channel are used to determine Higgs boson properties. Their reconstruction will be explained next.

Having found four jets there are three possibilities to pair them (Fig. 6.3):

- (12) (34)
- (13) (24)
- (14) (23)

Only one jet combination is true, the two others form a so-called “combinatorial” background.

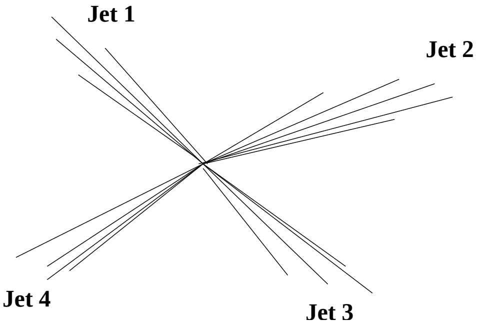

Figure 6.3: *The scheme of a four-jet topology event.*

The mass of every jet pair (di-jet) is calculated according to:

$$m_{2\mathrm{Jet}} = \sqrt{(E_{\mathrm{Jet1}} + E_{\mathrm{Jet2}})^2 - (\mathbf{p}_{\mathrm{Jet1}} + \mathbf{p}_{\mathrm{Jet2}})^2}, \tag{6.1}$$

where E_{Jet1}, E_{Jet2} are the energies of the first and the second jet, $\mathbf{p}_{\mathrm{Jet1}}$ and $\mathbf{p}_{\mathrm{Jet2}}$ are their momenta. In Fig. 6.4 the reconstructed di-jet mass sum and mass difference after the selection cuts are shown. Three entries per event contribute to these distributions, two of them form

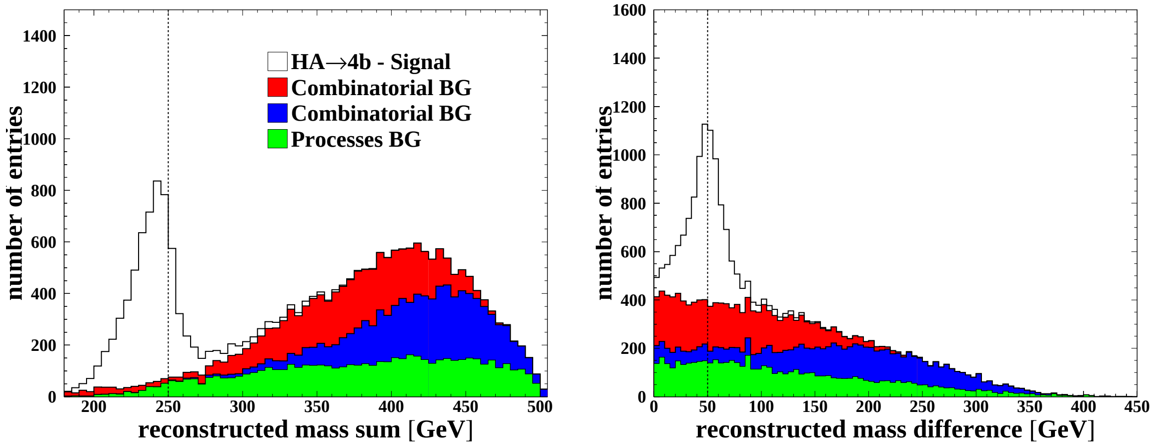

Figure 6.4: *Distributions of the di-jet mass sum (left figure) and di-jet mass difference (right figure) in the* $\mathrm{HA} \to \mathrm{b\bar{b}b\bar{b}}$ *channel for Higgs boson mass hypothesis* $(m_{\mathrm{H}},m_{\mathrm{A}})$ *= (150,100) GeV at* $\sqrt{s}$ *= 500 GeV after selection cuts. The three components of the signal are shown separately: two parts of the combinatorial background and one of the real signal. The background from the other processes is presented as well. The vertical lines correspond to a true mass sum of 250 GeV in the left figure and a true mass difference of 50 GeV in the right figure.*

combinatorial background and the third combination is a real signal. In the figure the background from the SM processes is also shown. The reconstructed di-jet mass sum is shifted to smaller values with respect to the true value mainly due to the missing energy from decay neutrinos, which are not detected. There is, however, the possibility to rescale the reconstructed jet energy and jet momentum using:

$$E_{\mathrm{Jet}}^{\mathrm{resc}} = E_{\mathrm{Jet}} \frac{\sqrt{s}}{E_{\mathrm{vis}}}, \tag{6.2}$$

$$\mathbf{p}_{\mathrm{Jet}}^{\mathrm{resc}} = \mathbf{p}_{\mathrm{Jet}} \frac{\sqrt{s}}{E_{\mathrm{vis}}}, \tag{6.3}$$

where $E_{\mathrm{Jet}}^{\mathrm{resc}}$, $\mathbf{p}_{\mathrm{Jet}}^{\mathrm{resc}}$ are jet energy and jet momentum after rescaling, E_{vis} is the visible energy. The resulting di-jet mass sum and mass difference after energy and momentum rescaling are shown in Fig. 6.5. As one can see the mass reconstruction is improved significantly and the shift in the reconstructed mass sum with respect to the true value has disappeared. In this figure, the SM background sources are shown separately.

A further improvement in mass reconstruction can be obtained using the 4C kinematic fit described in Section 4.4, where a conservation of four-momentum is required. This leads in total to four constraints. For the example hypothesis $(m_{\mathrm{H}},m_{\mathrm{A}})$ = (150,100) GeV the di-jet mass sum and mass difference, presented in Fig. 6.6, show that due to the kinematic fit the mass reconstruction resolution can be improved significantly.

A comparison of the raw mass spectra after all selection cuts, the spectra after the energy and momentum rescaling and after the kinematic fit is shown in Fig. 6.7. As one can see the kinematic fit is the most powerful tool for the mass reconstruction improvement.

A final improvement in di-jet mass reconstruction is done by making a cut on di-jet mass sum and mass difference as indicated by arrows in Fig. 6.6. The di-jet mass sum and mass difference after a cut on di-jet mass difference and di-jet mass sum, respectively, are shown in

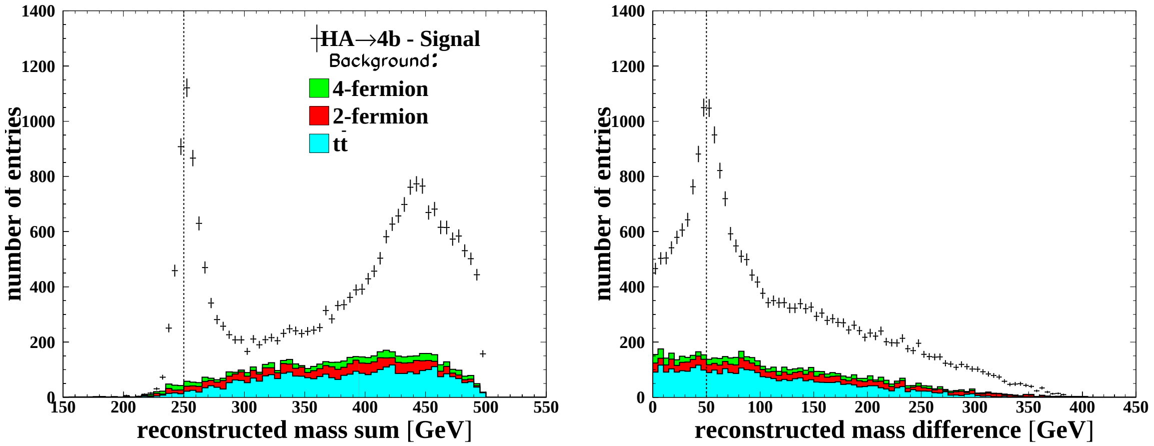

Figure 6.5: *Distributions of the di-jet mass sum (left figure) and di-jet mass difference (right figure) in the* HA → b$\bar{b}$b$\bar{b}$ *channel for Higgs boson mass hypothesis* (m_{H},m_{A}) = *(150,100) GeV at* $\sqrt{s}$ = *500 GeV after selection cuts and energy and momentum rescaling.*

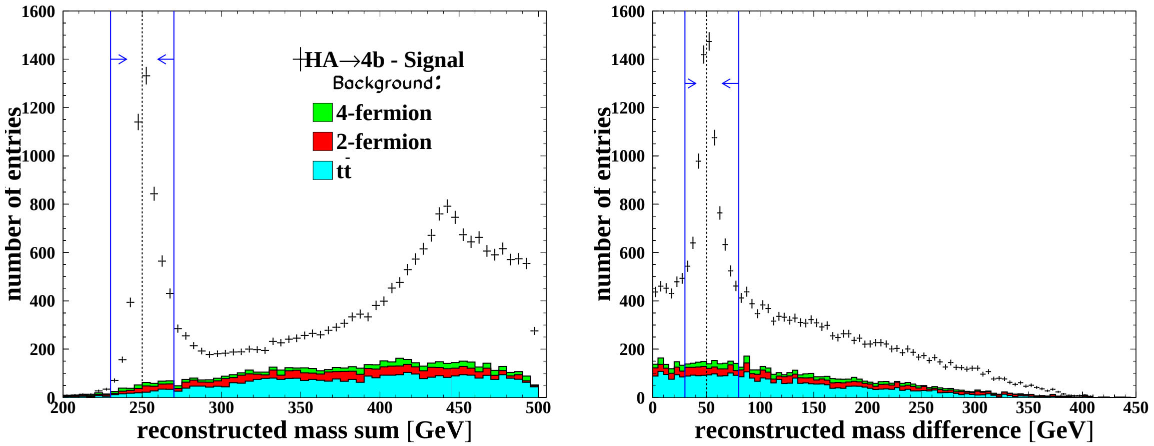

Figure 6.6: *Distributions of the di-jet mass sum (left figure) and di-jet mass difference (right figure) in the* HA → b$\bar{b}$b$\bar{b}$ *channel for Higgs boson mass hypothesis* (m_{H},m_{A}) = *(150,100) GeV at* $\sqrt{s}$ = *500 GeV after selection cuts and kinematic fit. The lines with arrows indicate two-dimensional cut.*

Fig. 6.8. The signal efficiencies, number of signal events and total background after selection cuts, represented in Table 6.1, and a cut on both di-jet mass sum and mass difference (two-dimensional cut) are given in Table 6.2.

The mass distributions in Fig 6.8 are fitted separately with the signal normalisation, the sum and the difference of the Higgs boson masses as free parameters. The background is approximated with a polynomial function. From the fit, a precision of $\delta\Sigma$ = 197 MeV and $\delta\Delta$ = 146 MeV can be achieved for the Higgs boson mass sum ($\Sigma = m_{\mathrm{A}} + m_{\mathrm{H}}$) and mass difference ($\Delta = |m_{\mathrm{A}} - m_{\mathrm{H}}|$), respectively. The di-jet mass sum and mass difference are found to be weakly correlated quantities. Hence, the statistical errors on the masses of the Higgs

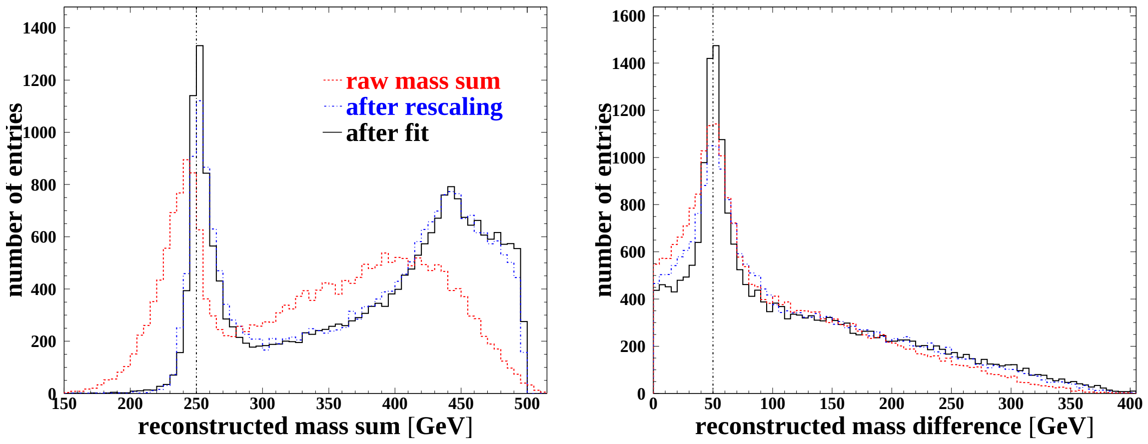

Figure 6.7: *Distributions of the reconstructed invariant mass sum (left figure) and mass difference (right figure) in the sample of the* HA → $b\bar{b}b\bar{b}$ *events with* $(m_{\mathrm{H}},m_{\mathrm{A}})$ *= (150,100) GeV at* $\sqrt{s}$ *= 500 GeV. Dashed red histograms show raw spectra obtained using only measured jet angles and energies. Dashed blue histograms are obtained after energy and momentum rescaling. Solid histograms show spectra obtained after applying 4C kinematic fit. Three entries per event contribute to these distributions, corresponding to the three possible di-jet pairings. The SM background is also included.*

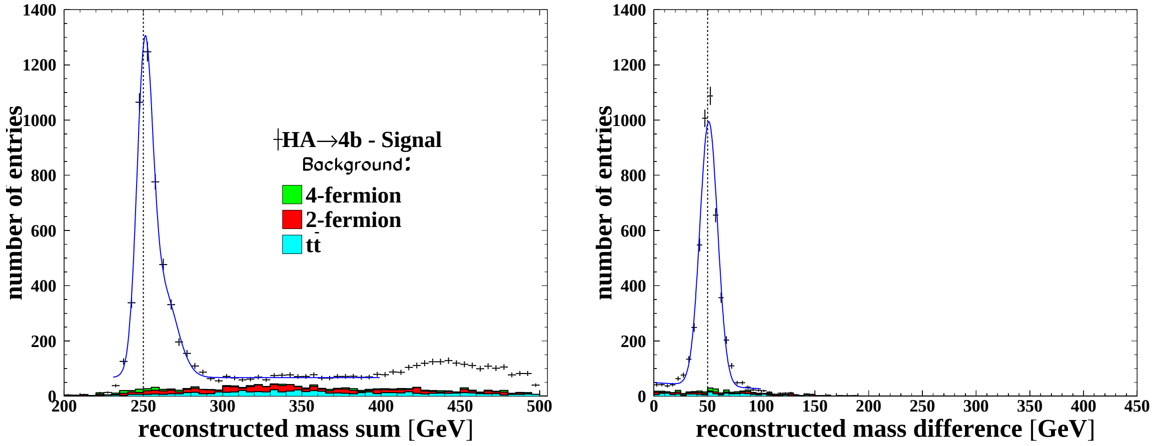

Figure 6.8: *Distribution of the di-jet mass sum after all selection cuts, kinematic fit and a cut on di-jet mass difference (left figure). Distribution of the di-jet mass difference after all selection cuts, kinematic fit and a cut on di-jet mass sum (right figure). Both distributions are in the* HA → $b\bar{b}b\bar{b}$ *channel for the Higgs boson mass hypothesis* $(m_{\mathrm{H}},m_{\mathrm{A}})$ *= (150,100) GeV at* $\sqrt{s}$ *= 500 GeV.*

	selection cuts	2-dim. cut
Signal efficiency [%]	43	31
Number of signal events	5805	4196
Total background	1960	132

Table 6.2: *The signal efficiencies, the number of signal and total background events after selection cuts and after cuts on both di-jet mass sum and mass difference for the mass combination* (m_{H},m_{A}) *= (150,100) GeV at* $\sqrt{s}$ *= 500 GeV with an assumed luminosity of 500* fb^{-1}. *The signal expectations are quoted for* $\sin^2(\beta-\alpha) = 1$ *and the Higgs boson branching fractions of* $\mathrm{Br}(\mathrm{H} \to \mathrm{b\bar{b}}) = \mathrm{Br}(\mathrm{A} \to \mathrm{b\bar{b}})$ = *90%.*

bosons can be calculated as follows:

$$\delta m_{\mathrm{H}} = \delta m_{\mathrm{A}} = \frac{1}{2}\sqrt{(\delta\Sigma^2 + \delta\Delta^2)},$$

where $\delta\Sigma$ and $\delta\Delta$ are statistical uncertainties in determination of the Higgs boson mass sum and mass difference. For the example mass hypothesis δm_{A} and δm_{H} are found to be 0.12 GeV.

The statistical relative error on the topological cross section is calculated as

$$\delta\sigma/\sigma = \frac{\sqrt{N_S + N_B}}{N_S}.$$

The notations N_S and N_B stand for the number of background and signal entries within the windows in the di-jet mass sum and mass difference distributions, where the signal is accumulated. The boundaries of these windows are optimised to yield a minimal relative error on the topological cross section. For the example Higgs mass hypothesis the topological cross section can be measured with relative precision of 1.6%.

6.2 Analysis for $\sqrt{s}$ = 800 GeV

Similar procedure described in Section 6.1 is applied for the $\sqrt{s}$ = 800 GeV with an assumed integrated luminosity of 500 fb^{-1}. In this section the analysis will be shown for one chosen mass hypothesis (m_{H},m_{A}) = (300,250) GeV. The simulated signal and background samples are described in Chapter 5.

Modified selection criteria are used to separate signal from background at $\sqrt{s}$ = 800 GeV in comparison with $\sqrt{s}$ = 500 GeV. Each event is required to pass the following cuts:

1. The visible energy E_{vis} must be greater than 600 GeV.
2. Each event is forced into four jets using the DURHAM algorithm and the number of tracks per jet is required to be greater than three.
3. To separate centrally produced H and A bosons from the WW and ZZ events, peaking in forward/backward direction, a cut on the polar angle of the thrust vector, $|\cos\theta_T| < 0.8$ is applied.
4. Further suppression of the WW and ZZ background events is achieved by requiring the event thrust value T to be less than 0.88.
5. Two-fermion background is suppressed by applying a cut on the DURHAM jet resolution parameter $\log_{10} y_{34} \geq -2.9$.

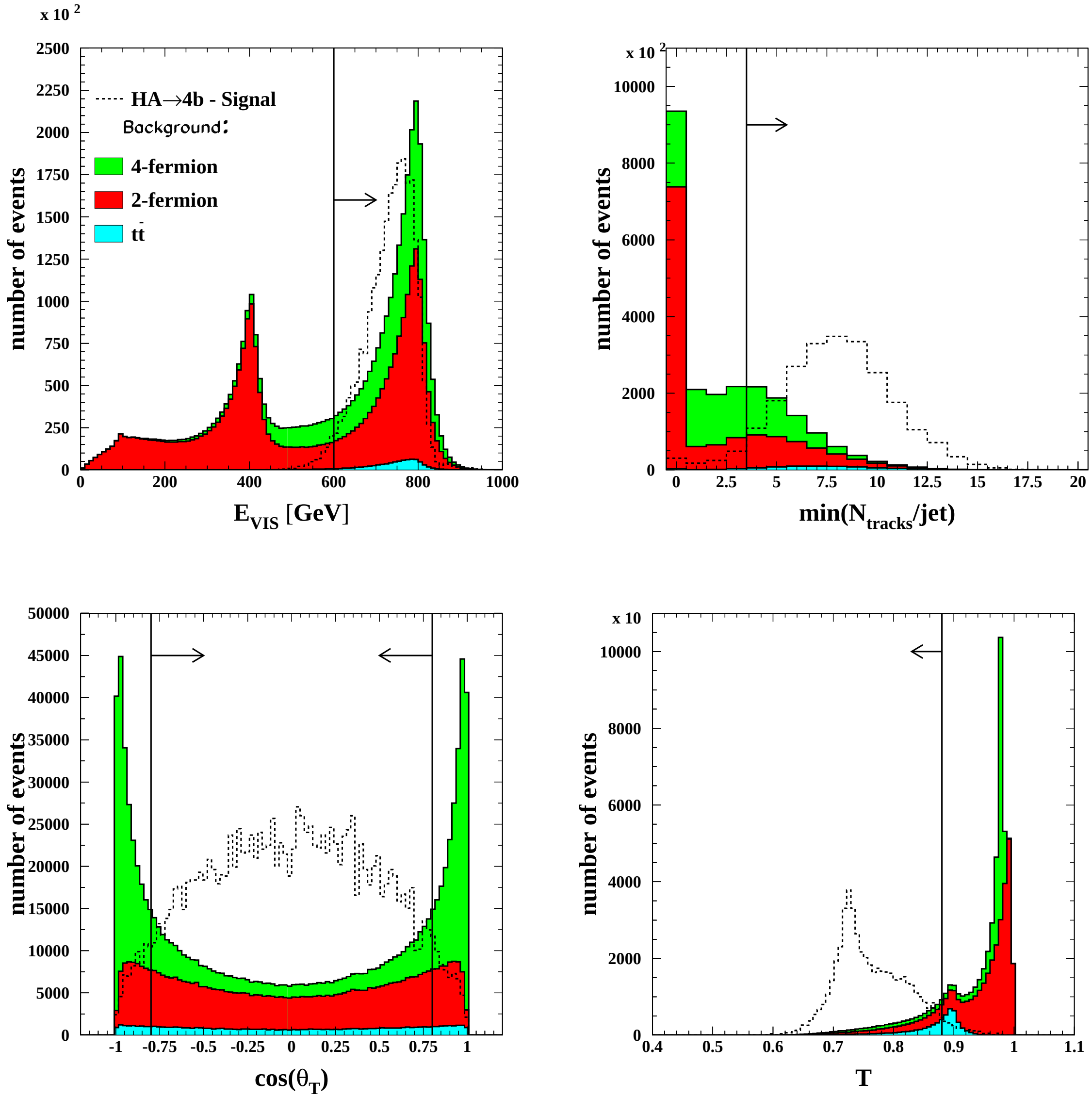

Figure 6.9: *Distributions of the selection variables (visible energy E_{vis}, number of tracks per jet N_{tracks}/jet, $\cos\theta_T$, thrust value T) at $\sqrt{s}$ = 800 GeV. The signal distributions for the channel* $\mathrm{HA} \rightarrow \mathrm{b\bar{b}b\bar{b}}$ *with* $(m_{\mathrm{H}}, m_{\mathrm{A}})$ *= (300,250) GeV are shown with arbitrary normalisation. The vertical lines with arrows indicate cuts, imposed on these variables. The distributions are shown after all cuts preceding the current variable.*

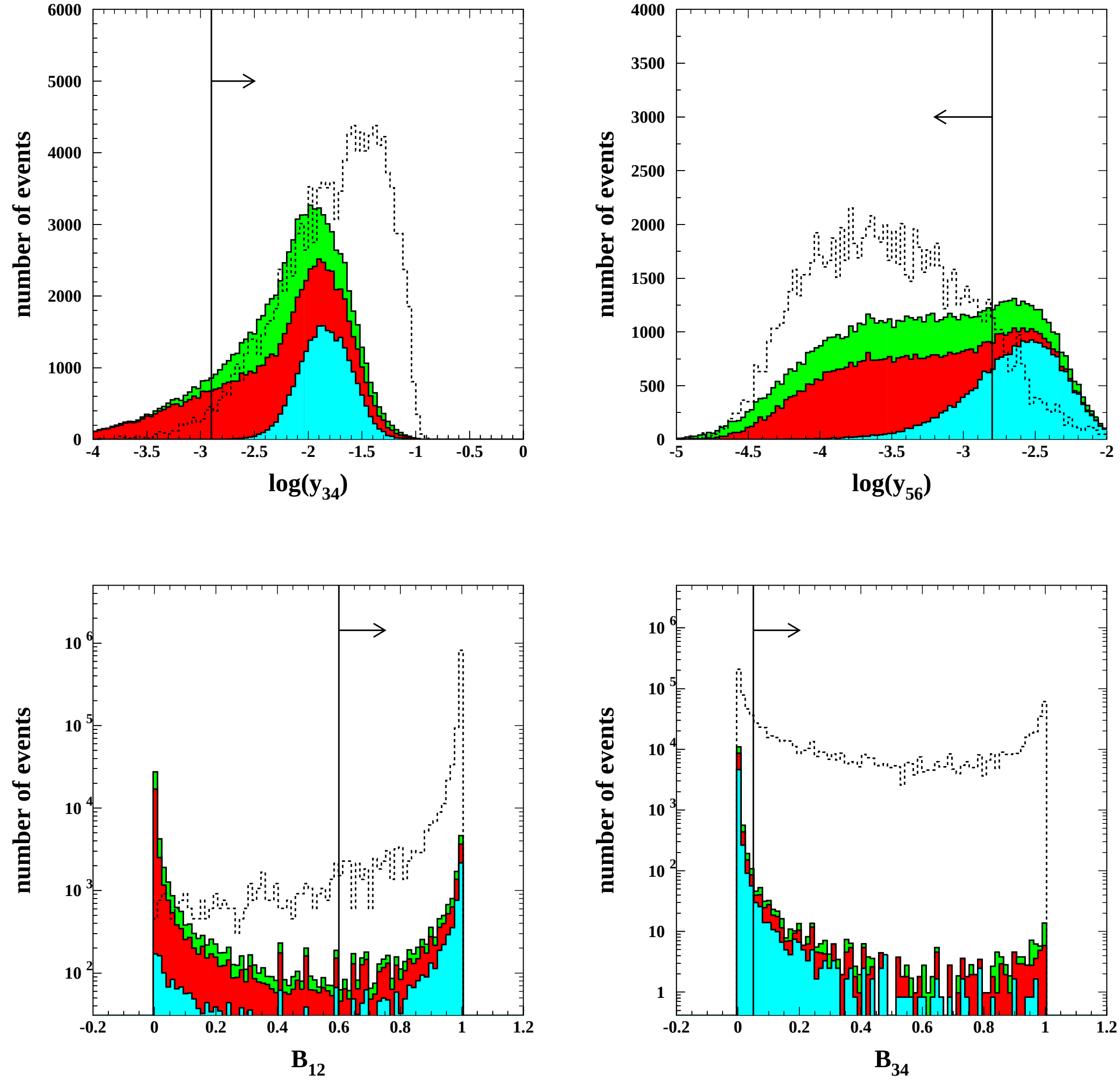

Figure 6.10: *Distributions of the selection variables (jet resolution parameters* $\log_{10} y_{34}$, $\log_{10} y_{56}$ *and b-tag variables* B_{12} *and* B_{34}*) at* $\sqrt{s}$ *= 800 GeV. The signal distributions for the channel* HA → $\mathrm{b\bar{b}b\bar{b}}$ *with* (m_{H},m_{A}) *= (300,250) GeV are shown with arbitrary normalisation. The vertical lines with arrows indicate cuts, imposed on these variables. The distributions are shown after all cuts preceding the current variable.*

Cut	Tot. BG	ZZ	WW	2-ferm.	$t\bar{t}$	Sig. eff. [%]	Signal
	4064500	87000	1170000	2725000	82500	100.0	3033
1	2376222	69491	922289	1307850	76592	97.23	2949
2	1007203	41522	462295	432605	70781	94.20	2857
3	542190	15305	154934	319818	52133	85.86	2604
4	90602	2328	21986	42023	24265	82.39	2499
5	78613	2117	20732	31502	24262	80.48	2441
6	54801	1937	16460	29276	7128	71.48	2168
7	12283	534	2075	4430	5244	69.14	2097
8	488	50	57	175	206	45.04	1366

Table 6.3: *Number of remaining background events, signal efficiencies and number of expected signal events after each of the eight cuts for the mass hypothesis* (m_{H},m_{A}) *= (300,250) GeV in the* HA → $\mathrm{b\bar{b}b\bar{b}}$ *channel at* $\sqrt{s}$ *= 800 GeV with an assumed luminosity of 500 fb*$^{-1}$*. The first column is the number of the cut, the second one is the number of total background events.*

	selection cuts	2-dim. cut
Signal efficiency [%]	45	36
Number of signal events	1366	1101
Total background	488	13

Table 6.4: *The signal efficiencies, the number of signal and total background events after selection cuts and after cuts on both di-jet mass sum and difference (2-dimensional cut) for the mass combination* (m_{H},m_{A}) *= (300,250) GeV at* $\sqrt{s} = 800\,\mathrm{GeV}$ *with an assumed luminosity of 500 fb*$^{-1}$*. The signal expectations are quoted for* $\sin^2(\beta-\alpha)$ *= 1 and the Higgs boson branching fractions of* $\mathrm{Br}(\mathrm{H}\to\mathrm{b\bar{b}}) = \mathrm{Br}(\mathrm{A}\to\mathrm{b\bar{b}})$ *= 90%.*

6. The background from $\mathrm{e^+e^-}\to\mathrm{t\bar{t}}$ events is further reduced by applying a cut on the jet resolution parameter $\log_{10} y_{56} \leq$ -2.8.

7. The value of b-tag quantity B_{12} has to be greater than 0.6.

8. The value of B_{34} is required to be greater than 0.05.

Fig. 6.9 and 6.10 show the distributions of the selection variables for the different sources of background and for the signal at $\sqrt{s}$ = 800 GeV. The number of expected signal and background events, retained after selection, and signal efficiencies for the example mass hypothesis with (m_{H},m_{A}) = (300,250) GeV at $\sqrt{s}$ = 800 GeV are presented in cutflow Table 6.3. It shows that the overall number of background events is twice smaller for $\sqrt{s}$ = 800 GeV case than for 500 GeV (4.1 million compared to 9.0 million events). This is connected with smaller cross sections of the background processes for 800 GeV, as indicated in Table 5.7. After all kinematic selection cuts the signal efficiency is 71.5% while the number of background events is significantly reduced (1.3% of the initial value). After all selection cuts only 0.01% of the initial background events survives, while the signal efficiency is 45%. The number of signal events remained after selection cuts is 2.8 times bigger than that of the background events.

For the example mass hypothesis the di-jet mass sum and mass difference after the kinematic fit are presented in Fig. 6.11. A final di-jet mass sum and di-jet mass difference after a cut on di-jet mass difference and mass sum, respectively, as indicated by arrows in Fig. 6.11,

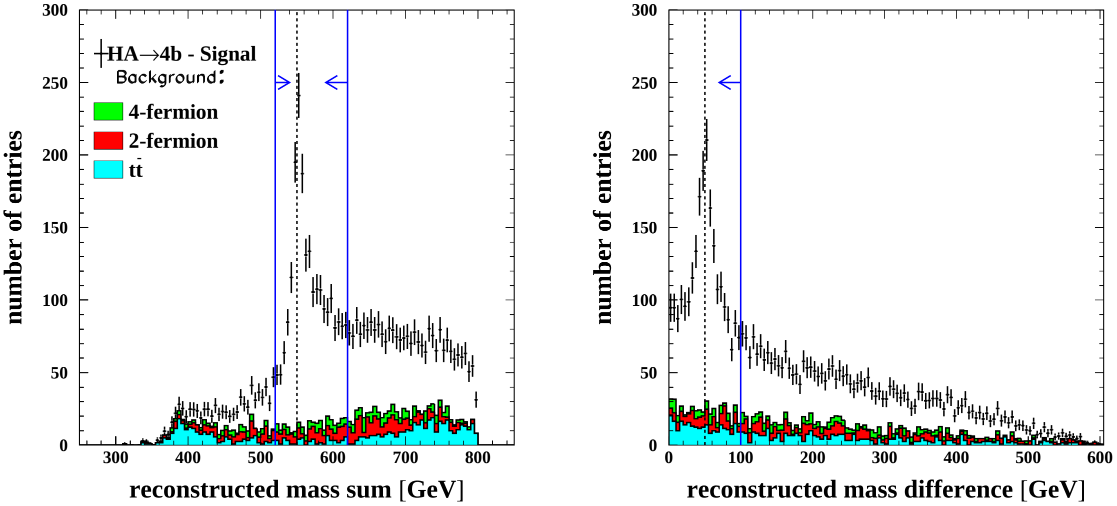

Figure 6.11: *Distributions of the di-jet mass sum (left figure) and di-jet mass difference (right figure) in the* HA → b$\bar{\rm b}$b$\bar{\rm b}$ *channel for Higgs boson mass hypothesis* ($m_{\rm H}$,$m_{\rm A}$) *= (300,250) GeV at* $\sqrt{s}$ *= 800 GeV after selection cuts and kinematic fit. The lines with arrows indicate two-dimensional cut.*

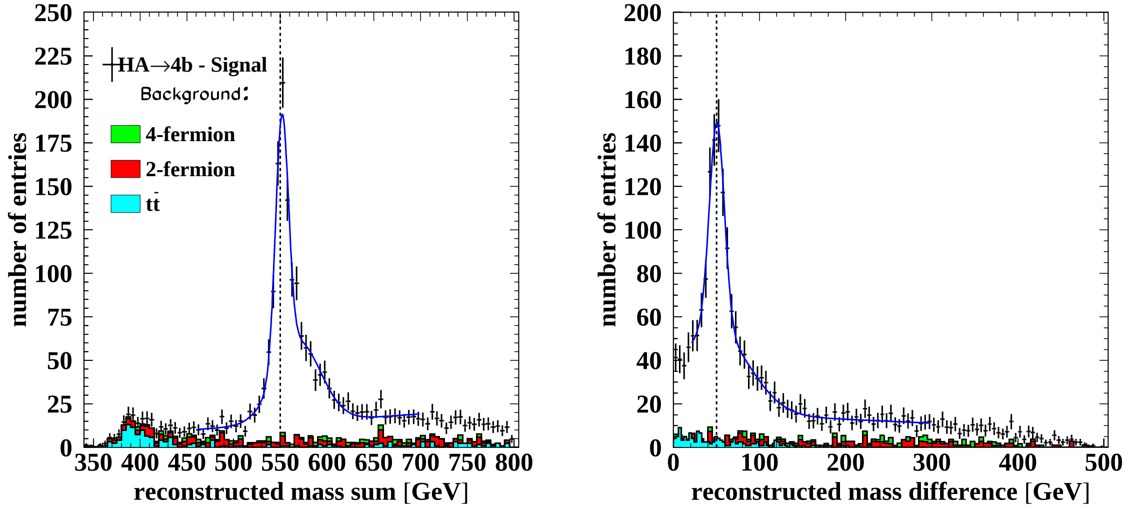

Figure 6.12: *Distribution of the di-jet mass sum after selection cuts, kinematic fit and a cut on di-jet mass difference (left figure). Distribution of the di-jet mass difference after selection cuts, kinematic fit and a cut on di-jet mass sum (right figure). Both distributions are in the* HA → b$\bar{\rm b}$b$\bar{\rm b}$ *channel for the Higgs boson mass hypothesis* ($m_{\rm H}$,$m_{\rm A}$) *= (300,250) GeV at* $\sqrt{s}$ *= 800 GeV.*

are shown in Fig. 6.12. The signal efficiencies, number of signal events and total background for the example mass hypothesis after selection cuts and cuts on both di-jet mass sum and difference (two-dimensional cut) are given in Table 6.4. From the fit of the mass distributions in Fig. 6.12, a precision of $\delta\Sigma = 525$ MeV and $\delta\Delta = 730$ MeV can be achieved for the Higgs boson mass sum and mass difference, respectively, from which δm_{A}, δm_{H} are found to be 0.45 GeV. The statistical relative error on the topological cross section is calculated as 3.0%.

6.3 Analysis of the Mass Grid

The analysis described in Sections 6.1 and 6.2 is extended for different Higgs mass hypotheses. The signal samples described in Table 5.1 are simulated for Higgs boson mass grid shown in Fig. 5.1 at $\sqrt{s} = 500$ and 800 GeV with an assumed luminosity of 500 fb^{-1}.

The signal efficiencies, number of signal events and total background for different Higgs mass hypotheses after selection cuts, described in previous sections, and cuts on both di-jet mass sum and mass difference are given in Table 6.5. The signal efficiency varies between 36% and 48% for both centre of mass energies after selection cuts and between 22% and 41% after two-dimensional di-jet mass cut.

Table 6.6 summarises the statistical accuracy of the Higgs mass measurements. It is $\sim$ 200 (400) MeV for the Higgs pair production far above kinematic threshold and degrades to $\sim$ 500 MeV (1 GeV) with approaching kinematic limit at $\sqrt{s} = 500$ (800) GeV, respectively. At the same time the statistical errors for the $\sqrt{s} = 800$ GeV are in general twice bigger than those for the 500 GeV.

$\sqrt{s}$ [GeV]	(m_{H},m_{A}) [GeV]	Sig. eff. [%]		Number of sig. events		Tot. backgr.	
		sel.cuts	2-d.cut	sel.cuts	2-d.cut	sel.cuts	2-d.cut
500	(150,100)	43	31	5805	4196	1960	132
	(200,100)	41	26	4194	2661		129
	(250,100)	36	28	2422	1851		182
	(150,140)	48	39	5469	4518		301
	(150,150)	45	41	4944	4407		144
	(200,150)	42	27	3192	2036		130
	(250,150)	36	22	1534	960		156
	(200,200)	37	33	1691	1510		185
800	(300,150)	43	33	1825	1427	488	38
	(290,200)	46	36	1763	1398		53
	(300,250)	45	36	1366	1101		13
	(300,300)	44	35	1011	823		26
	(350,350)	37	31	339	277		58
	(400,150)	37	26	969	678		27
	(400,200)	40	28	833	584		41
	(400,250)	40	28	597	414		49

Table 6.5: *The signal efficiencies, the number of signal and total background events after selection cuts and after cuts on both di-jet mass sum and mass difference (2-dimensional cut) in the* $\mathrm{HA} \to \mathrm{b\bar{b}b\bar{b}}$ *channel at* $\sqrt{s} = 500$ *and 800 GeV with an assumed luminosity of 500 fb*$^{-1}$*. The signal expectations are quoted for* $\sin^2(\beta-\alpha) = 1$ *and the Higgs boson branching fractions of* $\mathrm{Br}(\mathrm{H} \to \mathrm{b\bar{b}}) = \mathrm{Br}(\mathrm{A} \to \mathrm{b\bar{b}}) = 90\%$.

$\sqrt{s} = 500$ GeV		$\sqrt{s} = 800$ GeV	
(m_{H},m_{A}) [GeV]	δm_{H}, δm_{A} [GeV]	(m_{H},m_{A}) [GeV]	δm_{H}, δm_{A} [GeV]
(150,100)	0.12	(300,150)	0.33
(200,100)	0.15	(290,200)	0.33
(250,100)	0.27	(300,250)	0.45
(150,140)	0.13	(300,300)	0.48
(150,150)	0.12	(350,350)	0.97
(200,150)	0.26	(400,150)	0.47
(250,150)	0.48	(400,200)	0.74
(200,200)	0.31	(400,250)	0.99

Table 6.6: *Precision on the Higgs boson mass determination for the* $\mathrm{HA} \to \mathrm{b\bar{b}b\bar{b}}$ *process with different Higgs mass hypotheses at* $\sqrt{s}$ *= 500 and 800 GeV. Numbers are quoted for* $\sin^2(\beta-\alpha) = 1$ *and Higgs boson branching fractions of* $\mathrm{Br}(\mathrm{H} \to \mathrm{b\bar{b}}) = \mathrm{Br}(\mathrm{A} \to \mathrm{b\bar{b}}) = 90\%$*.*

$\sqrt{s} = 500$ GeV			$\sqrt{s} = 800$ GeV		
(m_{H},m_{A}) [GeV]	$\delta\sigma/\sigma$ [%]	S	(m_{H},m_{A}) [GeV]	$\delta\sigma/\sigma$ [%]	S
(150,100)	1.6	63	(300,150)	2.7	37
(200,100)	2.0	50	(290,200)	2.7	37
(250,100)	2.4	42	(300,250)	3.0	33
(150,140)	1.5	67	(300,300)	3.5	29
(150,150)	1.5	67	(350,350)	6.6	15
(200,150)	2.3	43	(400,150)	3.9	26
(250,150)	3.5	29	(400,200)	4.3	23
(200,200)	2.7	37	(400,250)	5.2	19

Table 6.7: *Relative statistical uncertainty in the topological cross section measurements and discovery significance S for the* $\mathrm{HA} \to \mathrm{b\bar{b}b\bar{b}}$ *process with different Higgs mass hypotheses at* $\sqrt{s}$ *= 500 and 800 GeV. Numbers are quoted for* $\sin^2(\beta-\alpha) = 1$ *and the Higgs boson branching fractions of* $\mathrm{Br}(\mathrm{H} \to \mathrm{b\bar{b}}) = \mathrm{Br}(\mathrm{A} \to \mathrm{b\bar{b}}) = 90\%$*.*

The statistical uncertainties on the topological cross sections are reported in Table 6.7. The topological cross sections can be measured with relative precision between 1.5% and 6.6%. A discovery significances S, defined as the number of Gaussian standard deviations of a signal excess over the background:

$$S = \frac{N_S}{\sqrt{N_S + N_B}}, \tag{6.4}$$

is presented in Table 6.7 as well. For all investigated Higgs boson mass combinations the discovery can be made with more than 5σ significance. However, approaching the kinematic limit, the discovery significance drops drastically.

For several Higgs mass combinations the distributions of the mass sum and mass difference after all selection cuts and kinematic fit at $\sqrt{s} = 500$ GeV are presented in Fig. 6.13. A final di-jet mass sum and mass difference after a cut on di-jet mass difference and mass sum, respectively, are shown in Fig. 6.14. Similar distributions for $\sqrt{s} = 800$ GeV are shown in Fig. 6.15, 6.16.

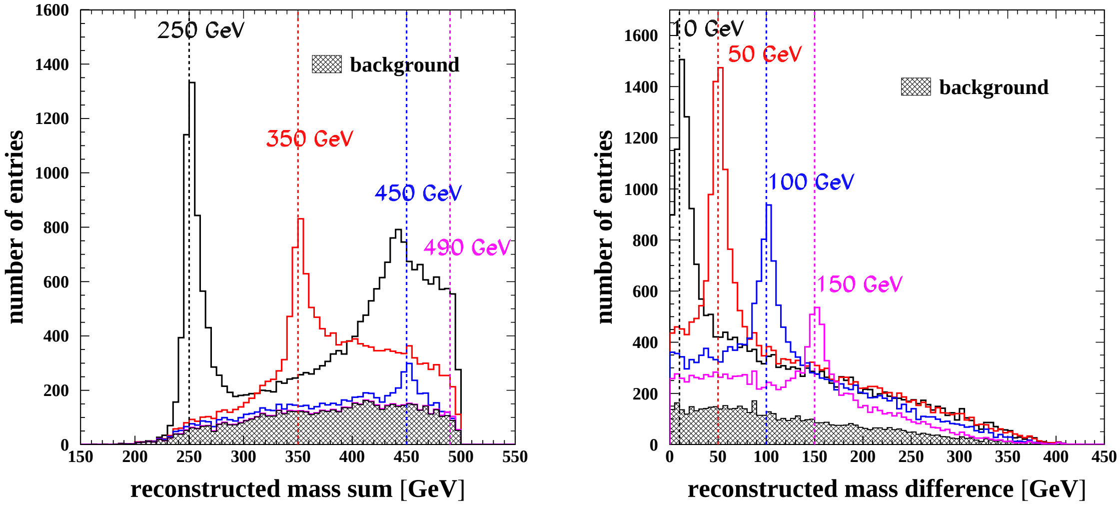

Figure 6.13: *Distributions of the di-jet mass sum (left figure) and di-jet mass difference (right figure) after kinematic fit in the* HA → $\mathrm{b\bar{b}b\bar{b}}$ *channel for different Higgs boson mass hypotheses at* $\sqrt{s} = 500$ *GeV.*

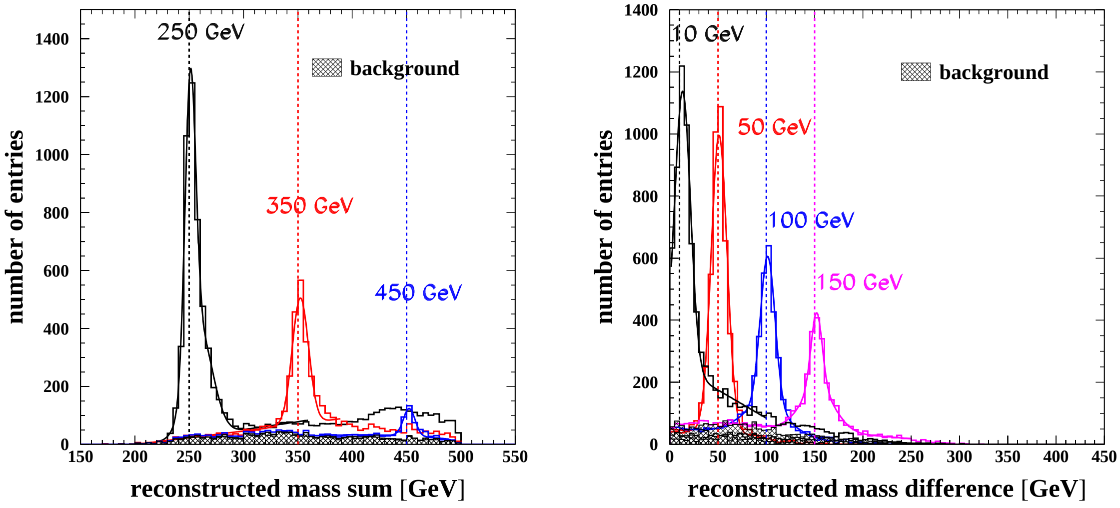

Figure 6.14: *Distributions of the di-jet mass sum (left figure) and di-jet mass difference (right figure) after kinematic fit and cut on di-jet mass difference and di-jet mass sum, respectively, in the* HA → $\mathrm{b\bar{b}b\bar{b}}$ *channel for different Higgs boson mass hypotheses at* $\sqrt{s} = 500$ *GeV.*

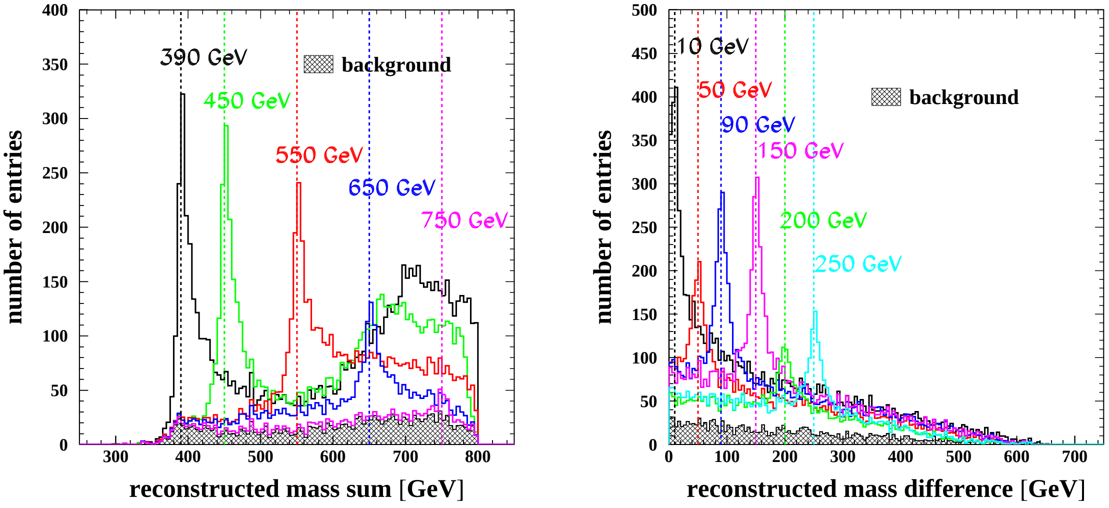

Figure 6.15: *Distributions of the di-jet mass sum (left figure) and di-jet mass difference (right figure) after kinematic fit in the* $\mathrm{HA} \rightarrow \mathrm{b\bar{b}b\bar{b}}$ *channel for different Higgs boson mass hypotheses at* $\sqrt{s} = 800$ *GeV.*

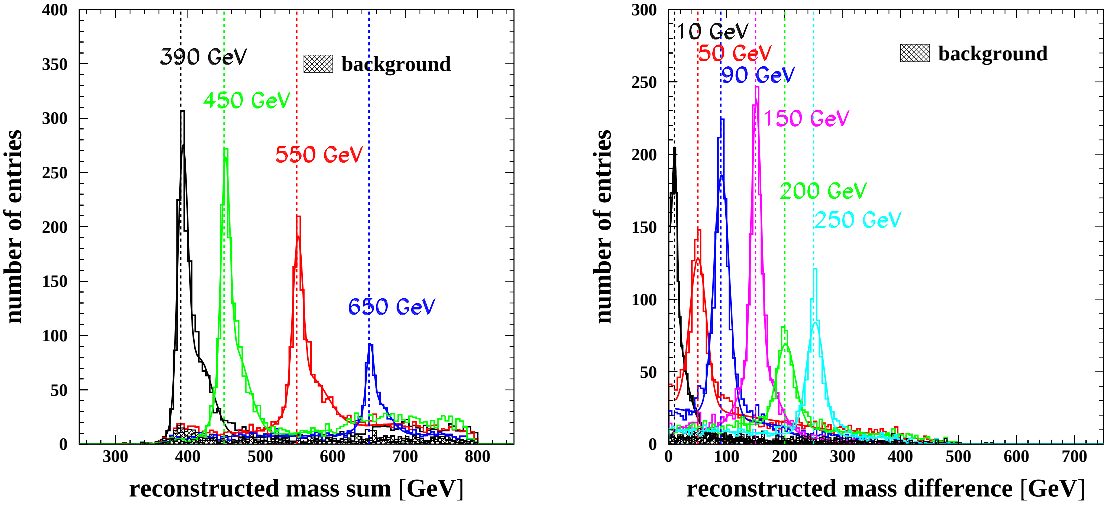

Figure 6.16: *Distributions of the di-jet mass sum (left figure) and di-jet mass difference (right figure) after kinematic fit and cut on di-jet mass difference and di-jet mass sum, respectively, in the* $\mathrm{HA} \rightarrow \mathrm{b\bar{b}b\bar{b}}$ *channel for different Higgs boson mass hypotheses at* $\sqrt{s} = 800$ *GeV.*

6.4 The Case of Mass Degenerate HA Production

A big part of SUSY parameter space leads to degenerate H and A Higgs boson masses. To investigate a discovery potential of such Higgs bosons close to the kinematic threshold at $\sqrt{s} = 800$ GeV, the following six signal hypotheses (m_{H},m_{A}), where m_{H}=m_{A}, are analysed:

- (300,300) GeV,
- (350,350) GeV,
- (360,360) GeV,
- (370,370) GeV,
- (380,380) GeV,
- (390,390) GeV.

Their cross sections and expected numbers of events are presented in Section 5.1. After all selection cuts and two-dimensional cut on di-jet mass sum and mass difference, described above, the statistical errors on the topological cross sections and the discovery significances are summarised in Table 6.8. The final distributions of the di-jet mass sum and mass difference for (m_{H},m_{A}) = (300,300) GeV are shown in Fig. 6.17. The mass difference equals zero for this mass hypothesis, therefore the distribution was mirrored to the negative values and then fitted.

The discovery significance as a function of m_{H} (=m_{A}) is presented in Fig. 6.18 (left figure). The red line corresponds to 5σ level. Approaching the kinematic limit, the significance drops below 5σ for the Higgs mass between 380 GeV and 390 GeV. The whole range of the significances for different Higgs masses is from 28.2 to 3.4.

Until now it was assumed that $\sin^2(\beta - \alpha) = 1$, i.e. maximal allowed cross section for the process $\mathrm{e}^+\mathrm{e}^- \rightarrow \mathrm{HA}$. The coefficient η^2 which relates a cross section, for which the 5σ discovery is guaranteed, to maximal allowed cross section, can be found from (6.4):

$$\frac{N_S \cdot \eta^2}{\sqrt{N_S \cdot \eta^2 + N_B}} = 5, \tag{6.5}$$

and the following expression for η^2 can be derived:

$$\eta^2 = \frac{25 + 5 \cdot \sqrt{25 + 4N_B}}{2N_S}. \tag{6.6}$$

(m_{H},m_{A}) [GeV]	$\delta\sigma/\sigma$ [%]	S
(300,300)	3.5	28.2
(350,350)	6.6	15.1
(360,360)	9.2	10.8
(370,370)	11.6	8.6
(380,380)	16.0	6.2
(390,390)	29.1	3.4

Table 6.8: *Relative statistical uncertainties on the topological cross section measurements and discovery significances S for the degenerate H and A Higgs pair production at* $\sqrt{s} = 800$ *GeV. Numbers are quoted for* $\sin^2(\beta - \alpha) = 1$ *and the Higgs boson branching fractions of* $\mathrm{Br(H \rightarrow b\bar{b}) = Br(A \rightarrow b\bar{b})} = 90\%$*.*

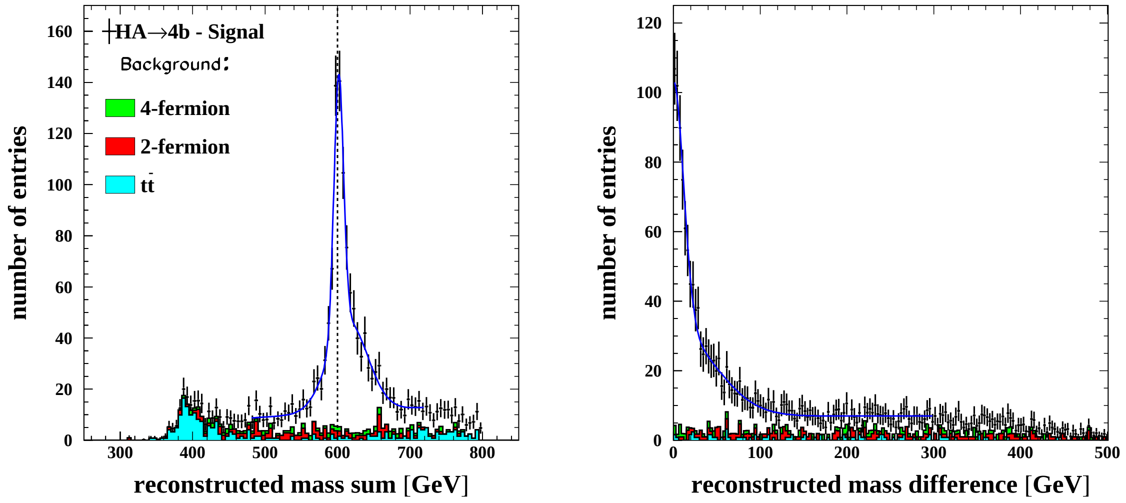

Figure 6.17: *Distribution of the di-jet mass sum after all selection cuts, kinematic fit and a cut on di-jet mass difference (left figure). Distribution of the di-jet mass difference after all selection cuts, kinematic fit and a cut on di-jet mass sum (right figure). Both distributions are for the degenerate Higgs boson mass hypothesis* $(m_{\mathrm{H}},m_{\mathrm{A}})$ *= (300,300) GeV at* $\sqrt{s}$ *= 800 GeV.*

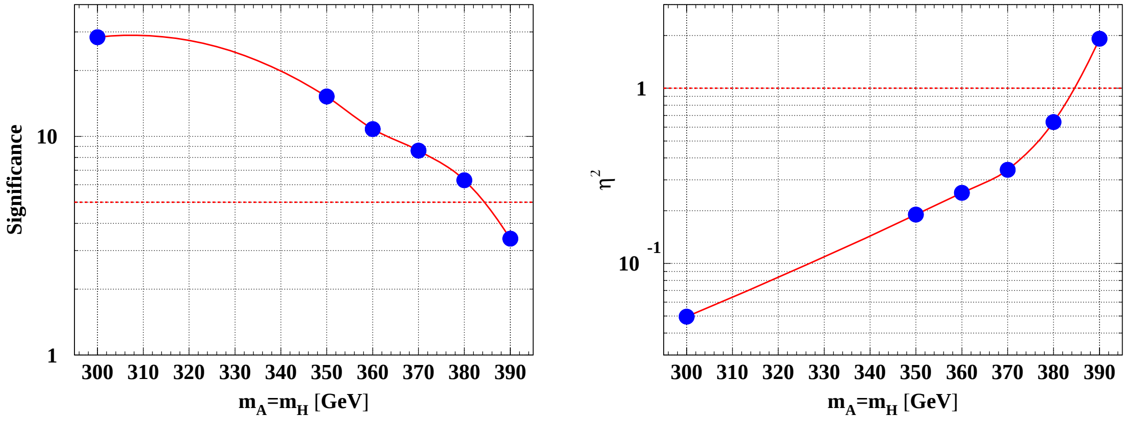

Figure 6.18: *Discovery significance as a function of the Higgs boson mass (assuming* $m_{\mathrm{H}} = m_{\mathrm{A}}$*) in the* $\mathrm{HA} \rightarrow \mathrm{b\bar{b}b\bar{b}}$ *channel at* $\sqrt{s}$ *= 800 GeV (left figure).* η^2 *as a function of the Higgs boson mass for the* 5σ *discovery requirement (right figure). Further explanations see in text.*

The 5σ discovery reach, i.e. η^2 as a function of m_{H} ($=m_{\mathrm{A}}$) is shown in Fig. 6.18 (right figure). The further from the kinematic limit, the lower can be cross section, relative to maximal allowed one, to reach a 5σ discovery level.

6.5 Higgs Mass Separation

To investigate the possibility of separating H and A Higgs boson masses if they are almost mass degenerate, a minigrid of such mass combinations is generated at $\sqrt{s} = 500$ GeV with an assumed integrated luminosity of 500 fb^{-1} (Table 5.3). Fig. 6.19 shows several di-jet mass sum and di-jet mass difference combinations after selection cuts, kinematic fit and a cut on di-jet mass difference and mass sum, respectively. From this figure it can be qualitatively deduced that the mass sum or mass difference can be distinguished with precision of ∼8 GeV. However, more systematic study is needed.

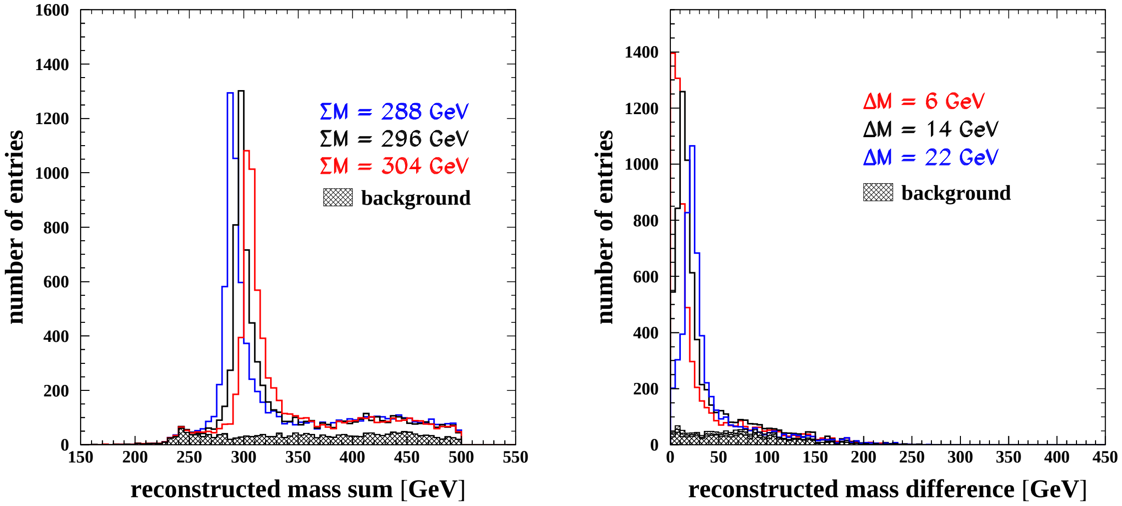

Figure 6.19: *Several Higgs mass combinations (m_{H},m_{A}) with close mass sums (left figure) and mass differences (right figure) at $\sqrt{s} = 500$ GeV. The distributions are received after selection cuts, kinematic fits and cuts on di-jet mass differences and mass sums, respectively.*

6.6 Application of the General Analysis

The general analysis, described in the previous sections, can be applied to investigate MSSM Higgs boson pair production in a certain model. In the next section the process $e^+e^- \to H_3H_2 \to b\bar{b}b\bar{b}$ will be analysed in two CP violating MSSM scenarios. Then, the general analysis will be applied for the SPS 1a point for SUSY searches.

6.6.1 CP Violating Scenarios

Two CP violating scenarios are chosen for the analysis. The first scenario is analysed at $\sqrt{s} = 500$ GeV, the second at 800 GeV with an assumed luminosity of 500 fb^{-1}. The MSSM parameters of these scenarios are summarised in Table 5.4 of Section 5.2. For

Cut	Tot. BG	H_1Z	H_2Z	Sig. eff. [%]	Signal
	9025337	17315	3022	100.0	6305
1	6055441	16640	2927	98.95	6239
2	2692591	14682	2612	93.61	5902
3	1372217	12853	2286	87.80	5536
4	344537	6702	1840	81.74	5154
5	315106	6661	1821	79.87	5036
6	273405	6511	1775	72.64	4580
7	155107	5503	1520	59.97	3781
8	47799	4616	1271	58.72	3702
9	3463	1184	319	47.56	2999

Table 6.9: *Number of remaining background events, signal efficiencies and number of expected signal events after each of the nine cuts for the first CP violating scenario with Higgs masses* (m_{H_3}, m_{H_2}) *= (154.7, 140.5) GeV in the* $H_3H_2 \to b\bar{b}b\bar{b}$ *channel analysed at* $\sqrt{s}$ *= 500 GeV with an assumed luminosity of 500 fb*$^{-1}$*. The first column is the number of the cut, the second one is the number of total background events, including* H_iZ *events.*

$\sqrt{s} = 500$ GeV the scenario is arbitrary chosen with $\tan\beta = 19$ and $m_{H^+} = 164$ GeV for which $m_{H_2} = 140.5$ GeV and $m_{H_3} = 154.7$ GeV. The CP violating phase $\arg(A_t) = 70°$. The second scenario, analysed at $\sqrt{s} = 800$ GeV, has parameters $\tan\beta = 5$ and $m_{H^+} = 300$ GeV. The Higgs masses are $m_{H_2} = 282.2$ GeV and $m_{H_3} = 292.2$ GeV. The CP violating phase of this scenario is small ($\arg(A_t) = 0.01°$).

The generated signal and background samples are summarised in Section 5.2. In addition to the SM background samples used in general analysis, it is possible to estimate the background coming from $e^+e^- \to H_iZ^0 \to b\bar{b}q\bar{q}$ (i=1,2,3) processes. However, the cross sections of these background contributions are several orders smaller than for SM background sources. Therefore, only H_1Z^0 and H_2Z^0 are included into the analysis.

The numbers of expected signal and background events, remaining after selection cuts

Cut	Tot. BG	H_1Z	H_2Z	Sig. eff. [%]	Signal
	4072869	8360	9	100.0	926
1	2381888	5658	8	97.44	902
2	1011374	4163	8	94.34	874
3	546006	3809	7	84.24	780
4	90659	52	5	80.89	749
5	78670	52	5	79.21	733
6	54856	50	5	70.33	651
7	12327	40	4	67.96	629
8	496	5	3	45.02	417

Table 6.10: *Number of remaining background events, signal efficiencies and number of expected signal events after each of the eight cuts for the second CP violating scenario with Higgs masses* (m_{H_3}, m_{H_2}) *= (292.2, 282.2) GeV in the* $H_3H_2 \to b\bar{b}b\bar{b}$ *channel analysed at* $\sqrt{s}$ *= 800 GeV with an assumed luminosity of 500 fb*$^{-1}$*. The first column is the number of the cut, the second one is the number of total background events, including* H_iZ *events.*

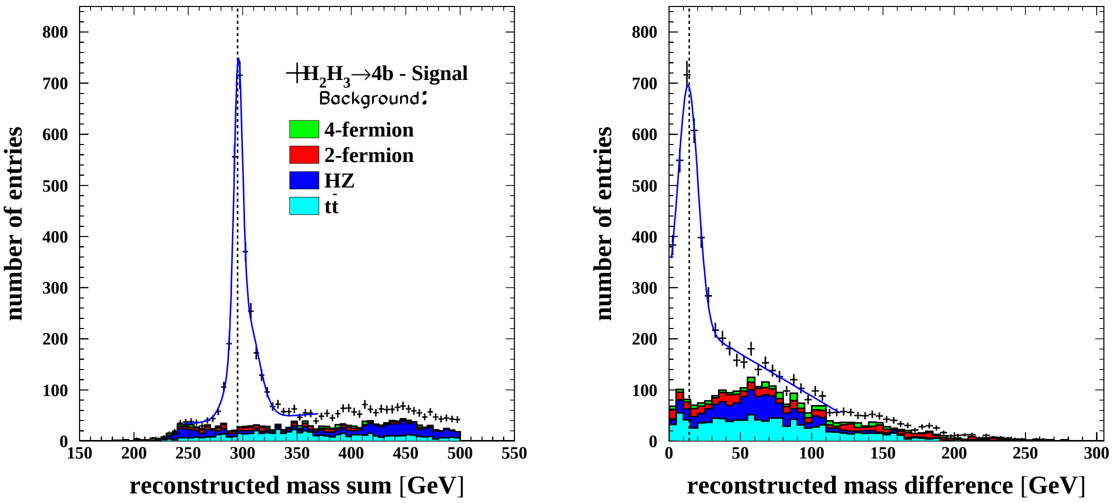

Figure 6.20: *Distribution of the di-jet mass sum after selection cuts, kinematic fit and a cut on di-jet mass difference (left figure). Distribution of the di-jet mass difference after selection cuts, kinematic fit and a cut on di-jet mass sum (right figure). Both distributions are in the* $H_3H_2 \rightarrow b\bar{b}b\bar{b}$ *channel for the first CP violation scenario with Higgs boson masses* (m_{H_3},m_{H_2}) *= (154.7, 140.5) GeV analysed at* $\sqrt{s} = 500$ *GeV.*

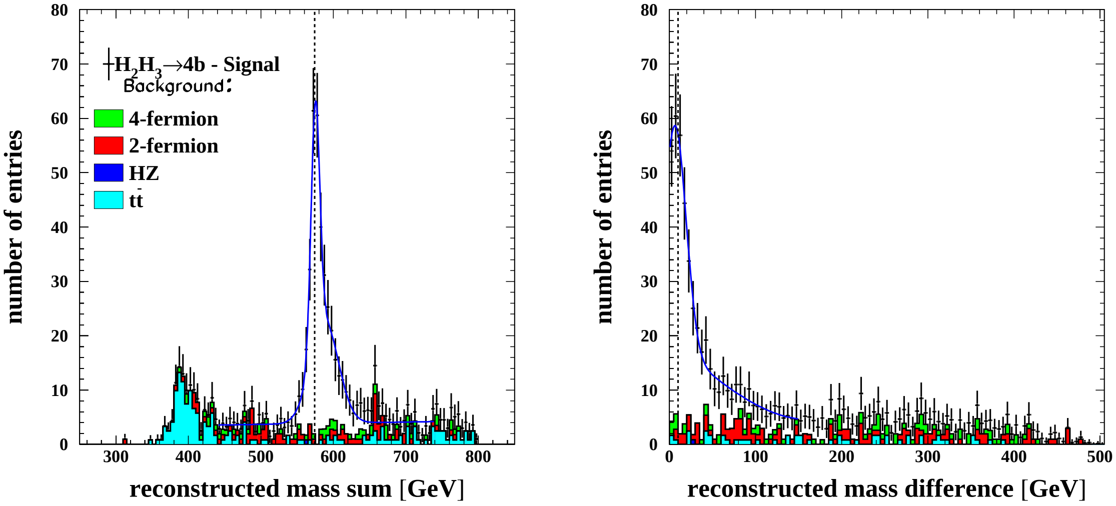

Figure 6.21: *Distribution of the di-jet mass sum after selection cuts, kinematic fit and a cut on di-jet mass difference (left figure). Distribution of the di-jet mass difference after selection cuts, kinematic fit and a cut on di-jet mass sum (right figure). Both distributions are in the* $H_3H_2 \rightarrow b\bar{b}b\bar{b}$ *channel for the second CP violation scenario with Higgs boson masses* (m_{H_3},m_{H_2}) *= (292.2, 282.2) GeV analysed at* $\sqrt{s} = 800$ *GeV.*

	Scenario N1 at 500 GeV		Scenario N2 at 800 GeV	
	selection cuts	2-dim. cut	selection cuts	2-dim. cut
Signal efficiency [%]	48	39	45	33
Number of signal events	2999	2477	417	302
Total background	3463	400	496	28

Table 6.11: *The signal efficiencies, the number of signal and total background events after selection cuts and after cuts on both di-jet mass sum and difference (2-dimensional cut) for the first CP violating scenario with mass combination* (m_{H_3},m_{H_2}) = *(154.7, 140.5) GeV analysed at* $\sqrt{s}$ = *500 GeV and the second CP violating scenario with* (m_{H_3},m_{H_2}) = *(292.2, 282.2) GeV analysed at* $\sqrt{s}$ = *800 GeV. An assumed luminosity is 500* fb^{-1}.

described in Sections 6.1 and 6.2, and signal efficiencies for the chosen CP violating scenarios analysed at $\sqrt{s}$ = 500 GeV and 800 GeV are presented in Tables 6.9 and 6.10, respectively. The total background includes the H_iZ events. The cutflow tables show that a cut on the thrust value is very effective against H_iZ background after which H_1Z events are two times reduced for the first scenario and 73 times for the second one.

Final distributions of the di-jet mass sum and di-jet mass difference after a cut on di-jet mass difference and mass sum, respectively, are shown in Fig. 6.20 and 6.21. The signal efficiencies, number of signal events and total background after selection cuts and two-dimensional cuts on di-jet mass sum and mass difference for both scenarios are given in Table 6.11. From the fit of mass distributions in Fig. 6.20 and 6.21, a precision of $\delta\Sigma$ = 219 MeV (860 MeV) and $\delta\Delta$ = 291 MeV (1.33 GeV) for the first (second) CP violating scenario can be achieved for the Higgs boson mass sum and mass difference, respectively. The Higgs boson masses can be measured with precision $\delta m_{\mathrm{H}_2} = \delta m_{\mathrm{H}_3}$ = 182 MeV (792 MeV) for the first (second) scenario. The statistical relative error on the topological cross section is calculated as 2.2% for the first scenario and 6.0% for the second one.

6.6.2 Analysis of the SPS 1a Benchmark Point

In this section the analysis will be applied to the SPS 1a benchmark point for SUSY searches [94]. This scenario was extensively investigated in the LHC/ILC studies [96, 97] and others. The SPS 1a point with $\tan\beta = 10$ and m_{A^0} = 394.7 GeV lies just on the boundary of the MSSM parameter space covered by the LHC (Fig. 3.5), between the potential observation of h^0 only and h^0 with $\mathrm{H}^\pm$. As was found, ATLAS can observe h^0 with m_h = 115 GeV in associated tth production (gg → tth) with $\Delta m_\mathrm{h} \approx 100$ MeV and $\Delta\sigma(\mathrm{tth}, \mathrm{h} \to \mathrm{bb})/\sigma(\mathrm{tth}, \mathrm{h} \to \mathrm{bb}) =$ 26%. The possibility of $\mathrm{H}^\pm$ observation should be checked. Therefore, it is interesting to check the capability of the ILC to discover the heavy neutral MSSM Higgs bosons for this point, where the LHC will not be able to see these particles. It will illustrate a complementarity of the ILC results in SUSY Higgs physics to the LHC.

The parameters for the SPS 1a point are summarised in Section 5.3. Neutral Higgs masses are m_{h^0} = 113.7 GeV, m_{A^0} = 394.7 GeV, m_{H^0} = 394.9 GeV. The analysis is done for the centre of mass energy of 1 TeV and an assumed integrated luminosity of 1000 fb^{-1}. The number of expected signal events is 640. The background from hZ process is not taken into account due to its small cross section (17 fb) in comparison with SM background sources (Table 5.7).

Modified selection criteria are used to separate signal from background at $\sqrt{s}$ = 1000 GeV in comparison with 500 and 800 GeV. Each event is required to pass the following cuts:

1. The visible energy E_{vis} must be greater than 790 GeV.
2. Each event is forced into four jets using the DURHAM algorithm and the number of tracks per jet is required to be greater than two.
3. To separate centrally produced H and A bosons from the WW and ZZ events, peaking in forward/backward direction, cut on the polar angle of the thrust vector, $|\cos\theta_T| < 0.8$ is applied.
4. Further suppression of the WW and ZZ backgrounds is achieved by requiring the event thrust value T to be less than 0.82.
5. Two-fermion background is suppressed by applying a cut on the DURHAM jet resolution parameter, $\log_{10} y_{34} \geq -2.5$.
6. The background from $e^+e^- \to t\bar{t}$ events is further reduced by applying a cut on the jet resolution parameter, $\log_{10} y_{56} \leq$ -2.9.
7. The value of b-tag quantity B_{12} has to be greater than 0.6.
8. The value of B_{34} is required to be greater than 0.05.

The numbers of expected signal and background events, retained after selection, and signal efficiencies for the SPS 1a point with (m_{H},m_{A}) = (394.9, 394.7) GeV at $\sqrt{s}$ = 1000 GeV are presented in Table 6.12. The Fig. 6.22 and 6.23 show the distributions of the selection variables for the different sources of background and for the signal at $\sqrt{s}$ = 1000 GeV. The signal efficiencies, number of signal events and total background after selection cuts and a two-dimensional cut on di-jet mass sum and mass difference are given in Table 6.13.

The results presented in Fig. 6.24 are the di-jet mass sum and mass difference after the selection cuts, kinematic fit and a cut on the di-jet mass difference and mass sum, respectively. The signal efficiency is 29% after selection cuts and 24% after cuts on both di-jet mass sum and difference. The H and A Higgs masses can be measured with precision of 1.3 GeV. The topological cross section can be measured with the relative statistical uncertainty of 9%.

Cut	Tot. BG	ZZ	WW	2-ferm.	$t\bar{t}$	Sig. eff. [%]	Signal
	5397316	9816	1741000	3533000	113500	100.0	640
1	2792330	7842	1143833	1542004	98651	94.94	608
2	1377114	6576	663638	615988	90912	93.11	596
3	745844	6016	224608	448635	66585	79.69	510
4	49758	15	21391	22767	5585	65.52	419
5	34575	10	15466	13567	5532	61.46	393
6	22926	9	10493	11430	994	49.83	319
7	4022	7	1716	1677	622	46.96	301
8	147	1	46	75	25	28.63	183

Table 6.12: *Number of remaining background events, signal efficiency and number of expected signal events after each of the eight cuts for the SPS 1a point with (m_{H},m_{A}) = (394.9, 394.7) GeV in the* $\text{HA} \to b\bar{b}b\bar{b}$ *channel at $\sqrt{s}$ = 1000 GeV with an assumed luminosity of 1000 fb^{-1}. The first column is the number of the cut, the second one is the number of total background events.*

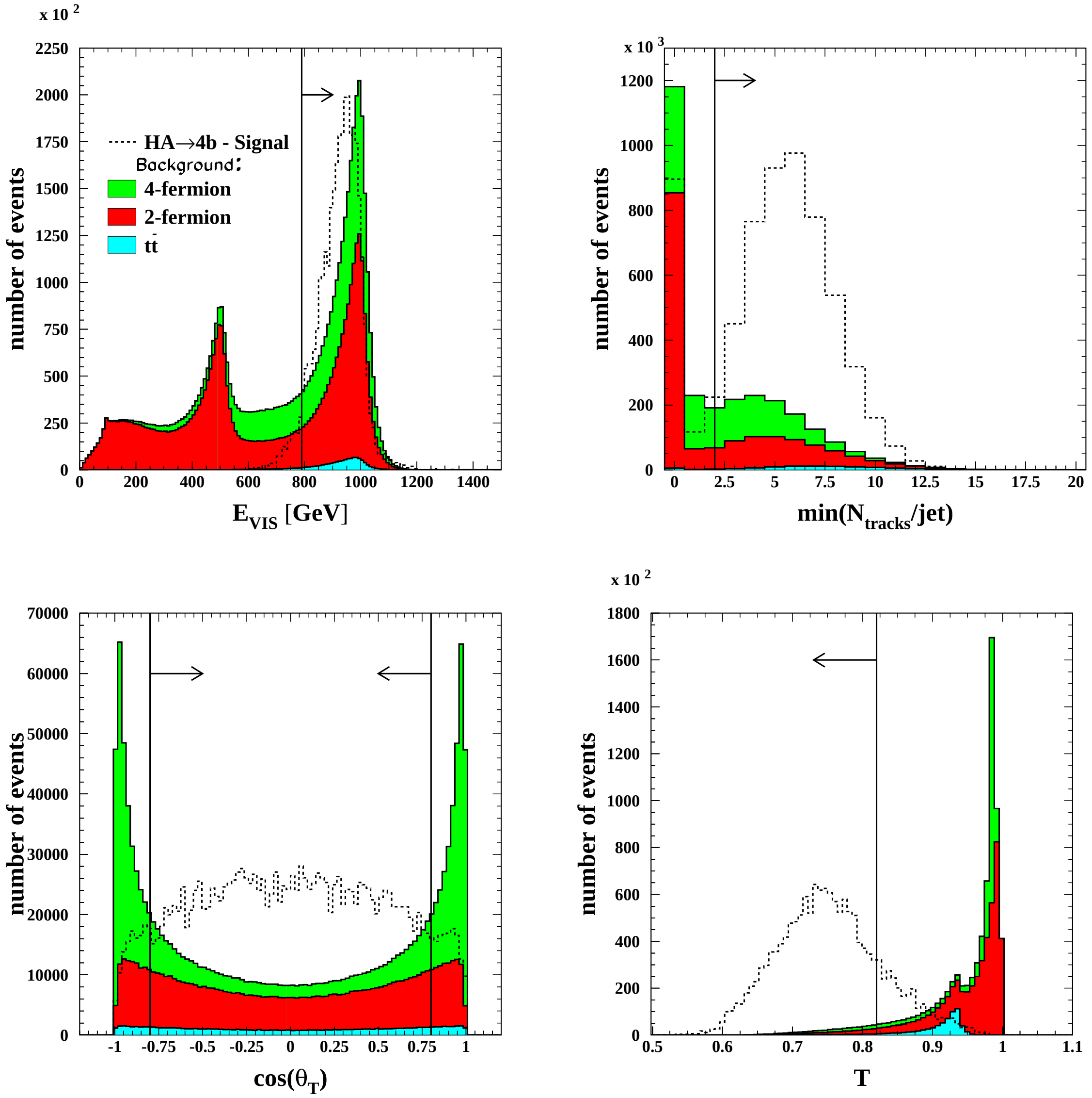

Figure 6.22: *Distributions of the selection variables (visible energy* E_{vis}*, number of tracks per jet* N_{tracks}/jet*,* $\cos\theta_T$*, thrust value* T*) at* $\sqrt{s} = 1000$ *GeV. The signal distributions for the* $\mathrm{HA} \rightarrow \mathrm{b\bar{b}b\bar{b}}$ *channel for the SPS 1a point with* $(m_{\mathrm{H}},m_{\mathrm{A}}) = (394.9,\ 394.7)$ *GeV are shown with arbitrary normalisation. The vertical lines with arrows indicate cuts, imposed on these variables. The distributions are shown after all cuts preceding the current variable.*

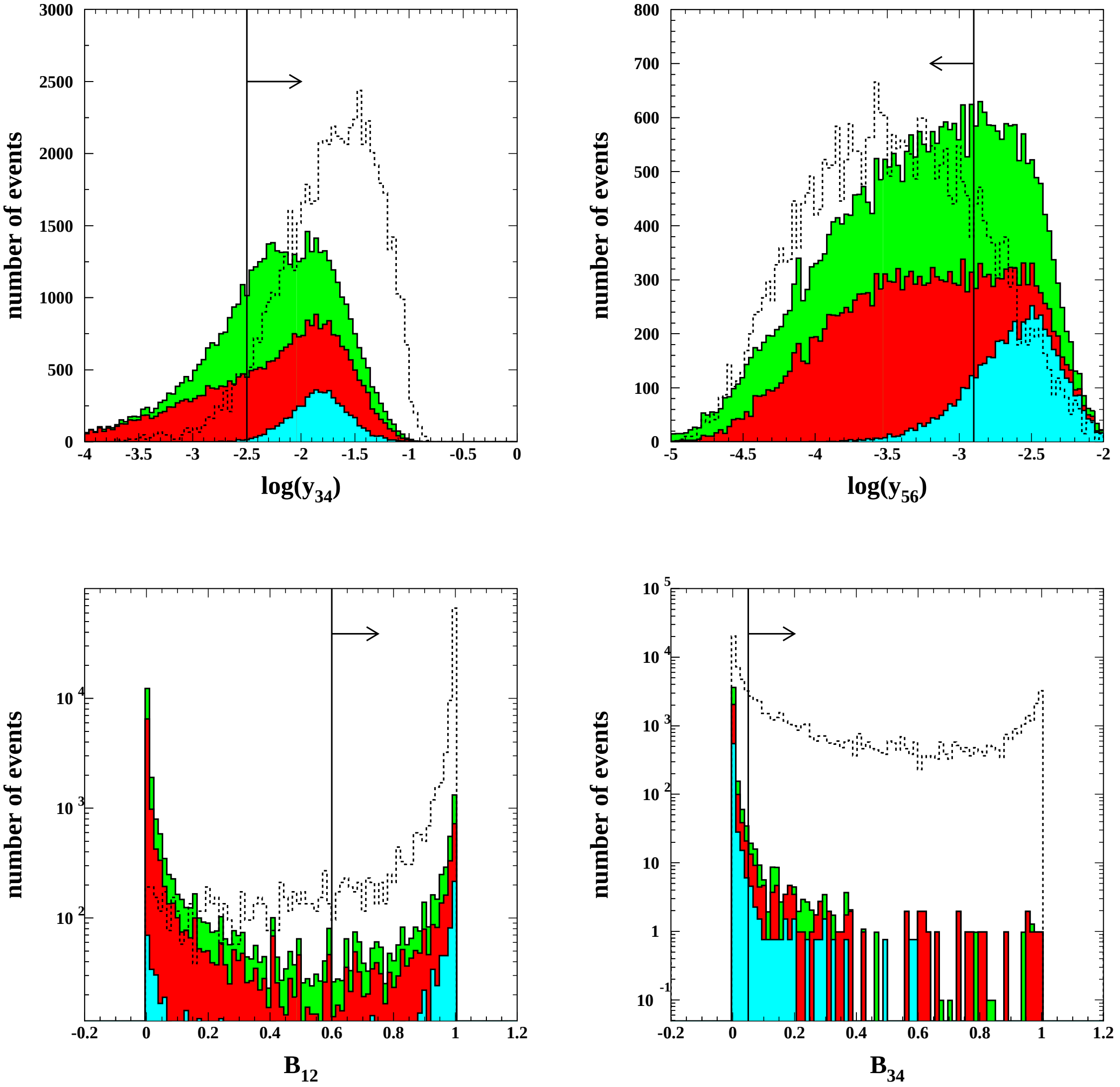

Figure 6.23: *Distributions of the selection variables (jet resolution parameters* $\log_{10} y_{34}$, $\log_{10} y_{56}$ *and b-tag variables* B_{12} *and* B_{34}*) at* $\sqrt{s}$ = *1000 GeV. The signal distributions for the* HA → $\mathrm{b\bar{b}b\bar{b}}$ *channel for the SPS 1a point with (*m_{H},m_{A}*) = (394.9, 394.7) GeV are shown with arbitrary normalisation. The vertical lines and arrows indicate cuts, imposed on these variables. The distributions are shown after all cuts preceding the current variable.*

	selection cuts	2-dim. cut
Signal efficiency [%]	29	24
Number of signal events	183	153
Total background	148	42

Table 6.13: *The signal efficiencies, the number of signal and total background events after selection cuts and after cuts on both di-jet mass sum and mass difference (2-dimensional cut) for the SPS 1a point with* (m_{H},m_{A}) *= (394.9, 394.7) GeV at* $\sqrt{s} = 1000\,\mathrm{GeV}$. *An assumed luminosity is 1000 fb*$^{-1}$.

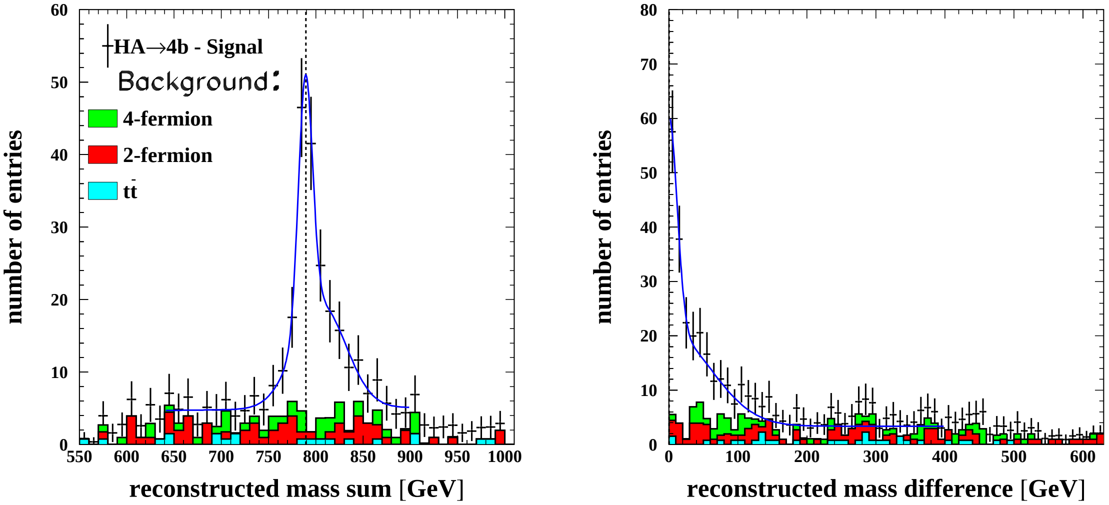

Figure 6.24: *Distribution of the di-jet mass sum after all selection cuts, kinematic fit and cut on di-jet mass difference (left figure). Distribution of the di-jet mass difference after all selection cuts, kinematic fit and cut on di-jet mass sum (right figure). Both distributions are in the* $\mathrm{HA} \to \mathrm{b\bar{b}b\bar{b}}$ *channel for the SPS 1a benchmark point with* (m_{H},m_{A}) *= (394.9, 394.7) GeV at* $\sqrt{s} = 1$ *TeV.*

6.7 Summary

The potential of a future Linear Collider detector for the determination of the MSSM Higgs boson properties exploiting associated Higgs boson pair production followed by the Higgs decays to b-quarks was investigated. It is shown that using the $\mathrm{HA} \to \mathrm{b\bar{b}b\bar{b}}$ channel the Higgs boson masses can be measured with an accuracy of up to several hundred MeV for Higgs pair production far above the kinematic threshold. The precision deteriorates to about 1 GeV when approaching the kinematic threshold. The topological cross section $\sigma(\mathrm{e^+e^-} \to \mathrm{HA} \to \mathrm{b\bar{b}b\bar{b}})$ can be measured with a relative statistical uncertainty varying between 1.5% and 6.6%.

The 5σ discovery limit corresponds to a Higgs mass of around 385 GeV for the degenerate Higgs boson masses in the $\mathrm{HA} \to \mathrm{b\bar{b}b\bar{b}}$ channel at $\sqrt{s} = 800$ GeV with an integrated luminosity of 500 fb^{-1}.

The analysis was applied to the process $\mathrm{e^+e^-} \to \mathrm{H_3H_2} \to \mathrm{b\bar{b}b\bar{b}}$ in the CP violating MSSM scenarios. Two such scenarios with ($m_{\mathrm{H_3}}$, $m_{\mathrm{H_2}}$) = (154.7, 140.5) GeV and (292.2, 282.2) GeV were investigated at $\sqrt{s} = 500$ GeV and 800 GeV, respectively. The heavy neutral Higgs masses can be measured with precision of 200 MeV for first CP violating scenario and 800 MeV for the second one. The statistical error on the topological cross section of the process $\mathrm{e^+e^-} \rightarrow \mathrm{H_3H_2} \rightarrow \mathrm{b\bar{b}b\bar{b}}$ is 2.2% for the first scenario and 6% for the second one.

The SPS 1a point for SUSY searches with $(m_{\mathrm{H}}, m_{\mathrm{A}}) = (394.9,\ 394.7)$ GeV was analysed at $\sqrt{s} = 1$ TeV with an assumed luminosity of 1000 fb^{-1}. The masses of heavy neutral Higgs bosons can be measured with precision of 1.3 GeV. The topological cross section of the process $\mathrm{e^+e^-} \rightarrow \mathrm{HA} \rightarrow \mathrm{b\bar{b}b\bar{b}}$ can be measured with the relative statistical uncertainty of 9%.

Chapter 7

Sensitivity to Parameters of the CP Violating MSSM

As was discussed in Section 1.2.4, the CP violation in the MSSM Higgs sector is predominantly mediated by the CP-odd phase of the soft SUSY-breaking trilinear coupling of the Higgs boson to the top and bottom squarks, $\arg(A_t)$ and $\arg(A_b)$, at the one-loop level, with $\arg(m_{\tilde{g}})$ entering at the two-loop level. The measurement of CP vioalting phases $\arg(A_t)$ and $\arg(A_b)$ is important because it will allow to reveal the CP violating effects in the MSSM Higgs sector, which can provide more CP violation in order to explain the observed baryon asymmetry (see Section 1.1.7). Moreover, these phases will influence on CP conserving observables such as the branching ratios of $\tilde{t}_1$ and $\tilde{b}_1$ decays in a large region of the MSSM parameter space [98].

Till now, only the possibility of the measurement of the absolute values of SUSY parameters like A_t and A_b has been studied by a global fit of measured masses, branching ratios and production cross sections. A_t and A_b are expected to be measured with 2-3% and 50% accuracy, respectively [99]. However, the possibility of the measurement of CP violating phases $\arg(A_t)$ and $\arg(A_b)$ has not been studied yet neither at the LHC nor at the ILC. In the present analysis, the sensitivity of Higgs sector observables to $\arg(A_{t,b})$ at a future Linear Collider will be demonstrated ($A_t = A_b$ will be assumed for simplicity).

As it is seen from (1.83) CP violating effects in the neutral Higgs-boson mass matrix become significant if the ratio $\mathrm{Im}(\mu A_t)/M_{\mathrm{SUSY}}^2$ is large. Motivated by this observation, a CP violating benchmark scenario (CPX) was introduced [74]:

$$\begin{aligned}
&\widetilde{M}_Q = \widetilde{M}_t = \widetilde{M}_b = M_{\mathrm{SUSY}}, \\
&\mu = 4M_{\mathrm{SUSY}}, \\
&|A_t| = |A_b| = 2M_{\mathrm{SUSY}}, \\
&\arg(A_t) = 90^\circ, \\
&|m_{\tilde{g}}| = 1\ \mathrm{TeV}, \\
&\arg(m_{\tilde{g}}) = 90^\circ.
\end{aligned} \tag{7.1}$$

The CPX scenario is not generated in simple scenarios for SUSY breaking, such as those based on minimal supergravity or gauge mediation. There are some possibilities of such a scenario realization in e.g. superstring theory [74]. However, the aim of the proposed scenario is to study the phenomenological consequences for Higgs searches for the most challenging values of the MSSM parameters, which allows to study the capability of the present and future colliders to explore the Higgs boson properties in the most generic framework.

Therefore, assuming the realization of the CP violating scenario in the MSSM, it is regarded

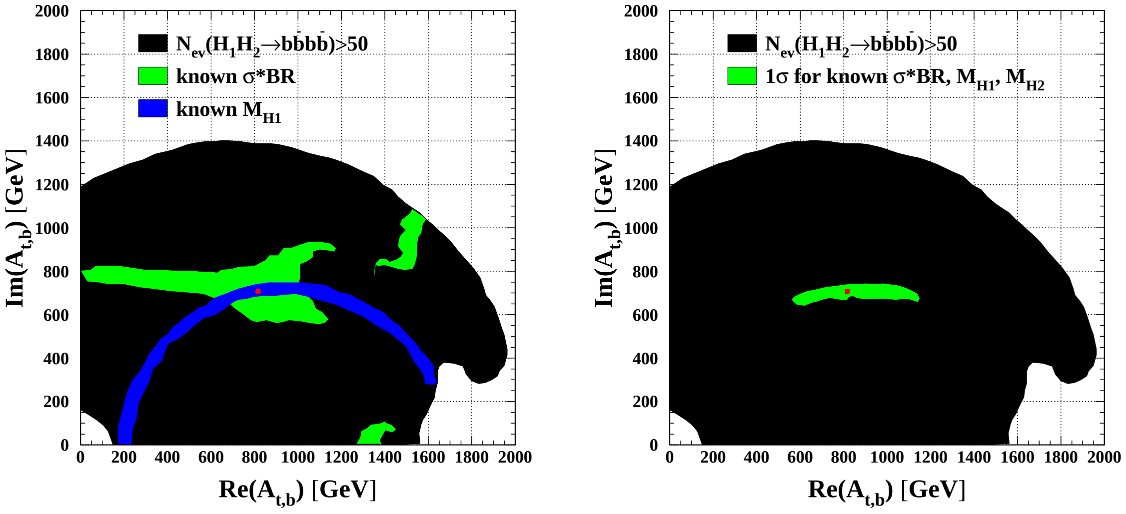

Figure 7.1: *1σ deviation for the observables* $\sigma \times \mathrm{Br}$ *for the process* $\mathrm{e^+e^-} \to \mathrm{H_1H_2} \to \mathrm{b\bar{b}b\bar{b}}$ *and* $m_{\mathrm{H_1}}$ *in the plane of two variables* $\mathrm{Im}(A_{t,b})$ *and* $\mathrm{Re}(A_{t,b})$ *(left figure). 1σ region for the combination of* $\sigma \times \mathrm{Br}$ *for the process* $\mathrm{e^+e^-} \to \mathrm{H_1H_2} \to \mathrm{b\bar{b}b\bar{b}}$*,* $m_{\mathrm{H_1}}$ *and* $m_{\mathrm{H_2}}$ *in the plane of two variables* $\mathrm{Im}(A_{t,b})$ *and* $\mathrm{Re}(A_{t,b})$ *(right figure).*

in present analysis that all parameters from CPX are known except of $\mathrm{Im}(A_{t,b})$ and $\mathrm{Re}(A_{t,b})$. Thus, we suppose, that $\tan\beta$ and μ could be measured in the chargino sector while $m_{\mathrm{H^+}}$ could be measured directly. We choose $\tan\beta = 3$ and $m_{\mathrm{H^+}} = 200$ GeV, $\mu = 2000$ GeV, corresponding to $M_{\mathrm{SUSY}} = 500$ GeV. For this parameter set it is possible to generate model points in the plane $(\mathrm{Im}(A_{t,b}), \mathrm{Re}(A_{t,b}))$ and choose any point supposing that this is realized in nature. The chosen point is $(\mathrm{Im}(A_{t,b}), \mathrm{Re}(A_{t,b})) = (750,\ 800)$ GeV. For the Monte Carlo generation the program HZHA [72] is used. The Higgs masses for the chosen scenario are $m_{\mathrm{H_1}} = 95$ GeV, $m_{\mathrm{H_2}} = 180$ GeV, $m_{\mathrm{H_3}} = 200$ GeV. Taking into account the dependence of the Higgs masses and Higgs boson production cross sections on CP violating parameter $\arg(A_{t,b})$ expressed in equations (1.80-1.83) and (3.7-3.8) it can be assumed, that knowing the Higgs masses and a cross section of some Higgs production process will allow to obtain the values for $\mathrm{Im}(A_{t,b})$ and $\mathrm{Re}(A_{t,b})$.

The analysis is done assuming a known cross section of the process $\mathrm{e^+e^-} \to \mathrm{H_1H_2} \to \mathrm{b\bar{b}b\bar{b}}$ and masses of $\mathrm{H_1}$ and $\mathrm{H_2}$, at a centre of mass energy $\sqrt{s} = 500$ GeV with an assumed integrated luminosity of 500 $\mathrm{fb^{-1}}$ and for the condition that the number of events exceeds 50 (it is 360 for the chosen analysis point).

The precision of a future Linear Collider measurements for $m_{\mathrm{H_1}}$ and $m_{\mathrm{H_2}}$ is assumed to be

$$\delta m_{\mathrm{H_1,H_2}} = 1 \text{ GeV}, \tag{7.2}$$

and for the topological cross section $\sigma_{\mathrm{H_1H_2}} \times \mathrm{Br}$ it is 10% (see Section 6.7 or [1, 78]):

$$\delta(\sigma_{\mathrm{H_1H_2}} \times \mathrm{Br}) = 0.1 \cdot \sigma_{\mathrm{H_1H_2}} \cdot \mathrm{Br}(\mathrm{H_1} \to \mathrm{b\bar{b}}) \cdot \mathrm{Br}(\mathrm{H_2} \to \mathrm{b\bar{b}}). \tag{7.3}$$

The 1σ deviations for the values $\sigma_{\mathrm{H_1H_2}} \times \mathrm{Br}$ and $m_{\mathrm{H_1}}$ in $(\mathrm{Im}(A_{t,b}),\ \mathrm{Re}(A_{t,b}))$ parameter space are presented in Fig. 7.1 (left figure) in green (light grey) and blue (dark grey) area, respectively. The 1σ deviation was calculated from the condition

$$\mathrm{Prob}(\chi^2) = 0.68, \tag{7.4}$$

where χ^2 for $\sigma_{\mathrm{H}_1\mathrm{H}_2} \times \mathrm{Br}$ is

$$\chi^2 = \frac{((\sigma_{\mathrm{H}_1\mathrm{H}_2} \times \mathrm{Br})^p - (\sigma_{\mathrm{H}_1\mathrm{H}_2} \times \mathrm{Br}))^2}{(\delta(\sigma_{\mathrm{H}_1\mathrm{H}_2} \times \mathrm{Br}))^2}, \tag{7.5}$$

and χ^2 for m_{H_1} is

$$\chi^2 = \frac{(m^p_{\mathrm{H}_1} - m_{\mathrm{H}_1})^2}{(\delta m_{\mathrm{H}_1})^2}. \tag{7.6}$$

The values $(\sigma_{\mathrm{H}_1\mathrm{H}_2} \times \mathrm{Br})^p$ and $m^p_{\mathrm{H}_1}$ should be the measured values. The black area in the figure represents the possible $(\mathrm{Im}(A_{t,b}), \mathrm{Re}(A_{t,b}))$ parameter space with the condition that the number of events for the process $\mathrm{e}^+\mathrm{e}^- \to \mathrm{H}_1\mathrm{H}_2 \to \mathrm{b\bar{b}b\bar{b}}$ exceeds 50.

The 1σ region for the combination of known $\sigma_{\mathrm{H}_1\mathrm{H}_2} \times \mathrm{Br}$ and m_{H_1} and m_{H_2} is presented in Fig. 7.1 (right figure). The real and imaginary parts of $A_{t,b}$ can, thus, be constrained to the overlapping region. The precision of the measurement is $\delta(\mathrm{Im}(A_{t,b})) \approx 50$ GeV and $\delta(\mathrm{Re}(A_{t,b})) \approx 300$ GeV. The measurement of m_{H_2} in addition to m_{H_1} does not give any new information about the region of the interest. However, not for any process with known production cross section it is possible to perform a successful reconstruction of an $\arg(A_{t,b})$ value when the corresponding 1σ bands overlap.

In this analysis the SUSY parameters were fixed according to the CPX benchmark scenario. Further studies are needed including varying of SUSY parameters.

Chapter 8

Conclusions and Outlook

In this thesis the potential of a detector at a future Linear Collider for the determination of the MSSM Higgs boson properties exploiting associated Higgs boson pair production followed by the Higgs decay to b-quarks was examined. These measurements can prove or reject the MSSM nature of the Higgs sector in the "wedge" parameter region, where the LHC can perform a 5σ discovery only of the lightest Higgs boson, without the possibility of distinguishing it from the SM one. Moreover, these measurements can be used to perform a Higgs mass measurement in the decoupling limit, when the neutral Higgs boson production via the fusion and Higgsstrahlung processes is significantly suppressed, whereas the cross section of the $\mathrm{e^+e^-} \rightarrow \mathrm{HA}$ process reaches its maximal value. The general analysis was done under the assumption of maximal cross section for the process of Higgs pair production, $\sin^2(\beta - \alpha) = 1$.

It is shown that using the $\mathrm{HA} \rightarrow \mathrm{b\bar{b}b\bar{b}}$ channel the Higgs boson masses can be measured with an accuracy of up to several hundred MeV for Higgs pair production far above the kinematic threshold. The precision deteriorates to about 1 GeV while approaching the kinematic threshold. The topological cross section $\sigma(\mathrm{e^+e^-} \rightarrow \mathrm{HA} \rightarrow \mathrm{b\bar{b}b\bar{b}})$ can be measured with a relative precision varying between 1.5% and 6.6%. The analysis can be improved by adding the channels $\mathrm{e^+e^-} \rightarrow \mathrm{HA} \rightarrow \mathrm{b\bar{b}}\tau^+\tau^-$ and $\mathrm{e^+e^-} \rightarrow \mathrm{HA} \rightarrow \tau^+\tau^-\mathrm{b\bar{b}}$ [1].

The 5σ discovery limit corresponds to a Higgs mass of around 385 GeV for the case of degenerate H and A Higgs boson masses using $\mathrm{HA} \rightarrow \mathrm{b\bar{b}b\bar{b}}$ production channel at $\sqrt{s} = 800$ GeV based on an integrated luminosity of 500 fb^{-1}. The general analysis was applied to the two CP violating scenarios and to the SPS 1a benchmark point.

The sensitivity of the Higgs sector observables to the CP violating parameter, the phase of the soft SUSY-breaking trilinear coupling of the top (bottom) squark to the Higgs boson, $\arg(A_{t,b})$, was demonstrated. The sensitivity of the observable Higgs masses and cross section for the process $\mathrm{e^+e^-} \rightarrow \mathrm{H_1H_2} \rightarrow \mathrm{b\bar{b}b\bar{b}}$ to the real and imaginary parts of $A_{t,b}$ has been analysed. Further conclusions, however, can only be drawn after a more detailed analysis.

In this thesis, the complementarity of the ILC to the *pp* collider LHC was demonstrated in revealing the supersymmetric nature of the Higgs sector. This complementarity is twofold: a future Linear Collider will be able to discover MSSM Higgs bosons in the parameter space inaccessible at the LHC and, in the case if the particles are discovered, the ILC will be able to perform a precision study of their properties.

Part II

Measurement of $F_2^{c\bar{c}}$ and $F_2^{b\bar{b}}$ at Low Q^2 DIS at H1

Chapter 9

Theoretical Context of Heavy Flavour Production

In this chapter the kinematic variables used to describe *ep* physics, will be introduced. Then, the theory of proton structure functions including the Quark Parton Model and QCD will be summarised. In the last section, the theoretical aspects of heavy quark production will be discussed, followed by heavy quark fragmentation models.

9.1 High Energy *ep* Collisions

Electron-proton scattering can be represented by two (simplified) Feynman diagrams in Fig. 9.1. The left diagram shows a neutral current (NC) process $ep \rightarrow eX$ where the exchanged boson is a γ^* or a Z. In the right diagram the exchanged boson is a W^+ or a W^- and the process is called the charged current (CC) process $ep \rightarrow \nu X$, where X is an outgoing hadronic final state.

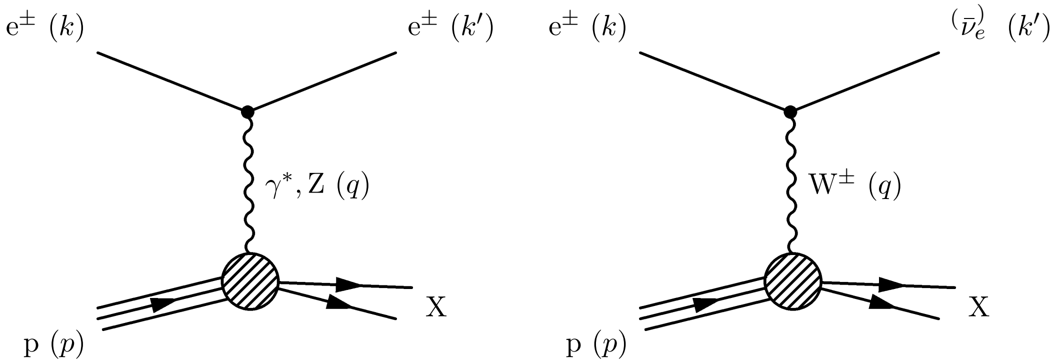

Figure 9.1: *Electron-proton scattering diagrams. The neutral current (NC) process with the exchange of a γ^* or a Z boson (left figure). The charged current (CC) process with the exchange of a $W^\pm$ boson (right figure). The four-momenta of the particles are indicated in brackets.*

The four-momenta of the interacting particles are given by:

k for the incoming electron [1],

k' for the outgoing lepton,

---

[1] The term “electron” will be used throughout this analysis for both electrons and positrons.

p for the incoming proton,

$q = k' - k$ for the exchanged boson.

The kinematics of the ep scattering process can be described by two independent variables for a fixed centre of mass energy $\sqrt{s}$, where $s = (p + k)^2$. The commonly used variables are the following:

Q^2: The virtuality of the gauge boson

$$Q^2 = -q^2 = -(k - k')^2, \quad Q^2 \geq 0, \tag{9.1}$$

y: The inelasticity variable y describes the relative energy transfer at the electron-boson vertex in the proton rest frame:

$$y = \frac{p \cdot q}{p \cdot k}, \quad 0 \leq y \leq 1, \tag{9.2}$$

x: The Bjorken scaling variable x is interpreted within the Quark Parton Model as the fraction of the proton's momentum carried by the interacting parton:

$$x = \frac{Q^2}{2p \cdot q}, \quad 0 \leq x \leq 1. \tag{9.3}$$

If $\sqrt{s}$ is much larger than the masses of the interacting particles, these kinematic variables are related as

$$Q^2 = xys. \tag{9.4}$$

In this thesis only neutral current events are analysed.

There are several methods of calculating the kinematic variables from the scattered particles energies and angles. In the present analysis the kinematic variables were reconstructed using the $e\Sigma$ method [100], which uses the scattered electron and the hadronic final states (HFS).

In the $e\Sigma$ method, Q^2 is determined from the scattered electron quantities and y is reconstructed from the hadronic final state according to the Σ prescription:

$$\begin{aligned} Q^2_{e\Sigma} &= Q^2_e = 4E^e E \cos^2 \frac{\theta}{2}, && (9.5) \\ y_{e\Sigma} &= \frac{2E^e\Sigma}{(\Sigma + E(1 - \cos\theta))^2}, && (9.6) \end{aligned}$$

where E and θ are the energy and angle of the scattered positron, E^e is the initial energy of the positron and Σ is defined as the sum of the scalar quantities $E_h - p_{z,h}$ of each particle belonging to the hadronic final state:

$$\Sigma = \sum_h (E_h - p_{z,h}). \tag{9.7}$$

The $e\Sigma$ method is characterised by a good precision at low x or high y. The Bjorken scaling variable x is obtained from $x = Q^2/sy$.

There are three different kinematic regimes for ep collisions depending on the Q^2 value:

1. **Photoproduction (γp):** $Q^2 < 1$ GeV^2.
   In this kinematic regime the exchange of massive Z bosons is suppressed. The dominant process is the exchange of quasi-real photons.

2. **Low Q^2 Deep Inelastic Scattering (DIS):** 1 GeV$^2 < Q^2 <$ 100 GeV^2.
   This is the main kinematic regime at HERA for the investigation of the structure of the proton. The dominant NC process is the exchange of the photon, and Z exchange is still suppressed. The analysis described in this thesis is performed in this kinematic region.

3. **High Q^2 DIS:** $Q^2 >$100 GeV^2.
   In this kinematic region the exchange of Z and W$^\pm$ also contribute to the cross section together with photon exchange. It is of big interest to search for new physics as well as to check pQCD predictions, e.g. for proton structure functions. The measurement of the proton structure functions in this kinematic region is important for future LHC experiment.

9.2 Inclusive DIS Cross Sections

The inclusive neutral current DIS cross section of the reaction $ep \to eX$ depends on two independent kinematic variables, chosen to be x and Q^2. In the one-photon exchange approximation (Born approximation) the neutral current double differential cross section is given by

$$\frac{d^2\sigma^{NC}}{dxdQ^2} = \frac{2\pi\alpha^2}{xQ^4}\left[y^2xF_1 + (1-y)F_2\right], \tag{9.8}$$

where F_1 and F_2 are the proton structure functions. This equation can also be expressed in terms of F_2 and the longitudinal structure function $F_L = F_2 - 2xF_1$:

$$\frac{d^2\sigma^{NC}}{dxdQ^2} = \frac{2\pi\alpha^2}{xQ^4}\left[(1+(1-y)^2)F_2 - y^2F_L\right], \tag{9.9}$$

For the presentation of the subsequent measurements it is convenient to define the NC *reduced cross section* $\tilde{\sigma}^{NC}(x,Q^2)$ in order to reduce the strong Q^2 dependence originating from the photon propagator:

$$\tilde{\sigma}^{NC}(x,Q^2) = \frac{xQ^4}{2\pi\alpha^2}\,\frac{1}{1+(1-y)^2}\,\frac{d^2\sigma^{NC}}{dxdQ^2}. \tag{9.10}$$

9.3 Quark Parton Model

The model, in which hadrons are viewed as composed of free quarks and antiquarks is called the Quark Parton Model (QPM) [101]. This can be done only if *ep* DIS processes are considered in a reference frame where the momentum of the proton is large, $|\vec{p}|^2 \gg m_p^2$, where m_p is the mass of the proton. In this case the proton can be described as a parallel stream of independent constituents (partons).

In the QPM deep inelastic scattering is interpreted as the elastic scattering of a positron from a single free quark. The other partons, which form the proton remnant, do not participate in the hard interaction and, therefore, are referred to as *spectator partons*. The *ep* cross section is obtained by the incoherent sum over all electron-quark scattering cross sections. The structure functions in this approximation can be expressed as

$$F_1(x) = \frac{1}{2}\sum_i e_i^2[q_i(x) + \bar{q}_i(x)], \tag{9.11}$$

$$F_2(x) = x\sum_i e_i^2[q_i(x) + \bar{q}_i(x)], \tag{9.12}$$

where the sum runs over all flavours of quarks with electric charge e_i which are allowed to participate in the interaction. The functions $q_i(x)$ describe the quark densities in the proton and $q_i(x)dx$ is the probability that the quark i carries a fraction of the proton momentum in the interval $[x, x + dx]$. The QPM predicts the *Bjorken scaling* of structure functions, which means that the structure functions do not depend on Q^2 and only depend on x. This was experimentally confirmed for medium x values, $x \approx 0.25$ [102]. For spin 1/2 partons in the QPM the Callan-Gross relation [103] holds:

$$F_2(x) = 2xF_1(x), \tag{9.13}$$

which implies that the longitudinal structure function $F_L = 0$, i.e. the partons cannot interact with longitudinally polarised photons.

However, there are some experimental observations which show that the naive QPM picture has to be modified. Firstly, the measurements of F_2 show "scaling violation", i.e. F_2 depends on Q^2 (Fig. 9.2). Secondly, F_L is not equal to zero. Thirdly, only ∼54% of a nucleon's momentum is carried by the u and d quarks (*valence quarks*). The explanation to all these experimental facts was found in the framework of quantum chronodynamics (QCD).

9.4 Quantum Chromodynamics

As was mentioned in Section 1.1, strong interactions are described by the non-Abelian gauge theory of Quantum Chromodynamics. It is based on the SU(3) colour symmetry group. In the strong interaction colour is the equivalent of charge in QED. Each quark can exist in three colours (red, green, blue) and the interaction between them proceeds via exchange of electrically neutral gauge bosons - the gluons, which form a colour charge octet. In contrast to photons, which are the carriers of the electromagnetic force and do not have electric charge, the gluons are not colour neutral and, therefore, can strongly interact with each other. This property leads to *asymptotic freedom*, which will be discussed in the next section.

In QCD, the proton is considered to have a more complicated structure, than it is assumed in the QPM. The other remaining ∼46% of the nucleon's momentum is carried by gluons, which are radiated and absorbed by quarks inside the nucleon. The gluons can create other $q\bar{q}$ pairs which are called *sea quarks*. Therefore, also gluons and gluon-induced pairs of quarks and antiquarks should be considered as proton constituents. As Q^2 increases, the number of resolved partons which share the proton's momentum, increases. There is an increased probability of finding a quark at small x and a decreased chance of finding one at high x, because high-momentum quarks lose momentum by radiating gluons. This explains the rise of structure function with rising Q^2 at low x (Fig. 9.2).

In QCD, parton radiation processes lead to non-zero values of F_L. Thus, F_L contains information about the gluon distribution and about the strong interaction dynamics which is complementary to that obtained from the analysis of the scaling violations in $F_2(x, Q^2)$.

9.5 Renormalisation and the Running Coupling α_s

The coupling of strong interactions α_s depends on the scale at which the QCD process occurs and is referred to as the *running coupling*. This property follows from the requirement of *renormalisation*. Due to perturbative corrections to the vertices and the propagation of particles in any Feynman graph the loop integrals will give large contributions (ultraviolet divergences) to the cross sections from momenta much larger than $\sqrt{s}$, i.e. from interactions that happen on time scales much smaller than $1/\sqrt{s}$. This comes from the fact that when the

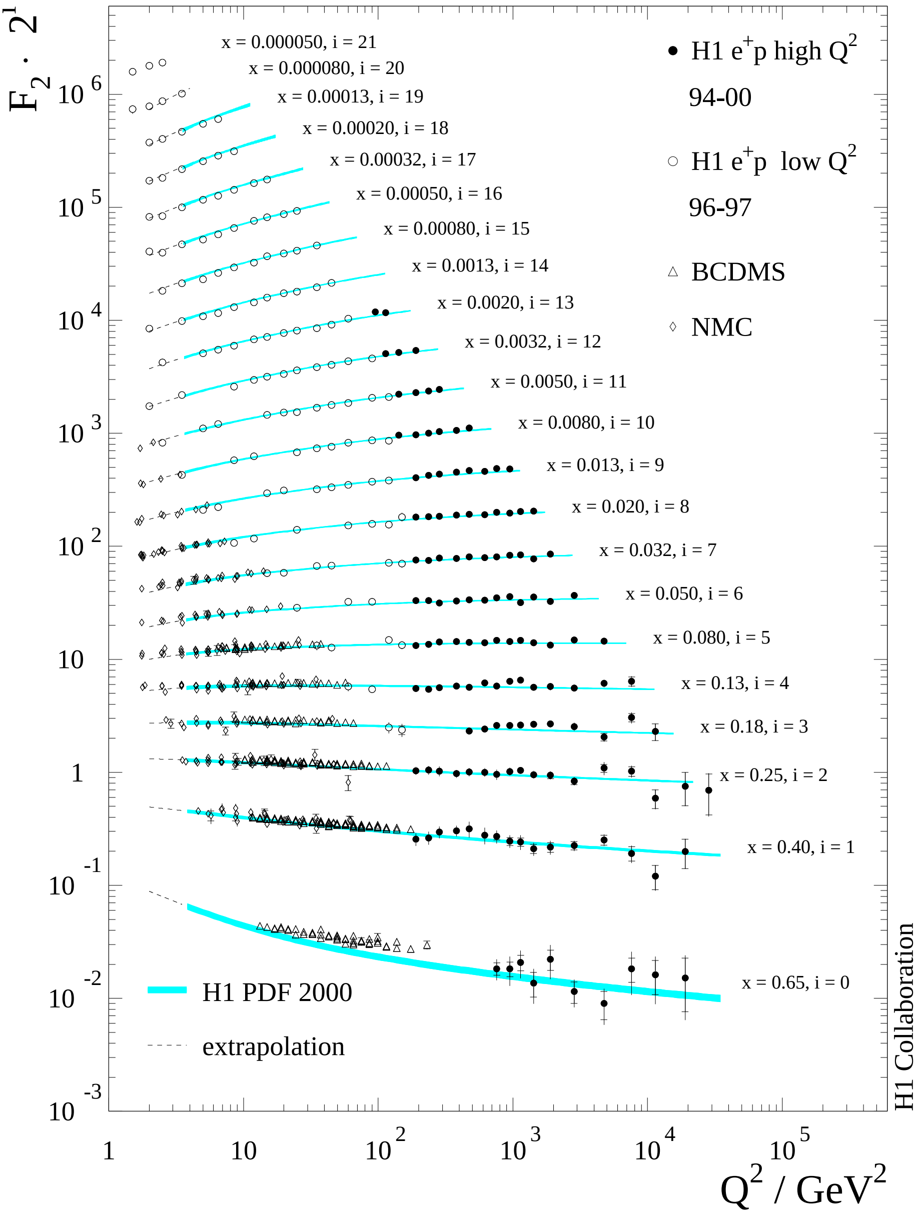

Figure 9.2: *The proton structure function F_2 measured at H1 [104] and fixed target experiments. The results are compared with the corresponding SM expectation determined from the H1 PDF 2000 fit (error bands).*

momentum in the loop goes to infinity, the contribution to the cross section is infinite as well. The effect of the fluctuations can be absorbed into changes in the couplings of the theory (the masses of the theory and the field operators are also modified). The procedure of absorbing very short-time physics into few parameters is called *renormalisation*.

The loop diagrams can be regularised either by cutting the integral at a mass scale M (an ultraviolet cutoff) or, as very often done in QCD, by a so-called *dimensional regularisation* [105]. Several renormalisation schemes exist in which some counterterms are added to the

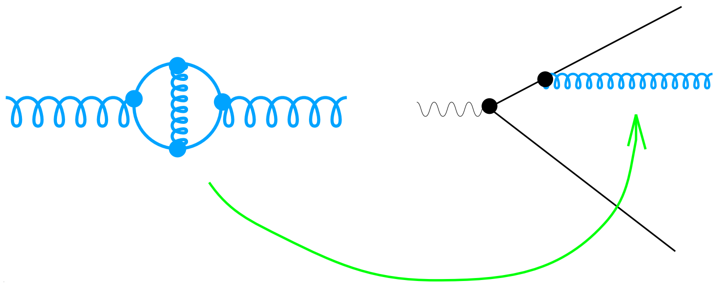

Figure 9.3: *The effect of the short-time fluctuations in the propagation of the gluon field (left diagram) is absorbed into running of the strong coupling (right diagram) [107].*

Lagrangian which cure the divergency. One of such schemes is the $\overline{\text{MS}}$ (Minimal Subtraction) renormalisation scheme [106] of dimensional regularisation. In such schemes a renormalisation scale μ_R is introduced. The physics of time scales $\ll 1/\mu_R$ are removed from the perturbative calculations. The value of the strong coupling is adjusted to account for the effect of the small time physics and depends on the scale that is used: $\alpha_s = \alpha_s(\mu_R)$. This procedure is illustrated in Fig. 9.3, where the short-time fluctuations in the propagation of the gluon, as indicated in the left figure, are absorbed into the running coupling that describes the probability for the quark to emit a gluon in the right figure.

The renormalisation procedure requires the introduction of a mass scale μ_R, but the physics must be insensitive to it. This leads to the *renormalisation group equations* (in a given scheme). Such an equation, for example, gives the dependence of the strong coupling on the scale μ_R, and in $\overline{\text{MS}}$ scheme looks like [106]:

$$\frac{d}{d\ln(\mu_R^2)}\frac{\alpha_s(\mu_R)}{\pi} = \beta(\alpha_s(\mu_R)) = -\beta_0\left(\frac{\alpha_s(\mu_R)}{\pi}\right)^2 - \beta_1\left(\frac{\alpha_s(\mu_R)}{\pi}\right)^3 + ..., \tag{9.14}$$

where the beta function $\beta(\alpha_s(\mu_R))$ is calculated perturbatively in QCD. The first coefficient is

$$\beta_0 = \frac{33 - 2N_f}{12}, \tag{9.15}$$

where N_f is the number of quark flavours. The renormalisation procedure of the adjustment of the strong coupling accounts for physics between times $1/M$ and $1/\mu_R$, where M is an ultraviolet cutoff (say, at a GUT scale). For an observable at a scale μ_R (i.e. $\mu_R = Q$) the renormalisation group equations can be solved perturbatively in terms of $\alpha_s(\mu_R)$. The solution of the renormalisation group equation (9.14) with all values of β_i beyond β_0 set to zero is:

$$\begin{aligned}\alpha_s(\mu_R) &\approx \alpha_s(M) - \left(\frac{\beta_0}{\pi}\right)\ln(\mu_R^2/M^2)\alpha_s^2(M) + \left(\frac{\beta_0}{\pi}\right)^2\ln^2(\mu_R^2/M^2)\alpha_s^3(M) + ...\\ &= \frac{\alpha_s(M)}{1+(\beta_0/\pi)\alpha_s(M)\ln(\mu_R^2/M^2)}.\end{aligned} \tag{9.16}$$

Here, the renormalisation group equation sums the effects of short-time fluctuations of the fields, i.e. a series in power of the strong coupling at the GUT scale $\alpha_s(M)$ are summed into a simple function of μ_R and $\alpha_s(M)$ appears as a parameter in the solution. In (9.16) the property of *asymptotic freedom* is illustrated: $\alpha_s(\mu_R)$ decreases as μ_R increases, i.e. the strong force becomes weaker if it is probed at high energy. This property has been proven and allows to make predictions for the properties of strong interactions in the perturbative QCD regime

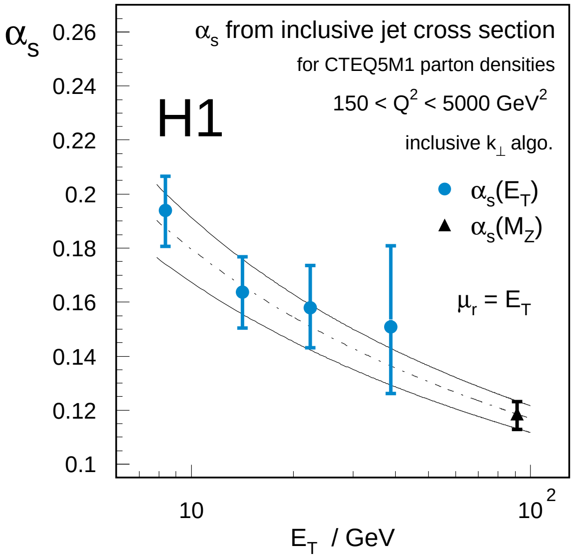

Figure 9.4: *The running coupling α_s measured by H1 [108]. The transverse jet energy E_T represents the renormalisation scale μ_R. The curves indicate the prediction of the renormalisation group equation for α_s energy evolution.*

(pQCD), in which $\alpha_s(\mu_R)$ is small (Fig. 9.4). A fixed order calculation, neglects contributions of terms in higher orders of α_s. A leading order (LO) calculation is a calculation in lowest power of α_s, at which an observable is non-zero. A next-to-leading order (NLO) calculation considers the next power of α_s with respect to LO. By *perturbative QCD* one means the computation of observables at high energies (short distances), by means of a truncated expansion of α_s. Long distance physics is usually referred to as non-perturbative QCD (npQCD).

The boundary values $\alpha_s(M)$ can be different and are determined from experiment. Another version of the expression for α_s can be constructed with the Λ_{QCD} parameter:

$$\alpha_s(\mu_R) \approx \frac{\pi}{\beta_0 \ln(\mu_R^2/\Lambda_{QCD}^2)}. \tag{9.17}$$

It is usually a standard to take a measured value of α_s at $\mu_R = M_Z$. In this case $\alpha_s(\mu_R)$ can be calculated from $\alpha_s(M_Z)$:

$$\alpha_s(\mu_R) \approx \frac{\alpha_s(M_Z)}{1 + (\beta_0/\pi)\alpha_s(M_Z)\ln(\mu_R^2/M_Z^2)}. \tag{9.18}$$

Another property of QCD, which keeps quarks bound into colourless hadrons and does not allow to observe the free quarks, is confinement. This property is reflected in (9.16): the strong coupling becomes larger with decreasing energy μ_R.

9.6 Parton Density Functions and Evolution Equations

As was discussed above, pQCD is applicable at short distances and can describe the interaction of high energy partons (hard subprocess). A long distance part, corresponding to low energy processes, cannot be calculated using pQCD due to the large value of $\alpha_s(\mu_R)$.

Apart from ultraviolet divergences there are other singularities which one encounters in QCD, namely *soft singularities* (when the energy of the gluon approaches zero) and *collinear singularities* (when, in a splitting like $q \rightarrow qg$ with massless quarks, the angle between quark and gluon approaches zero) [105, 109]. Considering the processes with partons in the initial state (e.g. $eq \rightarrow q'$) the collinear singularity associated with the radiation of a gluon from the initial state q, does not cancel. Therefore, it is necessary to cut the angular integration when the angle between quark and gluon approaches zero. This is achieved by setting a cutoff on the gluon transverse momentum k_T. The cutoff is interpreted as the *factorisation scale* μ_F. For $k_T > \mu_F$ the ep cross section is described by the perturbatively calculable partonic cross section $\hat{\sigma}_i$ (which is also called coefficient function), which describes the scattering of the positron on a parton i inside the proton. For $k_T < \mu_F$ the ep cross section can be represented as a convolution of the parton density function [2] (PDF) $f_i^p(\xi, \mu_F)$, depending on the factorisation scale μ_F, and the partonic cross section $\hat{\sigma}_i$:

$$d\sigma(ep \rightarrow e'X) = \sum_{partons\ i} \int_0^1 f_i^p(\xi, \mu_F) \cdot d\hat{\sigma}_i(\hat{s}, \alpha_s(\mu_R), \mu_R, \mu_F) \cdot d\xi, \tag{9.19}$$

where the $f_i^p(\xi, \mu_F)$ describes the probability to find parton i with a proton momentum fraction ξ. The $\hat{s}$ denotes the centre of mass energy of the boson-parton system, $\hat{s} = (\xi \cdot P + q)^2$. The equation (9.19) is also often referred as the *factorisation theorem* [110].

Similar to the renormalisation scale μ_R, the factorisation scale μ_F is often conventionally set to a hard scale relevant for the scattering process, e.g. Q. However, there is no prescription to set such scales. Very often, the dependence of the result on the variation of these scales is checked and interpreted as an estimate of the theoretical uncertainty of the prediction.

The Bjorken scaling violations of F_2 can be understood by interpreting structure functions as convolutions of PDFs and partonic cross sections and dealing with the collinear singularity. This introduced a factorisation scale dependence of the PDFs, which implies a Q^2 dependence of the structure functions as it is seen in Fig. 9.2.

In contrast to the hard subprocess cross sections, which are calculated in pQCD, the PDFs, being non-perturbative quantities, cannot be calculated from first principles. However, it is possible to calculate the evolution of the PDF, depending on x and μ_F, in the scale (x or/and μ_F). This is ruled by *parton evolution equations* which appear after the requirement that the physical cross sections do not depend on μ_F. Knowing the PDF at some scale, one can calculate it at another scale by solving the parton evolution equation at a given order of α_s.

There are several different parton evolution equations working in different phase-space regions of the ep scattering process. To illustrate the difference between them it is useful to choose a combination of reference frame and gauge for which the individual contributions to $\hat{\sigma}$ can be represented by ladder diagrams. These are formed from n parton emissions from partons with transverse momentum k_{Ti} and longitudinal momentum fraction x_i ($x_i > x_{i+1}$) (Fig. 9.5). The transverse momenta of the emitted partons are labeled p_{Ti}. The evolution of these diagrams involves nested integrations over the internal momenta. To simplify the calculation, a certain kinematic ordering of the emission processes is assumed, which is discussed next.

The DGLAP (Dokshitzer-Gribov-Lipatov-Altarelli-Parisi) evolution equation

In the DGLAP evolution equation [111], a strong ordering of the transverse momenta k_{Ti} is assumed:

$$Q_0^2 \ll k_{T1}^2 \ll ... \ll k_{Tn}^2 \ll \mu_F^2 = Q^2, \tag{9.20}$$

---

[2] The collinear singularities are reabsorbed, like in the case of ultraviolet divergences, using dimensional regularisation in, e.g. $\overline{\mathrm{MS}}$ scheme.

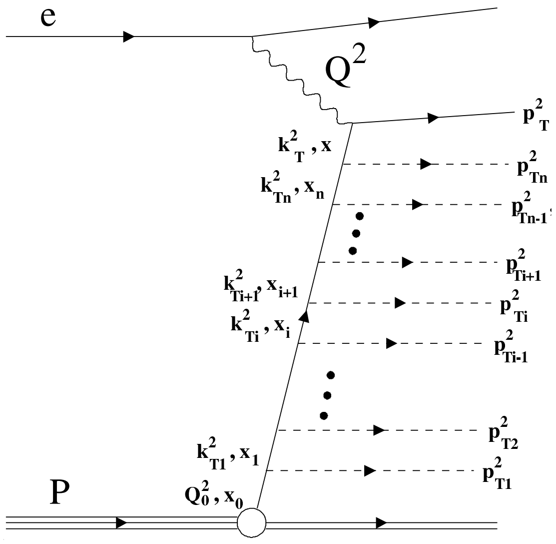

Figure 9.5: *Ladder diagram with n rungs illustrating parton evolution.*

where Q_0^2 is a chosen starting scale. The renormalisation group equations for massless parton density functions are given by:

$$\frac{df^p_{q_i}(x,\mu_F^2)}{d\ln(\mu_F^2)} = \frac{\alpha_s(\mu_R)}{2\pi}\int_x^1 \frac{d\xi}{\xi}\left[P_{qq}(\frac{x}{\xi})f^p_{q_i}(\xi,\mu_F^2) + P_{qg}(\frac{x}{\xi})f^p_g(\xi,\mu_F^2)\right], \quad (9.21)$$

$$\frac{df^p_g(x,\mu_F^2)}{d\ln(\mu_F^2)} = \frac{\alpha_s(\mu_R)}{2\pi}\int_x^1 \sum_j \frac{d\xi}{\xi}\left[P_{gq}(\frac{x}{\xi})f^p_{q_j}(\xi,\mu_F^2) + P_{gg}(\frac{x}{\xi})f^p_g(\xi,\mu_F^2)\right], \quad (9.22)$$

where the indices i and j run over the quarks and antiquarks of all flavours. $P_{ab}(\frac{x}{\xi}) = P_{ab}(z)$ are the perturbatively calculable *splitting functions*, which describe to leading order, the probability to find a parton of species a with momentum fraction x within a parton of species b with momentum fraction ξ, with a moving collinear to b. In equation (9.21), the number of quarks can be changed by two mechanisms: a quark originally at higher energy may loose momentum by radiating a gluon, or, a gluon inside the proton may produce a quark-antiquark pair. In equation (9.22), the number of gluons changes because a quark may radiate a gluon or because a gluon may split into two gluons.

In each splitting one can approximate $k_{T0}^2 = k_{T1}^2 = ... = k_{Ti}^2 = 0$, which means that the DGLAP approach is a collinear approximation, which is also seen in (9.21-9.22), where there is no k_T dependence.

In general, the structure functions can be expressed as a power series in α_s. The series contain both terms proportional to $\ln(\mu_F^2/Q_0^2)$ and to $\ln(\frac{1}{x})$. It can be shown, that solving the DGLAP evolution equations is equivalent to resumming terms of the form $\alpha_s \ln(\mu_F^2/Q_0^2)$ in the expansion of the cross section. Hence, the DGLAP approximation is only valid at large μ_F^2 where these terms will dominate.

The BFKL (Balitski-Fadin-Kuraev-Lipatov) evolution equation

In the small x kinematic region, it is essential to sum leading terms in $\ln(\frac{1}{x})$, independent of the value of $\ln(\mu_F^2/Q_0^2)$. At leading order, this is done by the BFKL [112] equation for the k_T

unintegrated distributions:

$$\frac{d\mathcal{G}(x,k_T^2)}{d\ln(\frac{1}{x})} = \int dk_T'^2 \; \mathcal{G}(x,k_T'^2)\cdot K(k_T^2,k_T'^2), \tag{9.23}$$

where the function K is the splitting kernel equivalent to P in the DGLAP equations. It should be mentioned, that here unintegrated parton density functions must be used, i.e. they must depend on k_T. The evolution is made in increasing $\ln(\frac{1}{x})$, since

$$x_0^2 \gg x_1^2 \gg ... \gg x_n^2 \gg x_{Bj}^2 \tag{9.24}$$

has been assumed. This implies that the emitted gluons will take a large fraction of the propagator momentum. However, there is no ordering in k^2 or k_T^2, so the collinear approximation cannot be used, and the incoming partons of the matrix elements must be taken off-shell (the particles can have a virtual mass).

The CCFM (Ciafaloni-Catani-Fiorani-Marchesini) evolution equation

QCD colour coherence implies *angular* ordering of emissions along the parton chain, so that it is necessary to work in terms of parton distributions $f_a(x,k_T^2,\mu^2)$, which are unintegrated over k_T. These distributions depend on two hard scales: k_T and the scale μ of the probe. They are described by the CCFM evolution equation [113], which is valid both at large and small x, since it resums terms of both the form $(\alpha_s\ln(\frac{1}{x}))^n$ and $(\alpha_s\ln(\frac{1}{1-x}))^n$. This means that at large x the CCFM evolution will be DGLAP-like, and at small x it will be BFKL-like, because both DGLAP and BFKL evolutions are the two limits of angular-ordered evolution. In the DGLAP collinear approximation, the angle increases due to the growth of k_T, while, in the BFKL approach, the angle ($\theta \simeq k_T/k_L$, where k_L is the longitudinal momentum) grows due to the decrease of the longitudinal momentum fraction, x, along the chain of parton emissions from the proton. The angular ordering is a consequence of the interference of soft gluon radiation (or coherence), which strongly effects the hard parton scattering close to the kinematic boundaries $x \to 0$ and 1.

The CCFM evolution includes angular ordering in the initial state cascade, which means that the emission angles of the partons with respect to the propagator increases as one moves towards the quark box,

$$\Xi \gg \xi_n \gg ... \gg \xi_1 \gg \xi_0, \tag{9.25}$$

where the maximum allowed angle Ξ is set by the hard quark box [114],

$$p_q + p_{\bar{q}} = \Upsilon(p_p + \Xi p_e) + Q_T. \tag{9.26}$$

Q_T is the transverse momentum of the quark pair and Υ is its light cone momentum fraction. Equation (9.26) is written in terms of Sudakov variables [115], where p_q, $p_{\bar{q}}$ are the four momenta of the produced quarks and p_p and p_e are the proton and electron momenta. The momenta of the emitted gluons can be written as

$$p_i = v_i(p_e + \xi_i p_p) + p_{Ti}, \quad \xi_i = \frac{p_{Ti}^2}{s v_i^2}, \tag{9.27}$$

where $v_i = (x_{i-1} - x_i)$ is the momentum fraction of the emitted gluon, p_T is the transverse momentum of the gluon, and $s = (p_e + p_p)^2$. It is assumed here, that all particles are massless. The CCFM equation can be written as

$$\bar{q}^2\frac{d}{d\bar{q}^2}\frac{x\mathcal{A}(x,k_T^2,\bar{q}^2)}{\Delta_s(\bar{q}^2,\mu_0^2)} = \int dz\frac{d\phi}{2\pi}\frac{\tilde{P}(z,k_T^2,(\bar{q}/z)^2)}{\Delta_s(\bar{q}^2,\mu_0^2)}x'\mathcal{A}(x',k_T'^2,(\bar{q}/z)^2), \tag{9.28}$$

where $\mathcal{A}(x, k_T^2, \bar{q}^2)$ is the gluon density unintegrated in k_T. It depends also on x and the evolution variables $\bar{q}_i^2$:

$$\bar{q}_i = \frac{p_{Ti}}{1 - z_i} = x_{i-1}\sqrt{s\xi_i}, \tag{9.29}$$

which are the rescaled transverse momenta of the emitted gluons and $z_i = \frac{x_i}{x_{i-1}}$. In this formalism, (9.25) becomes

$$q_i > z_{i-1} q_{i-1}. \tag{9.30}$$

The Sudakov form factor Δ_s [115] describes the probability that there are no emissions from the starting scale μ_0^2 to the maximum rescaled transverse momentum $\bar{q}_{max}^2$:

$$\Delta_s(\bar{q}, Q_0) = \exp\left(- \int_{Q_0^2}^{\bar{q}^2} \frac{dq^2}{q^2} \int_0^{1 - Q_0/q} dz \frac{\bar{\alpha}_s(q^2(1-z)^2)}{1-z} \right), \tag{9.31}$$

where $\bar{\alpha}_s = C_A \alpha_s/\pi$. For inclusive quantities at leading-logarithmic order the Sudakov form factor cancels the $1/(1-z)$ collinear singularity of the splitting function. The CCFM splitting function $\tilde{P}$ is defined as

$$\tilde{P}_g(z, k_T^2, (\bar{q}/z)^2) = \frac{\bar{\alpha}_s(q_i^2(1-z_i)^2)}{1 - z_i} + \frac{\bar{\alpha}_s(k_{Ti}^2)}{z_i}\Delta_{ns}(z_i, k_{Ti}^2, q_i^2). \tag{9.32}$$

The difference between the CCFM and the DGLAP splitting functions is that the CCFM splitting functions include the singular parts of the DGLAP splitting functions. There is also one additional function Δ_{ns}, called the non-Sudakov form factor, which originates from the fact that, in CCFM and BFKL, all virtual corrections in the gluon vertex are automatically taken into account. This is called the Reggeisation of the gluon vertex.

As it was discussed previously, the parton densities cannot be calculated from first principles. They have to be given at some reference scale and then they can be computed for any value of the scale. The determinations of the parton distributions are made with the evolution equations which fit q, $\bar{q}$ and g to data at a variety of Q^2. The determination of PDFs requires detailed treatments of experimental and theoretical uncertainties. Recent fits using DGLAP evolution equation have been made by MRST [116] and CTEQ [117, 118]. The fits using CCFM parton evolution equation have been made by [119, 114].

9.7 Heavy Flavour Production in DIS

A reliable formulation of heavy quark production is important for high energy physics because of its significant contribution to the total inclusive cross section at high energies. The charm contribution to the total structure function F_2 at small x, at HERA, is as large as 25%.

A quark can be called *heavy* if its mass $m_Q \gg \Lambda_{QCD} \sim 200$ MeV, where Λ_{QCD} is the energy scale above which the strong coupling becomes small (see Section 9.5), so that pQCD is applicable at the scale of the heavy quark masses (see (9.17)). The heavy flavours which can be produced at HERA are charm and beauty. The top quark cannot be produced at HERA because of its large mass.

If heavy quarks are treated as partons (see the explanation below) the LO NC heavy quark production process is the QPM process ($\gamma^* Q \to Q$), where $Q = c, \bar{c}, b, \bar{b}$ (left diagram in Fig. 9.6). The cross section for this process is proportional to α. The next order process in this case is where the gluon may produce a quark-antiquark pair, to which the virtual photon then couples ($\gamma^* g \to Q\bar{Q}$) (right diagram in Fig. 9.6). This process is called Photon Gluon Fusion (PGF). The cross section for this process is proportional to $\alpha\alpha_s$. If heavy quarks are

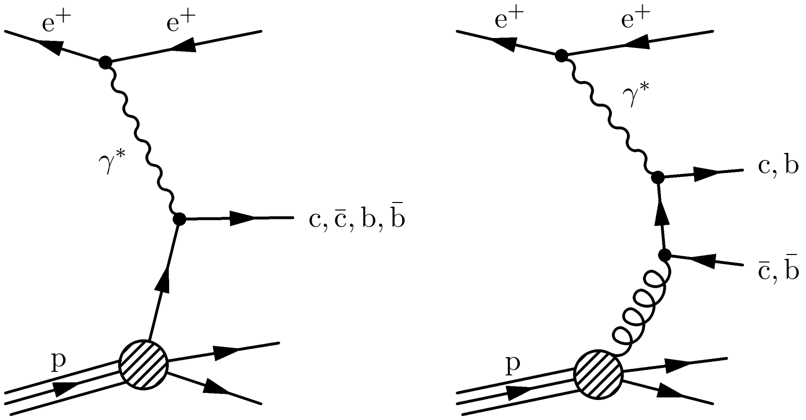

Figure 9.6: *Flavour excitation process (left diagram) and photon gluon fusion (PGF) process (right diagram) for heavy flavour production.*

massive and, therefore, are not treated as partons, the LO process for NC c and b production is PGF process.

Heavy quark production is a challenge in pQCD, because the mass m_Q provides an additional hard scale which complicates the situation. Typically the NLO energy spectrum of a heavy quark contains terms $\alpha_s \ln(Q^2/m^2_{c,b})$ which, for $Q^2 \gg m^2_{c,b}$, spoil the convergence of the perturbative expansion and need to be resummed [3]. Therefore, the perturbative series must be organised in different ways depending on the relative magnitudes of m_Q^2 and Q^2. Different schemes exist to describe heavy flavour production. They are discussed next.

Fixed Flavour Number Scheme (FFNS)

At low Q^2, when $Q^2 \ll m_Q^2$, heavy quark masses are taken into account in the calculations of the partonic cross sections, while the light quarks (u, d, s) are treated massless as required by the DGLAP formalism. Therefore, heavy flavour contributions to the proton structure function are neglected, i.e. they are never treated as partons, and the number of active flavours n_f includes only the light quarks ($n_f = 3$) and is fixed. Therefore this scheme is referred to as the *fixed flavour number scheme* (FFNS) or “massive scheme”.

The LO process in this scheme is photon gluon fusion (i.e. the process of the order of α_s). The NLO diagrams are of order α_s^2. The main contributions to the LO and NLO processes for FFNS are shown in Fig. 9.7.

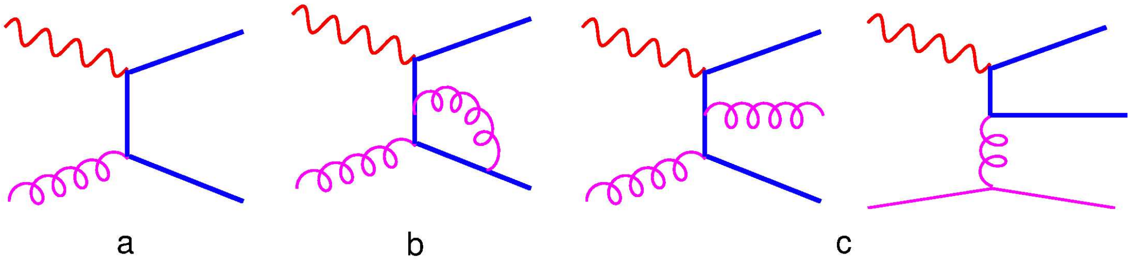

Figure 9.7: *Partonic processes for heavy quark production to NLO in the massive (FFNS) scheme.*

---

[3] Here, factorisation scale $\mu_F = Q$ is assumed.

The massive calculation is expected to be reliable in the low Q^2 regime. The contribution to deep inelastic scattering of a heavy quark can be calculated from the hard processes initiated by light quarks $(u, d, s, ...)$ and gluons, where all effects of the heavy quarks are contained in the perturbative coefficient functions. According to the factorisation theorem, at order $\mathcal{O}(\alpha_s)$, the structure function for a flavour i is [120]

$$F_i(x, Q^2, m_Q^2) = C_{i,k}^{FF}(Q^2/m_Q^2) \otimes f_k^{n_f}(Q^2), \tag{9.33}$$

where $C_{i,k}^{FF}(Q^2/m_Q^2)$ are the coefficient functions and $f_k^{n_f}(Q^2)$ are the partonic distribution functions. However, as Q^2 becomes large compared to m_Q^2, this approach becomes unreliable since the perturbative expansion will lead to the fact, that the coefficient functions will contain terms of the form $\alpha_s^n \ln^n(Q^2/m_Q^2)$ at any order n, which ruin the convergence of the series.

Zero-Mass Variable Flavour Number Scheme (ZM-VFNS)

At high Q^2, when $Q^2 \gg m_Q^2$, the heavy quark mass becomes negligible and the dominant scale is Q^2. The production of heavy quarks is expected to be insensitive to the threshold effects and, therefore it is more appropriate to treat the quarks like massless partons, in the same manner, like the light quarks are treated, and the large $\alpha_s^n \ln^n(Q^2/m_Q^2)$ (infra-red unsafe) terms are resummed via the DGLAP evolution equations. Therefore, heavy flavours must be treated as active partons in the proton and they are described by parton distribution functions. The number of active flavours n_f is changed and includes now also heavy partons, which are labeled as $n_f + 1$, assuming variable active flavour number ($n_f = 4$ after inclusion of charm quark and $n_f = 5$ after inclusion of charm and beauty). This scheme is also referred as the zero mass variable flavour number scheme (ZM-VFNS) or "massless" scheme.

The LO process in this scheme, i.e. zeroth order in α_s, is the QPM process, whereas the NLO processes are of order α_s just as for the case of total inclusive DIS structure functions. The LO and NLO diagrams are presented in Fig. 9.8.

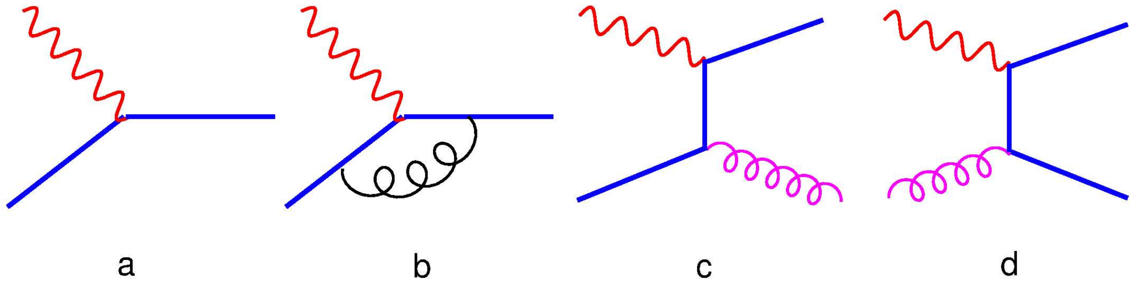

Figure 9.8: *Partonic processes for heavy quark production to NLO in the massless (ZM-VFNS) scheme.*

In this scheme, if $Q^2 \ll m_Q^2$, m_Q is taken to be infinite, and if $Q^2 \gg m_Q^2$, m_Q is taken to be zero. The structure function for a flavour i can be presented as [120]

$$F_i(x, Q^2, m_Q^2) = C_{i,j}^{ZMVF}(Q^2/m_Q^2) \otimes f_j^{n_f+1}(Q^2), \tag{9.34}$$

where the partons in different flavour-number regions are related perturbatively:

$$f_j^{n_f+1}(Q^2) = A_{jk}(Q^2/m_Q^2) \otimes f_k^{n_f}(Q^2). \tag{9.35}$$

Here, $A_{jk}(Q^2/m_Q^2)$ are perturbative matrix elements, which contain $\ln(Q^2/m_Q^2)$ terms and guarantee the correct evolution for both descriptions. Passing through a threshold $Q^2 = m_Q^2$ ZM-VFNS does not have any problems at LO. At NLO, the heavy flavour evolves from zero at $Q^2 = m_Q^2$ and the gluon loses corresponding momentum. However, there is no longer a smooth transition already at NNLO ($A_{jk}^{2,0} \neq 0$) and the heavy parton begins with a negative value at small x. Therefore, there are discontinuities in the parton distribution functions. Moreover, there are also discontinuities in the ZM-VFNS coefficient functions at the transition point due to a sudden change in the flavour number in the coefficient functions (which is true already at NLO). Therefore the ZM-VFNS is not feasible at NNLO, leading to a huge discontinuity in $F_2^Q(x, Q^2)$, which is significant in $F_2^{Tot}(x, Q^2)$ [120].

The ZM-VFNS formalism is implemented in the ACOT scheme (Aivasis, Collins, Olness, Tung) [121] and is implemented in i.e. CTEQ6M, CTEQ6D and CTEQ6L [118] global PDF fits.

Variable flavour number scheme (VFNS)

To account for the problems of the two previous models, which are individually unsatisfactory over the full energy range, a general *variable flavour number scheme* (VFNS) has been proposed, which combines massive and massless schemes interpolating between two well-defined limits of $Q^2 \leq m_Q^2$ and $Q^2 \gg m_Q^2$. The formalism uses different numbers of active flavours depending on Q^2 and similar to the conventional ZM-VFNS. However, it also incorporates non-zero heavy quark mass effects. Collins has shown [122] that, to all orders of perturbation expansion, factorisation of the DIS structure functions holds for massive partons to the same degree of rigor as in the zero-mass case. For example, the four-flavour scheme component of the general formalism includes the full heavy quark mass effects, after the infra-red unsafe part has been resummed.

The essential ingredients of the formalism are [123]:

- 3-flavour scheme at physical scales $Q \sim m_c$ and extending up;
- 4-flavour $m_c \neq 0$ scheme at asymptotic $Q \gg m_c$ and extending down;
- a set of matching conditions which relate the two schemes at some scale μ_m;
- a suitable transition scale μ_t at which one switches from one scheme to the other.

There is a flexibility in the choice of μ_m and μ_t, which partially account for the differences in proposed VFNS methods to treat the transition region.

The VFNS can be defined by demanding equivalence of the n_f and $(n_f + 1)$-flavour descriptions at all orders [120]:

$$\begin{aligned} F_i(x, Q^2, m_Q^2) &= C_{i,k}^{FF}(Q^2/m_Q^2) \otimes f_k^{n_f}(Q^2) = C_{i,j}^{VF}(Q^2/m_Q^2) \otimes f_j^{n_f+1}(Q^2) \\ &\equiv C_{i,j}^{VF}(Q^2/m_Q^2) \otimes A_{jk}(Q^2/m_Q^2) \otimes f_k^{n_f}(Q^2) \qquad (9.36) \\ \Longrightarrow C_{i,k}^{FF}(Q^2/m_Q^2) &= C_{i,j}^{VF}(Q^2/m_Q^2) \otimes A_{jk}(Q^2/m_Q^2). \qquad (9.37) \end{aligned}$$

There are several schemes, which describe the heavy quark components of the deep inelastic structure functions using VFNS. They differ in methods how to treat the transition region $Q^2 = m_Q^2$. The most common schemes are:

- ACOT(χ) scheme [123, 124]. In this method, the naive x is replaced with the kinematically natural rescaling variable χ:

$$\chi = x \, \left(1 + \frac{4m_Q^2}{Q^2}\right), \tag{9.38}$$

- TR-VFNS (Thorne, Roberts) scheme [125, 126],
- BMSN (Buza, Matiounine, Smith, van Neerven) scheme [127],
- CSN (Chuvakin, Smith, van Neerven) scheme [128].

9.8 Perturbative QCD Calculations for Heavy Flavour Production

The following QCD models were used in this analysis to compare data with theoretical predictions for $F_2^{c\bar{c}}$ and $F_2^{b\bar{b}}$ measurement at low Q^2 DIS:

MRST04 [129]. This version of the global parton analysis of deep inelastic data is performed in the $\overline{\text{MS}}$ renormalisation and factorisation scheme using the DGLAP evolution equations at NNLO. This PDF fit includes $\mathcal{O}(\alpha_{QED})$ corrections to the parton evolution, which introduced modified DGLAP equations. Also, photon parton distributions $\gamma(x, Q^2)$ of the proton has emerged. Heavy quark production is described in NLO according to the TR-VFNS (Thorne-Roberts) scheme.

CTEQ6HQ [124]. This global PDF fit uses generalised (non-zero quark mass) $\overline{\text{MS}}$ perturbative QCD framework up to NLO. The fit incorporates heavy quark production scheme according to the ACOT(χ) scheme (VFNS).

CCFM [119, 130]. In this scheme the predictions for the charm and beauty cross sections are obtained from the fits to HERA inclusive data based on CCFM evolution (see Section 9.6). The heavy quarks are produced in the FFNS, i.e. massive scheme, according to the photon-gluon fusion off-shell matrix elements (with $m_c = 1.5$ GeV and $m_b = 4.75$ GeV) convoluted with the CCFM k_T-unintegrated gluon density of the proton. The predictions are calculated using the Monte Carlo program CASCADE (see Section 9.10).

NNLO [120]. Till now, all developed schemes were limited to NLO order. This is connected to the fact that in NNLO $\mathcal{O}(\alpha_s^3)$ heavy flavour coefficient functions for $Q^2 \leq m_Q^2$ are not calculated, making NNLO FFNS problematic. Recently, predictions for inclusive heavy flavour production within a VFNS approach have been calculated at NNLO where approximations of the $\mathcal{O}(\alpha_s^3)$ matrix elements have been made. This was implemented according to modified Thorne-Roberts VFNS scheme. The method guarantees continuity of the physical observables, such as structure functions, despite the discontinuity in the NNLO parton distributions.

9.9 Heavy Quark Fragmentation

Confinement leads to the formation of colourless bound states, namely hadrons. In the QPM, hadrons formed with three valence quarks are called *baryons* (like protons or neutrons), and those formed with quark-antiquark pairs are called *mesons*. The process of hadron formation is called *fragmentation* [4].

In experiments only hadrons can be observed due to confinement. The perturbative treatment of hadron formation is not possible, therefore, phenomenological models have been developed to describe the fragmentation process.

In the fragmentation function formalism the short and long distance phenomena are separated. The fragmentation function $\mathcal{D}_i^h(z,\mu_F)$ is the probability that a hadron of type h be produced with momentum fraction z of the initial parton i. Similar to the inclusive ep cross section (9.19), short and long distance processes are factorised to compute the cross section $d\sigma_h(p)$ of the observable hadron h with momentum p from the perturbatively calculated cross sections $d\hat{\sigma}(\frac{p}{z},\mu_F)$ which describe the production of a parton i with momentum p/z at the factorisation scale μ_F:

$$d\sigma_h(p) = \sum_{\text{partons } i} \int_0^1 \mathcal{D}_i^h(z,\mu_F) \cdot d\hat{\sigma}(\frac{p}{z},\mu_F) \cdot dz. \tag{9.39}$$

This ansatz implies the independence of $\mathcal{D}_i^h(z,\mu_F)$ from the hard scattering process which is completely defined by $d\hat{\sigma}$. It is usually referred to as the *universality of the fragmentation process.*

For light quarks the functions $\mathcal{D}_i^h(z,\mu_F)$ are not calculable and must be fitted to data. However, for a heavy enough quark a perturbative treatment is partially possible and calculations in leading and next-to-leading order are available [131, 132]. Therefore, the fragmentation function $\mathcal{D}_Q^H(z,\mu_F)$, as a probability to produce a hadron H from a heavy quark Q, can be further split into short and long distance parts:

$$\mathcal{D}_Q^H(z,\mu_F) = \int_z^1 D_Q(x,\mu_F) \cdot D_{np}^H(\frac{z}{x}) \cdot dx, \tag{9.40}$$

where $D_Q(x,\mu_F)$ is the perturbative fragmentation function which describes via subsequent gluon emissions the transition of a heavy quark Q produced at the scale μ_F to a quark on mass shell. $D_{np}^H(\frac{z}{x})$ is a non-perturbative fragmentation function.

The parton fragmentation functions $D_Q(x,\mu_F)$ are analogous to the parton distributions in DIS scattering. In both cases, the simplest parton-model approach would predict a scale-independent x distributions which will be violated when QCD corrections are taken into account. The evolution of the parton fragmentation function $D_Q(x,\mu_F)$ with increasing scale μ_F, like that of parton distribution function $f_i^p(x,\mu_F)$ in Section 9.6, which compensates for higher order corrections omitted in the fixed order calculation of the partonic cross section in (9.39), is described by DGLAP evolution equation:

$$\mu_F^2 \frac{\partial}{\partial(\mu_F^2)} D_{Q_i}(x,\mu_F) = \sum_{Q_j} \int_x^1 \frac{dz}{z} \frac{\alpha_s}{2\pi} P_{Q_jQ_i}(z,\alpha_s) D_{Q_j}(\frac{x}{z},\mu_F). \tag{9.41}$$

Here, in contrast to (9.21-9.22), the splitting function is $P_{Q_jQ_i}$ rather than $P_{Q_iQ_j}$, because in this equation $D_{Q_i}(x,\mu_F)$ represents the fragmentation of the final parton. Because no evolution is necessary for a quark already produced on mass shell, the boundary condition for the evolution is

$$D_Q(x,m_Q) = \delta(1-x). \tag{9.42}$$

The introduction of a non-perturbative fragmentation functions has been criticised by some authors, since universality is not guaranteed by a factorisation theorem any more [133].

---

[4] Fragmentation is also sometimes referred to as *hadronisation*.

Although the scaling violation can be calculated perturbatively, the actual form of the parton fragmentation is non-perturbative. Perturbative evolution gives rise to a shower of quarks and gluons (parton showers). Phenomenological schemes are then used to model the carry-over of parton momenta and flavour to the hadrons. The most popular phenomenological fragmentation models are described next.

String fragmentation

This model involves colour flux tubes, or strings, each spanned between two quarks created during the perturbative event phase. The string can be viewed as a colour flux tube formed by gluon self-interaction as two coloured partons move apart. The gluons appear as kinks on the string. If the energy stored in the string is sufficient, a $q\bar{q}$ pair may be created from the vacuum. Therefore the string breaks up repeatedly into colour singlet systems as long as the invariant mass of the string pieces exceeds the on-shell mass of a hadron. The most known and wide-spread string hadronisation model is proposed by the Lund group [134] and realized in the JETSET [135] and PYTHIA [93] event generators.

Cluster fragmentation

In this approach [136] it is assumed that partons are combined into massive, colourless clusters before confinement and then they undergo hadronisation. It is physically motivated by the so-called preconfinement property of perturbative parton shower [137]. The gluons at the end of the parton shower evolution are split non-perturbatively into quark-antiquark pairs. Then the clusters are formed from quarks only. These clusters decay directly into two hadrons unless they are either too heavy, when they decay into two clusters, or too light, when they decay into a single hadron. The mechanism of heavy cluster splitting into lighter ones cannot be adequately described by isotropic decays. The two sub-clusters inherit a momentum fraction, which, with increasing cluster mass, is increasingly dominated by the momentum of the quark of the original cluster that is transferred to the respective sub-cluster. When the light cluster decays into a single hadron, momentum conservation is enforced by transferring momentum to a neighbouring cluster of larger mass. This model is implemented into HERWIG [138] Monte Carlo generator.

Independent fragmentation

In this approach each of the outgoing partons hadronise independently. The model describes the transition of a heavy quark Q to a bound meson state H. Independent fragmentation models neglect the influence of the recoil system on the final hadron, i.e. the properties of the initial quark define the fragmentation process completely. The quark and meson momenta are further assumed to be the only relevant parameters for the process. This assumption is known as Feynman scaling.

A $q\bar{q}$ quark pair is created from the vacuum at each iteration step. One quark of this pair is then combined with isolated parton Q to form a meson $(Q\bar{q})$ (Fig. 9.9). The other quark from the created pair remains an isolated parton for the next step. Since this method does not work for gluons, these are usually split into a quark-antiquark pair before hadronisation.

In this method, different parametrisations are used for a non-perturbative fragmentation function $D^H_{np}(z)$ from (9.40). One of the most popular fragmentation parametrisations for heavy quarks is the one suggested in 1983 by Peterson et al. [139]. It is based on the assumption that the amplitude T of the transition of a heavy quark Q into a heavy hadron $H{=}(Q\bar{q})$ plus a light quark is mainly determined by the energy difference between initial and final state:

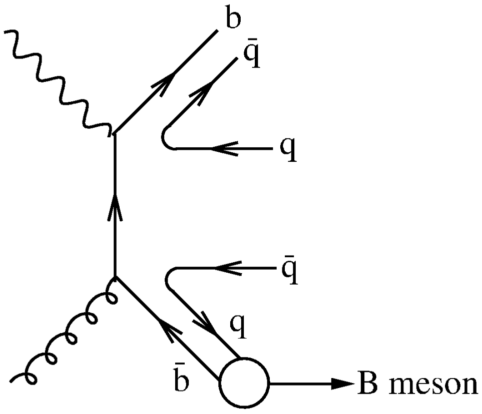

Figure 9.9: *Fragmentation of b-quarks into B-mesons in independent fragmentation model.*

$T \propto 1/\Delta E$. The fragmentation function $D^H_{np}(z)$ is a probability distribution of hadrons carrying a momentum fraction z from the initial quark Q, and it is proportional to the square of the amplitude T, i.e. proportional to $1/(\Delta E)^2$. Together with a phase space factor $1/z$, the Peterson fragmentation function is

$$D^H_{np}(z) = N\frac{1}{z}\left(1 - \frac{1}{z} - \frac{\epsilon_Q}{1-z}\right)^2, \tag{9.43}$$

where N is a normalisation factor. The Peterson parameter ϵ_Q describes the hardness of the fragmentation process [139]:

$$\epsilon_Q \sim (m_q/m_Q)^2, \tag{9.44}$$

where m_Q stands for the mass of the initial heavy quark and m_q is the mass of the quark, produced in the process. The parameter ϵ_Q cannot be calculated exactly, because the light quark mass put into the equation is a mere representation of the non-perturbative strong interaction scale. Therefore it is determined experimentally.

In Fig. 9.10 the Peterson function for ϵ_Q values extracted from $D-$ and $B-$meson spectra are shown: the fragmentation of the b quark is significantly harder than for the c quark, because the hadron formation is less sensitive to the production of the light quark pair due to the larger b mass (see (9.44)). The values of ϵ_Q have been extracted from the fit using NLO, i.e. $\mathcal{O}(\alpha_s)$, perturbative calculation. The following values of ϵ_Q have been found [140]:

- $\epsilon_c = 0.058$ from the fit to ARGUS D data;
- $\epsilon_c = 0.078$ from the fit to OPAL D data;
- $\epsilon_b = 0.0069$ from the fit to ALEPH B data.

While the Lund string model yields a description of the full hadronic final state, the Peterson model is only applicable for independent heavy flavour fragmentation. To profit still from the good description obtained in the heavy flavour sector, it has been optionally added to the Lund string model, where the Peterson function can be used to describe string breakups and the longitudinal momentum distribution of heavy quarks. The treatment of the momentum component perpendicular to the string and the fragmentation of light quarks remains unchanged in this case.

There are several intrinsic problems in the independent fragmentation scheme. It is hard to find an adequate termination of the iteration. If after creation of a hadron insufficient energy

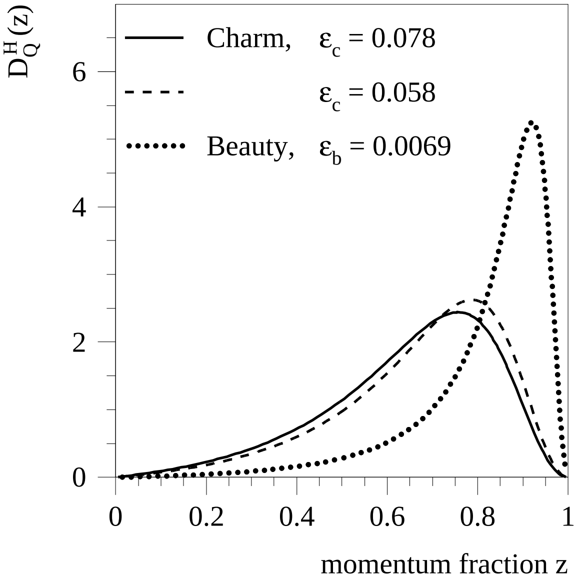

Figure 9.10: *Peterson fragmentation functions for values of ϵ_Q extracted in [140] for charm and beauty in LO.*

to form another hadron is left, the remaining isolated hadron is usually discarded which means that energy, longitudinal momentum, charge, colour and flavour are not strictly conserved in the hadronisation process. Jet correlations, as observed in data, are not included in this scheme. The suppression of the creation of heavy $q\bar{q}$ pairs (charm and beauty) has to be put in manually. Many properties of independent fragmentation have been clearly excluded by e^+e^- experimental data. Therefore this model has mostly been removed from current Monte Carlo generators. However, it still gives reasonable approximation for hadron collider data. This model is used in COJETS [141], ISAJET [142] MC generators, and is included as option in JETSET [135] and PYTHIA [93].

9.10 Monte Carlo Event Generators

Higher order processes are very difficult to calculate using pQCD. Moreover, in the experiments only hadrons can be detected, but not quarks. The transition from parton level to hadron level takes place over long distances where α_s is large, and pQCD is not valid here. To solve this problem, Monte Carlo (MC) generators are used. For each event, these programs generate all particles, their four-momenta and all the kinematic variables according to a certain theoretical model. The higher order gluon emissions are simulated by evolving the parton ladder according to some evolution equation (DGLAP, BFKL, CCFM etc.), and the transition to hadrons is implemented via hadronisation models. The following MC programs were used for event generation in this analysis:

RAPGAP [143]. This Monte Carlo program is used to generate heavy flavour events. The program combines $\mathcal{O}(\alpha_s)$ matrix elements with higher order QCD effects modelled by the emission of parton showers. The heavy flavour event samples are generated according to the massive PGF matrix element with the mass of the c and b quarks set to $m_c = 1.5$ GeV and $m_b = 4.75$ GeV, respectively. In the heavy flavour event generation, the DIS cross section is calculated using the parton distribution functions from [144]. DGLAP parton evolution equations are used. The partons are fragmented according to LUND string model implemented within the JETSET program [145]. The HERACLES program [146] was used for calculation of single photon radiative emissions off the lepton line, virtual and electroweak corrections.

DJANGO [147]. The Monte Carlo program DJANGO is used to generate light quark events. This program also, like RAPGAP, combines $\mathcal{O}(\alpha_s)$ matrix elements with higher order QCD effects modelled by the emission of parton showers. The PDFs are taken from [148]. The partonic system for all generated events is fragmented according to the LUND string model implemented within the JETSET program. The HERACLES program is used as in the case of RAPGAP for the calculation of single photon radiative emissions off the lepton line, virtual and electroweak corrections.

CASCADE [114]. This MC program is used to generate heavy flavour production. The program is based on the CCFM evolution equation (Section 9.6) and thus uses unintegrated parton densities and off-shell matrix elements. For technical reasons, a backward evolution is used, where first the hard scattering is generated and then the initial state cascade (the gluon ladder) is evolved from the quark box to the incoming particles. In this evolution only gluon emissions are treated, i.e. only splitting $g \to gg$ is considered. The hadronisation model, used in CASCADE, is the LUND string model in JETSET/PYTHIA.

PHOJET [149]. This Monte Carlo program is used to generate the background contribution from photoproduction events ($\gamma p \to X$). For parton fragmentation LUND model is used.

Chapter 10

H1 Experiment at HERA

The *ep* accelerator HERA (Hadron Elektron Ring Anlage) at DESY (Deutsches Elektronen Synchrotron) in Hamburg, Germany, consists of two separate storage rings located in a tunnel with a circumference of 6.3 km. A schematic overview of HERA including the injectors and a chain of pre-accelerators is shown in Fig. 10.1. Four experiments are located along the ring: two multi-purpose detectors H1 and ZEUS and two fixed target experiment HERMES and HERA-B. The latter stopped operation in 2003. HERA accelerates protons to an energy of 920 GeV (820 GeV before 1998) and electrons (or positrons) to an energy of 27.5 GeV which corresponds to an *ep* centre of mass energy $\sqrt{s} = 319$ GeV. The beam particles are spaced with 96 ns time intervals corresponding to a collision rate of 10.4 MHz.

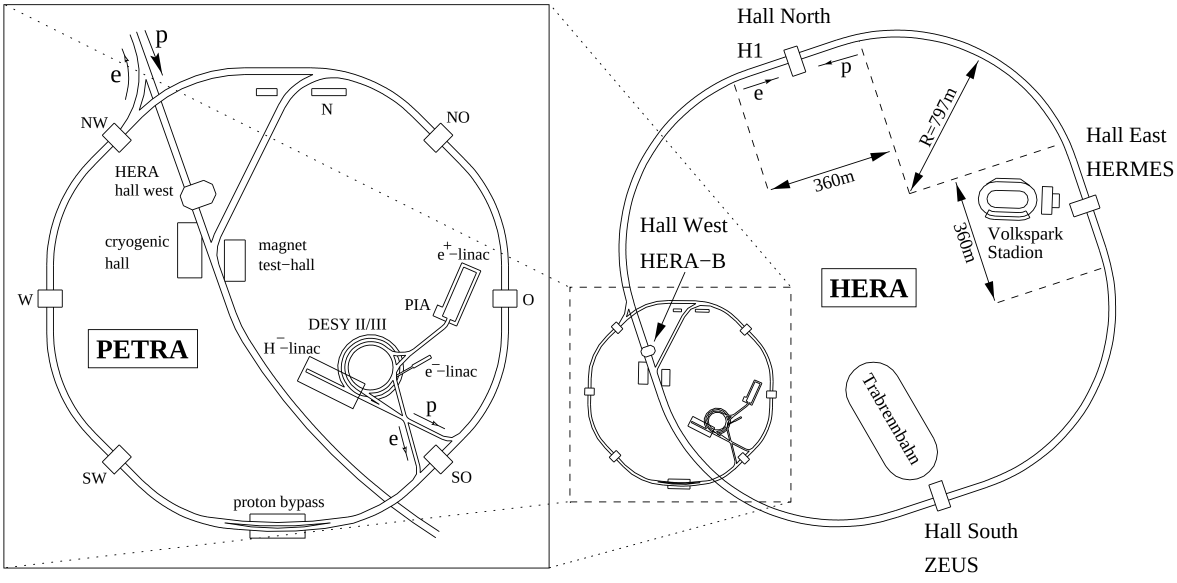

Figure 10.1: *The ep accelerator HERA and its pre-accelerators at DESY.*

10.1 H1 Detector

Only a short description of the H1 detector components, relevant to this analysis, will be given here; a full description may be found in [150]. The H1 detector is a general purpose detector for energy and momentum measurement of charged and neutral particles, the luminosity of the colliding beams and providing information for particle identification. A schematic view of the detector is given in Fig. 10.2. The detector is instrumented asymmetrically to account for the different proton and electron beam energy. A right-handed coordinate system is employed at H1 that has its z-axis pointing in the proton beam, or forward, direction and x (y) pointing in the horizontal (vertical) direction. The superconducting coil $\boxed{6}$ comprises the tracking detectors $\boxed{2}$ $\boxed{3}$ and the calorimeters $\boxed{4}$ $\boxed{5}$, reducing the amount of dead material in comparison with a setup where the solenoid is placed in between the trackers and the calorimeters. The central detector is surrounded by an instrumented iron return yoke $\boxed{10}$ serving as a muon detector. Further devices exist for the detection of electrons and protons scattered under very small angles.

10.1.1 Central Tracking Detector

The reconstruction of charged particle trajectories is done using the central tracking detector (CTD) $\boxed{2}$. With a uniform magnetic field of 1.15 T parallel to the z axis, provided by a superconducting coil $\boxed{6}$ located between the main calorimeter $\boxed{4}$ $\boxed{5}$ and the muon system $\boxed{9}$, a momentum measurement is also possible. The information on event vertices, marking the position of the ep interaction (primary vertex) and decays of long-lived particles (secondary vertices), is obtained by extrapolating the reconstructed tracks back to the beam axis. A side view of the H1 tracking systems is shown in Fig. 10.3. The CTD enables the momentum measurement of charged particles over the polar angle $20^\circ < \theta < 160^\circ$. It consists of the central jet chamber (CJC), the central silicon tracker (CST), the central inner and outer z-chambers (CIZ/COZ) and the central inner and outer proportional chambers (CIP/COP) which are used for triggering only. A radial view of the CTD is shown in Fig. 10.4.

Central Jet Chamber CJC

The CJC is the main component of the CTD. It consists of two gas-filled coaxial cylinders along the beam axis from z = -1.1 m to z = 1.1 m. The inner chamber CJC1 covers the angular range $11^\circ < \theta < 169^\circ$ and the outer chamber CJC2 covers $26^\circ < \theta < 154^\circ$. Anode sense wires and drift field shaping cathode wires running parallel to the beam axis are arranged in planes subdividing the CJC1 (CJC2) volume into 30 (60) identical cells. The wire planes are tilted by around 30° to account for the non-zero Lorenz angle due to the presence of the magnetic field (Fig. 10.4). The position of a crossing particle in the transverse plane can be measured with an accuracy of $\sigma_{r\phi} = 140\ \mu$m with a high time resolution of ≈ 0.5 ns. A transverse momentum resolution is $\sigma(p_T)/p_T \simeq 0.005\, p_T\, [\mathrm{GeV/c}] \oplus 0.015$, where $\oplus$ symbolises the quadratic sum. The charge is read out at both ends of the sense wires enabling the determination of the z-position of hits using charge division. The intrinsic resolution in the z direction is significantly worse (≥ 22 mm) than in the transverse plane. In order to improve the z resolution, hits in the CIZ and the COZ are used in the track reconstruction. Their signal wires are perpendicular to the z-axis resulting in an improved z-resolution by two orders of magnitude compared to the CJC alone. The single hit z resolution of z-chambers is 380 μm.

Central Silicon Tracker CST

The innermost tracking detector is the CST. It consists of two cylindrical layers of double sided silicon strip detectors arranged symmetrically around the beam axis at radii of 5.7 cm and 9.7 cm. The schematic $r\phi$ view of the CST is shown in Fig. 10.5. The active length of the CST is 35.6 cm which covers the polar angular range $30^\circ < \theta < 150^\circ$. The inner (outer) CST layer contains 12 (20) identical and slightly overlapping ladders, each composed of two

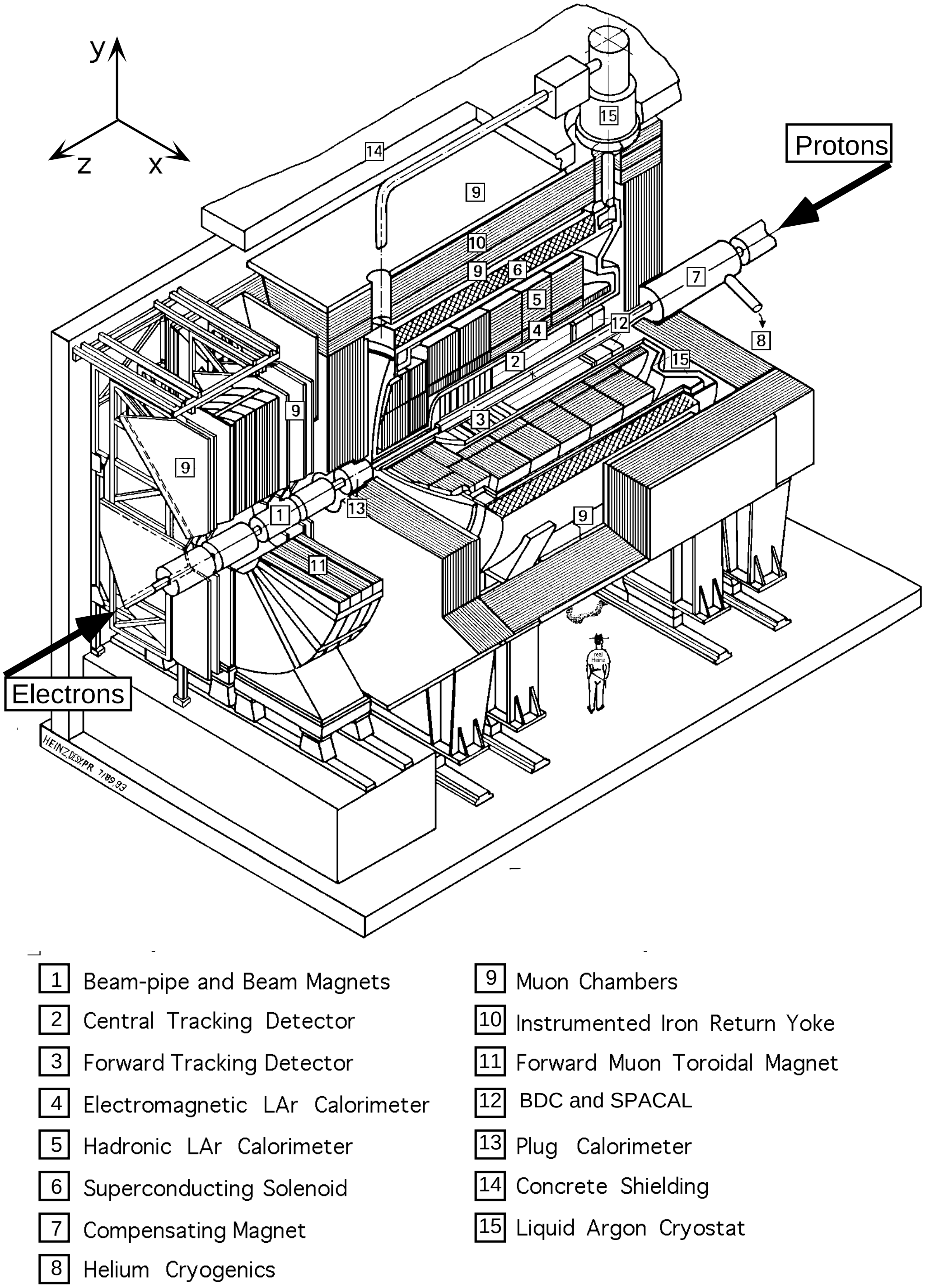

Figure 10.2: *A schematic view of the H1 detector.*

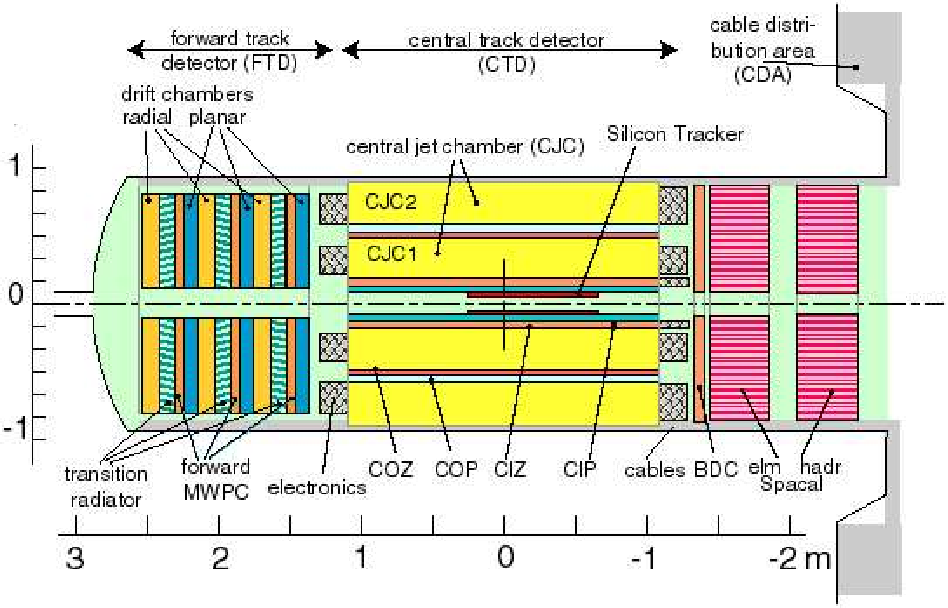

Figure 10.3: *Side view of the H1 tracking systems.*

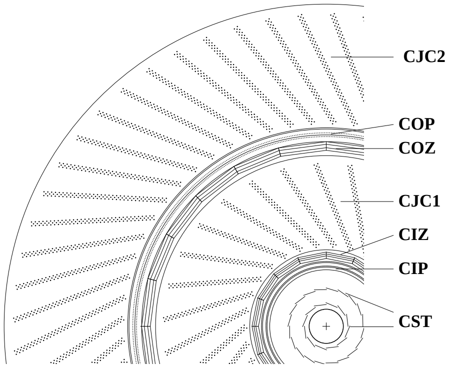

Figure 10.4: *Radial view of the H1 central tracking detector.*

identical half ladders of 22.1 cm length and 3.4 cm width (Fig. 10.6). Each half ladder consists of three silicon sensors and a hybrid structure carrying the readout electronics.

On the p-side (outer face) of each sensor there are 1280 p^+-acceptor strip implants running parallel to the z-axis with a pitch of 25 μm. Every second strip is read out leading to the single hit resolution in the $r\phi$ projection of 12 μm [151]. The n-side (opposite side) is used to determine the z-position of incident particles. Here, n^+-donator strip implants of 88 μm pitch are oriented perpendicular to the z-axis. Every n-side strip is read out via an additional metal layer. The intrinsic hit resolution in z is significantly worse than the $r\phi$ resolution due to the larger pitch. The z resolution depends on the incident angle of a track and has a minimum of 22 μm for $\theta \approx 90^\circ$ [152].

In a first step of the hit-finding algorithm [153], which is performed independently for the

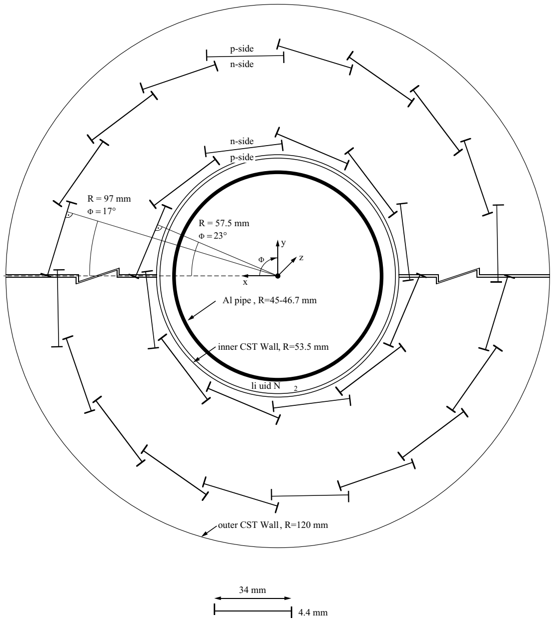

Figure 10.5: *Radial view of the CST.*

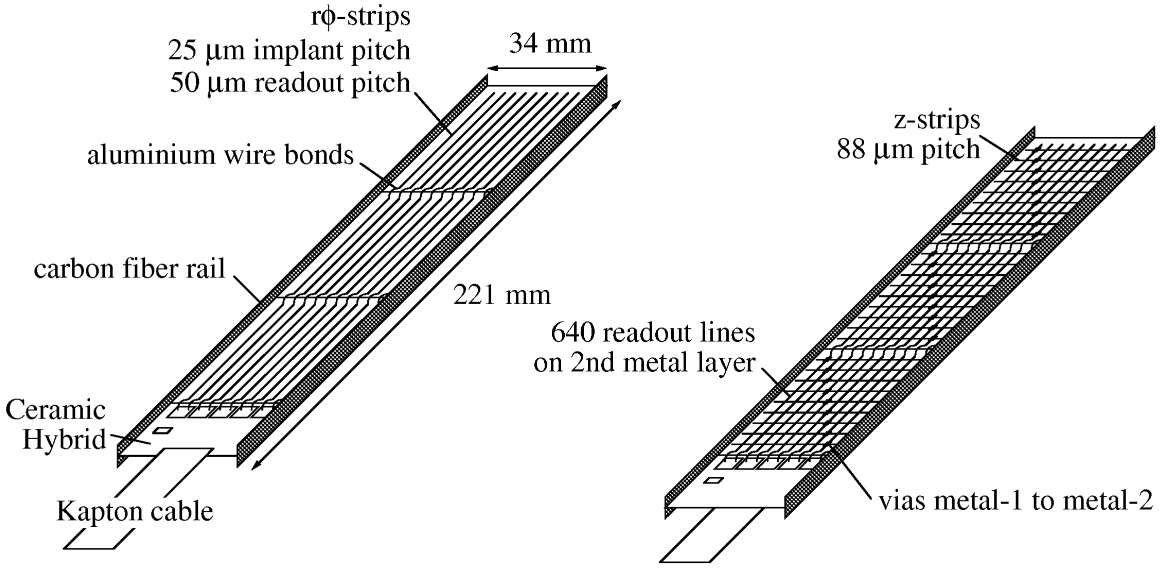

Figure 10.6: *CST half ladders. Left: p-side, right: n-side.*

p- and n-side, neighbouring strip signals are combined into clusters. The association of p- and n-side clusters in a second step results in three-dimensional space points.

10.1.2 Calorimeters

The track detectors are surrounded in the forward and central directions ($4° < \theta < 155°$) by a fine grained liquid argon calorimeter (LAr) and in the backward region ($153° < \theta < 178°$)

by a lead-scintillating fibre spaghetti calorimeter (SPACAL) [154] with electromagnetic and hadronic sections (Fig. 10.7). The LAr is important for energy and angular reconstruction of the hadronic final state particles. The SPACAL is used in this analysis to measure and identify the scattered positron in the low Q^2 DIS regime. In addition, a planar drift chamber (BDC) [155] positioned in front of the SPACAL ($151° < \theta < 178°$), allows suppression of photoproduction background, where particles from the hadronic final state fake a positron signal.

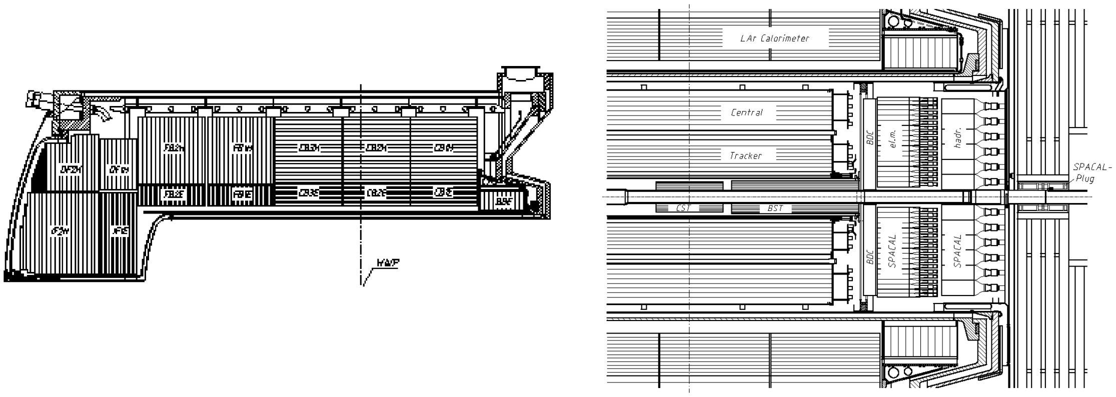

Figure 10.7: *Side view of the LAr (left figure) and the backward region of the H1 detector, including BDC and SPACAL (right figure).*

The Liquid Argon Calorimeter LAr

In the LAr calorimeter absorbing and readout plates form a cell structure containing liquid argon as active material which was chosen because of its good stability, simplicity of calibration, fine transverse granularity and homogeneity of the signal response. The liquid argon is cooled down to -183° C so that it is in liquid form and has to be placed inside a cryostat which in turn sits inside the magnetic solenoid. The inner electromagnetic region with high granularity and lead absorber plates is optimised for the detection of electrons and photons. The total thickness of the electromagnetic part varies between 20 and 30 radiation lengths. The energy resolution was determined in a test beam to be $\sigma_{em}(E)/E \approx (12\%/\sqrt{E[GeV]}) \oplus 1\%$ for electrons.

The outer part (hadronic section) is designed for the measurement of hadronic energy deposits with the total thickness between 4.7 and 8 nuclear interaction lengths λ. The cells of the hadronic section are larger and the absorber material is stainless steel. The achieved energy resolution as measured in test beams is $\sigma_{had}(E)/E \approx (50\%/\sqrt{E[GeV]}) \oplus 2\%$ for single pions.

The LAr is a non-compensating calorimeter, i.e. for the same primary energy an electromagnetically interacting particle leads to a larger signal than a hadron. In the energy reconstruction this has to be considered by an energy dependent signal reweighting of the hadronic energy scale.

The Backward Calorimeter SPACAL

The SPACAL has the cells consisting of scintillating fibres embedded in lead. It is divided into an electromagnetic and hadronic section with energy resolution of

$\sigma_{em}(E)/E \approx (7.1\%/\sqrt{E[GeV]}) \oplus 1\%$ and $\sigma_{had}(E)/E \approx (56\%/\sqrt{E[GeV]}) \oplus 3\%$, respectively. The hadronic section is needed to measure leakage of electromagnetic showers from the electromagnetic part and hadronic energy flow in the backward region.

10.1.3 Luminosity System

The luminosity measurement is based on the detection of photons produced in the electromagnetic *Bethe-Heitler* process $ep \rightarrow ep\gamma$, which has a high cross section and is theoretically very well understood. The main background source to this process is bremsstrahlung $eA \rightarrow eA\gamma$ off the residual gas in the beam pipe volume. Its rate is about 10% of the Bethe-Heitler process rate. This background can be subtracted using information from the *electron pilot bunches.* These have no counter-bunches to collide with so that electrons confined in them interact solely with the residual gas. The luminosity is calculated as

$$L = \frac{R_{\rm tot} - (I_{\rm tot}/I_0)R_0}{\sigma_{\rm vis}}, \tag{10.1}$$

where $R_{\rm tot}$ is the total rate of all events registered in the luminosity detector, R_0 is the rate from the pilot bunches, $I_{\rm tot}$ and I_0 are the beam currents of the colliding and pilot bunches and $\sigma_{\rm vis}$ is the visible part of the Bethe-Heitler cross section corrected for trigger efficiency and acceptance of the luminosity detector. The luminosity measurement precision is 1.5% for the years 1999 and 2000 which is relevant for this analysis. The value enters as a normalisation uncertainty in the total cross section systematic uncertainty.

10.1.4 Trigger System

The beam collision rate at HERA is 10.4 MHz, whereas the rate for an *ep* reaction at low Q^2 is of the order of 10 Hz. The rate of background processes coming mainly from collisions of the beam particles with rest gas atoms within the beam pipe (beam-gas interactions) is several orders of magnitude higher than the *ep* event rate. An additional background comes from halo muons, generated by proton losses around the ring and from muons coming from cosmic rays. In order to account for the limited bandwidth for the data transfer to mass storage devices (data logging) and to avoid a high experimental “dead-time” (when the experiment is blind to new events while reading out data), the event rate of typically 100 kHz has to be reduced to a logging rate of about 10 Hz. The task of a trigger system is to provide a fast selection of *ep* processes and background rejection.

The H1 trigger system consists of four trigger levels from L1 to L4 (Fig. 10.8):

L1: Many of the detectors incorporate trigger systems which provide information called *trigger elements* (TE), for example, a calorimeter may provide TEs for an energy measurement above a certain threshold or a tracker may provide the number of tracks. The trigger subsystems typically each provide 8 different TEs which are sent to the Central Trigger. There are currently 207 TEs. The decision whether to accept or to reject an event is made within 2.3 μs. This is achieved by putting the signals of the L1 system into a pipeline. The trigger elements, usually from different subsystems, are combined by the Central Trigger logic into up to 128 logical conditions, which are referred to as L1 *subtriggers* $s0 ... s127$. A positive decision to keep the event on this trigger level is reached if at least one subtrigger condition is fulfilled (*L1 keep*). If a specific subtrigger has a too high rate, it can be scaled down by a factor of N (*prescale factor*). That means that only every Nth positive decision of this subtrigger is taken into account, effectively reducing the integrated luminosity seen by the subtrigger by 1/N. The L1 output rate is of the order of a few hundred Hz. This level is dead time free.

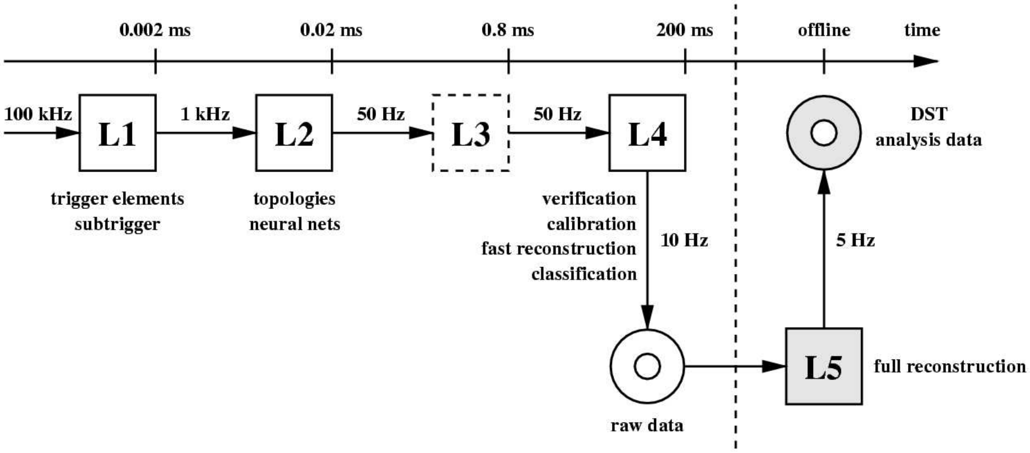

Figure 10.8: *Scheme of the H1 trigger system.*

L2: The L2 decision is formed by two hardware systems: a topological trigger (L2TT) and a neural network (L2NN). The time to make a decision on the second level is 20 μs. Therefore the L2 system can evaluate more complex information than L1. L2 is able to study correlations between different sub-detectors. The L2 output rate is required to be below 50 Hz.

L3: This level was not implemented during HERA-I run period. After an upgrade it is a software trigger that includes a fast track trigger (FTT) and a jet trigger.

L4: The fourth level trigger is based on software. A fast online event reconstruction and determination of calibration factors is performed. The events containing a “hard scale” e.g. high p_T jet or an exclusive final state e.g. D^* are assigned to a physics class and kept for subsequent analysis. The remaining events are downscaled (randomly rejected) and have L4-weights assigned. The L4 output rate is restricted to 10 Hz and the maximal allowed decision time is 100 ms. The *raw data* of an event which has been accepted by the L4 system are written to the *production output tapes* (POT).

After the data has been recorded on POT an additional calibration of the data is performed and is referred to as level-5 (L5). The output after compression is permanently stored on data summary tapes (DST), which are the starting point for physics analysis.

A recorded event is labelled in a unique way by a run number and an event number. The events belonging to a given run have been recorded with a constant trigger setup and under similar experimental conditions.

10.2 The Detector Simulation

The samples of events generated for *uds*, *c*, and *b* production are passed through a detailed simulation of the detector response based on the GEANT3 program [69], and through the same reconstruction software as is used for the data.

The example of a low Q^2 DIS event in the H1 detector with deposited energy in the SPACAL is shown in Fig. 10.9. The scattered positron is detected in SPACAL.

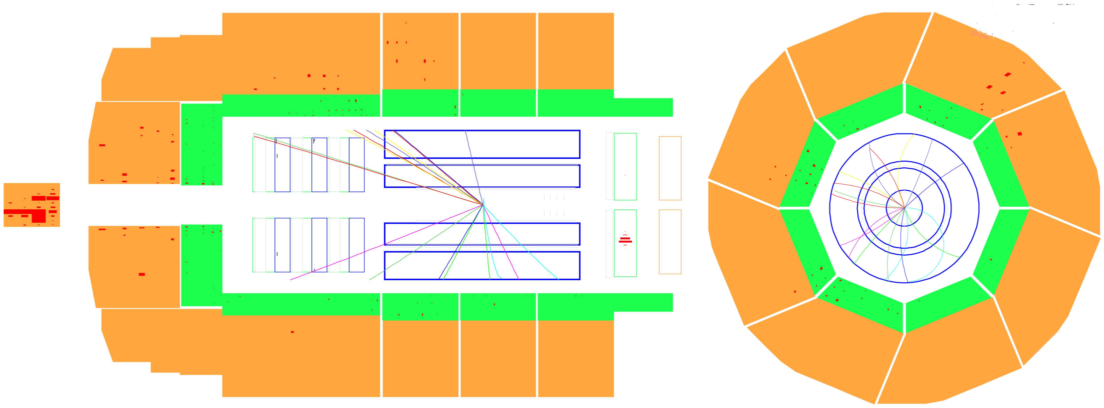

Figure 10.9: *Side view (left figure) and radial view (right figure) of low Q^2 DIS event in H1 detector. The scattered positron is detected in SPACAL.*

Chapter 11

Heavy Flavour Production at H1

The main goal of this analysis is to measure the charm and beauty content in low Q^2 neutral current *ep* interactions and to calculate charm and beauty contributions $F_2^{c\bar{c}}$ and $F_2^{b\bar{b}}$ to the proton structure function. For this purpose the property of the long lifetime of charm and beauty hadrons is exploited. The measurements are done inclusively, looking at the distance of closest approach of all tracks linked to the H1 vertex detector (CST). This allows to separate charm, beauty and light quark contributions.

In this chapter, the experimental signatures of heavy flavour production will be described. Different methods of heavy quark detection, used in *ep* collision experiments, will be compared. The inclusive impact parameter method, used in the present analysis, will be described.

11.1 Experimental Signatures of Heavy Quarks

Due to confinement quarks cannot be detected "freely". They hadronise and are detected using the products of hadronisation. A large fraction of particles produced by the fragmentation are unstable and decay into stable or almost stable ones, which can be observed. In the following, the description will concentrate on charm and beauty hadron production in *ep* collisions (top quark production is kinematically not accessible at HERA). The fragmentation fractions of c and b quarks to charm and beauty hadrons are given in Table 11.1.

	fragm. fraction
$c \to D^0$	0.55
$c \to D^+$	0.23
$c \to D_s^+$	0.10
$c \to \Lambda_c^+$	0.08

	fragm. fraction
$b \to B^0$	0.40
$b \to B^+$	0.40
$b \to B_s^0$	0.10
$b \to \Lambda_b^0$	0.10

Table 11.1: *Fragmentation fractions of c quarks to charm hadrons [156] (left table) and of b quarks to beauty hadrons [157] (right table).*

The properties of charm and beauty hadrons, like masses and lifetimes are summarised in Table 11.2. Hadrons coming from heavy quarks, have large masses in comparison to hadrons, coming from light quarks. Moreover, the masses of beauty hadrons are more than twice larger on average, than those of charm hadrons. The other property of beauty hadrons which differs from charm hadrons is their longer lifetime leading to decay length of ≈150-500 μm compared to ≈100-300 μm of charm hadrons. These two properties (mass and lifetime) of heavy hadrons are usually used to separate them from light quarks and from each other.

hadron	quark content	mass [MeV]	lifetime τ [ps]	decay length $c\tau$ [μm]
D^0	$c\bar{u}$ ($\bar{c}u$)	1864.6 ± 0.5	0.4103 ± 0.0015	123
$D^\pm$	$c\bar{d}$ ($\bar{c}d$)	1869.4 ± 0.5	1.040 ± 0.007	312
$D_s^\pm$	$c\bar{s}$ ($\bar{c}s$)	1968.3 ± 0.5	0.490 ± 0.009	147
Λ_c^+	udc	2284.9 ± 0.6	0.2 ± 0.006	59.9
B^0	$d\bar{b}$ ($\bar{d}b$)	5279.4 ± 0.5	1.536 ± 0.014	460
$B^\pm$	$u\bar{b}$ ($\bar{u}b$)	5279.0 ± 0.5	1.671 ± 0.018	501
B_s^0	$s\bar{b}$ ($\bar{s}b$)	5369.6 ± 2.4	1.461 ± 0.057	438
$B_c^\pm$	$c\bar{b}$ ($\bar{c}b$)	6400 ± 400	$0.46^{+0.18}_{-0.16}$	138
Λ_b^0	udb	5624 ± 9	1.229 ± 0.080	368

Table 11.2: *Properties of some charm and beauty hadrons [158].*

Because of the larger beauty mass, the average number of decay particles is larger for beauty than for charm hadrons. The average decay charged multiplicities for charm and beauty quarks are taken from [159] and [157], respectively.

11.2 Heavy Quark Tagging Methods

Different heavy quark measurement methods exploit different signatures of hadrons, coming from them. All the methods can be divided into exclusive and inclusive ones.

11.2.1 Exclusive Methods

The method can be called *exclusive* when a particular decay channel of the heavy hadrons is used. There are several exclusive methods used for heavy flavour tagging at HERA:

$D^{*\pm}$ **method for charm tagging [160, 161, 162, 163, 164]**

This method for charm tagging is based on the identification of $D^{*\pm}$ mesons using the decay channel

$$D^{*+} \to D^0\pi^+_{slow} \to (K^-\pi^+)\pi^+_{slow} \ (+c.c.).$$

The $D^{*\pm}$ is reconstructed using the $D^* - D^0$ method [165]. The fragmentation fraction $f(c \to K\pi\pi_{slow})$ is $< 1\%$. Moreover, only a limited kinematic region is accessible for the measurement of D^* mesons. Therefore, in order to determine the open charm contribution $F_2^{c\bar{c}}(x, Q^2)$ to the proton structure function, the observed cross section is extrapolated to the full kinematic region in $p_T(D^*)$ and $\eta(D^*)$ [1]. The extrapolation factors vary from 4.7 to 1.5 in p_T and η decreasing with increasing Q^2. The uncertainty on the extrapolation has been estimated to be 10-20% [164].

From the D^* measurements the contribution of charm to the proton structure function, $F_2^{c\bar{c}}$, has been derived by correcting for the fragmentation fraction $f(c \to D^*)$ and extrapolation factors. The results are found to be in good agreement with pQCD predictions.

$D^*\mu$ **correlations method for charm and beauty production [166]**

The separation of charm and beauty contributions in this method is based on different

---

[1] The pseudorapidity value η is defined as $\eta = -\ln\left(\tan\frac{\theta}{2}\right)$.

correlations of the charges and angles between the D^* meson and the muon in the reactions $ep \to eb\bar{b}X \to eD^*\mu X$ and $ep \to ec\bar{c}X \to eD^*\mu X$.

Muon-jet method for beauty production [167, 168]

This method exploits the long lifetime and (or) the large mass of beauty hadrons to identify beauty quarks using the process $ep \to eb\bar{b}X \to ej\mu X'$, where j is a jet in the Breit frame. In this process the muon coming from the decay of a beauty hadron is associated to the jet in the Breit frame. The B-hadron mass leads to a broad distribution of the transverse momentum p_T^{rel} of decay muons relative to the beauty quark jet direction. The B-hadron lifetime is reflected in the large impact parameters δ of the decay muon tracks relative to the primary vertex. The fraction of beauty events in the data is extracted from a fit of p_T^{rel} and (or) δ distributions. The differential cross sections measured in bins of the muon pseudorapidity η^μ and transverse momentum of the muon p_t^μ are shown in Fig. 11.1. In both plots the data are higher than NLO QCD calculations in the massive scheme [168]. In this method, the electron instead of the muon can also be used.

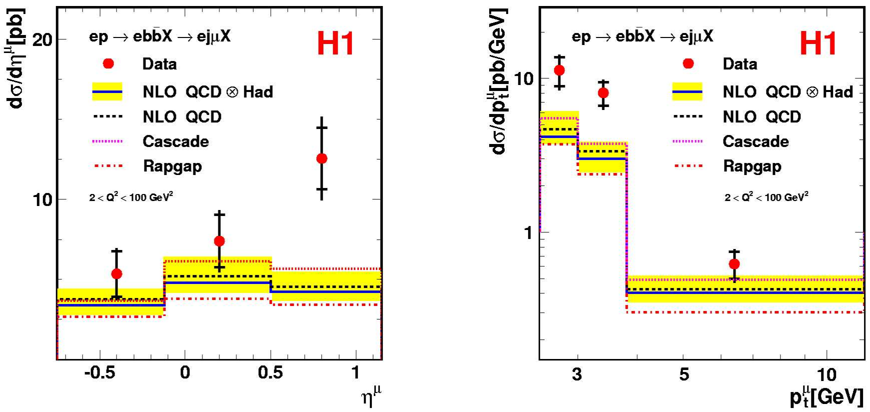

Figure 11.1: *Differential cross sections for the process $ep \to eb\bar{b}X \to ej\mu X'$ in the kinematic range 2 GeV$^2 < Q^2 <$ 100 GeV^2 as functions of the muon pseudorapidity η^μ and transverse momenta of the muon p_t^μ [168]. The data are compared to NLO QCD predictions and Monte Carlo programs using heavy quark production in a massive scheme.*

11.2.2 Inclusive Methods

The disadvantage of exclusive methods is that they are statistically limited. Moreover, they require model dependent extrapolations. To overcome these problems a more inclusive method can be used which is less dependent on the final state. There are several inclusive methods used for heavy flavour tagging at HERA. They are based on lifetime information of the hadrons coming from heavy quarks:

Explicit reconstruction of a secondary vertex [169]

This method is based on explicit reconstruction of a secondary decay vertex and measuring a decay length of heavy hadrons. However, this method can be difficult due to limited statistics because at least two tracks are needed to reconstruct a secondary vertex, which leads to low detection efficiency.

Impact parameter or distance of closest approach (DCA) method [4]

To increase statistics in the measurement and to reduce the model dependence it was proposed to use the impact parameter (which is equivalent to the distance of closest approach) of all tracks measured with the help of the vertex detector. The idea of the method was first used by ALEPH [170]. At HERA, this method has already been used in the measurements of the charm and beauty contributions to the inclusive proton structure function F_2 in deep inelastic scattering, with $Q^2 > 150$ GeV^2 [4]. In this high Q^2 region a fraction of $\sim 18\%$ ($\sim 3\%$) of DIS events contains c (b) quarks. It was found that pQCD calculations at next-to-leading order gave a good description of the data.

In this thesis, a similar method is employed, using data from the same running period, to extend the measurements to the range of lower Q^2, $12 \leq Q^2 \leq 60$ GeV^2 and of Bjorken x, $0.000197 \leq x \leq 0.005$. In this kinematic range the threshold effects at $Q^2 \sim m_{c,b}^2$ play an important role in heavy flavour production. In pQCD the production of heavy quarks over the whole Q^2 range is described by the variable flavour number scheme (VFNS) (see Section 9.7). The aim of this analysis is to check the validity of such a description and to measure the structure functions $F_2^{c\bar{c}}$ and $F_2^{b\bar{b}}$. This is the first $F_2^{b\bar{b}}$ measurement in the low Q^2 kinematic range. The results of this analysis have been published in [5] and [6]. The method is described in details in the next section.

11.3 Impact Parameter Method for Inclusive Heavy Flavour Analysis

Taking into account the difficulties of exclusive methods and explicit secondary vertex reconstruction for heavy flavour measurements, a new inclusive method of charm and beauty measurement was proposed which is less model dependent. It is based on the lifetime information of heavy hadrons which is reflected in different impact parameter (δ) or distance of closest approach distributions of the tracks coming from secondary decays of heavy hadrons in comparison to tracks coming from primary decays of light hadrons. The measurement of the tracks, used in the analysis, was improved by the H1 vertex detector Central Silicon Tracker (CST). In the following, all the definitions will be made in the $r\phi$ plane due to the better H1 detector resolution for track measurements.

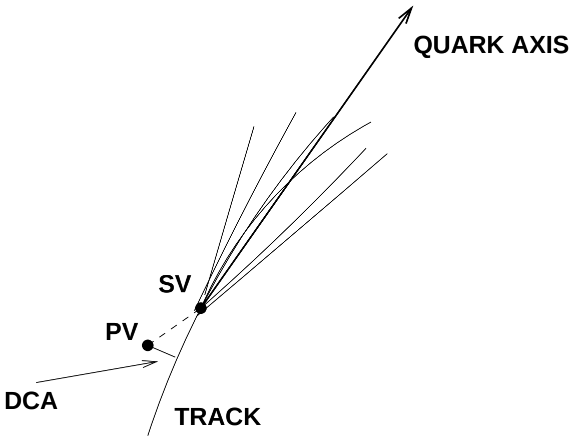

Figure 11.2: *Distance of closest approach (DCA) definition in the $r\phi$ plane.*

The definition of the DCA is illustrated in Fig. 11.2. Heavy hadrons, produced at the primary vertex (PV) according to quark fragmentation decay at the secondary vertex (SV). Firstly, in the analysis a jet coming from a certain quark decay is reconstructed. In this case the direction of the quark (*quark axis*) ϕ_{quark} is defined by the azimuthal angle of the jet with the highest transverse momentum. In contrast to the high Q^2 analysis, where also the angle θ was used, at low Q^2 the correlation between θ of the struck quark and θ of the hadronic final state (HFS) breaks down. Therefore, in this analysis only ϕ information will be used. If there are no jets reconstructed in the event, the quark axis is determined from the azimuthal angle of the scattered positron $\phi_{quark} = 180° - \phi_{\text{elec}}$ (see Section 12.5). The distance of closest approach δ is determined for each CST improved track associated to the quark axis within $|\Delta\phi| < \pi/2$.

Different signs are assigned to the DCA. If the angle between the quark axis and the line joining the primary vertex to the point of the DCA is less than 90°, δ is defined as positive, and is defined as negative otherwise (Fig. 11.3). The long lifetimes of c and b flavoured hadrons lead to larger track displacements than for light quark events, that leads to the excess of heavy flavour events in positive values of the DCA. The hadrons from light quarks come from the primary vertex and, therefore, their contribution to the signed DCA should peak at zero. However, due to the finite detector resolution it is spread symmetrically around zero. Moreover, there is some excess in positive DCA values due to the decays of K^0_s ($c\tau = 2.7$ cm).

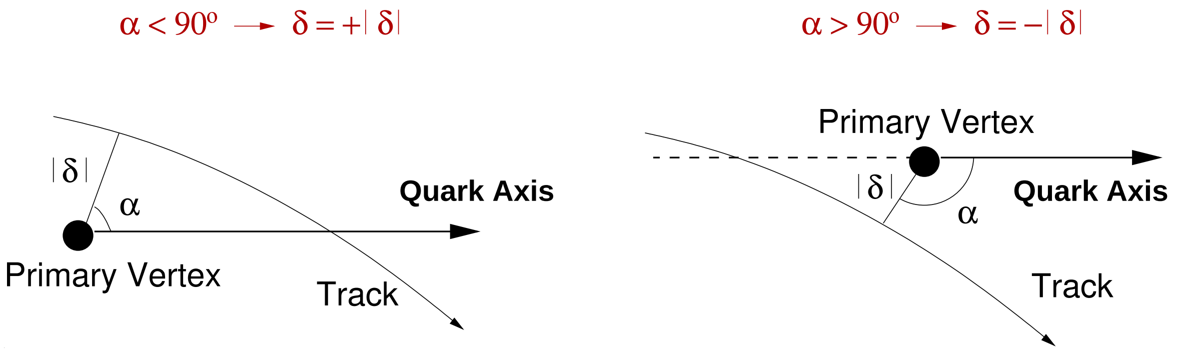

Figure 11.3: *Signed DCA definition in the $r\phi$ plane.*

The measurements at low Q^2 benefit from increased statistics when compared to those at high Q^2. However, the low Q^2 region is experimentally more challenging because the final state does not have as large a transverse boost in the laboratory frame. The separation between b and c events is also difficult since, although the c fraction is expected to be similar as at high Q^2, the b fraction is expected to be much smaller ($\sim 0.6\%$ at $Q^2 = 12$ GeV^2 [124, 129]).

11.4 Monte Carlo Samples

In this analysis, MC event generators are used to obtain the shape of charm, beauty and light quark event distributions and then to use them in the fit to the data to obtain the measured cross section of different quark flavour processes in dependence of MC scaling factors. This procedure is used to correct for the effects of the finite detector resolution, acceptance and efficiency.

The Monte Carlo programs used in the analysis are described in Section 9.10. The heavy flavour events for the processes $ep \rightarrow eb\bar{b}X$ and $ep \rightarrow ec\bar{c}X$ at low Q^2 DIS are generated with

Sample	Program	Fragmentation	L [pb^{-1}]
uds	DJANGO	LUND	90
$c\bar{c}$	RAPGAP	LUND	162.9
$b\bar{b}$	RAPGAP	LUND	981.3
$c\bar{c}$	RAPGAP	Peterson	124.54
$b\bar{b}$	RAPGAP	Peterson	969.05
$c\bar{c}$	CASCADE	LUND	124.6
$b\bar{b}$	CASCADE	LUND	671.53
γp	PHOJET	LUND	2.576

Table 11.3: *The Monte Carlo samples with fragmentation schemes and luminosities generated for the analysis.*

the RAPGAP Monte Carlo program. For the estimation of the systematic error from the fragmentation model, additional $c\bar{c}$ and $b\bar{b}$ samples are generated with RAPGAP using the Peterson fragmentation function instead of the LUND model (Section 9.9). For the systematic uncertainty due to the QCD modelling the MC program CASCADE is used to generate additional heavy flavour samples. Light quark (uds) events are generated with DJANGO. The photoproduction background ($\gamma p \to X$) is generated using the PHOJET Monte Carlo program. All generated event samples with their luminosities are summarised in Table 11.3. The parameters of the MC generators were optimised in order to obtain charged particle multiplicities, fragmentation fractions and the lifetimes of the D and B hadrons, consistent with the world average values (see Section 11.1).

All the MC event samples are passed through the H1 detector simulation program (see Section 10.2).

Chapter 12

Event Reconstruction and Selection

In this chapter, a standard selection procedure for low Q^2 deep inelastic scattering events will be described. The impact parameter inclusive analysis requires a CST improved track selection and quark axis determination which will be explained here. In the last section, basic DCA and significance distributions will be constructed.

12.1 Selection of Low Q^2 DIS Events

The analysis is based on a low Q^2 sample of e^+p neutral current scattering events corresponding to an integrated luminosity of 57.4 pb^{-1}, taken in the years 1999-2000, at an *ep* centre of mass energy $\sqrt{s} = 319$ GeV, with a proton beam energy of 920 GeV.

The events are selected by requiring:

- A compact electromagnetic cluster in the SPACAL associated with a track segment in the BDC to define the scattered positron candidate.
- The SPACAL cluster radius of the positron candidate (ECRA) should be less than 4 cm.
- The distance between the SPACAL cluster and a track segment in the BDC is required to be in the range $0 < R_{\text{BDC}-\text{SPACAL}} < 2.5$ cm.
- In order to have good acceptance for low Q^2 DIS events in the SPACAL, events are selected in the range $6.3 < Q^2 < 120$ GeV^2.
- The z position of the interaction vertex, reconstructed by one or more charged tracks in the tracking detectors, must be within ±20 cm of the centre of the detector to match the acceptance of the CST.
- Photoproduction events are suppressed by requiring $\sum_i (E_i - p_{z,i}) > 35$ GeV. Here, E_i and $p_{z,i}$ denote the energy and longitudinal momentum components of a particle and the sum is over all final state particles including the scattered positron and the hadronic final state (HFS).
- The analysis is restricted to $0.07 < y < 0.7$ to ensure that the direction of the quark which is struck by the photon is mostly in the CST angular range. A further cut of $y < 0.63$ is imposed for events with $Q^2 < 18$ GeV^2 to reduce photoproduction background.

The HFS particles are reconstructed using a combination of tracks and calorimeter deposits in an energy flow algorithm that avoids double counting. The event kinematics, Q^2 and the inelasticity variable y, are reconstructed with the $e\Sigma$ method (Section 9.1).

12.2 Trigger Selection

The triggers used in the analysis require a SPACAL energy deposit in association with a loose track requirement. Although these triggers are almost 100% efficient, not all events could be recorded, due to the large rate for low Q^2 events. A fraction of events is rejected at the first trigger level (L1) and final trigger level (L4). The Monte Carlo events are assigned weights to account for the events rejected at L1 and weights are assigned to the data events to account for the events rejected at L4. The weights are largest for those events with an electron at low radius and low energy. The overall effect of the trigger is a reduction of the effective luminosity by a factor of about 10 for the lowest Q^2 bin and 1.4 for the highest.

After applying the event weights and the inclusive selection detailed above the total number of events is about 1.5 million. Neutral current control distributions after selection cuts and trigger selection for the values of $\log_{10} Q^2$, $\log_{10} x$, energy of the scattered positron E, θ and ϕ angles of the scattered positron and the z coordinate of the vertex position are shown in Fig. 12.1. The poins represent H1 data. Red dashed curves correspond to photoproduction background, which is estimated from the PHOJET Monte Carlo simulation. In most of the y range this background is negligible and does not exceed 9% in any x-Q^2 bin used in this analysis. Magenta curves represent the sum of the light flavour events simulated by DJANGO Monte Carlo and heavy flavour events simulated by RAPGAP Monte Carlo. Black curves represent the total number of Monte Carlo events, consisting of the sum of light and heavy flavour events as well as photoproduction background. All the distributions are described by the MC simulation reasonably. The shape of the control distributions is affected by different L1 trigger acceptance regions. The discrepancy between the data and the MC simulation in the positron energy distribution E in the region of 10-15 GeV is covered by the systematic uncertainties.

12.3 Acceptance

The quark acceptance is defined as the fraction of c, b events which have a quark in the acceptance region of the CST ($30^o < \theta_q < 150^o$, $(p_T)_q > 0.5$ GeV) and have a generated z-vertex within ±20 cm. The track acceptance is defined as the fraction of c, b events which have a charged track in the acceptance region of the CST ($30^o < \theta_q < 150^o$, $(p_T)_q > 0.5$ GeV) and have a generated z-vertex within ±20 cm.

The quark acceptance distributions in the ($\log_{10} Q^2$, $\log_{10} x$) plane for the RAPGAP and CASCADE simulations are shown in Fig. 12.2. The lower x bound corresponds to upper y cut, the upper x bound corresponds to lower y cut. The parameter space ($\log_{10} Q^2$, $\log_{10} x$) is divided into six bins. The bin centres are chosen according to measurements of the inclusive cross section [155]. The acceptance is high in all bins for both c and b Monte Carlo simulations. The distributions for the track acceptance are shown in Fig. 12.3.

The quark and track acceptances for every bin as well as an integrated acceptance over all bins are summarised in Table 12.1 for the RAPGAP simulation. The quark acceptance for c is 63-97%, for b it is 84-94%. The track acceptance for c is 68-89% and for b it is in the range 93-99%. The track acceptance for two charged tracks to be in the acceptance region of the CST is 32-63% for c and 75-93% for b events. The track acceptance for three charged tracks to be in the acceptance region of the CST is 12-34% for c and 51-79% for b events. For the b events the track acceptance is higher than the quark acceptance. Moreover, b track acceptance is higher than c track acceptance because b hadrons have higher mass, higher transverse momentum p_T and higher decay charged multiplicity.

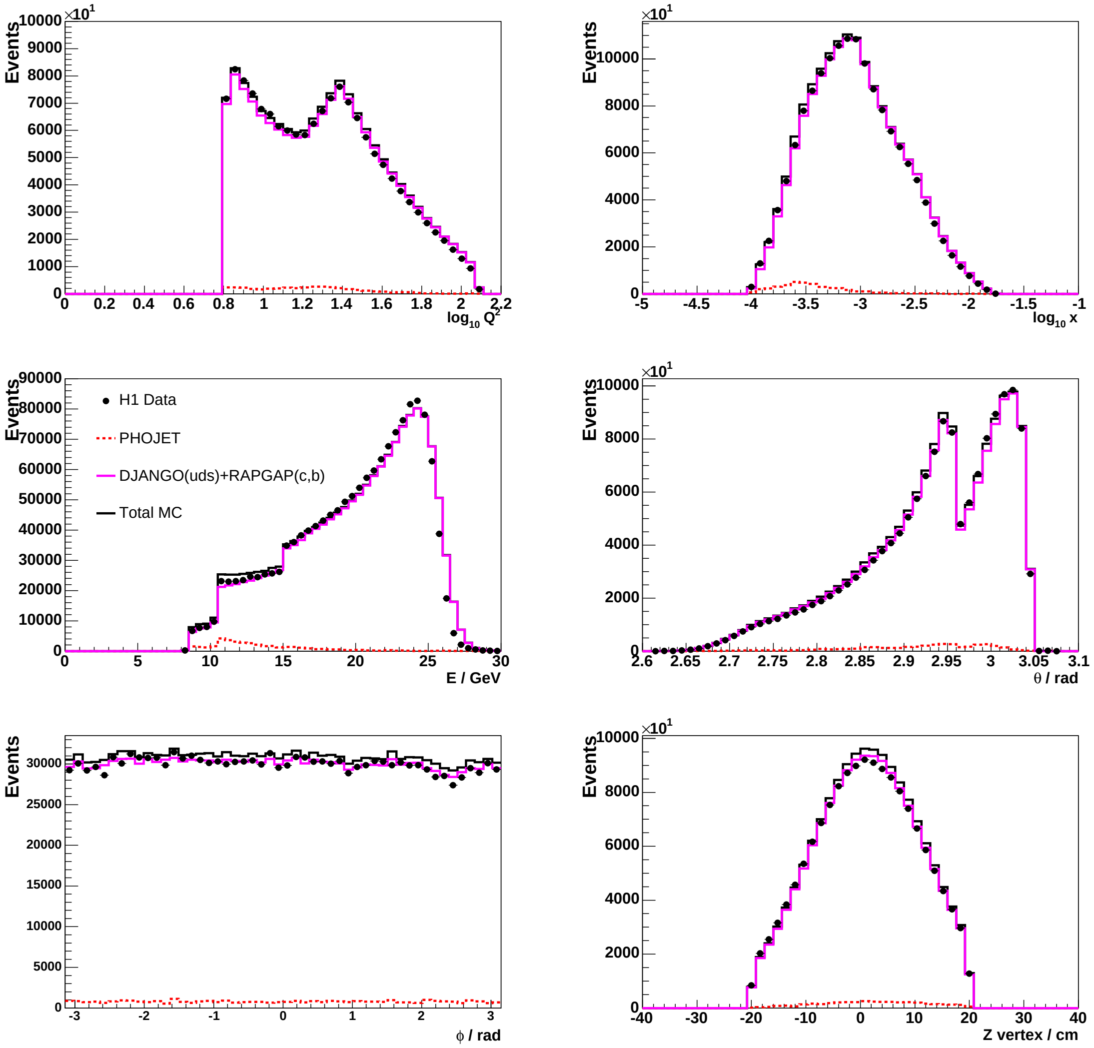

Figure 12.1: *Control distributions after selection cuts and trigger selection for the values of* $\log_{10} Q^2$, $\log_{10} x$, *energy of the scattered positron* E, θ *and* ϕ *angles of the scattered positron and* z *coordinate of the vertex position.*

12.4 Track Reconstruction and Selection

The association of the CST hits to the CJC tracks to determine the combined CJC-CST track parameters is crucial for the lifetime tag. First, the CJC tracks are reconstructed. The reconstruction algorithm determines the track parameters $\vec{T} = (\kappa, \phi_0, d_{ca})$ (Appendix A) of the particle trajectory, in the transverse plane, because the hit resolution in $r\phi$ is with $\mathcal{O}(200\ \mu\text{m})$ superior to the z resolution by two orders of magnitude. For the track fit a circular trajectory is assumed. The parameters (θ, z_0) describing the longitudinal track component are determined from a straight line fit in the zs plane, where s is the arclength.

To improve track reconstruction, the CST information is added to CJC tracks with a combined CJC-CST track fit, which determines CST improved track parameters (Fig. 12.4). The fit is done separately in the $r\phi$- and sz-plane. The CST space points and the measured CJC track parameters are used as input. A circle fit in $r\phi$ minimises the following χ^2 function

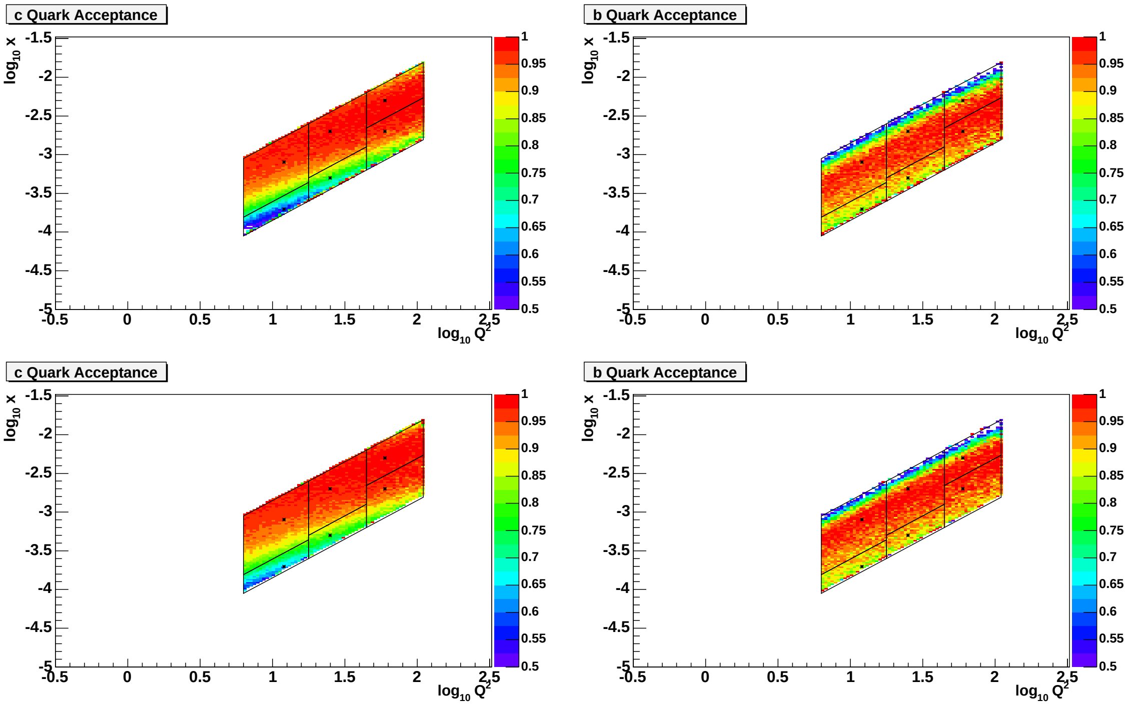

Figure 12.2: *The quark acceptance distributions for c and b events in the* ($\log_{10} Q^2$, $\log_{10} x$) *plane for the RAPGAP simulation (two upper figures) and for the CASCADE simulation (two lower figures).*

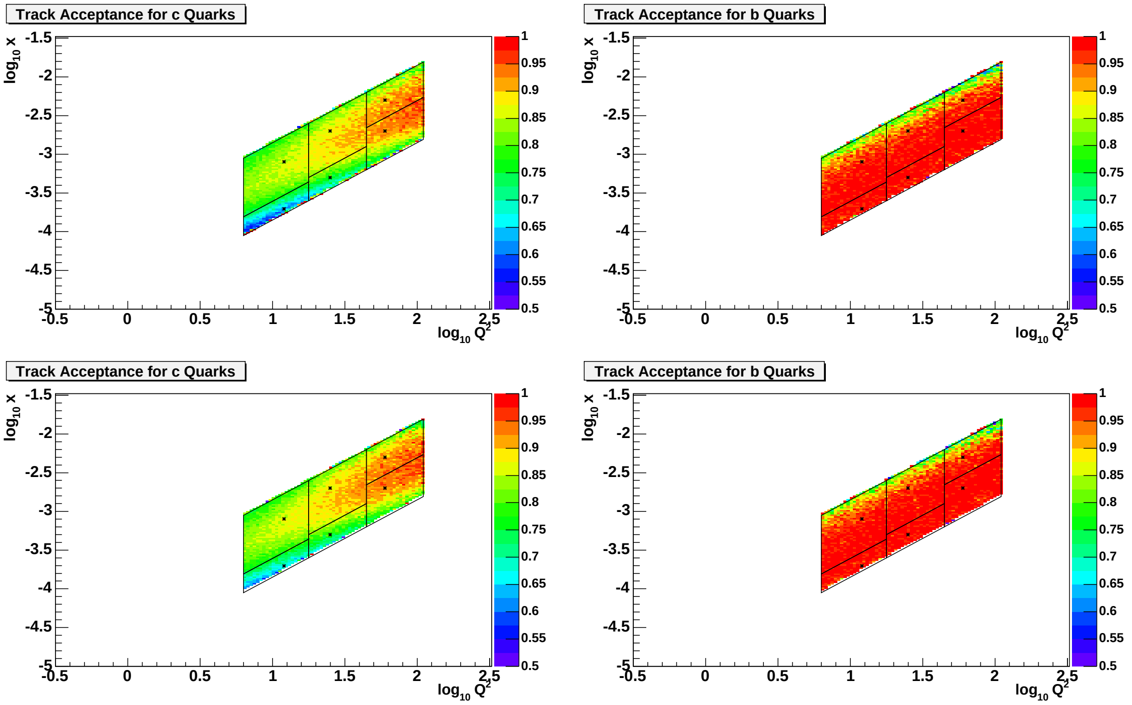

Figure 12.3: *The track acceptance distributions for c and b events in the* ($\log_{10} Q^2$, $\log_{10} x$) *plane for the RAPGAP simulation (two upper figures) and for the CASCADE simulation (two lower figures).*

bin	Q^2 [GeV^2]	x ($\cdot 10^{-3}$)	quark acc. [%]		track acc. [%]	
			c	b	c	b
1	12	0.197	63	87	68	98
2	12	0.800	92	90	82	96
3	25	0.500	78	90	78	98
4	25	2.000	96	90	87	95
5	60	2.000	92	94	89	99
6	60	5.000	97	84	89	93
Integrated			88	90	82	96

Table 12.1: *The quark and track acceptances for c and b events for the RAPGAP simulation. The values are shown for every bin Q^2-x as well as the integrated acceptance.*

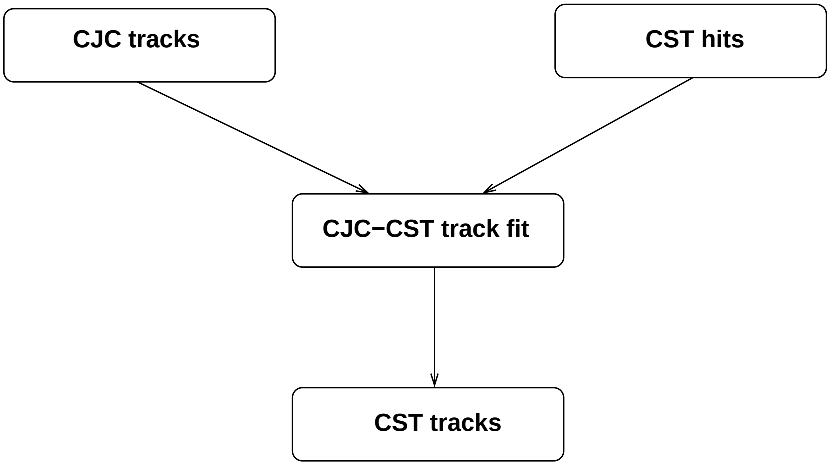

Figure 12.4: *CST track reconstruction.*

to determine the new track parameters $\vec{T}$:

$$\chi^2 = (\vec{T} - \vec{T}_{\mathrm{CJC}})^t V_{\mathrm{CJC}}^{-1} (\vec{T} - \vec{T}_{\mathrm{CJC}}) + \sum_{\text{hits } j} \frac{\Delta(\vec{T}, \mathrm{hit}_j)^2}{\sigma_\Delta^2}, \tag{12.1}$$

where $\vec{T}_{\mathrm{CJC}}$ and V_{CJC} denote the track parameters and their covariance matrix measured with the CJC. $\Delta(\vec{T}, \mathrm{hit}_j)$ and σ_Δ stand for the Euclidean distance between the track and the j-th CST space point and its calculated error. The sum runs over all CST hits linked to the CJC track. If the circle fit converges, it is followed by a straight line fit, which determines the parameters in the zs-plane. The combined CJC tracks with CST information are referred to as *CST tracks* in this thesis.

The link probability of the CST hits with the CJC tracks is defined as

$$\mathcal{P}_{\mathrm{track}}(\chi^2, N) = \frac{1}{\sqrt{2^N}\,\Gamma(N/2)} \int_{\chi^2}^{\infty} e^{-\frac{1}{2}t} t^{-\frac{1}{2}N-1} dt, \tag{12.2}$$

where χ^2 is defined in (12.1), and N denotes the number of linked CST hits. The efficiency to obtain a CST track from a CTD track is 76%, within the angular range of the CST.

The impact parameter of a track is defined as the transverse distance of closest approach (DCA) of the track to the primary vertex point. The primary event vertex in $r\phi$ is reconstructed from all tracks (with or without CST hits) and the position and spread of the beam interaction region [4]. The DCA is only determined for tracks which fulfil the following conditions:

- Tracks are measured in the CTD and have at least two CST hits linked (referred to as *CST tracks*).
- The link probability of the CST hits with the CTD tracks should be > 0.1.
- Only CST tracks with a transverse momentum $p_T > 0.5$ GeV are included in the DCA and related distributions that are used to separate the different quark flavours.
- The radius of the initial track point in the CJC is required to be $R_{\text{start}} < 50$ cm.
- The length of the track in the CJC should be more than 10 cm.
- The CST hits should be within a z region of $-18 < z_{\text{CST}} < 18$ cm, where z_{CST} is measured at the outer surface of the CST.

The distributions of p_T and θ of all CST tracks are shown in Fig. 12.5. The data are well described by the Monte Carlo. The positron candidates with an associated track in the CJC can be seen at large values of θ and are well described by the MC simulation.

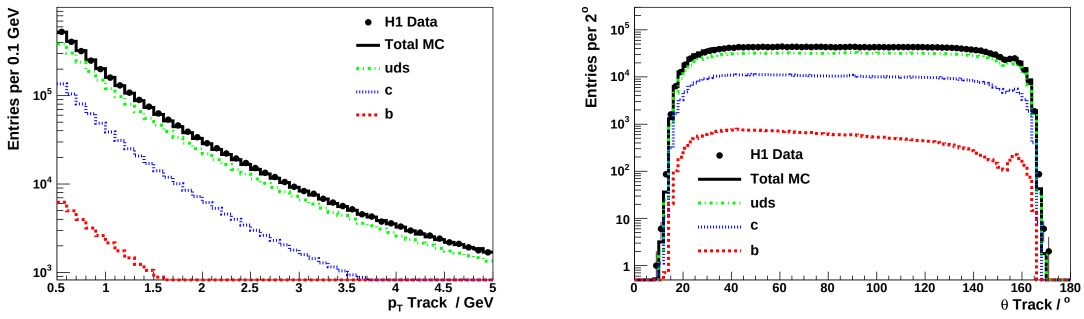

Figure 12.5: *The transverse momentum p_T (left figure) and the angle θ (right figure) of all CST tracks. The contributions from the various quark flavours are shown after applying the scale factors obtained from the fit to the subtracted significance distributions of the data (see Section 13.1).*

12.5 Jet Reconstruction and Selection

In order to determine a signed impact parameter (δ) for a track, the azimuthal angle of the struck quark ϕ_{quark} must be determined for each event. The angle ϕ_{quark} is defined as the azimuthal angle of the jet with the highest transverse momentum or, if there is no jet reconstructed in the event, as $180^\circ - \phi_{\text{elec}}$, where ϕ_{elec} is the azimuthal angle of the electron in degrees. The direction defined in the transverse plane by ϕ_{quark} and the primary vertex is called the *quark axis*.

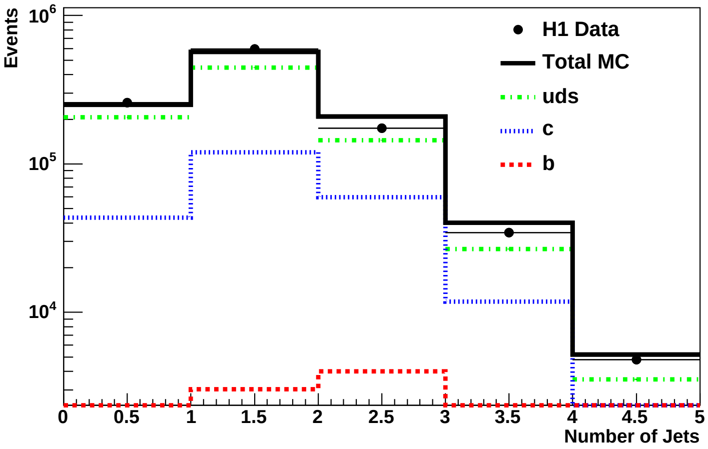

Figure 12.6: *The number of jets per event. The contributions from the various quark flavours are shown after applying the scale factors obtained from the fit to the subtracted significance distributions of the data (see Section 13.1).*

bin	Q^2 [GeV^2]	x $(\cdot 10^{-3})$	Data jet fraction	MC c jet fraction	MC b jet fraction
1	12	0.197	0.59	0.68	0.94
2	12	0.800	0.63	0.70	0.93
3	25	0.500	0.74	0.80	0.96
4	25	2.000	0.88	0.87	0.95
5	60	2.000	0.94	0.95	0.98
6	60	5.000	0.98	0.97	0.97

Table 12.2: *The jet fraction for data events and c and b RAPGAP Monte Carlo events in different Q^2-x bins.*

Jets are found using the invariant k_T algorithm [171, 172, 173] in the laboratory frame using all reconstructed HFS particles. In this analysis, a minimum p_T of 2.5 GeV and the angular range $15^\circ < \theta < 155^\circ$ are required for a jet. Approximately 81% (95%) of c (b) events have ϕ_{quark} reconstructed from a jet, as determined from a Monte Carlo simulation. In Fig. 12.6 the distribution of the number of jets is presented. In most cases there is one reconstructed jet per event.

Table 12.2 summarises the reconstructed *jet fraction* (the fraction of events with at least one reconstructed jet as defined above) in data events and heavy flavour events simulated using the RAPGAP Monte Carlo in different Q^2-x bins. According to the simulation the jet fraction for c events increases with Q^2 whereas the jet fraction for b events is fairly constant with Q^2. The jet fraction for data events, dominated by the *uds* component (see also Fig. 12.7), increases with Q^2 and with x. The overall jet fraction is 82% for c simulated events, 95% for b simulated events and 79% for data events. Similar fractions are obtained using the CASCADE MC.

Fig. 12.7 shows the number of events with at least one jet for different Q^2-x bins. There is a reasonable description of the overall jet fraction, which is dominated by the *uds* component. The first four bins show a higher number of jet events for higher x in the same Q^2 bin, i.e. there

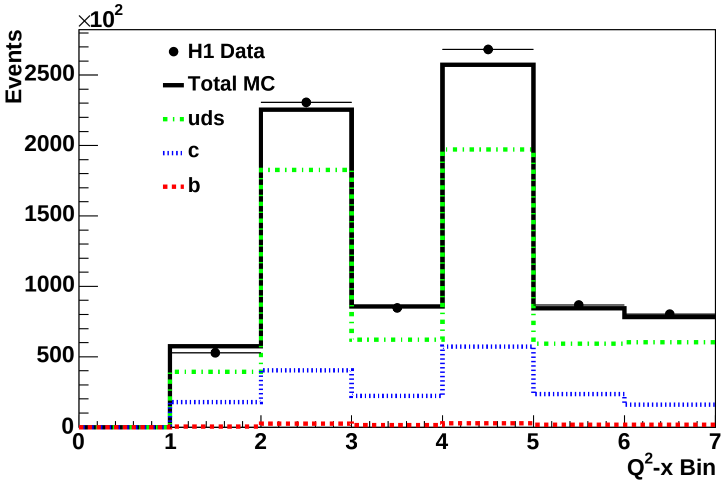

Figure 12.7: *The number of events with at least one jet for different Q^2-x bins. The contributions from the various quark flavours are shown after applying the scale factors obtained from the fit to the subtracted significance distributions of the data (see Section 13.1).*

are more *uds* jet events at higher x. Therefore for the two lower Q^2 bins at higher x more events are needed to distinguish c and b from *uds* events. In the other bins the number of c events with at least one reconstructed jet becomes comparable to the number of *uds* jet events.

The distributions of the transverse momentum p_T and angle θ of all jets are shown in Fig. 12.8. The events are dominated by small p_T jets. The description of the p_T distribution degrades towards larger p_T values due to a poor description of the light component. The distribution of the jet angle θ is described reasonably well by the MC.

In Fig. 12.9 the distributions of the jet transverse momentum p_T and angle θ of the events after subtracting events with $S_2 < 0$ (negative subtraction) and requiring $S_2 > 2$ are shown (see Section 13.1). These events are dominated by heavy flavours and the contribution of light quarks is very small. The description of the jet p_T is significantly improved.

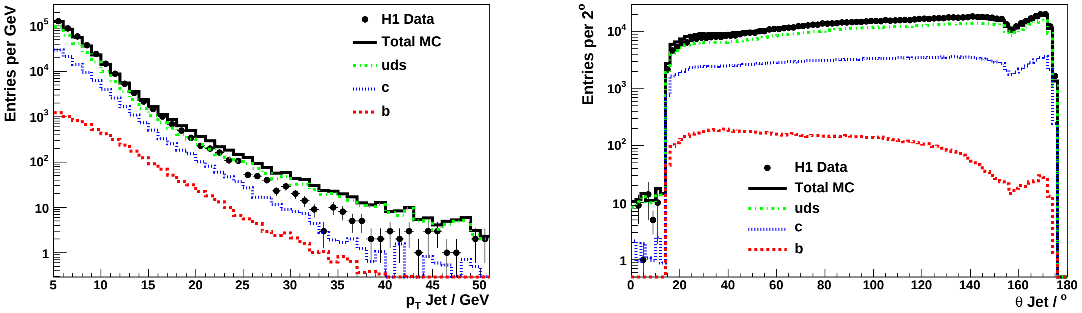

Figure 12.8: *The jet p_T (left figure) and θ (right figure). The contributions from the various quark flavours are shown after applying the scale factors obtained from the fit to the subtracted significance distributions of the data (see Section 13.1).*

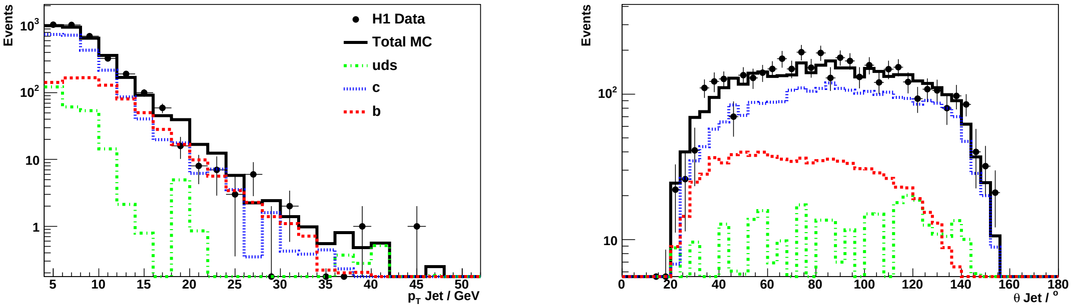

Figure 12.9: *The jet p_T (left figure) and θ (right figure) after subtracting events with $S_2 < 0$ and requiring $S_2 > 2$ (see Section 13.1). The contributions from the various quark flavours are shown after applying the scale factors obtained from the fit to the subtracted significance distributions of the data (see Section 13.1).*

12.6 Quark Axis Description

As it was explained in the previous section, the quark direction ϕ_{quark} is defined as the azimuthal angle of the jet with the highest transverse momentum or, if there is no jet reconstructed in the event, as $180° - \phi_{\text{elec}}$. The difference between the reconstructed and the true ϕ_{quark} is estimated from the Monte Carlo simulation to have a resolution of about 5° for events with a reconstructed jet and 35° for the rest. The resolution of ϕ_{quark} is checked with events containing a reconstructed D* meson. Fig. 12.10 shows the difference between the reconstructed D* azimuthal angle and ϕ_{quark} for events with and without a reconstructed jet. Both distributions are well described by the Monte Carlo simulation.

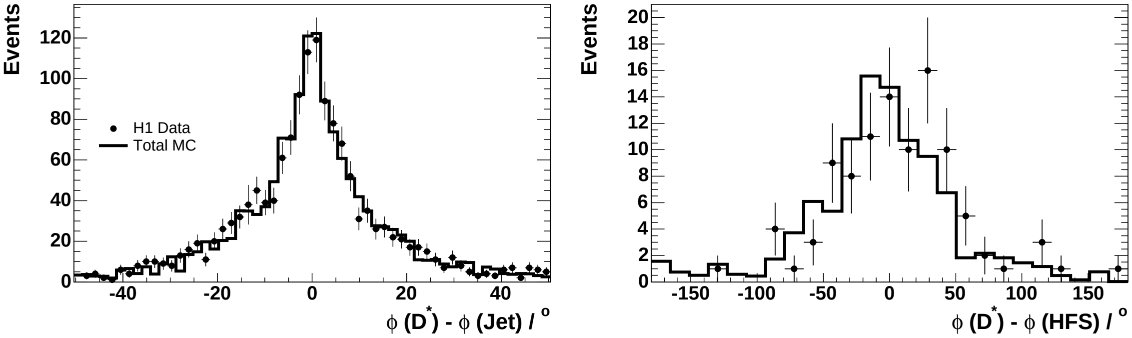

Figure 12.10: *The azimuthal difference between the D^* and the quark axis for those events where the quark axis is defined by a jet (left figure) and by $180° - \phi_{\text{elec}}$ (right figure). Included in the figure is the expectation from the Monte Carlo simulation normalised to the number of data events (see Section 13.1).*

12.7 Matching of Tracks to Quark Axis

For the calculation of the DCA only tracks matched to the quark axis in ϕ ($|\Delta\phi| < \pi/2$) are used. Tracks with azimuthal angle outside of a ±90° cone around ϕ_{quark} are rejected. Fig. 12.11 shows the distributions of the number of CST tracks per event before and after track association to the quark axis. It can be seen that 80% of the events have at least one CST track, and 71% of the events have at least one CST track associated to the quark axis within $|\Delta\phi| < \pi/2$, i.e. the efficiency of track matching to the quark axis is 89%.

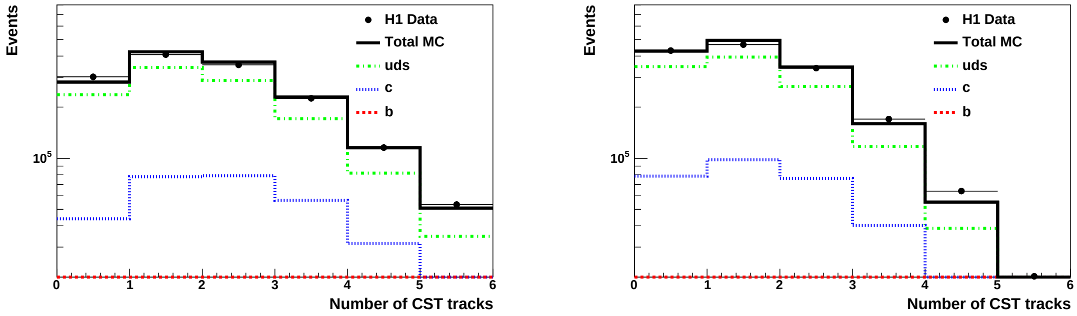

Figure 12.11: *The number of CST tracks per event before (left figure) and after (right figure) track association to the quark axis. The contributions from the various quark flavours are shown after applying the scale factors obtained from the fit to the subtracted significance distributions of the data (see Section 13.1).*

12.8 Distance of Closest Approach and Significance

The δ distribution defined in Section 11.3, constructed using tracks matched to the quark axis in ϕ ($|\Delta\phi| < \pi/2$), is shown in Fig. 12.12. It is seen to be asymmetric with positive values in excess of negative values indicating the presence of long lived particles. It is found to be well described by the Monte Carlo simulation. Tracks with $|\delta| > 0.1$ cm are rejected from the analysis to suppress light quark events containing long lived strange particles. The distribution of the error on DCA $\sigma(\delta)$ is shown in Fig. 12.13.

The significance of each track S_i is defined as

$$S_i = \frac{\delta}{\sigma(\delta)}, \tag{12.3}$$

where $\sigma(\delta)$ is the error on DCA. It is constructed to enhance the contribution of well measured tracks. The distribution of S_i for all tracks is shown in Fig. 12.14. Like the DCA distribution, it shows an excess of positive values over negative values due to the presence of long lived particles.

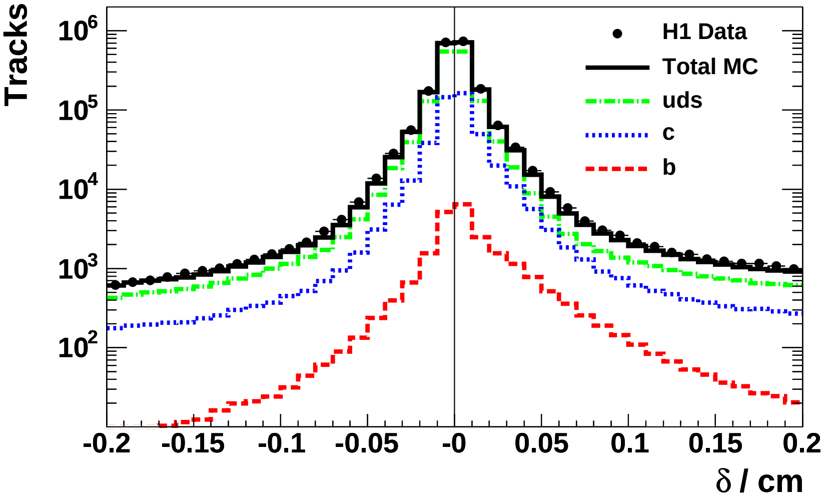

Figure 12.12: *The signed impact parameter δ of a track to the primary vertex in the xy plane. The contributions from the various quark flavours are shown after applying the scale factors obtained from the fit to the subtracted significance distributions of the data (see Section 13.1).*

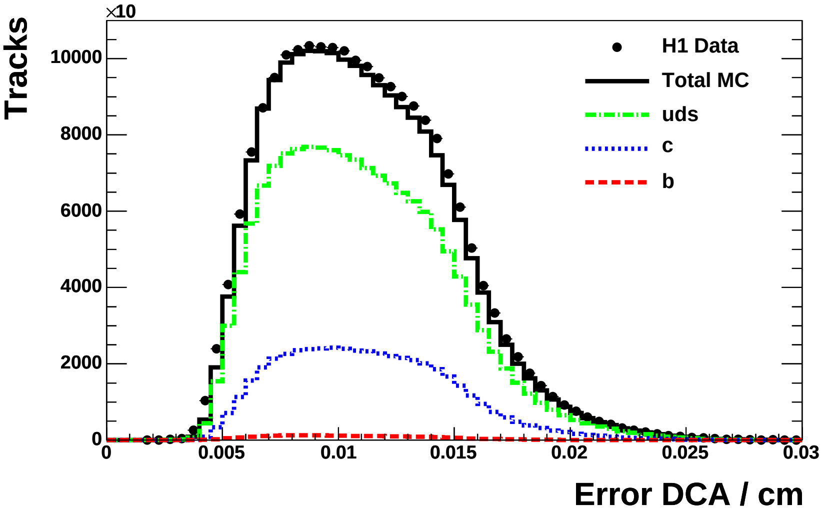

Figure 12.13: *The error on DCA $\sigma(\delta)$. The contributions from the various quark flavours are shown after applying the scale factors obtained from the fit to the subtracted significance distributions of the data (see Section 13.1).*

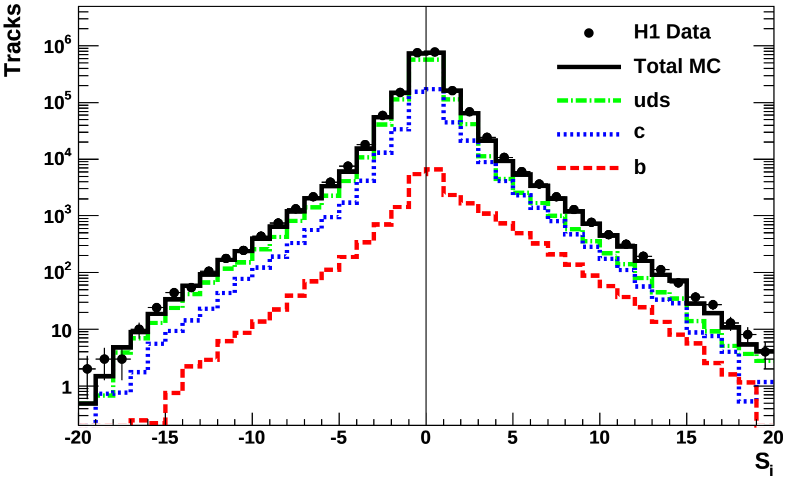

Figure 12.14: *Significance of each track. The contributions from the various quark flavours are shown after applying the scale factors obtained from the fit to the subtracted significance distributions of the data (see Section 13.1).*

Chapter 13

Measurement of $F_2^{c\bar{c}}$ and $F_2^{b\bar{b}}$ at Low Q^2

In this chapter, the separation of charm, beauty and light flavour events, using a fit of specially constructed significance distributions, will be explained. The systematic errors of the measurements will be briefly summarised. In the last section, the procedure of the cross section calculation as well as the extraction of the structure functions $F_2^{c\bar{c}}$ and $F_2^{b\bar{b}}$ will be explained.

13.1 Quark Flavour Separation

The method used in [4] to distinguish between the c, b and light quark flavours has been modified in the present analysis because here the fraction of b quarks is smaller. The quantities S_1, S_2 and S_3 are defined as the significance ($\delta/\sigma(\delta)$) of the track with the highest, second highest and third highest absolute significance, respectively, where $\sigma(\delta)$ is the error on δ (see Section 12.8). Distributions of each of these quantities are made. The events contributing to the S_2 distribution also contribute to the S_1 distribution. Similarly, those contributing to the S_3 distribution also contribute to the S_2 and S_1 distributions. Events in which S_1 and S_2 have opposite signs are excluded from the S_2 distribution. Events in which S_1, S_2 and S_3 do not all have the same sign are excluded from the S_3 distribution.

Fig. 13.1 (left figures) shows the three significance distributions. The simulation gives a reasonable description of the data. In order to substantially reduce the uncertainty due to the resolution of δ and the light quark normalisation, the contents of the negative bins in the significance distributions are subtracted from the contents of the corresponding positive bins. The subtracted distributions are shown in Fig. 13.1 (right figures). It can be seen that the resulting distributions are dominated by c quark events, with a b fraction increasing with significance. The light quarks contribute a small fraction for all the values of the significance. The numbers of data events contributing to S_1, S_2 and S_3 as well as their subtracted distributions are summarised in Table 13.1.

The fractions of c, b and light quarks of the data are extracted in each Q^2–x interval using a least squares simultaneous fit to the subtracted S_1, S_2 and S_3 distributions (as in Fig. 13.1) and the total number of inclusive events before any CST track selection. The c, b and uds Monte Carlo simulation samples are used as templates. The Monte Carlo c, b and uds contributions in each Q^2–x interval are scaled by factors P_c, P_b and P_l, respectively, to give the best fit to the observed subtracted S_1, S_2, S_3 and total distributions. Only the statistical errors of the data and Monte Carlo simulation are considered in the fit. The fit to the subtracted significance distributions mainly constrains P_c and P_b, whereas the overall

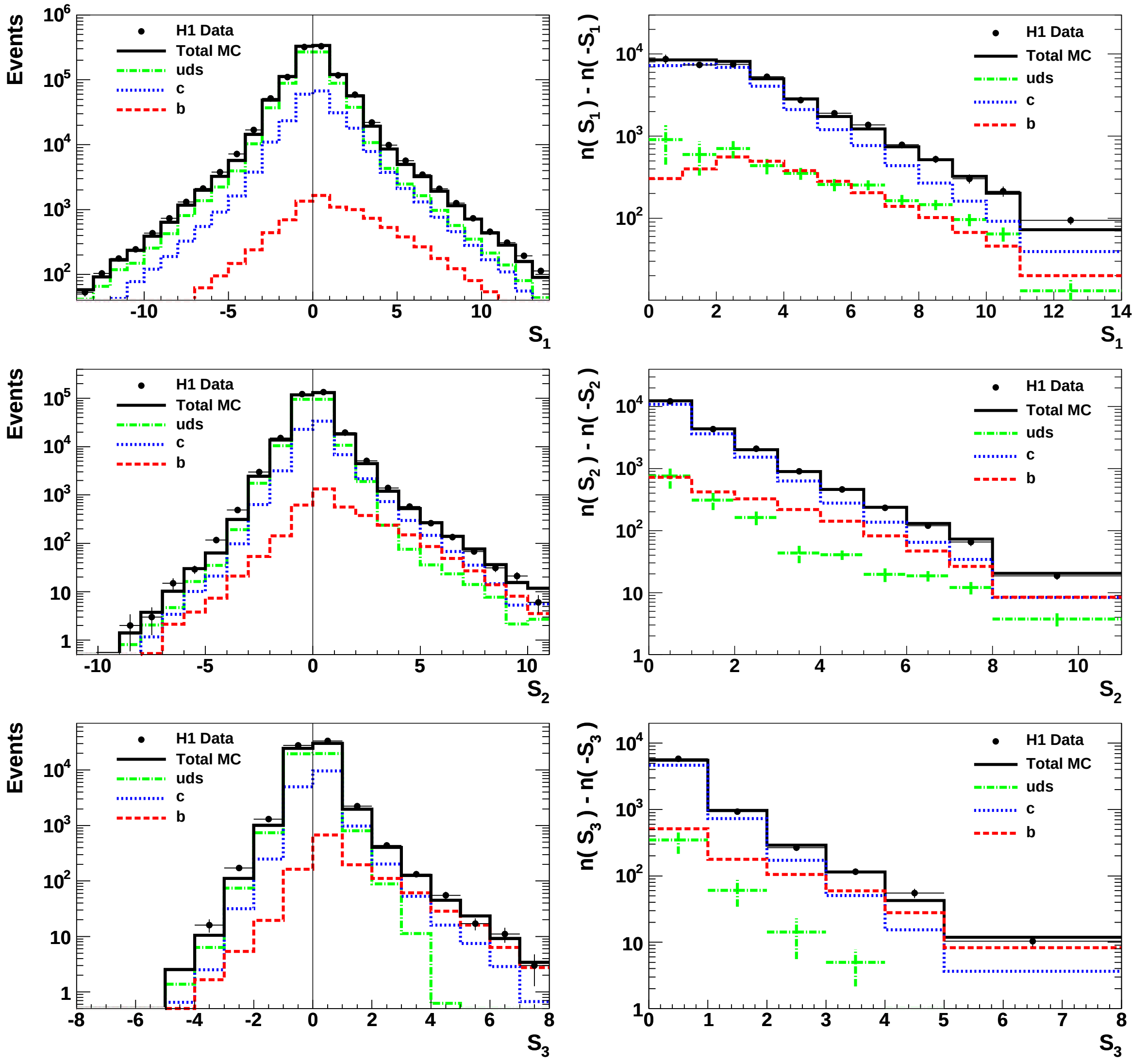

Figure 13.1: *The significance* $\delta/\sigma(\delta)$ *distribution of the highest absolute significance track* S_1*, of the track with the second highest absolute significance* S_2 *and of the track with the third highest absolute significance* S_3 *(left figures). The subtracted distributions of* S_1*,* S_2 *and* S_3 *(right figures). The contribution from the various quark flavours are shown after applying the scale factors obtained from the fit to the subtracted significance distributions of the data.*

	N_{events}		N_{events}
S_1	850363	subtracted S_1	36742
S_2	255769	subtracted S_2	20374
S_3	59038	subtracted S_3	7172

Table 13.1: *The number of data events contributing to S_1, S_2 and S_3 as well as to their subtracted distributions.*

normalisation constrains P_l.

The results of the fit to the complete data sample are shown in Fig. 13.1. The fit gives a good description of all the significance distributions, with a $\chi^2/n.d.f.$ of 18.0/25. The following scale factors for different MC contributions are obtained:

$$\begin{aligned} P_c &= 1.28 \pm 0.04, \\ P_b &= 1.55 \pm 0.16, \\ P_l &= 0.95 \pm 0.01. \end{aligned} \tag{13.1}$$

The c and b scale factors are found to be anticorrelated with an overall correlation coefficient of -0.70. Acceptable χ^2 values are also found for the fits to the samples in the separate x–Q^2 intervals. Since the same event may enter the S_1, S_2 and S_3 distributions, it was checked using a high statistics Monte Carlo simulation that this has negligible effect on the results of the fits with the present data statistics.

13.2 Systematic Errors

The systematic uncertainties on the measured cross sections are estimated by applying variations to the Monte Carlo simulation. The following sources of systematic error have been considered:

DCA resolution. An uncertainty in the δ resolution of the tracks is estimated by varying the resolution by an amount that encompasses the differences between the data and simulation (Fig. 12.12, 13.1). This was achieved by applying an additional Gaussian smearing in the Monte Carlo of 200 μm to 5% of randomly selected tracks and 25 μm to the rest. The significance distributions S_1, S_2, S_3 are shown in Fig. 13.2 with the Monte Carlo simulations before (black lines) and after (red dashed lines) DCA smearing in linear (left figures) and logarithmic (right figures) scales.

Track efficiency. A track efficiency uncertainty of 2% due to the CTD and of 1% due to the CST.

Meson multiplicity error. The uncertainties on the various D and B meson lifetimes, decay branching fractions and mean charge multiplicities are estimated by varying the input values of the Monte Carlo simulation by the errors on the world average measurements. For the branching fractions of b quarks to hadrons and the lifetimes of the D and B mesons the central values and errors on the world averages are taken from [174]. For the branching fractions of c quarks to hadrons the values and uncertainties are taken from [156], which are consistent with measurements made in DIS at HERA [175]. For the mean charged track multiplicities the values and uncertainties for c and b quarks are taken from MarkIII [159] and LEP/SLD [157] measurements, respectively.

Fragmentation function error. An uncertainty on the fragmentation function of the heavy quarks is estimated using the Peterson fragmentation function [139] with parameters $\epsilon_c = 0.058$ and $\epsilon_b = 0.0069$, instead of the LUND fragmentation model.

QCD model. An uncertainty on the QCD model of heavy quark production is estimated by using the CASCADE Monte Carlo where CCFM evolution equation is used for parton distribution functions instead of the RAPGAP Monte Carlo with DGLAP evolution equation.

Light quark DCA asymmetry. The uncertainty on the asymmetry of the light quark δ distribution is estimated by repeating the fits with the subtracted light quark significance distributions (Fig. 13.1 (right figures)) changed by ±50%. The light quark asymmetry was checked to be within this uncertainty by comparing the asymmetry of Monte Carlo events to that of the data, in the region $0.1 < |\delta| < 0.5$ cm, where the light quark asymmetry is enhanced. This is demonstrated in Fig. 13.3. In the left figure, the mass of two tracks is plotted for the negative subtracted events with $0.1 < |\delta| < 0.5$ cm where strangeness is enhanced. The figure shows a clear K^0 peak at $m_{K^0} = 498$ MeV. In the right figure, the variation of the Monte Carlo simulation by ±50% is shown.

Quark axis error. An error on the quark axis is estimated by shifting the quark axis by 2° (5°) for events with (without) a reconstructed jet. These shifts were estimated by comparing the difference between ϕ_{quark} and the track azimuthal angle in data and Monte Carlo (see also Fig. 12.10).

Hadronic energy scale. A 4% uncertainty on the hadronic energy scale.

Input structure functions error. Uncertainties on the acceptance and bin centre correction due to the input structure functions used are estimated by reweighting the input $\tilde{\sigma}^{c\bar{c}}$ distribution by $x^{\pm 0.1}$ and $1 \pm 0.2 \ln[Q^2/(10\ \text{GeV}^2)]$ and $\tilde{\sigma}^{b\bar{b}}$ by $x^{\pm 0.3}$ and $1 \pm 0.4 \ln[Q^2/(10\ \text{GeV}^2)]$. The range of variation of the input structure functions was estimated by comparing to the measured values obtained in this analysis.

Photoproduction background. An uncertainty on the photoproduction background is estimated by assigning ±100% of the expected number of events from the PHOJET simulation that enter the significance distributions.

Other sources of systematic error pertaining to the NC selection were also considered [155]: a 1.5% uncertainty on the luminosity measurement; an uncertainty on the scattered positron polar angle of 0.3 mrad and energy of 0.3–1.0% depending on the energy; a 0.5% uncertainty on the scattered positron identification efficiency; a 0.5–2% uncertainty on the positron track-cluster link efficiency; a $\leq 1\%$ uncertainty on the trigger efficiency and a 1% uncertainty on the cross section evaluation due to QED radiative corrections.

A detailed list of the systematic effects on each cross section measurement is given in Table 13.2. The contributions from errors correlated between all cross section bins are separated from systematic errors which are uncorrelated from bin to bin. The correlated systematic error means that for example a 1σ shift upward for the systematic error can cause a shift of all cross section points. The uncorrelated errors are assumed to be due to local fluctuations or deficiencies and can cause a change of the cross section value in some kinematic range without having impact in other kinematic range.

The systematic error in Table 13.2 is larger for the b measurement than it is for the c because the b fraction is much smaller than the c fraction. The errors which contribute

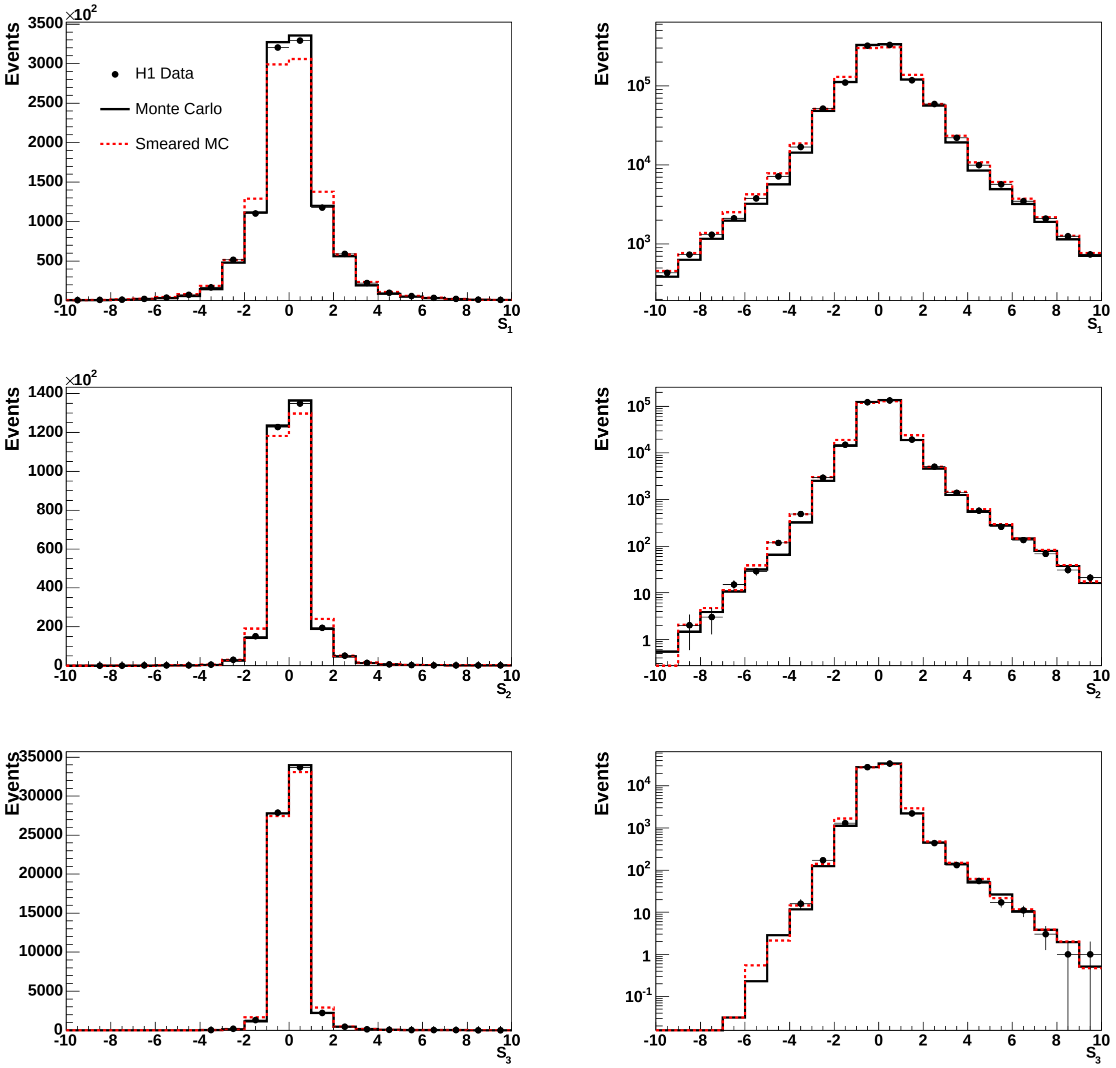

Figure 13.2: *The significance distributions S_1, S_2, S_3 in linear (left figures) and logarithmic (right figures) scales. The Monte Carlo simulations are shown before (black lines) and after (red dashed lines) DCA smearing.*

most to the uncorrelated systematic error are, at low Q^2 and high y, the uncertainty on the photoproduction background and, elsewhere, the uncertainty on the acceptance and bin centre correction due to the input structure function.

13.3 Cross Section and $F_2^{c\bar{c}}$, $F_2^{b\bar{b}}$ Measurements

The results of the fit in each Q^2–x interval are converted to a measurement of the 'reduced c cross section' defined from the differential cross section, according to (9.10), as

$$\tilde{\sigma}^{c\bar{c}}(x, Q^2) = \frac{\mathrm{d}^2\sigma^{c\bar{c}}}{\mathrm{d}x\,\mathrm{d}Q^2}\frac{xQ^4}{2\pi\alpha^2(1+(1-y)^2)}, \qquad (13.2)$$

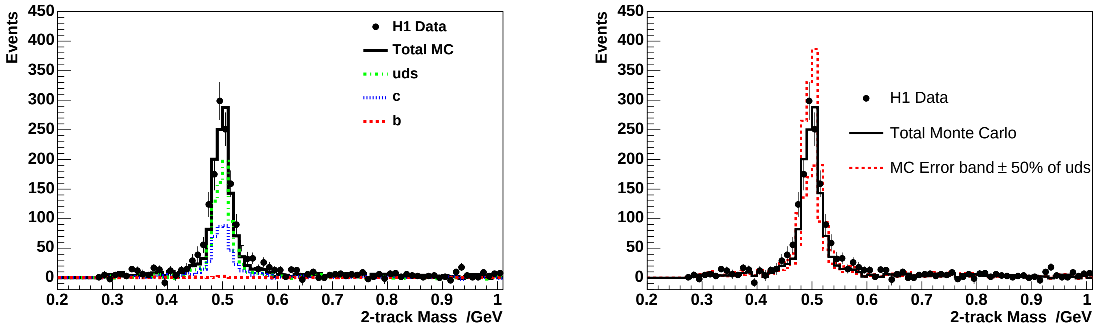

Figure 13.3: *The mass of two tracks for the negative subtracted events with* $0.1 < |\delta| < 0.5$ cm *(left figure). The contribution from the various quark flavours are shown after applying the scale factors obtained from the fit to the subtracted significance distributions of the data. The variation of the Monte Carlo simulation by* ±50% *(right figure).*

using:

$$\tilde{\sigma}^{c\bar{c}}(x,Q^2) = \tilde{\sigma}(x,Q^2)\frac{P_c N_c^{\rm MCgen}}{P_c N_c^{\rm MCgen} + P_b N_b^{\rm MCgen} + P_l N_l^{\rm MCgen}}\delta_{\rm BCC}, \qquad (13.3)$$

where $\tilde{\sigma}(x,Q^2)$ is the measured inclusive reduced cross section from H1 [155] and $N_c^{\rm MCgen}$, $N_b^{\rm MCgen}$ and $N_l^{\rm MCgen}$ are the number c, b and light quark events generated from the Monte Carlo in each bin. A bin centre correction $\delta_{\rm BCC}$ is applied using an NLO QCD expectation for

	Q^2–x bin	$\delta_{\rm res}$ [%]	$\delta_{\rm eff}$ [%]	$\delta_{\rm Dmul}$ [%]	$\delta_{\rm Bmul}$ [%]	$\delta_{\rm frag}$ [%]	$\delta_{\rm model}$ [%]	δ_{uds} [%]	δ_{ϕ} [%]	C_{cb}	$\delta_{\rm unc}$ [%]	$\delta_{\rm sys}$ [%]
c	1	+3.2	-1.4	-3.1	-0.3	-0.7	-1.9	-5.0	+2.0	-0.62	11	13
	2	+2.5	-1.7	-3.2	-0.2	-0.4	-2.2	-5.2	+2.0	-0.68	5.6	9.4
	3	+3.1	-1.4	-3.1	-0.3	-0.7	-1.9	-5.0	+2.0	-0.66	6.8	10
	4	+2.6	-1.6	-3.1	-0.2	-0.5	-2.1	-5.2	+2.0	-0.72	4.1	8.6
	5	+3.2	-1.4	-3.1	-0.3	-0.7	-1.9	-5.0	+2.0	-0.74	3.5	8.3
	6	+2.7	-1.6	-3.1	-0.2	-0.5	-2.1	-5.1	+2.0	-0.76	3.8	8.5
b	1	-13	-7.5	-2.9	+3.0	+4.6	+8.9	-4.8	+1.3	-0.62	12	22
	2	-21	-10	-5.4	+3.1	+6.9	+15	-7.7	+1.7	-0.68	13	33
	3	-13	-7.6	-3.0	+3.0	+4.7	+9.1	-4.8	+1.3	-0.66	9.1	21
	4	-18	-9.4	-4.7	+3.1	+6.3	+13	-6.8	+1.6	-0.72	9.8	28
	5	-13	-7.5	-2.9	+3.0	+4.6	+8.8	-4.7	+1.3	-0.74	6.2	20
	6	-16	-8.8	-4.1	+3.0	+5.8	+12	-6.1	+1.5	-0.76	7.4	25

Table 13.2: *First 8 columns represent a* 1σ *shift upward for the correlated systematic error contributions for different* Q^2–x *bins from: track resolution, track efficiency, D multiplicity, B multiplicity, fragmentation, QCD model, light quarks and quark axis* $\phi_{\rm quark}$. *The* 1σ *shifts downward errors are the negative of the upward errors. The errors are correlated between charm and beauty but uncorrelated to inclusive data, apart from a normalisation uncertainty of* 1.5% *which is* 100% *correlated. The last three columns are the correlation coefficients* (C_{cb}), *the uncorrelated systematic error* ($\delta^{\tilde{\sigma}}_{\rm unc}$) *and the total systematic error* ($\delta^{\tilde{\sigma}}_{\rm sys}$).

$\tilde{\sigma}^{c\bar{c}}$ to convert the bin averaged measurement into a measurement at a given Q^2–x point. The NLO QCD expectation is calculated from the results of a fit similar to that performed in [176] but using the FFNS scheme to generate heavy flavours. A small correction ($\leq 2.6\%$) is applied, using the NLO QCD expectation, to the measurement of $\tilde{\sigma}(x, Q^2)$ which was performed at a lower centre of mass energy of 301 GeV than the data presented here. The cross section is defined so as to include a correction for pure QED radiative effects. Events that contain c hadrons via the decay of b hadrons are not included in the definition of the c cross section. The differential b cross section is evaluated in the same manner. The measured values of $\tilde{\sigma}^{c\bar{c}}$ and $\tilde{\sigma}^{b\bar{b}}$ in different bins with bin centre correction values δ_{BCC} are presented in Table 13.3 together with statistical and systematic errors.

The structure function $F_2^{c\bar{c}}$ is evaluated from (9.9), using a measured reduced cross section (13.3):

$$F_2^{c\bar{c}} = \tilde{\sigma}^{c\bar{c}} + \frac{y^2}{1+(1-y)^2} F_L^{c\bar{c}}, \tag{13.4}$$

where the longitudinal structure function $F_L^{c\bar{c}}$ is estimated from the NLO QCD expectation. The structure function $F_2^{b\bar{b}}$ is evaluated in the same manner. The measured values of $F_2^{c\bar{c}}$ and $F_2^{b\bar{b}}$ in different bins are presented in Table 13.4 together with $F_L^{c\bar{c}}$ and $F_L^{b\bar{b}}$ corrections to structure functions.

quark	Q^2 [GeV^2]	x ($\cdot 10^{-3}$)	y	$\delta_{\rm BCC}$	$\tilde{\sigma}^{q\bar{q}}$	$\delta_{\rm stat}$ [%]	$\delta_{\rm sys}$ [%]	$\delta_{\rm tot}$ [%]
c	12	0.197	0.600	1.09453	0.412	12	13	18
	12	0.800	0.148	1.05705	0.185	8.8	9.4	13
	25	0.500	0.492	1.00018	0.318	8.7	10	13
	25	2.000	0.123	0.96833	0.212	5.2	8.6	10
	60	2.000	0.295	0.98073	0.364	6.2	8.3	10
	60	5.000	0.118	1.00185	0.200	7.8	8.5	12
b	12	0.197	0.600	1.21786	0.0045	55	22	60
	12	0.800	0.148	1.12054	0.0048	30	33	45
	25	0.500	0.492	0.96400	0.0122	22	21	31
	25	2.000	0.123	0.89229	0.0061	26	28	39
	60	2.000	0.295	0.92090	0.0189	21	20	29
	60	5.000	0.118	0.96241	0.0130	26	25	36

Table 13.3: *The bin centre correction $\delta_{\rm BCC}$, the measured reduced NC cross section ($\tilde{\sigma}$) for charm (c) and beauty (b) quarks, the statistical error ($\delta^{\tilde{\sigma}}_{\rm stat}$), the systematic error ($\delta^{\tilde{\sigma}}_{\rm sys}$), the total error ($\delta^{\tilde{\sigma}}_{\rm tot}$) in different Q^2–x bins.*

quark	Q^2 [GeV^2]	x ($\cdot 10^{-3}$)	y	$F_2^{q\bar{q}}$	$F_L^{q\bar{q}}$ correction
c	12	0.197	0.600	0.435	1.05586
	12	0.800	0.148	0.186	1.00217
	25	0.500	0.492	0.331	1.04073
	25	2.000	0.123	0.212	1.00175
	60	2.000	0.295	0.369	1.01278
	60	5.000	0.118	0.201	1.00173
b	12	0.197	0.600	0.0045	1.01379
	12	0.800	0.148	0.0048	1.00059
	25	0.500	0.492	0.0123	1.01447
	25	2.000	0.123	0.0061	1.00068
	60	2.000	0.295	0.0190	1.00775
	60	5.000	0.118	0.0130	1.00109

Table 13.4: *The measured structure functions $F_2^{c\bar{c}}$ and $F_2^{b\bar{b}}$ in different Q^2–x bins, obtained from the measured cross sections using the NLO QCD fit to correct for $F_L^{c\bar{c}}$ and $F_L^{b\bar{b}}$. The last column represents $F_L^{c\bar{c}}$ and $F_L^{b\bar{b}}$ corrections to structure functions.*

Chapter 14

Discussion of the Results

The measurements of $\tilde{\sigma}^{c\bar{c}}$ are listed in Table 13.3 and shown in Fig. 14.1 as a function of x for fixed values of Q^2. The measurements in the two highest Q^2 bins ($Q^2 = 200$, $650\ \mathrm{GeV}^2$) are taken from [4]. The H1 data for $\tilde{\sigma}^{c\bar{c}}$ are compared with the results extracted from D* meson measurements by H1 [163] and ZEUS [164] obtained using an NLO program [177] based on DGLAP evolution to extrapolate the measurements outside the visible D* range. The measurements for $\tilde{\sigma}^{c\bar{c}}$ from the present analysis and the D* extraction methods are in good agreement.

The $\tilde{\sigma}^{c\bar{c}}$ data are compared with two VFNS predictions using NLO QCD (see Section 9.8) from MRST [129] and CTEQ [124], and with predictions based on CCFM [119] parton evolution with a massive scheme for heavy flavour production. The predictions provide a reasonable description of the present data.

The measurements of $\tilde{\sigma}^{b\bar{b}}$ are also listed in Table 13.3 and are shown in Fig. 14.2 as a function of x for fixed values of Q^2. This is the first measurement of $\tilde{\sigma}^{b\bar{b}}$ in this kinematic range. The $\tilde{\sigma}^{b\bar{b}}$ data are also compared with the two VFNS NLO QCD predictions and the CCFM prediction. The difference between the two VFNS NLO QCD calculations, which reaches a factor 2 at the lowest Q^2 and x, arises from the different treatments of threshold effects in the region $Q^2 \sim m_{c,b}^2$ by MRST and CTEQ. Within the current experimental errors these differences cannot be resolved.

The measurements of $F_2^{c\bar{c}}$ and $F_2^{b\bar{b}}$ are listed in Tab. 13.4 and shown as a function of Q^2 in Fig. 14.3 and Fig. 14.4. This is the first $F_2^{b\bar{b}}$ measurement in low Q^2 region. The measurements of $F_2^{c\bar{c}}$ and $F_2^{b\bar{b}}$ show positive scaling violations which increase with decreasing x. The data are compared with the VFNS QCD predictions from MRST and CTEQ at NLO and a recent calculation at NNLO [120]. The data are more precise than the spread in predictions of the QCD calculations which increases towards low x and low Q^2, where threshold effects play a larger role. In the lowest x bins the $F_2^{c\bar{c}}$ data tend to follow the MRST predictions. For $F_2^{b\bar{b}}$ more statistics are needed to differentiate between the models.

The measurements are also presented in Table 14.1 and Fig. 14.5 in the form of the fractional contribution to the total *ep* cross section

$$f^{c\bar{c}} = \frac{\mathrm{d}^2\sigma^{c\bar{c}}}{\mathrm{d}x\,\mathrm{d}Q^2} \Big/ \frac{\mathrm{d}^2\sigma}{\mathrm{d}x\,\mathrm{d}Q^2}. \tag{14.1}$$

The b fraction $f^{b\bar{b}}$ is defined in the same manner. In the present kinematic range the value of $f^{c\bar{c}}$ is around 24% on average and increases slightly with increasing Q^2 and decreasing x. The value of $f^{b\bar{b}}$ increases rapidly with Q^2 from 0.4% at $Q^2 = 12\ \mathrm{GeV}^2$ to 1.5% at $Q^2 = 60\ \mathrm{GeV}^2$. The NLO QCD predictions of MRST, based on VFNS, are found to describe the data reasonably

quark	Q^2 [GeV^2]	x ($\cdot 10^{-3}$)	y	$f_{q\bar{q}}$	$\delta^{qq}_{\mathrm{stat}}$ (%)	$\delta^{qq}_{\mathrm{sys}}$ (%)	$\delta^{qq}_{\mathrm{tot}}$ (%)
c	12	0.197	0.600	0.316	12	12	17
	12	0.800	0.148	0.188	8.6	9.1	12
	25	0.500	0.492	0.232	8.7	9.8	13
	25	2.000	0.123	0.215	5.1	8.0	10
	60	2.000	0.295	0.291	6.1	8.0	10
	60	5.000	0.118	0.223	7.7	7.8	11
b	12	0.197	0.600	0.0034	55	22	60
	12	0.800	0.148	0.0049	30	33	45
	25	0.500	0.492	0.0089	22	21	30
	25	2.000	0.123	0.0062	26	28	38
	60	2.000	0.295	0.0151	21	20	29
	60	5.000	0.118	0.0144	26	25	36

Table 14.1: *The measured charm ($f^{c\bar{c}}$) and beauty ($f^{b\bar{b}}$) fractional contributions to the total ep cross section, shown with statistical ($\delta^{c\bar{c}}_{\mathrm{stat}}$, $\delta^{b\bar{b}}_{\mathrm{stat}}$), systematic ($\delta^{c\bar{c}}_{\mathrm{sys}}$, $\delta^{b\bar{b}}_{\mathrm{sys}}$) and total ($\delta^{c\bar{c}}_{\mathrm{tot}}$, $\delta^{b\bar{b}}_{\mathrm{tot}}$) errors in different Q^2–x bins.*

well. The figure shows that the b data at low Q^2 are most sensitive to the threshold behaviour, which is successfully modelled by the QCD calculations.

The results from different analyses on beauty production are summarised in Fig. 14.6 where the ratio of the cross section $\sigma^{b\bar{b}}$ measured at HERA to the NLO QCD prediction $\sigma^{b\bar{b}}_{\mathrm{NLO\ QCD}}$ is shown as a function of Q^2. The horizontal line at one is the NLO QCD prediction using the massive scheme with the CTEQ5F PDF. The two blue lines correspond to the NLO QCD predictions for the inclusive b cross section using VFNS calculations from MRST [129] and CTEQ [124]. The inclusive measurements are compatible with the three predictions. There is, as yet, no final state VFNS NLO QCD program available to calculate exclusive cross sections. However, the large difference in the inclusive predictions suggests that the uncertainties of NLO QCD are large for different PDF parametrisations.

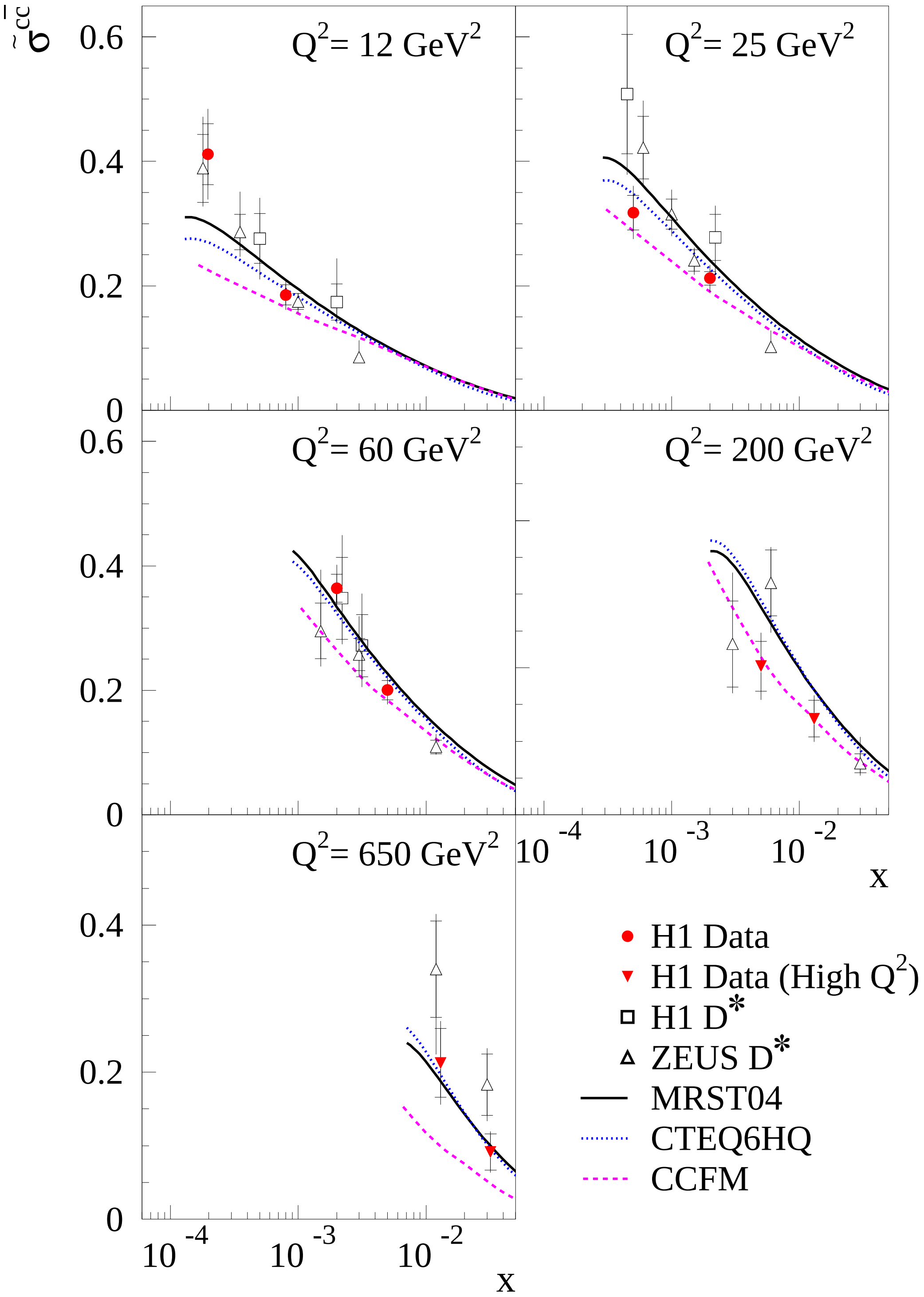

Figure 14.1: *The measured reduced cross section* $\tilde{\sigma}^{c\bar{c}}$ *shown as a function of* x *for 5 different* Q^2 *values. The inner error bars show the statistical error, the outer error bars represent the statistical and systematic errors added in quadrature. The measurements of* $\tilde{\sigma}^{c\bar{c}}$ *from H1 at high values of* Q^2 *[4], the measurements obtained from* D* *mesons from H1 [163] and ZEUS [164] and predictions of QCD are also shown.*

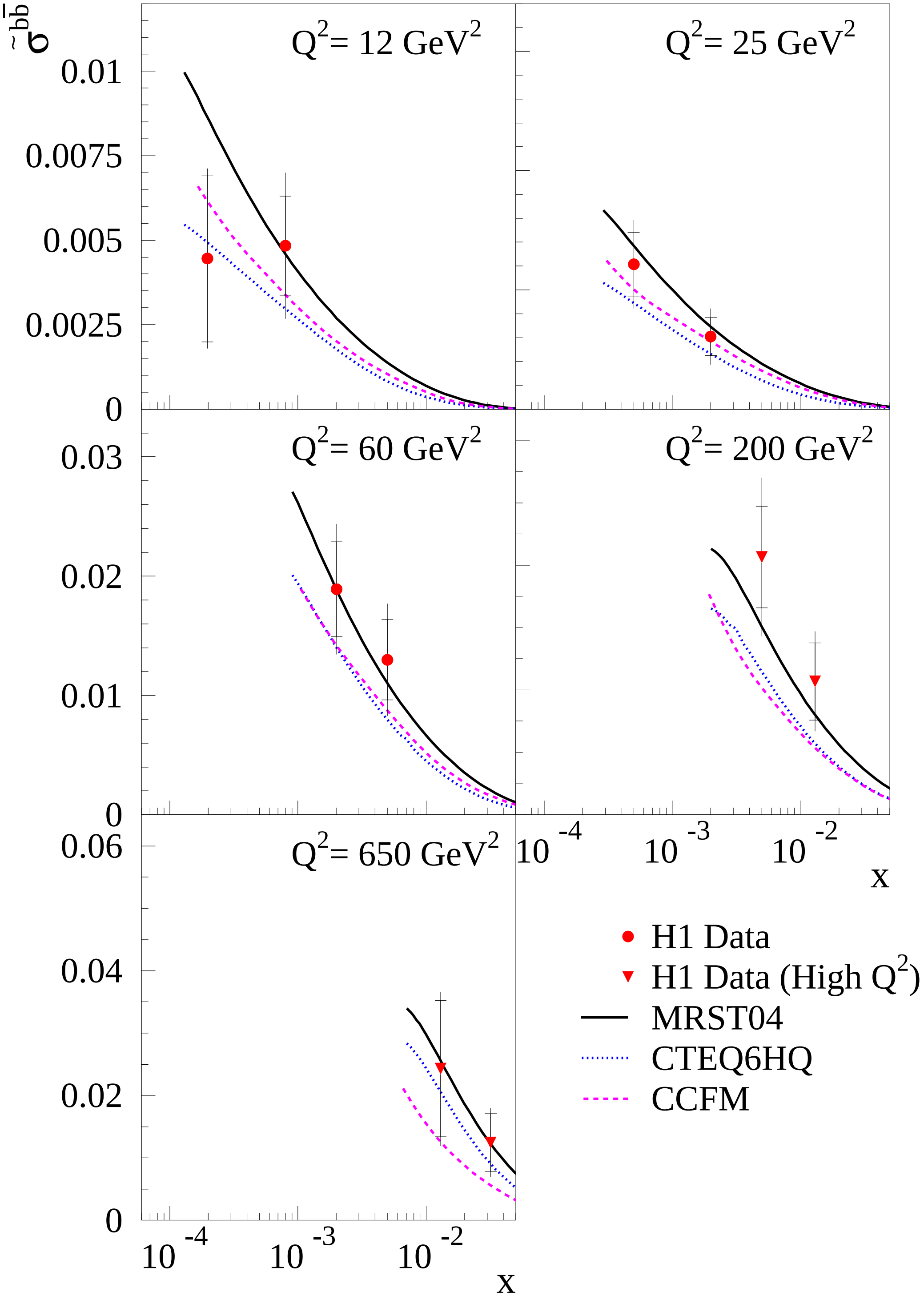

Figure 14.2: *The measured reduced cross section* $\tilde{\sigma}^{b\bar{b}}$ *shown as a function of* x *for 5 different* Q^2 *values. The inner error bars show the statistical error, the outer error bars represent the statistical and systematic errors added in quadrature. The measurements of* $\tilde{\sigma}^{b\bar{b}}$ *from H1 at high values of* Q^2 *[4] and predictions of QCD are also shown.*

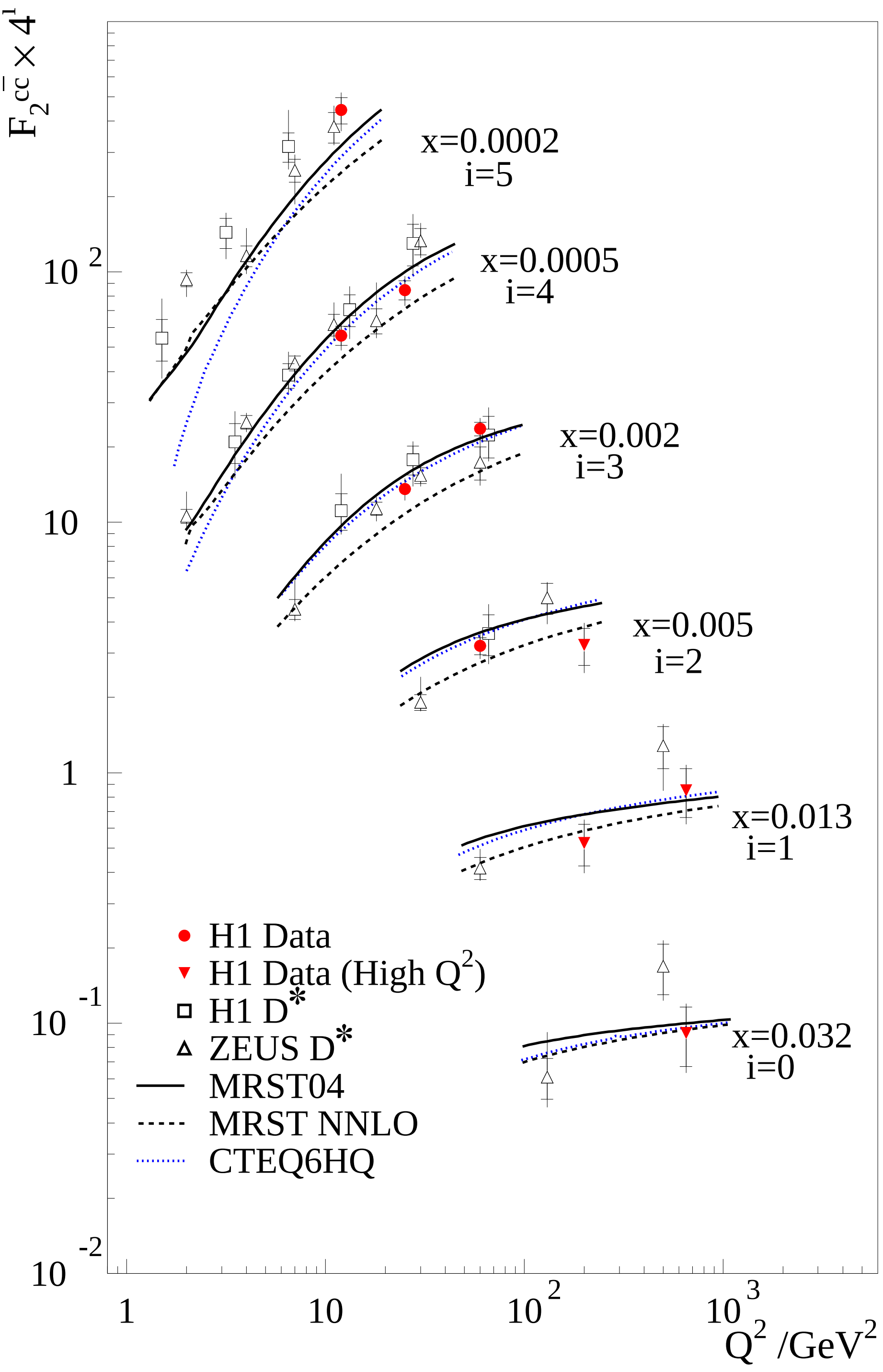

Figure 14.3: *The measured $F_2^{c\bar{c}}$ shown as a function of Q^2 for various x values. The inner error bars show the statistical error, the outer error bars represent the statistical and systematic errors added in quadrature. The $F_2^{c\bar{c}}$ from H1 at high values of Q^2 [4], the measurements obtained from* D* *mesons from H1 [163] and ZEUS [164] and predictions of QCD are also shown.*

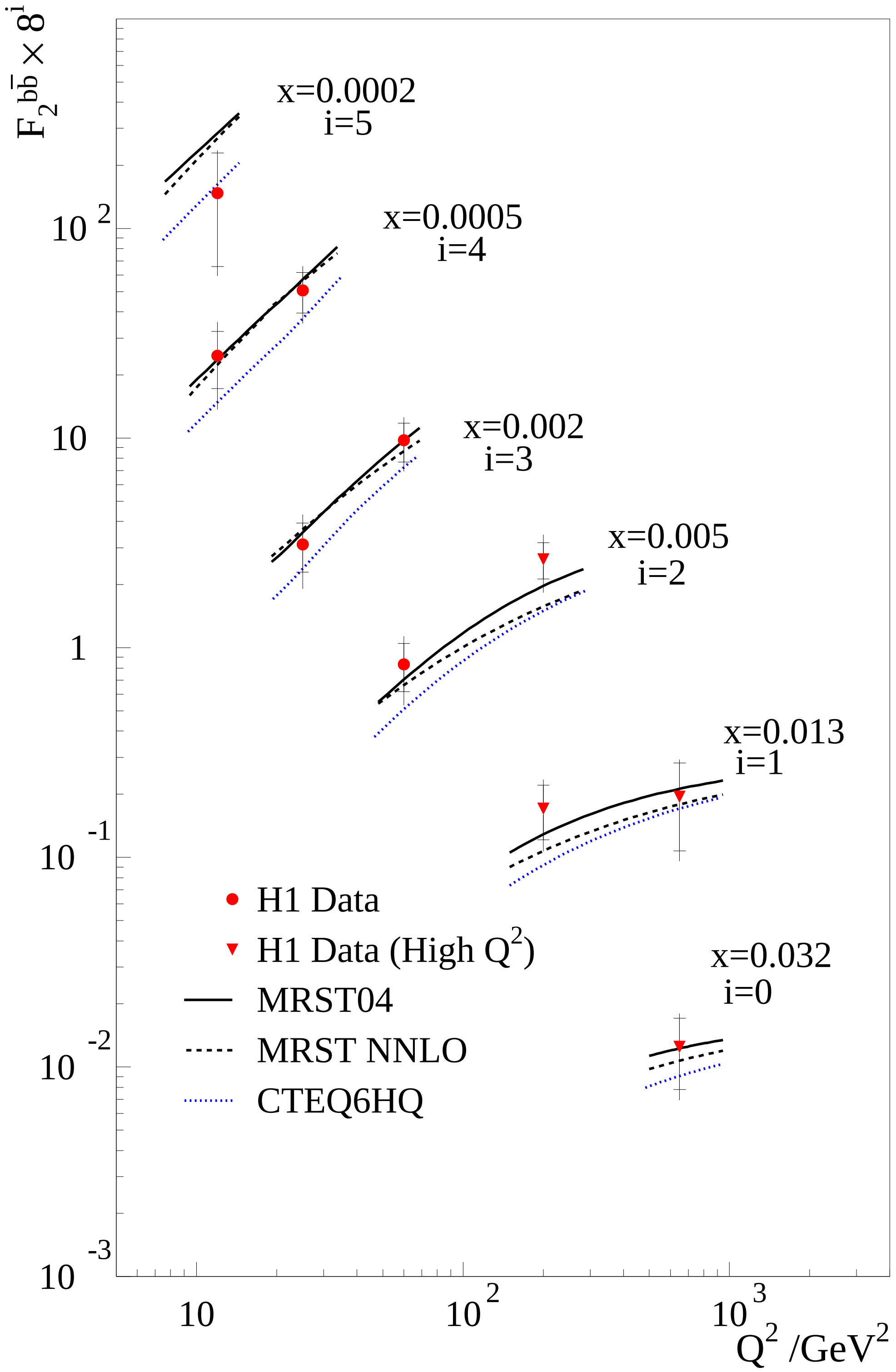

Figure 14.4: *The measured* $F_2^{b\bar{b}}$ *shown as a function of* Q^2 *for various* x *values. The inner error bars show the statistical error, the outer error bars represent the statistical and systematic errors added in quadrature. The* $F_2^{b\bar{b}}$ *from H1 at high values of* Q^2 *[4] and predictions of QCD are also shown.*

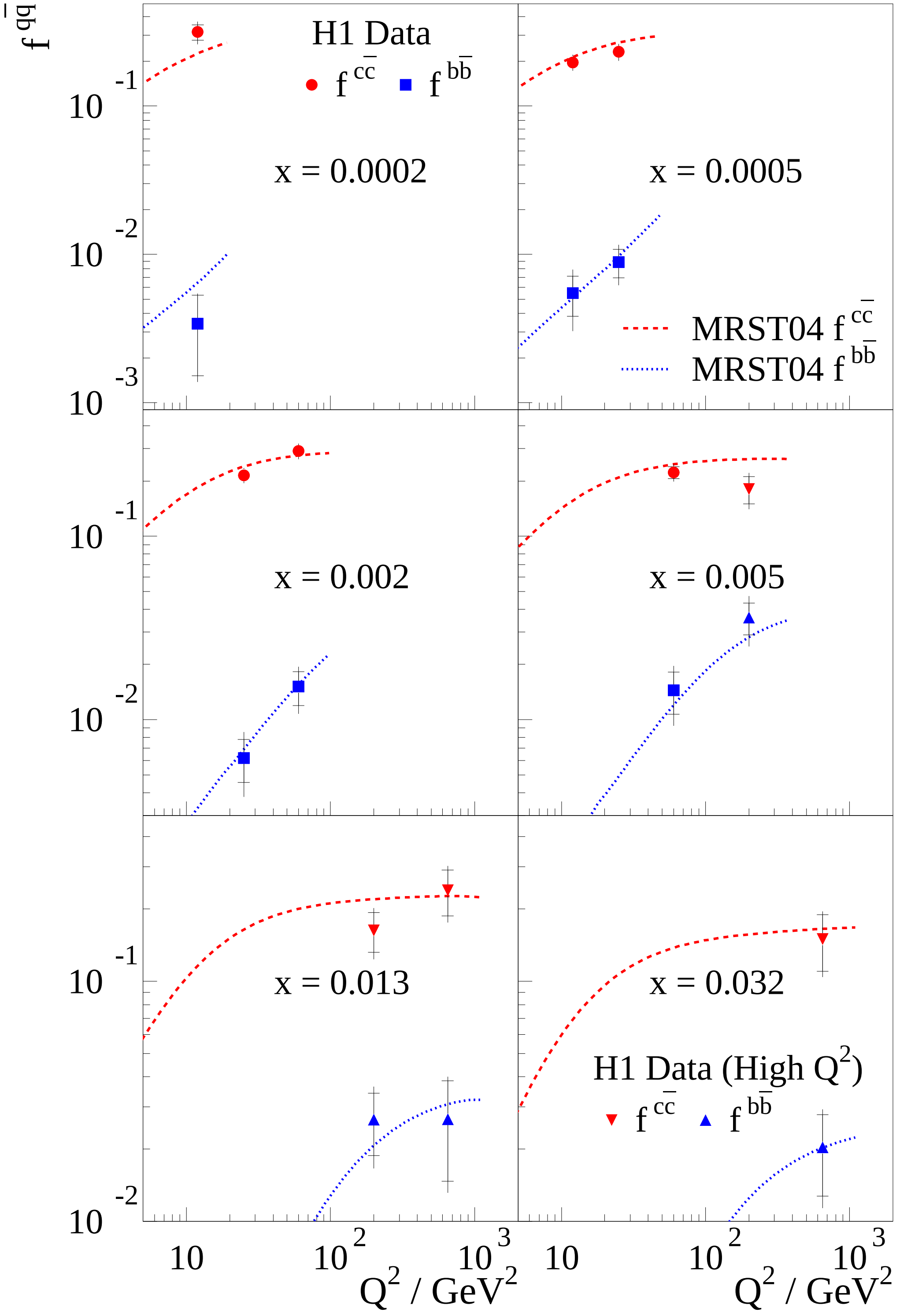

Figure 14.5: *The contributions to the total cross section* $f^{c\bar{c}}$ *and* $f^{b\bar{b}}$ *shown as a function of* Q^2 *for 6 different* x *values. The inner error bars show the statistical error, the outer error bars represent the statistical and systematic errors added in quadrature. A prediction of NLO QCD is also shown.*

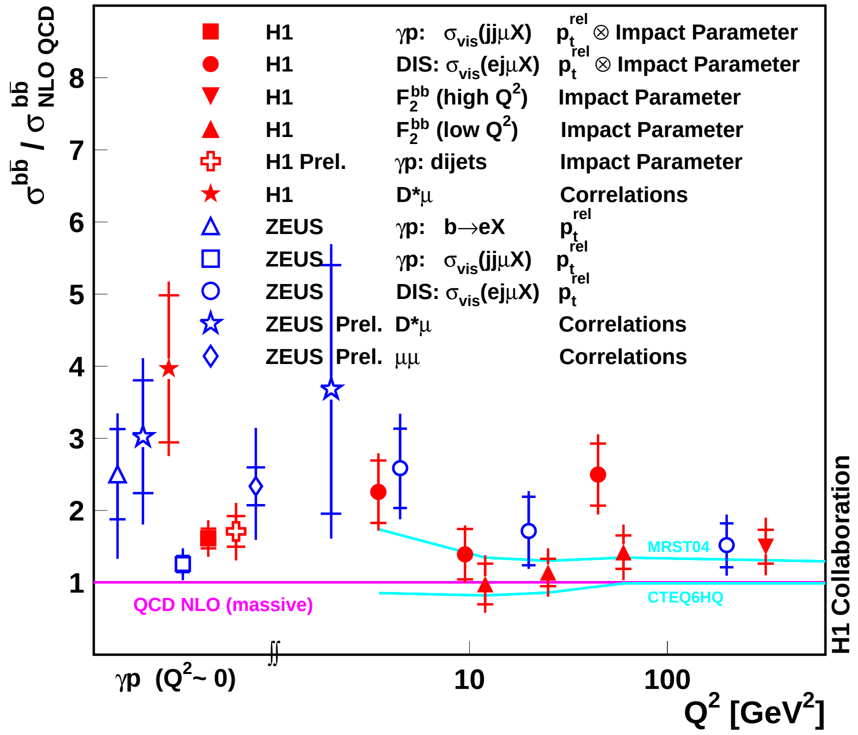

Figure 14.6: *The ratio of cross section $\sigma^{b\bar{b}}$ measured at HERA to NLO QCD prediction $\sigma^{b\bar{b}}_{\text{NLO QCD}}$ is shown as a function of Q^2. The horizontal line at one is the NLO QCD prediction using the massive scheme with the CTEQ5F PDF. The two blue lines correspond to the NLO QCD predictions for the inclusive b cross section using VFNS calculations from MRST [129] and CTEQ [124]. The results of present analysis correspond to three red triangular points.*

Chapter 15

Conclusions and Outlook

In this thesis the measurements in deep inelastic scattering of the charm and beauty contributions $F_2^{c\bar{c}}$ and $F_2^{b\bar{b}}$ to the proton structure function have been performed at low Q^2 and Bjorken x at e^+p collisions at HERA using the H1 detector. The method is based on the impact parameter, in the transverse plane, of tracks from decays of long lived c and b hadrons as reconstructed from the vertex detector. The measurements of $F_2^{c\bar{c}}$ and $F_2^{b\bar{b}}$ showed strong scaling violations. This is the first measurement of $F_2^{b\bar{b}}$ in the low Q^2 kinematic region.

The measurements are compared with perturbative QCD calculations using the variable flavour number scheme (VFNS) and the massive scheme for heavy flavour production. The structure functions $F_2^{c\bar{c}}$ and $F_2^{b\bar{b}}$ are found to be well described by the predictions. The measurements of $F_2^{c\bar{c}}$ are also in agreement with other measurements obtained using D^* cross sections. In the low Q^2 kinematic region the charm cross section contributes on average 24% of the inclusive ep cross section, and the beauty fraction increases from 0.4% at $Q^2 = 12$ GeV^2 to 1.5% at $Q^2 = 60$ GeV^2. The measurements of the reduced cross sections $\tilde{\sigma}^{c\bar{c}}$ and $\tilde{\sigma}^{b\bar{b}}$ are found to be in good agreement with perturbative QCD calculations.

The VFNS perturbative QCD calculations try to improve the description of heavy flavour production over the whole Q^2 kinematic range, taking into account the threshold effects in transition Q^2 region, when $Q^2 \sim m_{c,b}^2$. The data are more precise than the spread in predictions of the QCD calculations which increases towards low x and low Q^2, where threshold effects play a larger role. In the lowest x bins the $F_2^{c\bar{c}}$ data tend to follow the MRST predictions. For $F_2^{b\bar{b}}$ more statistics are needed to differentiate between the models, which differ by a factor of two at the lowest Q^2.

In the future, these measurements can be improved with increased statistics using HERA II data. Moreover, similar analysis will be possible with the ZEUS detector, which has a vertex detector since HERA II. It will allow to combine H1 and ZEUS measurements of $F_2^{b\bar{b}}$ and $F_2^{c\bar{c}}$. The method described in this thesis is also used for c and b production cross section measurements at H1 in photoproduction region [178].

The measurement of single and di-jet cross sections using b-tagged jets will be possible at HERA with increased statistics. This will be a good basis to test models relevant for the calculation of heavy quark jet production at the LHC.

Appendix A

Track Parameters

The track of a particle is described by a helix and parametrised in H1 coordinates as a function of the arclength s by

$$\begin{aligned} x(s) &= +(d_{ca} - \frac{1}{\kappa}) \cdot \sin(\phi_0) + \frac{1}{\kappa} \cdot \sin(\phi_0 + \kappa s), \\ y(s) &= -(d_{ca} - \frac{1}{\kappa}) \cdot \cos(\phi_0) - \frac{1}{\kappa} \cdot \cos(\phi_0 + \kappa s), \quad s \geq 0, \\ z(s) &= z_0 + s \cdot \cot(\theta). \end{aligned} \tag{A.1}$$

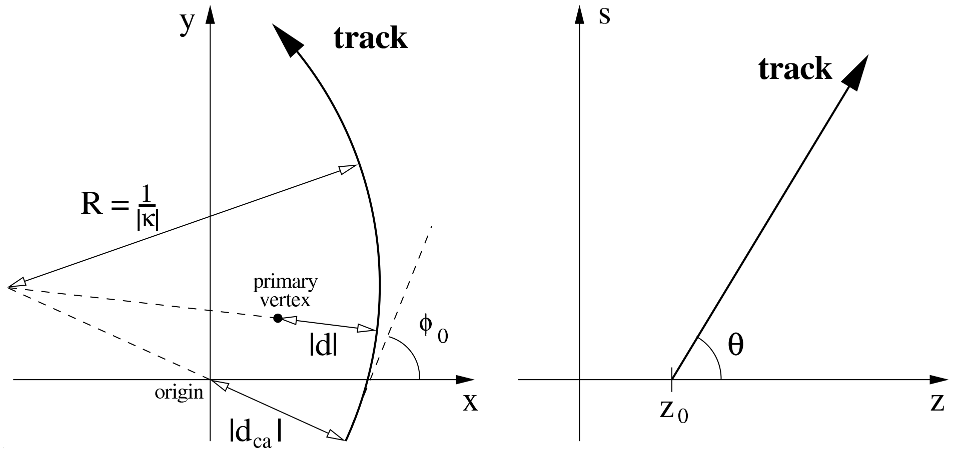

Figure A.1: *Definition of the track parameters.*

The five track parameters $(\kappa, \phi_0, \theta, d_{ca}, z_o)$ describe the helix with respect to the origin of the H1 coordinate system (Fig. A.1):

- the absolute value of the curvature κ equals the inverse bending radius with the sign opposite to the electric charge of the particle;
- the azimuthal angle ϕ_0 gives the flight direction in the radial plane at the point of closest approach to the z axis which is seen as the starting point of the helix: $s = 0$;
- d_{ca} is the distance of closest approach. The sign of d_{ca} is chosen equal to the sign of κ, if the z axis is included in the circle which describes the track in the radial plane, otherwise it is chosen opposite to it;

- in the zs plane the track is described by a straight line with a z-axis intercept at $z = z_0$ and a slope $\cot(\theta)$;
- polar angle θ gives the flight direction with respect to the positive z-axis.

Only three parameters (κ, ϕ_0, d_{ca}) describe helix in $r\phi$ plane.

Acknowledgements

First of all I would like to thank my Professor Dr. Rolf-Dieter Heuer and the leader of the FLC group Ties Behnke for giving me the opportunity to work at DESY and make my PhD thesis in such an interesting field like particle physics, for their permanent support, care and useful advices. I am very grateful to Klaus Desch for his supervision in the analysis of the MSSM Higgs boson production at a future Linear Collider. My special thanks to Thorsten Kuhl, Philip Bechtle and Alexei Raspereza for their help and support during the work on this analysis and for many useful discussions.

Concerning heavy flavour analysis at H1, I would like to thank Felix Sefkow for his support and valuable advices. I am very grateful to Paul Thompson and Andy Mehta for their very effective and generous collaboration. My appreciation to HERA machine group and H1 collaboration, without their efforts this analysis would not be possible.

My gratitude to Klaus Desch, Ties Behnke, Paul Thompson, Felix Sefkow, Alexei Raspereza, Thomas Krämer and Oliver Wendt for careful reading of the whole or some parts of the manuscript of this thesis. Many thanks to Sven Heinemeyer and Gennaro Corcella for reading the theoretical parts and their valuable comments.

I would like to thank Prof. Dr. Beate Naroska and Prof. Dr. Peter Schleper for examining this work.

My appreciation to the colleagues from the FLC group, who helped and supported me during the work on this PhD thesis. My special thanks to Vasiliy Morgunov and his wife Valentina for many interesting conversations. I am very thankful to the whole FLC group for the pleasant working atmosphere and many interesting events. Many thanks to Ramona Matthes, the secretary of our group, for her permanent care of us. Also my sincere appreciation to all other people who supported and took care of me.

Bibliography

[1] K. Desch, T. Klimkovich, T. Kuhl, and A. Raspereza, *Study of Higgs boson pair production at Linear Collider* (2004), [hep-ph/0406229], [spires].

[2] T. Klimkovich, *MSSM Higgs bosons at a future linear collider. Heavy quark production at HERA*, Eur. Phys. J. **C40 S2**(2005) 1, [spires].

[3] F. Maltoni, Z. Sullivan, and S. Willenbrock, *Higgs-boson production via bottom-quark fusion*, Phys. Rev. **D67**(2003) 093005, [hep-ph/0301033], [spires].

[4] H1 Collaboration, A. Aktas *et al.*, *Measurement of $F_2^{c\bar{c}}$ and $F_2^{b\bar{b}}$ at high Q^2 using the H1 vertex detector at HERA*, Eur. Phys. J. **C40**(2005) 349, [hep-ex/0411046], [spires].

[5] H1 Collaboration, A. Aktas *et al.*, *Measurement of $F_2^{c\bar{c}}$ and $F_2^{b\bar{b}}$ at low Q^2 and x using the H1 vertex detector at HERA*, Eur. Phys. J. **C45**(2006) 23, [hep-ex/0507081], [spires].

[6] T. Klimkovich, *Measurement of $F_2^{c\bar{c}}$ and $F_2^{b\bar{b}}$ at low and high Q^2 using the H1 vertex detector*, Proceedings for DIS 2005, Madison, Wisconsin (2005), available from `http://www.hep.wisc.edu/dis05/`.

[7] J. D. Bjorken and S. L. Glashow, *Elementary particles and SU(4)*, Phys. Lett. **11**(1964) 255, [spires].

[8] S. L. Glashow, *Partial symmetries of weak interactions*, Nucl. Phys. **22**(1961) 579, [spires].

S. Weinberg, *A model of leptons*, Phys. Rev. Lett. **19**(1967) 1264, [spires].

A. Salam, *Weak and electromagnetic interactions* Originally printed in Svartholm: Elementary Particle Theory, Proceedings Of The Nobel Symposium Held 1968 At Lerum, Sweden, Stockholm 1968, 367-377.

[9] P. W. Higgs, *Broken symmetries, massless particles and gauge fields*, Phys. Lett. **12**(1964) 132, [spires].

P. W. Higgs, *Broken symmetries and the masses of gauge bosons*, Phys. Rev. Lett. **13**(1964) 508, [spires].

P. W. Higgs, *Spontaneous symmetry breakdown without massless bosons*, Phys. Rev. **145**(1966) 1156, [spires].

F. Englert and R. Brout, *Broken symmetry and the mass of gauge vector mesons*, Phys. Rev. Lett. **13**(1964) 321, [spires].

G. S. Guralnik, C. R. Hagen, and T. W. B. Kibble, *Global conservation laws and massless particles*, Phys. Rev. Lett. **13**(1964) 585, [spires].

[10] S. L. Glashow, J. Iliopoulos, and L. Maiani, *Weak interactions with lepton - hadron symmetry*, Phys. Rev. **D2**(1970) 1285, [spires].

[11] ALEPH, DELPHI, L3, OPAL, LEP Higgs WG Collaboration, R. Barate *et al.*, *Search for the Standard Model Higgs boson at LEP*, Phys. Lett. **B565**(2003) 61, [hep-ex/0306033], [spires].

[12] H. Fritzsch, M. Gell-Mann, and H. Leutwyler, *Advantages of the color octet gluon picture*, Phys. Lett. **B47**(1973) 365, [spires].

[13] D. J. Gross and F. Wilczek, *Ultraviolet behavior of non-abelian gauge theories*, Phys. Rev. Lett. **30**(1973) 1343, [spires].

[14] H. D. Politzer, *Reliable perturbative results for strong interactions?*, Phys. Rev. Lett. **30**(1973) 1346, [spires].

[15] L. H. Ryder, *Quantum field theory* Cambridge, Uk: Univ. Pr. (1985) 443p.

[16] D. J. Griffiths, *Introduction to elementary particles* NEW YORK, USA: WILEY (1987) 392p.

[17] G. 't Hooft and M. J. G. Veltman, *Regularization and renormalization of gauge fields*, Nucl. Phys. **B44**(1972) 189, [spires].

[18] M. Spira and P. M. Zerwas, *Electroweak symmetry breaking and Higgs physics* (1997), Lectures given at 36. Internationale Universitaetswochen fuer Kernphysik und Teilchenphysik, Schladming, Austria, [hep-ph/9803257], [spires].

[19] J. F. Gunion, H. E. Haber, G. L. Kane, and S. Dawson, *The Higgs hunter's guide* SCIPP-89/13.

[20] B. W. Lee, C. Quigg, and H. B. Thacker, *The strength of weak interactions at very high-energies and the Higgs boson mass*, Phys. Rev. Lett. **38**(1977) 883, [spires].

[21] T. Hambye and K. Riesselmann, *Matching conditions and Higgs mass upper bounds revisited*, Phys. Rev. **D55**(1997) 7255, [hep-ph/9610272], [spires].

[22] ALEPH Collaboration, A. Heister *et al.*, *Final results of the searches for neutral Higgs bosons in e^+e^- collisions at $\sqrt{s}$ up to 209 GeV*, Phys. Lett. **B526**(2002) 191, [hep-ex/0201014], [spires].

[23] *LEP electroweak working group* (2005), `http://lepewwg.web.cern.ch/LEPEWWG/`.

[24] The D0 Collaboration, t. T. E. W. Group, *Combination of CDF and D0 results on the top-quark mass* (2005), [hep-ex/0507091], [spires].

[25] E. W. Kolb and M. S. Turner, *The Early universe*, Addison-Wesley, Redwood City, USA (1990), Frontiers in physics, 69.

[26] A. D. Sakharov, *Violation of CP invariance, C asymmetry, and baryon asymmetry of the universe*, Pisma Zh. Eksp. Teor. Fiz. **5**(1967) 32, [spires].

[27] G. R. Farrar and M. E. Shaposhnikov, *Baryon asymmetry of the universe in the standard electroweak theory*, Phys. Rev. **D50**(1994) 774, [hep-ph/9305275], [spires].

G. R. Farrar and M. E. Shaposhnikov, *Baryon asymmetry of the universe in the minimal Standard Model*, Phys. Rev. Lett. **70**(1993) 2833, [hep-ph/9305274], [spires].

M. B. Gavela, P. Hernandez, J. Orloff, O. Pene, and C. Quimbay, *Standard model CP violation and baryon asymmetry. Part 2: Finite temperature*, Nucl. Phys. **B430**(1994) 382, [hep-ph/9406289], [spires].

P. Huet and E. Sather, *Electroweak baryogenesis and Standard Model CP violation*, Phys. Rev. **D51**(1995) 379, [hep-ph/9404302], [spires].

[28] M. Carena, J. M. Moreno, M. Quiros, M. Seco, and C. E. M. Wagner, *Supersymmetric CP-violating currents and electroweak baryogenesis*, Nucl. Phys. **B599**(2001) 158, [hep-ph/0011055], [spires].

[29] C. L. Bennett *et al.*, *First year Wilkinson Microwave Anisotropy Probe (WMAP) observations: Preliminary maps and basic results*, Astrophys. J. Suppl. **148**(2003) 1, [astro-ph/0302207], [spires].

[30] S. P. Martin, *A supersymmetry primer* (1997), [hep-ph/9709356], [spires].

[31] D. I. Kazakov, *Beyond the Standard Model (in search of Supersymmetry)* (2000), [hep-ph/0012288], [spires].

[32] W. de Boer, *Grand unified theories and Supersymmetry in particle physics and cosmology*, Prog. Part. Nucl. Phys. **33**(1994) 201, [hep-ph/9402266], [spires].

[33] U. Amaldi, W. de Boer, and H. Furstenau, *Comparison of grand unified theories with electroweak and strong coupling constants measured at LEP*, Phys. Lett. **B260**(1991) 447, [spires].

[34] G. L. Kane *et al.*, *Perspectives on supersymmetry*, Singapore (1998), World Scientific.

[35] P. Fayet, *Supersymmetry and weak, electromagnetic and strong interactions*, Phys. Lett. **B64**(1976) 159, [spires].

P. Fayet, *Spontaneously broken supersymmetric theories of weak, electromagnetic and strong interactions*, Phys. Lett. **B69**(1977) 489, [spires].

P. Fayet, *Relations between the masses of the superpartners of leptons and quarks, the goldstino couplings and the neutral currents*, Phys. Lett. **B84**(1979) 416, [spires].

G. R. Farrar and P. Fayet, *Phenomenology of the production, decay, and detection of new hadronic states associated with supersymmetry*, Phys. Lett. **B76**(1978) 575, [spires].

[36] L. J. Hall, J. Lykken, and S. Weinberg, *Supergravity as the messenger of supersymmetry breaking*, Phys. Rev. **D27**(1983) 2359, [spires].

S. K. Soni and H. A. Weldon, *Analysis of the supersymmetry breaking induced by n=1 supergravity theories*, Phys. Lett. **B126**(1983) 215, [spires].

I. Affleck, M. Dine, and N. Seiberg, *Dynamical supersymmetry breaking in four-dimensions and its phenomenological implications*, Nucl. Phys. **B256**(1985) 557, [spires].

[37] H. E. Haber and R. Hempfling, *Can the mass of the lightest Higgs boson of the minimal supersymmetric model be larger than m_Z?*, Phys. Rev. Lett. **66**(1991) 1815, [spires].

Y. Okada, M. Yamaguchi, and T. Yanagida, *Upper bound of the lightest Higgs boson mass in the minimal supersymmetric standard model*, Prog. Theor. Phys. **85**(1991) 1, [spires].

J. R. Ellis, G. Ridolfi, and F. Zwirner, *Radiative corrections to the masses of supersymmetric Higgs bosons*, Phys. Lett. **B257**(1991) 83, [spires].

J. R. Ellis, G. Ridolfi, and F. Zwirner, *On radiative corrections to supersymmetric Higgs boson masses and their implications for LEP searches*, Phys. Lett. **B262**(1991) 477, [spires].

R. Barbieri, M. Frigeni, and F. Caravaglios, *The supersymmetric Higgs for heavy superpartners*, Phys. Lett. **B258**(1991) 167, [spires].

[38] G. Degrassi, S. Heinemeyer, W. Hollik, P. Slavich, and G. Weiglein, *Towards high-precision predictions for the MSSM Higgs sector*, Eur. Phys. J. **C28**(2003) 133, [hep-ph/0212020], [spires].

[39] A. Pilaftsis, *Higgs scalar-pseudoscalar mixing in the minimal supersymmetric standard model*, Phys. Lett. **B435**(1998) 88, [hep-ph/9805373], [spires].

[40] A. Pilaftsis and C. E. M. Wagner, *Higgs bosons in the minimal supersymmetric standard model with explicit CP violation*, Nucl. Phys. **B553**(1999) 3, [hep-ph/9902371], [spires].

[41] M. Carena, J. R. Ellis, A. Pilaftsis, and C. E. M. Wagner, *Renormalization-group-improved effective potential for the MSSM Higgs sector with explicit CP violation*, Nucl. Phys. **B586**(2000) 92, [hep-ph/0003180], [spires].

[42] R. Brinkmann *et al.*, *TESLA: The superconducting electron positron Linear Collider with an integrated X-ray laser laboratory. Technical Design Report. Pt. 2: The accelerator* (2001), DESY-01-011.

[43] American Linear Collider Working Group Collaboration, T. Abe *et al.*, *Linear collider physics resource book for Snowmass 2001. 1: Introduction* (2001), [hep-ex/0106055], [spires].

[44] ACFA Linear Collider Working Group Collaboration, K. Abe *et al.*, *Particle physics experiments at JLC* (2001), [hep-ph/0109166], [spires].

[45] *International Technology Recommendation Pannel Report* (2004), Available from `http://www.fnal.gov/directorate/icfa/`.

[46] K. Desch, A. Imhof, N. Meyer, and A. Raspereza, *Impact of hadronic backgrounds on selected Higgs physics analyses at a Linear Collider* (2004), LC-PHSM-2004-009.

[47] G. Alexander *et al.*, *Undulator-based production of polarized positrons. A proposal for the 50-GeV beam in the FFTB* (2003), The E-166 Project Website: `http://www-project.slac.stanford.edu/lc/local/PolarizedPositrons/index.htm`, [SLAC-PROPOSAL-E-166(bis)].

[48] V. Balakin and A. Mikhailichenko, *The conversion system for obtaining high polarized electrons and positrons* (1979) 79, [Preprint BINP].

[49] T. Behnke, S. Bertolucci, R. D. Heuer, R. Settles, *et al.*, *TESLA: The superconducting electron positron linear collider with an integrated X-ray laser laboratory. Technical design report. Pt. 4: A detector for TESLA* DESY-01-011.

[50] C. J. S. Damerell, *A CCD based vertex detector for TESLA* (2001), LC-DET-2001-023.

[51] K. D. Stefanov and C. J. S. Damerell, *A CCD-based vertex detector for the future Linear Collider* (2003), LC-DET-2003-060.

[52] M. Winter *et al.*, *A CMOS based VTX detector* (2001), LC-DET-2001-017.

[53] P. Fischer *et al.*, *A DEPFET based pixel vertex detector for the detector at TESLA* (2002), LC-DET-2002-004.

[54] M. Battaigla *et al.*, *A pixel vertex tracker for the detector at TESLA* (2001), LC-DET-2001-042.

[55] R. Settles *et al.*, *A TPC for a future Linear Collider* (2002), LC-DET-2002-008.

[56] R. Bouclier *et al.*, *The gas electron multiplier (GEM)*, IEEE Trans. Nucl. Sci. **44**(1997) 646, [spires].

[57] Y. Giomataris, P. Rebourgeard, J. P. Robert, and G. Charpak, *MICROMEGAS: A high-granularity position-sensitive gaseous detector for high particle-flux environments*, Nucl. Instrum. Meth. **A376**(1996) 29, [spires].

[58] J. Hauschildt, *Studies on a silicon intermediate tracker for the TESLA detector* (2001), LC-DET-2001-036.

[59] *ATLAS inner detector: Technical design report. Vol. 1* CERN-LHCC-97-16.

[60] *ATLAS inner detector: Technical design report. Vol. 2* CERN-LHCC-97-17.

[61] F. Badaud *et al.*, *Si-W calorimeter performances* (2001), LC-DET-2001-058.

[62] P. Hassler *et al.*, *The hadronic tile calorimeter for the TESLA detector, design, construction and installation* (2001), LC-DET-2001-049.

[63] E. Garutti *et al.*, *A high-granularity scintillator hadronic-calorimeter with SiPM readout for a Linear Collider detector* (2004), LC-DET-2004-027.

[64] G. Acquistapace *et al.*, *CMS the magnet project: Technical design report* (1997), CERN-LHCC-97-10.

[65] R. Santonico and R. Cardarelli, *Development of resistive plate counters*, Nucl. Instrum. Meth. **187**(1981) 377, [spires].

[66] H. M. Araujo, A. Stahl, and D. J. Miller, *A lead tungstate detector with integrated light readout for the TESLA luminosity calorimeter* (2001), LC-DET-2001-080.

[67] RD42 Collaboration, W. Adam *et al.*, *Review of the development of diamond radiation sensors*, Nucl. Instrum. Meth. **A434**(1999) 131, [spires].

[68] M. Pohl and H. J. Schreiber, *SIMDET - Version 4: A parametric Monte Carlo for a TESLA detector* (2002), [hep-ex/0206009], [spires].

[69] R. Brun, R. Hagelberg, M. Hansroul, and J. C. Lassalle, *GEANT: Simulation program for particle physics experiments. User guide and reference manual* CERN-DD-78-2-REV.

[70] T. Behnke and G. A. Blair, *BRAHMS - Version 102: A Monte Carlo for a detector at a 500 GeV to 800 GeV Linear Collider* LC-PHSM-2001-005.

[71] T. Ohl, *CIRCE version 1.0: Beam spectra for simulating Linear Collider physics*, Comput. Phys. Commun. **101**(1997) 269, [hep-ph/9607454], [spires].

[72] M. L. Mangano *et al.*, *Event generators for discovery physics* (1996), [hep-ph/9602203], [spires].

[73] A. Djouadi, *HPROD: A Program for SM and MSSM Higgs boson production in e^+e^- Collisions,* `http://w3.lpm.univ-montp2.fr/~djouadi/GDR/programs/hprod.html`.

[74] M. Carena, J. R. Ellis, A. Pilaftsis, and C. E. M. Wagner, *CP-violating MSSM Higgs bosons in the light of LEP 2*, Phys. Lett. **B495**(2000) 155, [hep-ph/0009212], [spires].

[75] A. Djouadi, J. Kalinowski, and M. Spira, *HDECAY: A program for Higgs boson decays in the Standard Model and its supersymmetric extension*, Comput. Phys. Commun. **108**(1998) 56, [hep-ph/9704448], [spires].

[76] A. Djouadi, J. Kalinowski, and P. M. Zerwas, *Two- and three-body decay modes of SUSY Higgs particles*, Z. Phys. **C70**(1996) 435, [hep-ph/9511342], [spires].

[77] *ATLAS: Detector and physics performance technical design report. Volume 1* CERN-LHCC-99-14.

[78] ECFA/DESY LC Physics Working Group Collaboration, J. A. Aguilar-Saavedra *et al.*, *TESLA Technical Design Report Part III: Physics at an e^+e^- Linear Collider* (2001), [hep-ph/0106315], [spires].

[79] A. Andreazza and C. Troncon, *Study of HA production in e^+e^- collisions at $\sqrt{s}$ = 800 GeV* Prepared for Joint ECFA / DESY Study: Physics and Detectors for a Linear Collider (Preceded 1st Workshop at Frascati 5- 6 Feb 1996 and 2nd workshop in July whose location and dates are to be determined), Hamburg, Germany, 20-22 Nov 1996.

[80] D. M. Asner, J. B. Gronberg, and J. F. Gunion, *Detecting and studying Higgs bosons in two-photon collisions at a Linear Collider*, Phys. Rev. **D67**(2003) 035009, [hep-ph/0110320], [spires].

[81] M. M. Muhlleitner, M. Kramer, M. Spira, and P. M. Zerwas, *Production of MSSM Higgs bosons in photon photon collisions*, Phys. Lett. **B508**(2001) 311, [hep-ph/0101083], [spires].

[82] V. L. Morgunov, *Calorimetry design with energy-flow concept (imaging detector for high-energy physics)* Prepared for 10th International Conference on Calorimetry in High Energy Physics (CALOR 2002), Pasadena, California, 25-30 Mar 2002.

[83] S. Catani, Y. L. Dokshitzer, M. Olsson, G. Turnock, and B. R. Webber, *New clustering algorithm for multi-jet cross-sections in e^+e^- annihilation*, Phys. Lett. **B269**(1991) 432, [spires].

[84] N. Brown and W. J. Stirling, *Finding jets and summing soft gluons: A new algorithm,* Z. Phys. **C53**(1992) 629, [spires].

[85] JADE Collaboration, W. Bartel *et al.*, *Experimental studies on multi-jet production in e^+e^- annihilation at PETRA energies*, Z. Phys. **C33**(1986) 23, [spires].

[86] JADE Collaboration, S. Bethke *et al.*, *Experimental investigation of the energy dependence of the strong coupling strength*, Phys. Lett. **B213**(1988) 235, [spires].

[87] D. J. Jackson, *A topological vertex reconstruction algorithm for hadronic jets*, Nucl. Instrum. Meth. **A388**(1997) 247, [spires].

[88] R. Hawkings, *Vertex detector and flavor tagging studies for the TESLA linear collider* LC-PHSM-2000-021.

[89] S. M. Xella Hansen, M. Wing, D. J. Jackson, N. De Groot, and C. J. S. Damerell, *Update on flavour tagging studies for the future Linear Collider using the BRAHMS simulation* LC-PHSM-2003-061.

[90] S. Xella-Hansen, D. J. Jackson, R. Hawkings, and C. J. S. Damerell, *Flavour tagging studies for the TESLA Linear Collider* LC-PHSM-2001-024.

[91] ALEPH Collaboration, R. Barate *et al.*, *A measurement of R_b using a lifetime-mass tag*, Phys. Lett. **B401**(1997) 150, [spires].

[92] N. Kjaer and R. Moller, *Reconstruction of invariant masses in multi-jet events* .

[93] T. Sjostrand, L. Lonnblad, and S. Mrenna, *PYTHIA 6.2: Physics and manual* (2001), [hep-ph/0108264], [spires].

[94] B. C. Allanach *et al.*, *The Snowmass points and slopes: Benchmarks for SUSY searches*, Eur. Phys. J. **C25**(2002) 113, [hep-ph/0202233], [spires].

[95] S. Heinemeyer, W. Hollik, and G. Weiglein, *FeynHiggs and FeynHiggsFast: Programs for higher-order calculations in the neutral CP-even Higgs boson sector of the MSSM* LC-TH-2001-065.

[96] LHC/LC Study Group Collaboration, G. Weiglein *et al.*, *Physics interplay of the LHC and the ILC* (2004), [hep-ph/0410364], [spires].

[97] M. Duehrssen, *Prospects for the measurement of Higgs boson coupling parameters in the mass range from 110 - 190 GeV/c^2* .

[98] A. Bartl, S. Hesselbach, K. Hidaka, T. Kernreiter, and W. Porod, *Impact of SUSY CP phases on stop and sbottom decays in the MSSM* (2003), [hep-ph/0306281], [spires].

A. Bartl, S. Hesselbach, K. Hidaka, T. Kernreiter, and W. Porod, *Impact of CP phases on stop and sbottom searches*, Phys. Lett. **B573**(2003) 153, [hep-ph/0307317], [spires].

[99] A. Bartl and S. Hesselbach, *Physics possibilities at a Linear Collider*, Pramana **63**(2004) 1101, [hep-ph/0407178], [spires].

[100] U. Bassler and G. Bernardi, *On the kinematic reconstruction of deep inelastic scattering at HERA: The Sigma method*, Nucl. Instrum. Meth. **A361**(1995) 197, [hep-ex/9412004], [spires].

U. Bassler and G. Bernardi, *Structure function measurements and kinematic reconstruction at HERA*, Nucl. Instrum. Meth. **A426**(1999) 583, [hep-ex/9801017], [spires].

[101] J. D. Bjorken and E. A. Paschos, *Inelastic electron proton and gamma proton scattering, and the structure of the nucleon*, Phys. Rev. **185**(1969) 1975, [spires].

[102] M. Breidenbach *et al.*, *Observed behavior of highly inelastic electron - proton scattering*, Phys. Rev. Lett. **23**(1969) 935, [spires].

[103] J. Callan, Curtis G. and D. J. Gross, *High-energy electroproduction and the constitution of the electric current*, Phys. Rev. Lett. **22**(1969) 156, [spires].

[104] H1 Collaboration, C. Adloff *et al.*, *Measurement and QCD analysis of neutral and charged current cross sections at HERA*, Eur. Phys. J. **C30**(2003) 1, [hep-ex/0304003], [spires].

[105] R. K. Ellis, W. J. Stirling, and B. R. Webber, *QCD and collider physics*, Camb. Monogr. Part. Phys. Nucl. Phys. Cosmol. **8**(1996) 1, [spires].

[106] J. C. Collins, *Renormalization. An introduction to renormalization, the renormalization group, and the operator product expansion* Cambridge, Uk: Univ. Pr. (1984) 380p.

[107] D. E. Soper, *Basics of QCD perturbation theory* (2000), [hep-ph/0011256], [spires].

[108] H1 Collaboration, C. Adloff *et al.*, *Measurement and QCD analysis of jet cross sections in deep- inelastic positron proton collisions at* $\sqrt{s}$ *of 300 GeV*, Eur. Phys. J. **C19**(2001) 289, [hep-ex/0010054], [spires].

[109] G. Corcella (2005), private communication.

[110] J. C. Collins, D. E. Soper, and G. Sterman, *Factorization for short distance hadron - hadron scattering*, Nucl. Phys. **B261**(1985) 104, [spires].

[111] V. N. Gribov and L. N. Lipatov, *Deep inelastic ep scattering in perturbation theory*, Sov. J. Nucl. Phys. **15**(1972) 438, [spires].

L. N. Lipatov, *The parton model and perturbation theory*, Sov. J. Nucl. Phys. **20**(1975) 94, [spires].

G. Altarelli and G. Parisi, *Asymptotic freedom in parton language*, Nucl. Phys. **B126**(1977) 298, [spires].

Y. L. Dokshitzer, *Calculation of the structure functions for deep inelastic scattering and* e^+e^- *annihilation by perturbation theory in quantum chromodynamics. (In Russian)*, Sov. Phys. JETP **46**(1977) 641, [spires].

[112] V. S. Fadin, E. A. Kuraev, and L. N. Lipatov, *On the Pomeranchuk singularity in asymptotically free theories*, Phys. Lett. **B60**(1975) 50, [spires].

E. A. Kuraev, L. N. Lipatov, and V. S. Fadin, *Multi - reggeon processes in the Yang-Mills theory*, Sov. Phys. JETP **44**(1976) 443, [spires].

E. A. Kuraev, L. N. Lipatov, and V. S. Fadin, *The Pomeranchuk singularity in non-abelian gauge theories*, Sov. Phys. JETP **45**(1977) 199, [spires].

I. I. Balitsky and L. N. Lipatov, *The Pomeranchuk singularity in quantum chromodynamics*, Sov. J. Nucl. Phys. **28**(1978) 822, [spires].

[113] M. Ciafaloni, *Coherence effects in initial jets at small Q^2/s*, Nucl. Phys. **B296**(1988) 49, [spires].

S. Catani, F. Fiorani, and G. Marchesini, *Small x behavior of initial state radiation in perturbative QCD*, Nucl. Phys. **B336**(1990) 18, [spires].

[114] H. Jung, *The CCFM Monte Carlo generator CASCADE*, Comput. Phys. Commun. **143**(2002) 100, [hep-ph/0109102], [spires].

[115] V. V. Sudakov, *Vertex parts at very high-energies in quantum electrodynamics*, Sov. Phys. JETP **3**(1956) 65, [spires].

[116] A. D. Martin, R. G. Roberts, W. J. Stirling, and R. S. Thorne, *MRST2001: Partons and α_s from precise deep inelastic scattering and Tevatron jet data*, Eur. Phys. J. **C23**(2002) 73, [hep-ph/0110215], [spires].

[117] H. L. Lai *et al.*, *Global QCD analysis and the CTEQ parton distributions*, Phys. Rev. **D51**(1995) 4763, [hep-ph/9410404], [spires].

[118] J. Pumplin *et al.*, *New generation of parton distributions with uncertainties from global QCD analysis*, JHEP **07**(2002) 012, [hep-ph/0201195], [spires].

[119] M. Hansson and H. Jung, *Status of CCFM: Un-integrated gluon densities* (2003), [hep-ph/0309009], [spires].

[120] R. S. Thorne, *A variable flavour number scheme at NNLO* (2005), [hep-ph/0506251], [spires].

[121] M. A. G. Aivazis, J. C. Collins, F. I. Olness, and W.-K. Tung, *Leptoproduction of heavy quarks. 2. A unified QCD formulation of charged and neutral current processes from fixed target to collider energies*, Phys. Rev. **D50**(1994) 3102, [hep-ph/9312319], [spires].

F. I. Olness and S. T. Riemersma, *Leptoproduction of heavy quarks in the fixed and variable flavor schemes*, Phys. Rev. **D51**(1995) 4746, [hep-ph/9409208], [spires].

[122] J. C. Collins, *Hard-scattering factorization with heavy quarks: A general treatment*, Phys. Rev. **D58**(1998) 094002, [hep-ph/9806259], [spires].

[123] W.-K. Tung, S. Kretzer, and C. Schmidt, *Open heavy flavor production in QCD: Conceptual framework and implementation issues*, J. Phys. **G28**(2002) 983, [hep-ph/0110247], [spires].

[124] S. Kretzer, H. L. Lai, F. I. Olness, and W. K. Tung, *CTEQ6 parton distributions with heavy quark mass effects*, Phys. Rev. **D69**(2004) 114005, [hep-ph/0307022], [spires].

[125] R. S. Thorne and R. G. Roberts, *A practical procedure for evolving heavy flavour structure functions*, Phys. Lett. **B421**(1998) 303, [hep-ph/9711223], [spires].

[126] R. S. Thorne and R. G. Roberts, *An ordered analysis of heavy flavour production in deep inelastic scattering*, Phys. Rev. **D57**(1998) 6871, [hep-ph/9709442], [spires].

[127] M. Buza, Y. Matiounine, J. Smith, and W. L. van Neerven, *Charm electroproduction viewed in the variable-flavour number scheme versus fixed-order perturbation theory*, Eur. Phys. J. **C1**(1998) 301, [hep-ph/9612398], [spires].

M. Buza, Y. Matiounine, J. Smith, and W. L. van Neerven, *Comparison between the various descriptions for charm electroproduction and the HERA-data*, Phys. Lett. **B411**(1997) 211, [hep-ph/9707263], [spires].

W. L. van Neerven, *Charm production in deep inelastic lepton hadron scattering*, Acta Phys. Polon. **B28**(1997) 2715, [hep-ph/9708452], [spires].

J. Smith, *Theoretical aspects of heavy-flavour electroproduction* (1997), [hep-ph/9708212], [spires].

[128] A. Chuvakin, J. Smith, and W. L. van Neerven, *Comparison between variable flavor number schemes for charm quark electroproduction*, Phys. Rev. **D61**(2000) 096004, [hep-ph/9910250], [spires].

[129] A. D. Martin, R. G. Roberts, W. J. Stirling, and R. S. Thorne, *Parton distributions incorporating QED contributions*, Eur. Phys. J. **C39**(2005) 155, [hep-ph/0411040], [spires].

[130] M. Hansson, H. Jung, and L. Jonsson, *The unintegrated gluon density in the photon and heavy quark production* (2004), [hep-ph/0402019], [spires].

[131] B. Mele and P. Nason, *The fragmentation function for heavy quarks in QCD*, Nucl. Phys. **B361**(1991) 626, [spires].

[132] S. Frixione, M. L. Mangano, P. Nason, and G. Ridolfi, *Heavy-quark production*, Adv. Ser. Direct. High Energy Phys. **15**(1998) 609, [hep-ph/9702287], [spires].

[133] B. A. Kniehl and F. Sefkow, *Summary of the heavy flavour session, DIS03* (2003), [hep-ph/0312054], [spires].

[134] B. Andersson, G. Gustafson, and C. Peterson, *A semiclassical model for quark jet fragmentation*, Zeit. Phys. **C1**(1979) 105, [spires].

B. Andersson, G. Gustafson, G. Ingelman, and T. Sjostrand, *Parton fragmentation and string dynamics*, Phys. Rept. **97**(1983) 31, [spires].

[135] T. Sjostrand, *High-energy physics event generation with PYTHIA 5.7 and JETSET 7.4*, Comput. Phys. Commun. **82**(1994) 74, [spires].

[136] B. R. Webber, *A QCD model for jet fragmentation including soft gluon interference*, Nucl. Phys. **B238**(1984) 492, [spires].

[137] D. Amati and G. Veneziano, *Preconfinement as a property of perturbative QCD*, Phys. Lett. **B83**(1979) 87, [spires].

[138] G. Marchesini *et al.*, *HERWIG: A Monte Carlo event generator for simulating hadron emission reactions with interfering gluons. Version 5.1 - April 1991*, Comput. Phys. Commun. **67**(1992) 465, [spires].

G. Corcella *et al.*, *HERWIG 6: An event generator for hadron emission reactions with interfering gluons (including supersymmetric processes)*, JHEP **01**(2001) 010, [hep-ph/0011363], [spires].

[139] C. Peterson, D. Schlatter, I. Schmitt, and P. M. Zerwas, *Scaling violations in inclusive* e^+e^- *annihilation spectra*, Phys. Rev. **D27**(1983) 105, [spires].

[140] P. Nason and C. Oleari, *A phenomenological study of heavy-quark fragmentation functions in* e^+e^- *annihilation*, Nucl. Phys. **B565**(2000) 245, [hep-ph/9903541], [spires].

[141] R. Odorico, *COJETS 6.23: A Monte Carlo simulation program for $\bar{p}p$, pp collisions and e^+e^- annihilation*, Comput. Phys. Commun. **72**(1992) 238, [spires].

[142] H. Baer, F. E. Paige, S. D. Protopopescu, and X. Tata, *ISAJET 7.48: A Monte Carlo event generator for pp, $\bar{p}p$, and e^+e^- reactions* (1999), [hep-ph/0001086], [spires].

[143] H. Jung, *Hard diffractive scattering in high-energy ep collisions and the Monte Carlo generation RAPGAP*, Comp. Phys. Commun. **86**(1995) 147, see also `http://www.desy.de/~jung/rapgap.html`, [spires].

[144] A. D. Martin, W. J. Stirling, and R. G. Roberts, *Parton distributions of the proton*, Phys. Rev. **D50**(1994) 6734, [hep-ph/9406315], [spires].

[145] T. Sjostrand *et al.*, *High-energy-physics event generation with PYTHIA 6.1*, Comput. Phys. Commun. **135**(2001) 238, [hep-ph/0010017], [spires].

[146] A. Kwiatkowski, H. Spiesberger, and H. J. Mohring, *HERACLES: An event generator for ep interactions at HERA energies including radiative processes: Version 1.0*, Comp. Phys. Commun. **69**(1992) 155, [spires].

[147] K. Charchula, G. A. Schuler, and H. Spiesberger, *Combined QED and QCD radiative effects in deep inelastic lepton-proton scattering: The Monte Carlo generator DJANGO6*, Comput. Phys. Commun. **81**(1994) 381, see also `http://www.desy.de/~hspiesb/django6.html`.

[148] M. Gluck, E. Reya, and A. Vogt, *Dynamical parton distributions of the proton and small x physics*, Z. Phys. **C67**(1995) 433, [spires].

[149] R. Engel and J. Ranft, *Hadronic photon-photon interactions at high energies*, Phys. Rev. **D54**(1996) 4244, [hep-ph/9509373], [spires].

[150] H1 Collaboration, I. Abt *et al.*, *The H1-detector at HERA*, Nucl. Instrum. Meth. **A386**(1997) 310 and 348, DESY-H1-96-01.

[151] D. Pitzl *et al.*, *The H1 silicon vertex detector*, Nucl. Instrum. Meth. **A454**(2000) 334, [hep-ex/0002044], [spires].

[152] J. Gassner, *Messung der Ortsaufloesung des H1-Siliziumvertexdetektors* (1996), Diploma ETH Zuerich.

[153] M. Kausch-Blecken von Schmeling, *The silicon microvertex detector of the H1 experiment: Readout, event reconstruction, and studies on heavy quark decays* DESY-THESIS-1998-033.

[154] H1 SPACAL Group Collaboration, T. Nicholls *et al.*, *Performance of an electromagnetic lead/scintillating fiber calorimeter for the H1 detector*, Nucl. Instrum. Meth. **A374**(1996) 149, [spires].

[155] H1 Collaboration, C. Adloff *et al.*, *Deep-inelastic inclusive ep scattering at low x and a determination of α_s*, Eur. Phys. J. **C21**(2001) 33, [hep-ex/0012053], [spires].

[156] L. Gladilin, *Charm hadron production fractions* (1999), [hep-ex/9912064], [spires].

[157] D. Abbaneo *et al.*, *LEP/SLD Heavy Flavour Working Group* (2004), LEPHF 2001-01. Available from `http://lepewwg.web.cern.ch/LEPEWWG/heavy/`.

[158] S. Eidelman *et al.*, *Review of Particle Physics*, Phys. Lett. **B592**(2004) 1, `http://pdg.lbl.gov`.

[159] MARK-III Collaboration, D. Coffman *et al.*, *Measurement of the inclusive decay properties of charmed mesons*, Phys. Lett. **B263**(1991) 135, [spires].

[160] H1 Collaboration, C. Adloff *et al.*, *Inclusive D^0 and $D^{*\pm}$ production in neutral current deep inelastic ep scattering at HERA*, Z. Phys. **C72**(1996) 593, [hep-ex/9607012], [spires].

[161] ZEUS Collaboration, J. Breitweg *et al.*, *D^* production in deep inelastic scattering at HERA*, Phys. Lett. **B407**(1997) 402, [hep-ex/9706009], [spires].

[162] H1 Collaboration, C. Adloff *et al.*, *Measurement of D^* meson cross sections at HERA and determination of the gluon density in the proton using NLO QCD*, Nucl. Phys. **B545**(1999) 21, [hep-ex/9812023], [spires].

[163] H1 Collaboration, C. Adloff *et al.*, *Measurement of $D^{*\pm}$ meson production and F_2^c in deep inelastic scattering at HERA*, Phys. Lett. **B528**(2002) 199, [hep-ex/0108039], [spires].

[164] ZEUS Collaboration, S. Chekanov *et al.*, *Measurement of $D^{*\pm}$ production in deep inelastic $e^{\pm}p$ scattering at HERA*, Phys. Rev. **D69**(2004) 012004, [hep-ex/0308068], [spires].

[165] G. J. Feldman *et al.*, *Observation of the decay $D^{*+} \to D^0\pi^+$*, Phys. Rev. Lett. **38**(1977) 1313, [spires].

[166] H1 Collaboration, A. Aktas *et al.*, *Measurement of charm and beauty photoproduction at HERA using D^* μ correlations*, Phys. Lett. **B621**(2005) 56, [hep-ex/0503038], [spires].

[167] ZEUS Collaboration, S. Chekanov *et al.*, *Measurement of beauty production in deep inelastic scattering at HERA*, Phys. Lett. **B599**(2004) 173, [hep-ex/0405069], [spires].

[168] H1 Collaboration, A. Aktas *et al.*, *Measurement of beauty production at HERA using events with muons and jets*, Eur. Phys. J. **C41**(2005) 453, [hep-ex/0502010], [spires].

[169] S. Mangano, *Charm production in charged current interactions and charm and beauty production in neutral current interactions at high Q^2* DISS-ETH-15969.

[170] ALEPH Collaboration, D. Buskulic *et al.*, *A precise measurement of* $\Gamma_{\mathrm{Z}\to b\bar{b}}/\Gamma_{\mathrm{Z}\to\mathrm{hadrons}}$, Phys. Lett. **B313**(1993) 535, [spires].

[171] J. M. Butterworth, J. P. Couchman, B. E. Cox, and B. M. Waugh, *KtJet: A C++ implementation of the K_T clustering algorithm*, Comput. Phys. Commun. **153**(2003) 85, [hep-ph/0210022], [spires].

[172] S. D. Ellis and D. E. Soper, *Successive combination jet algorithm for hadron collisions*, Phys. Rev. **D48**(1993) 3160, [hep-ph/9305266], [spires].

[173] S. Catani, Y. L. Dokshitzer, M. H. Seymour, and B. R. Webber, *Longitudinally invariant K_t clustering algorithms for hadron hadron collisions*, Nucl. Phys. **B406**(1993) 187, [spires].

[174] Particle Data Group Collaboration, K. Hagiwara *et al.*, *Review of particle physics*, Phys. Rev. **D66**(2002) 010001, [spires].

[175] H1 Collaboration, A. Aktas *et al.*, *Inclusive production of D^+, D^0, D_s^+ and D^{*+} mesons in deep inelastic scattering at HERA*, Eur. Phys. J. **C38**(2005) 447, [hep-ex/0408149], [spires].

[176] H1 Collaboration, C. Adloff *et al.*, *Measurement of neutral and charged current cross-sections in positron proton collisions at large momentum transfer*, Eur. Phys. J. **C13**(2000) 609, [hep-ex/9908059], [spires].

[177] B. W. Harris and J. Smith, *Charm quark and $D^{*\pm}$ cross sections in deeply inelastic scattering at HERA*, Phys. Rev. **D57**(1998) 2806, [hep-ph/9706334], [spires].

[178] L. Finke, *Measurement of beauty and charm photoproduction at H1 using inclusive lifetime tagging*, Proceedings for DIS 2005, Madison, Wisconsin (2005), available from `http://www.hep.wisc.edu/dis05/`.